SECONDARY ION MASS SPECTROMETRY IMAGING OF SURFACE-BOUND MICROBIAL COMMUNITIES

BY

SAGE JEROLDS BIRTCHER DUNHAM

DISSERTATION

Submitted in partial fulfillment of the requirements
for the degree of Doctor of Philosophy in Chemistry
in the Graduate College of the
University of Illinois at Urbana-Champaign, 2018

Urbana, Illinois

Doctoral Committee:

Professor Jonathan V. Sweedler, Chair
Professor Mary L. Kraft
Assistant Professor Thomas E. Kehl-Fie
Professor Paul W. Bohn, University of Notre Dame

ABSTRACT

As we move into the heart of the 21st century we are finally beginning to understand the extent of microbial influence over everyday life. Truth be told, we humans are but guests on a planet ruled by a largely unseen, and often undiscovered, microbial population. In order to understand how the microbial dimension influences our own we must first understand the microbes themselves. Far from existing as a collection of single cells floating about aimlessly, bacteria largely reside in highly cooperative multicellular communities where they work in concert to colonize and mold their surrounding environments, harvest nutrients, and wage warfare. How can these seemingly simple life forms facilitate such complicated behaviors? The answer largely resides in chemistry, for the backbone of microbial influence is built with the chemicals that they produce, secrete, sense, and consume. With clever implementation of the proper analytical tools this chemical information is ripe for our discovery and exploitation.

This dissertation primarily focuses on the adaptation and application of an existing chemical imaging technique, secondary ion mass spectrometry (SIMS) imaging, to study the chemistry underlying surface-bound microbial communities. The first chapter provides a general overview of the dissertation. The second chapter provides an introduction to mass spectrometry imaging – which encompasses a broad family of techniques including SIMS imaging – with a focus on its application to microbiology. The remaining six chapters, detailed below, describe both method development for SIMS imaging and application of the technique to explore several questions in microbiology.

SIMS is applied in conjunction with a complimentary analytical technique, confocal Raman microscopy (CRM), to study early stage biofilms formed by the gram-negative bacterium *Pseudomonas aeruginosa*, which is an opportunistic pathogen for both plants and humans. In addition to methodological advancements, this work revealed that *P. aeruginosa* accumulates highly concentrated clusters of alkyl-quinolines – including 2-heptyl-4-quinoline-*N*-oxide (HQNO) and 2-nonyl-4-quinoline-*N*-oxide (NQNO) – during the early stages of biofilm formation. HQNO and NQNO are known to disrupt the formation of healthy communities of gram-positive bacteria, and their high abundance during biofilm development suggests that *P. aeruginosa* utilizes these molecules for a competitive advantage for establishing new colonies.

In a purely methodological study, we examined the effects of applying a thin (~2 nm) layer of gold to the biofilm surface prior to SIMS imaging. This investigation revealed a signal enhancement for cluster-SIMS that, remarkably, only applied to analytes contained within biological samples. Examination of gold coated standards deposited on hard silicon wafers did not yield a signal enhancement, suggesting that the SIMS community needs to look beyond simple standard formulations when developing or adapting sample treatment strategies. Separately, a simple nitrogen desiccation procedure was developed for imaging microbial communities on semi-solid agar, which can be a challenging substrate due to the high water content. Traditionally, most SIMS studies are carried out using hard, conductive surfaces, however microbiology assays commonly require growth on semi-solid agar.

Both analyte-to-analyte differences in ionization efficiency and interfering signal from compounds with the same or similar mass-to-charge ratio (*m/z*) have largely prevented biological SIMS imaging from becoming a quantitative technique; the distribution of an analyte can be determined however the absolute quantity usually cannot. We therefore developed a quantitative SIMS imaging strategy where (1) SIMS product ion imaging is used to increase analyte specificity, (2) analyte-analyte differences in ionization efficiency are accommodated through calibration to an external quadratic calibration curve, and (3) competing ion signal is algebraically removed from each image pixel. This strategy is demonstrated by imaging the surface density of two different alkyl quinolone/quinoline isomeric pairs across several agar-based *P. aeruginosa* bacterial biofilms.

Another major challenge for SIMS imaging is the regiospecific differences in ionization efficiency, which impede direct comparison of ion intensity to analyte abundance. Heterogeneous ionization efficiency arises from a myriad of factors, including changes in the chemical microenvironment, local morphology, and conductivity of the sample. A microspot array methodology for evaluating regiospecific differences in ionization efficiency is presented, and its utility is demonstrated by evaluating several different strains of *P. aeruginosa* cultivated on semi-solid agar.

In a highly collaborative study that required the expertise of three separate research groups, the spatiochemical response of *P. aeruginosa* to antibiotic exposure was examined with SIMS imaging, CRM, and a number of traditional microbiology techniques. This study showed that *P. aeruginosa* swarms migrate away from the antibiotic source and increase their production

of several alkyl quinolones in a dose-dependent manner. Interestingly, the quorum sensing molecule known as *Pseudomonas* quinolone signal (PQS) was found to be more abundant in regions closest to the antibiotic. These results suggest that PQS is regulated independent of the other alkyl quinolones, and acts as a transient, short-range signal.

In an effort with relevance to microbial induced corrosion, a method is presented for cultivating, preparing, and examining drip-flow biofilms on metallic surfaces. Two species of bacteria, *Pseudomonas putida* and *Shewanella oneidensis*, were cultivated on both stainless and low carbon steel and examined with SIMS imaging, matrix-assisted laser desorption/ionization mass spectrometry imaging, scanning electron microscopy, and energy-dispersive x-ray spectroscopy. This study partially identifies and maps the distribution of 25 lipids and polysaccharides on *P. putida* drip-flow biofilms, examines the spatiochemical interactions between *P. putida* and *S. oneidensis* grown adjacent to one another, and examines the chemical and morphological environment of the two bacteria on corroding low-carbon steel.

Taken together, the research described in this dissertation enhances our fundamental knowledge of the chemistry underlying microbial communities. The developed analytical methodologies can be applied by other researchers to further advance our collective understanding of the microbial world.

ACKNOWLEDGEMENTS

The University of Illinois at Urbana-Champaign (UIUC) and the surrounding community is exceptionally supportive. Members of this community have made my PhD experience richer, more meaningful, and more productive. Many individuals with whom I interacted with during my time at UIUC – from my fellow students and members of my journal club, to the professors, the staff of the core facilities, and the administrative personnel – played a pivotal role in helping me accomplish the research represented in this dissertation.

I will begin by thanking Prof. Jonathan Sweedler, who is a talented and imaginative advisor and perhaps an even better person. Prof. Sweedler has created a highly supportive research group that encourages creativity and scientific exploration. My experience in Sweedler group was above and beyond what I expected out of graduate school. I also acknowledge the members of my doctoral committee: Profs. Paul Bohn, Thomas Kehl-Fie, and Mary Kraft. Their advice, support, and guidance was invaluable throughout graduate school.

I would also like to thank my colleagues in the Sweedler group who I worked closely with over these last few years, including, Amit Patel, Krishna Anapindi, Kisurb Choe, Emily Tillmaand, Elizabeth Neumann, Joseph Ellis, and Drs. Stanislav Rubakhin, Elena Romanova, Eric Lanni, Bin Li, James Checco, Troy Comi, Qian Wu, and Erik Jansson. I am particularly indebted to Dr. Eric Lanni, who left me with a great instrument that was the foundation of many of my experiments. Stephanie Baker also deserves recognition for her outstanding assistance with manuscript composition. Over the course of graduate school I also had the great opportunity to work with an extremely talented group of undergraduate students, including Kaudee Racelis, Kyungwon Ko, Stephanie Lozano, Robert Mowery, Kaitlin Medland, Kelsey Winchell, and Margaret Crotser. Their intellectual and analytical contributions can be found throughout this dissertation.

I am grateful for my academic collaborators, both those at UIUC and those at other institutions. I greatly enjoyed working with Hyunkyu Moon from UIUC, whose optimism and resolve constantly amaze me. I would like to thank Drs. Nameera Baig and Nydia Morales-Soto from the University of Notre Dame for their tireless effort, much of which was expended at the behest of my scientific curiosities.

I am indebted to many people outside of graduate school, for much in my life led me to the pursuit of a PhD and this dissertation would not exist without their contributions. I must thank my mother for teaching me what it means to be curious and creative and my father for teaching me the value and meaning of work. My wife has encouraged me to pursue my dreams and has been incredibly supportive throughout the entire process despite the hardships that it imposed. I would also like to thank Vinod and Neeru Khosla for pushing me into higher education, for this is a route that I would have been unlikely to pursue without their encouragement and support. My undergraduate education at Westminster College in Salt Lake City was invaluable. Two professors in particular, Prof. William Deutschman and Prof. Robin Hyde, had an outsized impact on my scientific development. Prof. Deutschman provided me with my earliest opportunities to work in a lab and pursue meaningful Analytical Chemistry, and was a patient mentor despite my obvious incompetence. Prof. Robyn Hyde taught me most of what I know about Organic Chemistry and the scientific process and gave me the freedom and resources to pursue independent research projects. My friends and fellow students at Westminster College enhanced my learning and helped to make the in-between times more enjoyable.

Finally I must acknowledge the financial support that allowed me to fully dedicate my efforts to this research. The research discussed here was primarily funded through the National Institutes of Health, the Department of Energy, and the Department of Defense. My salary, tuition, and travel stipends were provided through individual fellowships from the Robert C. and Carolyn J. Springborn Graduate Fellowship Program, the National Science Foundation Graduate Fellowship Program, and the Eastman Chemical Company.

TABLE OF CONTENTS

CHAPTER 1: Introduction and Dissertation Overview.....1

CHAPTER 2: Mass Spectrometry Imaging of Complex Microbial Communities.....11

CHAPTER 3: Multimodal Chemical Imaging of Molecular Messengers in Emerging *Pseudomonas aeruginosa* Bacterial Communities.....28

CHAPTER 4: Metal-Assisted Polyatomic SIMS and Laser Desorption/Ionization for Enhanced Small Molecule Imaging of Bacterial Biofilms.....45

CHAPTER 5: Quantitative SIMS Imaging of Agar-Based Microbial Communities.....70

CHAPTER 6: Method for Evaluating Heterogeneous Ionization Efficiency in Biomolecular Mass Spectrometry Imaging.....96

CHAPTER 7: Antibiotic Exposure Induces Spatially Dependent Variations in Alkyl Quinolone Signaling During *Pseudomonas aeruginosa* Swarming.....122

CHAPTER 8: A Versatile Workflow for Chemical and Architectural Characterization of Drip Flow Microbial Biofilms.....148

CHAPTER 1

Introduction and Dissertation Overview

According to the American Chemical Society, "Analytical Chemistry is the science of obtaining, processing, and communicating information about the composition and structure of matter. In other words, it is the art and science of determining what matter is and how much of it exists."[1] An ideal analytical tool would therefore be capable of examining a material in its entirety and providing the comprehensive chemical composition and organizational structure. Unfortunately, the natural and manufactured materials that we interact with on a daily basis have an incredibly complicated chemical composition and organization. Materials often contain functionally relevant features that are fractions of a micrometer to meters in size, and can be made up of thousands of distinct and heterogeneously distributed chemical entities. When viewed from this perspective, the task of an analytical chemist can appear extraordinarily daunting. Fortunately, the modern measurement scientist has a full quiver of analytical instrumentation and methodologies at their disposal. Each component of this proverbial quiver has been highly adapted over decades or centuries to target specific chemistries or organizational structures that make up the materials around us. By carefully selecting and modifying the contents of this quiver we can begin to tackle the grand challenges of Analytical Chemistry and help to move science and technology forward into the next period of innovation.

One technique that has emerged over the last few decades to become an integral tool for understanding chemical composition and organization is mass spectrometry imaging (MSI). MSI utilizes a focused microprobe of light, ions, charged solvent droplets, or some combination thereof, to desorb and ionize chemicals from the surface of a material. The resulting ions are focused into a mass spectrometer, where they can be analyzed to determine their mass-to-charge ratio (*m/z*), and, with some additional analysis, their elemental composition and molecular structure. Ion images are generated by sequentially examining multiple positions on the sample and associating the resulting signals to their point of origin through post-processing. The distributions of the analytes of interest are then represented using false-color maps. In contrast to many other chemical imaging techniques, MSI is highly multiplexed, meaning that hundreds or thousands of ions can be simultaneously analyzed with minimal *a priori* knowledge.

This dissertation primarily discusses one specific subset of MSI, known as secondary ion mass spectrometry (SIMS) imaging. SIMS is so named because it utilizes a highly focused beam of ions to desorb "secondary ions" from the sample surface for subsequent mass spectrometric analysis. In comparison to other ionization modalities used in MSI, SIMS is capable of achieving a superior spatial resolution, is especially good for imaging small molecules with a *m/z* less than 1000, and requires minimal sample pre-treatment.

In the first year of my dissertation research, I was fortunate to work beside a talented graduate student, Dr. Eric Lanni, who had spent the previous four years designing and constructing a custom SIMS instrument (**Figure 1.1**). The details of this instrument, referred to as the "C_{60}-SIMS", can be found in Dr. Lanni's graduate dissertation[2] and in our research manuscript.[3] This instrument has several innovative features that are important for the research described herein. First, it is equipped with a Buckminsterfullerene (C_{60}) primary ion source, which – in contrast to the traditional SIMS sources that commonly utilize gold, cesium, or bismuth ions – generates a much "softer" ionization profile. This means that the sample experiences less surface damage during analysis and that the secondary ions are more often left intact, and are therefore more readily detectable and assignable to the chemical species from

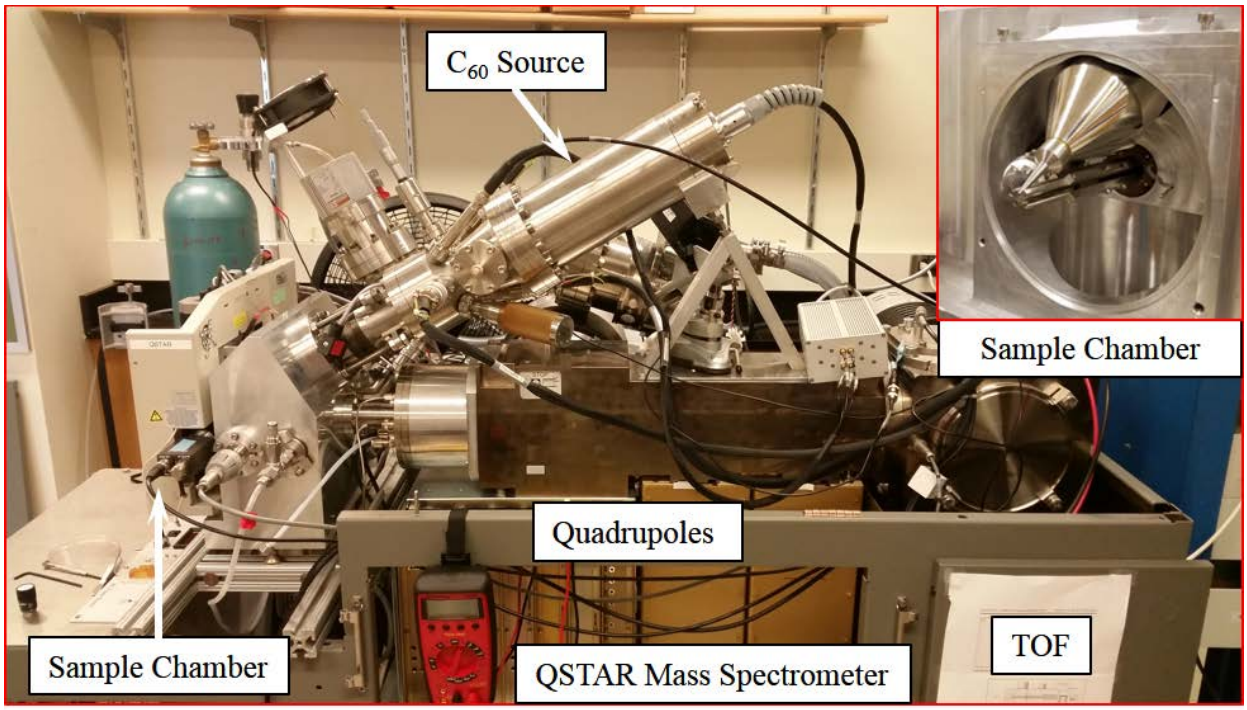

Figure 1.1. The lab-built C_{60}-SIMS QSTAR XL imaging mass spectrometer in all its glory. The inset image shows the interface between the ion source, the first quadrupole, and the electron detector.

which they originate. Second, the C_{60} primary ion source is coupled to an AB SCIEX QSTAR XL mass spectrometer, which is equipped with a series of focusing and mass selective quadrupoles, an argon collision cell, and an orthogonal time-of-flight (TOF) mass analyzer. These components are incredibly important for SIMS imaging of biological materials. The mass selective quadrupole provides ion fragmentation and tandem MS capabilities, which are needed for *in situ* chemical identification and highly specific ion imaging. The orthogonal TOF mass analyzer decouples the secondary ion generation event from the detection event, enabling analysis of surfaces with irregular morphologies and allowing for a continuous primary ion beam – which makes analysis faster and more sensitive.

The following chapters describe the application of this C_{60}-SIMS imaging mass spectrometer to examine the chemistry underlying surface bound microbial communities. Much of the focus surrounds the gram-negative bacterium *Pseudomonas aeruginosa*, which is an opportunistic pathogen for both plants and humans. As of February of 2017, *P. aeruginosa* has been classified by the World Health Organization as a Priority 1 pathogen in critical need of novel antibiotics.[4] In humans, *P. aeruginosa* primarily infects individuals with a compromised immune system, such as burn victims and patients with cystic fibrosis (CF). CF is a genetic disorder that leads to the buildup of mucus in the lungs. Once established, *P. aeruginosa* infections can be incredibly difficult to eradicate, partially because the organism creates a protective environment that allows it to survive and adapt in the face of antibiotic treatment. This protective environment, which is comprised of a chemical milieu of extracellular DNA, proteins, polysaccharides, lipids and a host of small molecules, is commonly referred to as a "biofilm".

P. aeruginosa infections can be incredibly problematic for patients with CF. The mucoid filled lungs act as an especially attractive environment for bacterial colonization, and antibiotic treatment only serves to temporarily halt the infection, not fully eradicate it. Over multiple years of treatment the *P. aeruginosa* community contained within the pulmonary tract becomes highly resistant to antibiotics, allowing it to survive and persist indefinitely. Nearly 80% of CF adults from 25 to 34 years of age are infected with *P. aeruginosa*[5] and the primary cause of death in most CF individuals is chronic pulmonary disease – which is caused by *P.* aeruginosa and several other microrganisms.[6] Although much is known about the genes and proteins involved in *P. aeruginosa* biofilm formation and chronic pulmonary infection, there is a large gap in our

collective knowledge around the role that small molecules play. One goal of my graduate work has been to develop new tools and workflows to help sample this small molecule dimension.

The next chapter of this dissertation, **Chapter 2**, provides a brief overview of MSI in microbiology. It includes a general introduction to MSI technology and highlights several important applications in microbiology. **Chapter 2**, which was adapted from an article originally published in *Accounts of Chemical Research*,[7] also highlights a series of developmental challenges that must be overcome to move the field forward.

Chapter 3 is adapted from an original research article published in *Analyst*.[8] This chapter describes the combination of two complementary chemical imaging modalities, confocal Raman microscopy (CRM) and C_{60}-SIMS, to examine emerging *P. aeruginosa* biofilms (**Figure 1.2)**. CRM – which is a vibrational imaging technique – can be used to identify analytes based on the presence of chemical functional groups. It is capable of achieving a better spatial resolution than most imaging mass spectrometers and can be applied to living systems. By combining the strengths of CRM with the specificity of C_{60}-SIMS imaging, we found several important molecules to be present in high abundance during early stage *P. aeruginosa* biofilm development. From a methodological standpoint, this chapter also contains one of the earliest examples of SIMS product ion imaging, which is a sampling approach used heavily throughout much of the research contained in this dissertation.

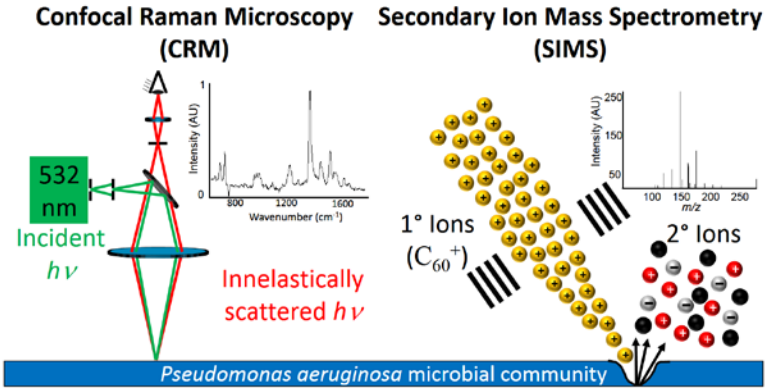

Figure 1.2. Schematic of confocal Raman microscopy (CRM) and secondary ion mass spectrometry (SIMS). Reproduced with permission from ref. 8. Copyright 2015 Royal Society of Chemistry.

Chapter 4, which is adapted from a research article published in *Biointerphases*,[9] describes of a method for enhancing ion signal with both C_{60}-SIMS and laser desorption ionization (LDI). Application of a ~2.5 nm layer of gold to the biofilm surface results in an increase in the molecular ion signal for two specific molecular classes, 2-alkyl-quinolones and rhamnolipids, by up to 150%. Although the exact mechanism of this enhancement were beyond the scope of this manuscript, we observed a simultaneous suppression in the fragmentation and ionization of background polymers from the cell culture medium, suggesting that a reduction in

ion suppression may be one cause. One of the most noteworthy aspects of this study was that the enhancement was not observed for standards on a hard silicon surface. The substrate-specific enhancement suggests that the SIMS community may be overlooking promising sample treatment strategies by focusing their method development efforts exclusively on standards contained within extremely controlled environments.

In **Chapter 5**, methodologies are presented for (1) preparing agar-based microbial communities for high-vacuum conditions, and (2) absolute quantitation with SIMS imaging. Biofilms cultivated on flat surfaces, such as the silicon wafers employed in **Chapters 3** and **4**, offer an excellent model for understanding chemical content and microscopic distribution, however the resulting samples are macroscopically homogeneous and devoid of large-scale spatial information. Semi-solid agar is one of the most common mediums used for microbiology assays, however the high water content of this material presents a challenge for vacuum compatibility (which is necessary for SIMS imaging). We therefore developed a simple dehydration-based method for preserving biofilms cultivated on agar. The changes in sample morphology and chemical distribution resulting from dehydration were carefully examined. This chapter further describes a polynomial-based calibration methodology for generating quantitative SIMS images (**Figure 1.3**). The capabilities of the sample preparation and quantitation strategies were explored by imaging several agar-based *P. aeruginosa* colony biofilms. A modified version of **Chapter 5** is published in *Analytical Chemistry*.[10]

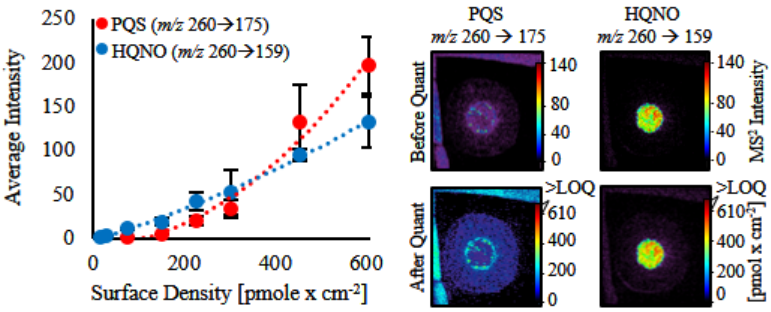

Figure 1.3. Quantitative SIMS imaging of agar-based microbial communities. Intensity values are converted to surface density via external quadratic calibration and fragmentation correction. Adapted with permission from *Analytical Chemistry*, ref. 10. Article In Press, copyright 2018 American Chemical Society.

In addition to quantitation, one of the biggest challenges facing the MSI community is regiospecific variations in ionization efficiency, which are caused by local differences in the chemical microenvironment, sample morphology, conductivity, and a myriad of other factors. Taken together, these factors largely prohibit direct correlation between ion intensity and analyte abundance. In **Chapter 6**, a microdroplet array methodology is presented for: (1) evaluating

regiospecific variations in ionization efficiency, (2) utilization as a fiducial system for multimodal chemical and morphological characterization of ion suppression, and (3) use for evaluating the efficacy of different data normalization and data collection strategies. The utility of this methodology is demonstrated by evaluating ion images generated from agar-based *P. aeruginosa* colony biofilms (**Figure 1.4**). As of April 16th, 2018 a modified version of **Chapter 6** is in the final stages of preparation for submission to a peer reviewed scientific journal.

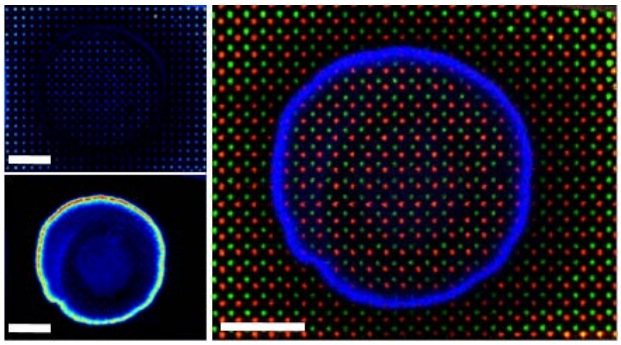

Figure 1.4. Utilization of a microspot array to evaluate ion images of generated from *P. aeruginosa* colony biofilms. Shown are ion images for both exogenous and endogenous analytes in a pqsA$^-$ mutant biofilm. All scale bars represent 5 cm.

Chapter 7 covers the results of a large collaborative study between the laboratories of Profs. Jonathan Sweedler, Paul Bohn, and Joshua Shrout. In this work, a modified version of which is published in the *Journal of Biological Chemistry*,[11] the spatial and chemical organization of *P. aeruginosa* swarming communities is examined during exposure to tobramycin and carbenicillin – two antibiotics used to treat *P. aeruginosa* infections. During swarming, *P. aeruginosa* cells exhibit a remarkably cooperative behavior in which they form rafts and migrate to colonize new regions of this surface. This phenotype is known to confer an increased resistance to antibiotics, however the reasons for this resistance are not fully understood.[12] Using a combination of quantitative C_{60}-SIMS product ion imaging (**Figure 1.5**), CRM, and several traditional microbiology techniques, we show that *P. aeruginosa* swarms migrate

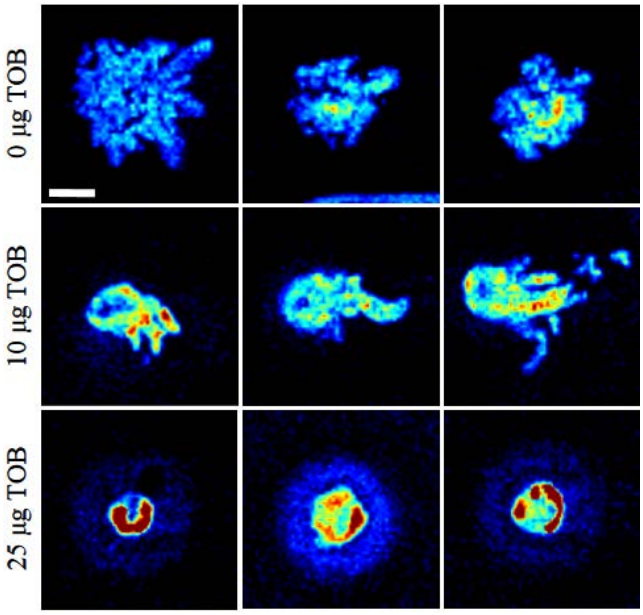

Figure 1.5. Ion images for *Pseudomonas* quinolone signal in nine *P. aeruginosa* swarms exposed to 0, 10, and 25 µg tobramycin. The scale bar represent 2 mm. Adapted with permission from the *Journal of Biological Chemistry*, ref. 11. Article In Press, copyright 2018 American Society for Biochemistry and Molecular Biology.

away from the antibiotic source, begin to initiate biofilm formation, and alter their produce several important cell-to-cell signaling molecules, including *Pseudomonas* quinolone signal. **Chapter 7** also describes how *P. aeruginosa* varies its chemical and physical response depending on the antibiotic source, and shows that a genetic mutant deficient in the production of *Pseudomonas* quinolone signal exhibits increased survival in the presence of tobramycin.

In the final chapter (**Chapter 8**) a set of methodologies for examining flow-cell biofilms is presented. Here the focus shifts to a different microbial system with relevance to microbial induced corrosion (MIC, also referred to as "biocorrosion"), which is the degradation of metal or stone caused by, or increased by, the presence of microbes. MIC causes extensive damage to both private and public infrastructure, with an estimated annual cost in the hundreds of billions of dollars.[13-14] **Chapter 8** describes a versatile flow-cell biofilm reactor, details a procedure for cultivating biofilms on metal substrates, and describes methods for imaging the resulting samples with a host of analytical techniques, including SIMS, matrix-assisted laser desorption/ionization (MALDI), and scanning electron microscopy (**Figure 1.6**). We demonstrate the methodologies by examining two species of bacteria, *Pseudomonas putida* and *Shewanella oneidensis*, under a

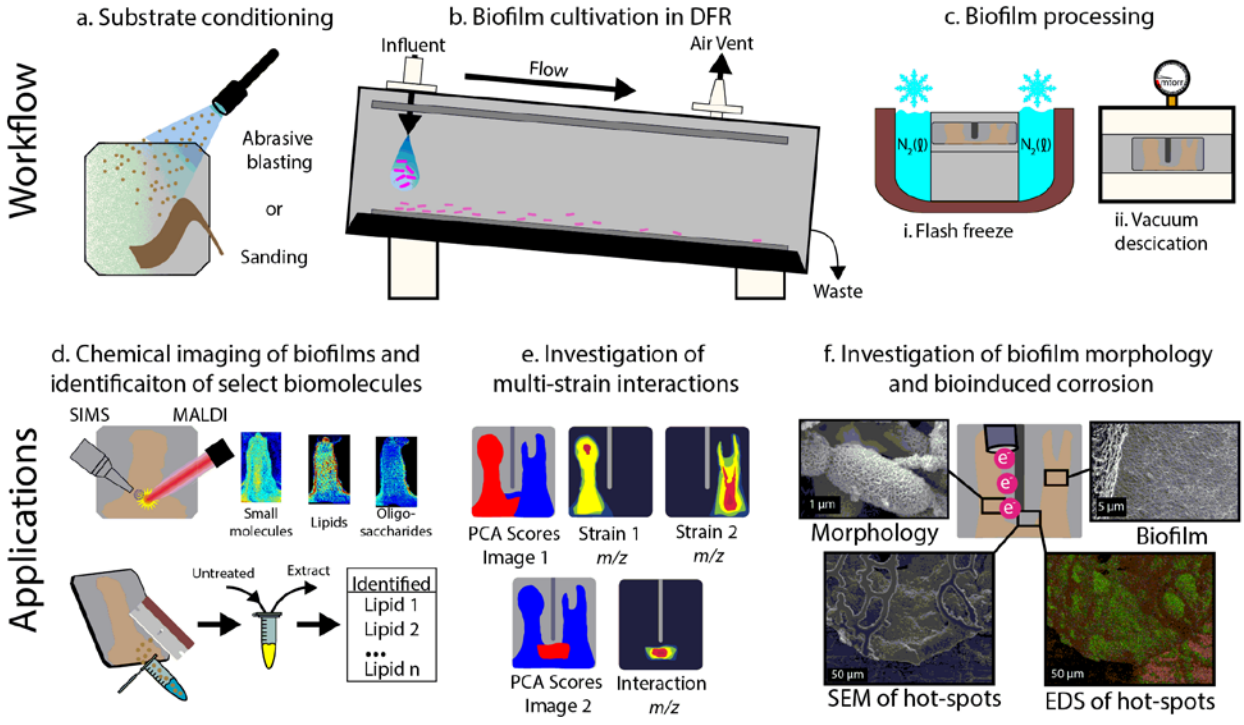

Figure 1.6. Workflow for cultivating and characterizing drip-flow biofilms. Adapted with permission from *Analytical Chemistry*, submitted for publication. Unpublished work copyright 2018 American Chemical Society.

variety of growth conditions, including co-cultures on both stainless and low carbon (corroding) steel. As of April 16th, 2018, the work presented in **Chapter 8** is undergoing peer review for possible publication in *Analytical Chemistry*.

The primary focus of this dissertation is on SIMS imaging of microbial communities, however, as an analytical chemist in a diverse lab, I have had the great pleasure of working on many different projects, some of which are available in published research articles and some of which remain unpublished. I wish to highlight some of this work here.

This includes the initial design and construction of the C_{60}-SIMS instrument. In this work Dr. Eric Lanni and I imaged cultured neurons and neural networks from the sea slug *Aplysia californica* (**Figure 1.7)**, and demonstrated a sublimation-based matrix application method for improved SIMS signal.[3] Since the original construction of the C_{60}-SIMS, I have worked with my colleagues (primarily Dr. Troy Comi and Joe Ellis) to: (1) install a secondary electron collector, which is vital for tuning and evaluating the primary ion beam; (2) add a second power supply for the main instrument turbomolecular pumps, optimize the pump layout, and install a series of cooling fans – modifications that have improved the instrument stability and durability; (3) install insulated jacketing for the primary ion beam, which helps provide a stable primary ion beam current; and (4) upgrade the primary ion beam to 40 kV, which provides greater secondary ion yields and an improved spot size. I also collaborated with Dr. Troy Comi, Dr. Thanh Do, and Dr. Stanislav Rubakhin to modify the C_{60}-SIMS instrument for application to high-throughput single-cell profiling.[15] The primary focus of the single-cell profiling work was the chemical differentiation of dorsal root ganglia neurons into distinct subpopulations based off of their lipid composition.[15]

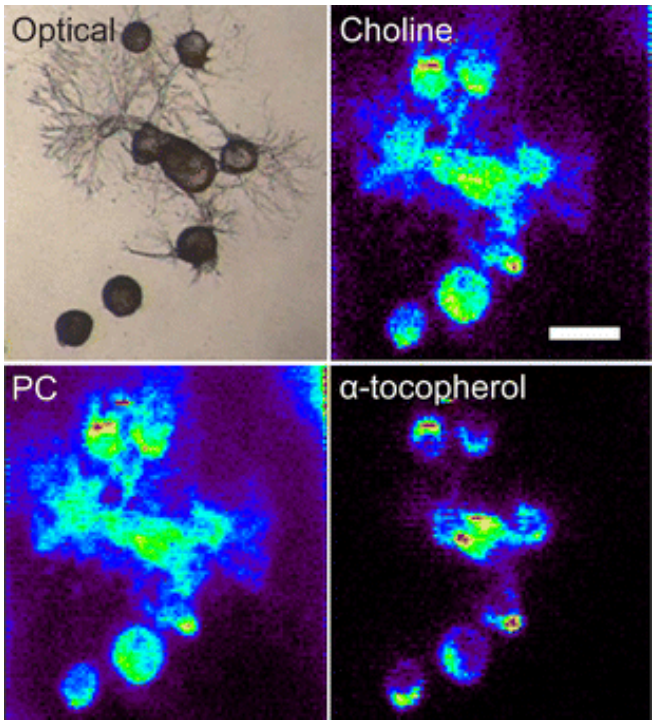

Figure 1.7. C_{60}-SIMS imaging of choline, the phosphocholine headgroup, and α-tocopherol in cultured neurons from *Aplysia californica*. The scale bar is 200 μm. Adapted with permission from ref. 3., copyright 2014 American Chemical Society.

Early in my graduate career I worked with Drs. Eric Lanni, Rachel Masyuko, and Callen Driscoll, to develop a microdroplet array approach to correlate high resolution SIMS and CRM images of static *P. aeruginosa* biofilms.[16] We used this methodology to image small alkyl quinolone pockets on the biofilm surface and applied *in situ* tandem-MS to identify several analytes. Along with several other manuscripts authored by Drs. Eric Lanni abd Rachel Masyuko, this work laid the initial groundwork for much of the research presented in the main chapters of this dissertation.

I also collaborated with Drs. Bin Li, Troy Comi, and Tong Si to develop a sample preparation methodology for agar-based *Bacillus subtilis* biofilms for MALDI imaging.[17] In MALDI, the sample must be coated in a light absorbing organic matrix before analysis, which can be complicating factor due to the propensity for the matrix solvent to absorb into the agar and degrade or distort the sample. In this work, two spray-based methodologies were optimized to apply MALDI matrix directly to the hydrated agar. Remarkably, the gas flow acts to almost completely dehydrate the sample, and a simple 1 h stint in the vacuum dissector is all that is needed for full preparation.[17]

Finally, I would like to highlight an ongoing project, part of which was published as a conference proceedings[18] but is currently in preparation for a full research manuscript. Here, I collaborated with Hyunkyu Moon and Dr. Troy Comi to design and build an analytical platform that combines thermal desorption atomic force microscopy (AFM) with mass spectrometry to perform high resolution chemical imaging (**Figure 1.8**). In this method, the sharp AFM tip is brought in close proximity to the sample surface and electrical current is used to rapidly heat the tip and induce a localized thermal desorption event. The desorption plume is transported into a vacuum chamber for collection and offline chemical analysis. Because this approach is capable of sampling an entire 3-D voxel (as opposed to only a small region near the sample surface), it is expected to be capable of imaging at a spatial resolution of better than 1 μm.

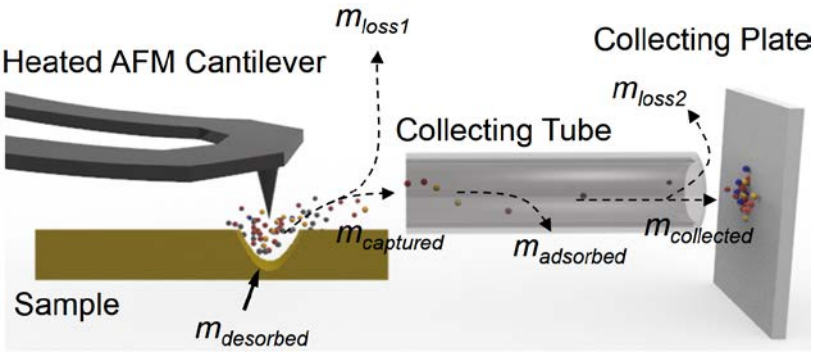

Figure 1.8. Schematic of the thermal desorption AFM-MS setup. The material on the collection plate can be sampled with any number of mass spectrometry modalities.

1.1. References

1. Society, A. C. What is Analytical Chemistry". https://www.acs.org/content/acs/en/careers/college-to-career/areas-of-chemistry/analytical-chemistry.html (accessed November 1, **2017**).
2. Lanni, E. J. Molecular imaging with mass spectrometry: Instrumental and methodological advances for biological applications. Doctoral, University of Illinois at Urbana-Champaign, Urbana, IL, USA, **2014**.
3. Lanni, E. J.; Dunham, S. J. B.; Nemes, P.; Rubakhin, S. S.; Sweedler, J. V., Biomolecular Imaging with a C60-SIMS/MALDI Dual Ion Source Hybrid Mass Spectrometer: Instrumentation, Matrix Enhancement, and Single Cell Analysis. *Journal of The American Society for Mass Spectrometry* **2014,** *25* (11), 1897-1907.
4. E Tacconelli, N. M., Global Priority List of Antibiotic-Resistant Bacteria to Guide Research, Discovery, and Development of New Antibiotics. Organization, W. H., Ed. World Helth Organization: 2017; p 7.
5. LiPuma, J. J., The Changing Microbial Epidemiology in Cystic Fibrosis. *Clinical Microbiology Reviews* **2010,** *23* (2), 299-323.
6. O'Sullivan, B. P.; Freedman, S. D., Cystic fibrosis. *The Lancet* **2009,** *373* (9678), 1891-1904.
7. Dunham, S. J. B.; Ellis, J. F.; Li, B.; Sweedler, J. V., Mass Spectrometry Imaging of Complex Microbial Communities. *Accounts of Chemical Research* **2017,** *50* (1), 96-104.
8. Baig, N. F.; Dunham, S. J. B.; Morales-Soto, N.; Shrout, J. D.; Sweedler, J. V.; Bohn, P. W., Multimodal chemical imaging of molecular messengers in emerging Pseudomonas aeruginosa bacterial communities. *Analyst* **2015,** *140* (19), 6544-6552.
9. Dunham, S. J. B.; Comi, T. J.; Ko, K.; Li, B.; Baig, N. F.; Morales-Soto, N.; Shrout, J. D.; Bohn, P. W.; Sweedler, J. V. Metal-assisted polyatomic SIMS and laser desorption/ionization for enhanced small molecule imaging of bacterial biofilms *Biointerphases* [Online], **2016**, p. 02A325.
10. Dunham, S. J. B.; Ellis, J. F.; Baig, N. F.; Morales-Soto, N.; Cao, T.; Shrout, J. D.; Bohn, P. W.; Sweedler, J. V., Quantitative SIMS Imaging of Agar-Based Microbial Communities. *Analytical Chemistry* **2018**, In Press.
11. Morales-Soto, N.; Dunham, S. J. B.; Baig, N. F.; Ellis, J. F.; Madukoma, C. S.; Bohn, P. W.; Sweedler, J. V.; Shrout, J. D., Spatially-dependent alkyl quinolone signaling responses to antibiotics in Pseudomonas aeruginosa swarms. *Journal of Biological Chemistry* **2018**, In Press.
12. Overhage, J.; Bains, M.; Brazas, M. D.; Hancock, R. E. W., Swarming of Pseudomonas aeruginosa Is a Complex Adaptation Leading to Increased Production of Virulence Factors and Antibiotic Resistance. *Journal of Bacteriology* **2008,** *190* (8), 2671-2679.
13. Kip, N.; van Veen, J. A., The dual role of microbes in corrosion. *ISME Journal* **2015,** *9* (3), 542-551.
14. Koch, K. H.; Brongers, M. P. H.; Thompson, N. G.; Virmani, Y. P.; Prayer, J. H., Corrosion Costs and Preventive Strategies in the United States. Administration, U.S. Department of Transportation Federal Highway Administration, Publication No. FHWA-RD-01-156 2002; 1-12.
15. Do, T. D.; Comi, T. J.; Dunham, S. J. B.; Rubakhin, S. S.; Sweedler, J. V., Single Cell Profiling Using Ionic Liquid Matrix-Enhanced Secondary Ion Mass Spectrometry for Neuronal Cell Type Differentiation. *Analytical Chemistry* **2017,** *89* (5), 3078-3086.
16. Lanni, E. J.; Masyuko, R. N.; Driscoll, C. M.; Dunham, S. J. B.; Shrout, J. D.; Bohn, P. W.; Sweedler, J. V., Correlated Imaging with C(60)-SIMS and Confocal Raman Microscopy: Visualization of Cell-Scale Molecular Distributions in Bacterial Biofilms. *Analytical Chemistry* **2014,** *86* (21), 10885-10891.
17. Li, B.; Comi, T. J.; Si, T.; Dunham, S. J. B.; Sweedler, J. V., A one-step matrix application method for MALDI mass spectrometry imaging of bacterial colony biofilms. *Journal of Mass Spectrometry* **2016,** *51* (11), 1030-1035.
18. Moon, H.; Comi, T. J.; Dunham, S. J. B.; Kwon, B.; Sweedler, J. V.; King, W. P., Microscale transport physics during atomic force microscopy mass spectrometry and improved sampling efficiency. *TRANSDUCERS* **2017**, 24-47.

CHAPTER 2

Mass Spectrometry Imaging of Complex Microbial Communities

2.1. Acknowledgements

This chapter was originally published as an Account in *Accounts of Chemical Research* **2017**, 50 (1), 96-104 and has been adapted here with permission from the American Chemical Society. Sage J. B. Dunham, Joseph F. Ellis, Bin Li, and Jonathan V. Sweedler contributed to the original manuscript and are coauthors. The manuscript was principally written by SJBD, however JFE, BL and JVS all made significant contributions. Financial support was provided by the National Institute of Allergy and Infectious Diseases of the National Institutes of Health under Award R01AI113219 and the Department of Energy through a subcontract from Oak Ridge National Laboratory (PTX-UT-Battelle) under Award ORNL-4000134575.

2.2. Introduction

Bacteria influence nearly every aspect of life on earth. The estimated one trillion bacterial species on our planet have successfully colonized most habitable environments, from the depths of the Mariana Trench to the limits of the stratosphere.[1-3] Far from behaving as isolated and independent organisms, bacteria usually reside in surface-bound multicellular communities where they work in concert to efficiently harness surrounding nutrients, protect one another from adverse environmental conditions, and launch coordinated expeditions in search of new territory. The influence of microbial communities on humankind is beyond dispute: bacteria, archaea, and fungi are both partners and adversaries to our health, and they interact with plants and animals to influence growth, vitality, disease, and many processes critical to life. In an affirmation of the significance of these multispecies ecosystems, our nation's newest national research initiative—the National Microbiome Initiative—seeks to develop a better understanding of complex microbial communities and their relationship to food, energy, and health.[4-5]

Dynamic molecular processes define many aspects of microbial life, including behavioral coordination, antibiotic resistance, and competition between groups. How do distinct single cell organisms coordinate their actions? Intra- and interspecies bacterial communication occurs via a density-dependent molecular exchange process termed quorum sensing, in which individual cells

secrete and sequester small-molecule messengers and "sense" the surrounding population. As a result of altered translation of ancillary genes, quorum sensing leads to the coordinated onset of many complex behavioral patterns, including surface colonization, biofilm formation, virulence, and programed cell lysis.[6] For example, in the Gram-negative bacterium *Pseudomonas aeruginosa*, a well-studied model for biofilm formation, the interplay between two quorum-sensing molecules (acyl-homoserine lactones from the las and rhl systems) control the expression of up to 10% of the total genome.[7] Outside of cell–cell communication, lipids, proteins, polysaccharides, and extracellular DNA (collectively termed the "extracellular polymeric substance" or EPS) shape the local microenvironment and form a three-dimensional scaffolding, or biofilm, that supports colony survival. From these examples and others, it is apparent that molecular-level scientific evaluations are necessary both for understanding how microbial systems function and for influencing this function.

Much of our existing knowledge about the chemical environment in microbial communities has arisen from genomics and transcriptomics, which enable genes and their expected products to be probed without prior knowledge of their identity. These studies are often followed by targeted analytical approaches, such as bioluminescence, fluorescence microscopy, or autoradiography, all of which provide temporal and spatial detail but require analyte preselection. Oftentimes, less targeted molecular characterization is required. Today's most chemically information-rich approaches include nuclear magnetic resonance, vibrational spectroscopy and, to a greater extent, offline chromatographic techniques such as liquid chromatography (LC) and gas chromatography coupled to mass spectrometry (GC–MS).

One attractive approach that complements traditional chemical measurement techniques by providing untargeted and highly multiplexed chemical imaging data is mass spectrometry imaging (MSI). In MSI, the sample is bombarded with a focused microprobe to induce desorption of chemical compounds into the gas phase, where they are ionized and discriminated on the basis of the mass-to-charge ratio (*m/z*) (**Figure 2.1**). The desorption and ionization process is sequentially repeated over the entire sample, and postprocessing of the position-correlated mass spectra provides a series of false-color ion maps that display the distribution and abundance of each ion.

Since the first applications of MSI to microbiology in the early 2000s,[8] the approach has been used in more than 100 studies ranging from quantitative subcellular imaging of symbiotic

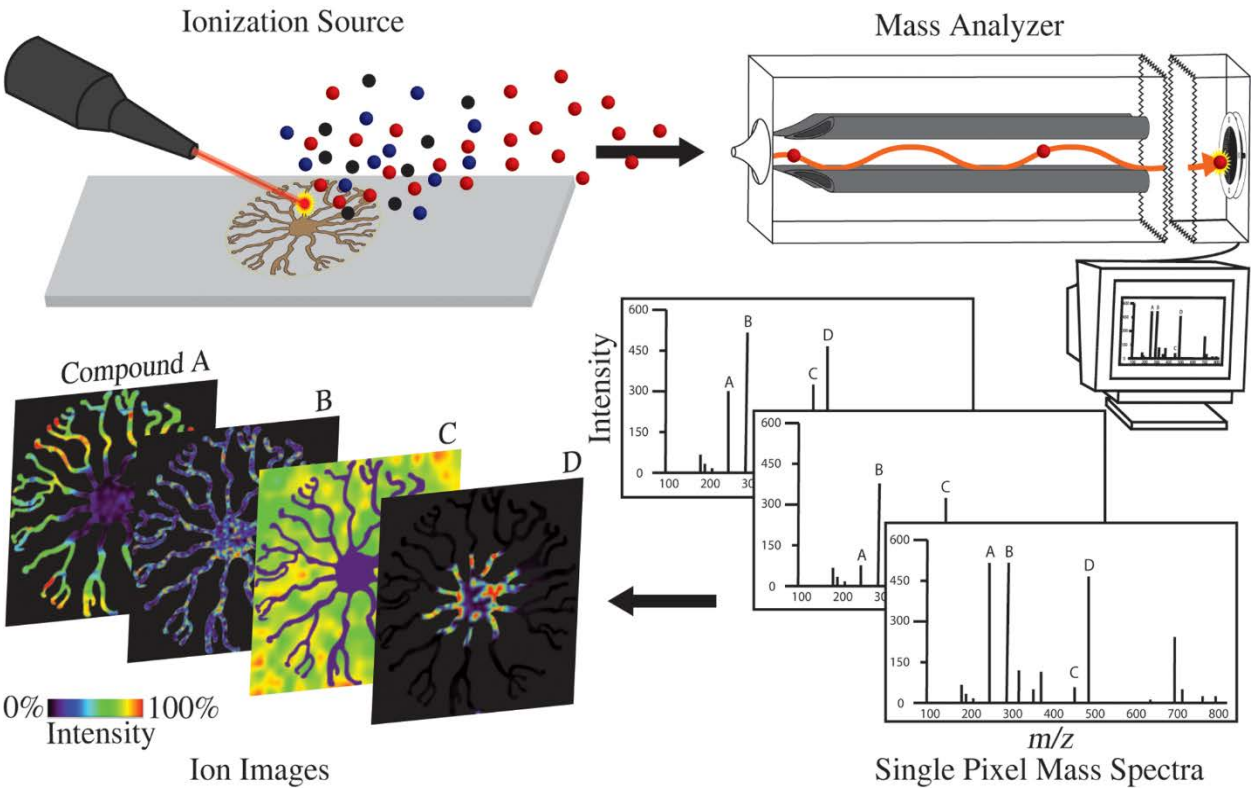

Figure 2.1. General overview of MSI. A focused microprobe desorbs molecules into the gas phase, where they are ionized and electrically focused into the mass analyzer. Subsequent mass-to-charge ratio (*m/z*) differentiation and detection produce a mass spectrum for each point across the sample. The abundance of each ion of interest is then plotted as a function of location to produce false-color ion images of specific molecular features.

nitrogen fixation by bacteria inside shipworm gills[9] to profiling microbial metabolites across the human skin surface.[10] Because of its unique capability to interrogate complex samples with spatial and chemical specificity and its complementarity to genomic and transcriptomic measurements, MSI continues to offer unmatched molecular detail on ever more complex microbial ecologies.

This Account provides an overview of the instrumentation and sample preparation strategies for microbial MSI, highlights applications that demonstrate the enormous potential of the technique, and describes several existing measurement challenges and the potential routes by which these challenges can be overcome. Interested readers are referred to a comprehensive review of MSI[11] and its specific application to microbiology.[12]

2.3. Current State of Technology

Much as a surgeon's choice of scalpel is contingent upon the incision to be made, the microbiologist's choice of MSI sampling procedure and instrumentation should be determined

by the constraints imposed by the specific sample under examination. A comprehensive survey of a chemically complex microbial community is not possible with a single MSI experiment, as any given measurement ensemble is capable of providing information on only a fraction of the molecules present. The details of the chosen sample preparation and MSI instrumentation determine which of these chemicals are observable.

2.3.1. Ionization and Sample Preparation in Microbial MSI

Often the first choice made when designing a microbial MSI experiment is the ionization method, as this decision influences the obtainable chemical coverage, the achievable spatial resolution, and the requirements for sample preparation. Of the wide array of ionization approaches reported in the literature, only three are commercially available and commonly used in microbiology. These three approaches utilize focused probes of light, primary ions, or electrospray solvents to facilitate the process of desorption and ionization and are termed matrix-assisted laser desorption/ionization (MALDI), secondary ion mass spectrometry (SIMS), and desorption electrospray ionization (DESI), respectively.

2.3.1.1. Matrix-Assisted Laser Desorption/Ionization

Representing approximately half of all microbial MSI publications, MALDI offers the most comprehensive coverage of molecular species. Lipids, peptides, and proteins are all accessible with the proper matrix selection, and the technique commonly achieves a spatial resolution of better than 100 μm for microbial samples. The ultimate achievable spatial resolution in an MSI experiment—generally defined as the measure of how closely two objects can be and still be resolved—is a function of not only instrument parameters (e.g., microprobe size, raster width, sensitivity) but also properties inherent to the sample itself, such as feature size and chemical abundance. Although uncommon, resolutions of better than 5 μm have been demonstrated in MALDI applications outside of microbiology by using specially adapted ion optics and matrix application procedures.[13-14]

Important applications of MALDI MSI in microbiology include the visualization of chemical interactions between different species of *Pseudomonas aeruginosa* and *Staphylococcus aureus* (**Figure 2.2a**),[15] characterization of surfactants and peptides produced by different strains of *Bacillus subtilis* (**Figure 2.2b**),[16] imaging of nutritionally dependent *P. aeruginosa* proteins produced in a heterogeneous drip-flow reactor (**Figure 2.2c**),[17] and characterization of the chemical response of *P. aeruginosa* to the addition of the antibiotic azithromycin (**Figure**

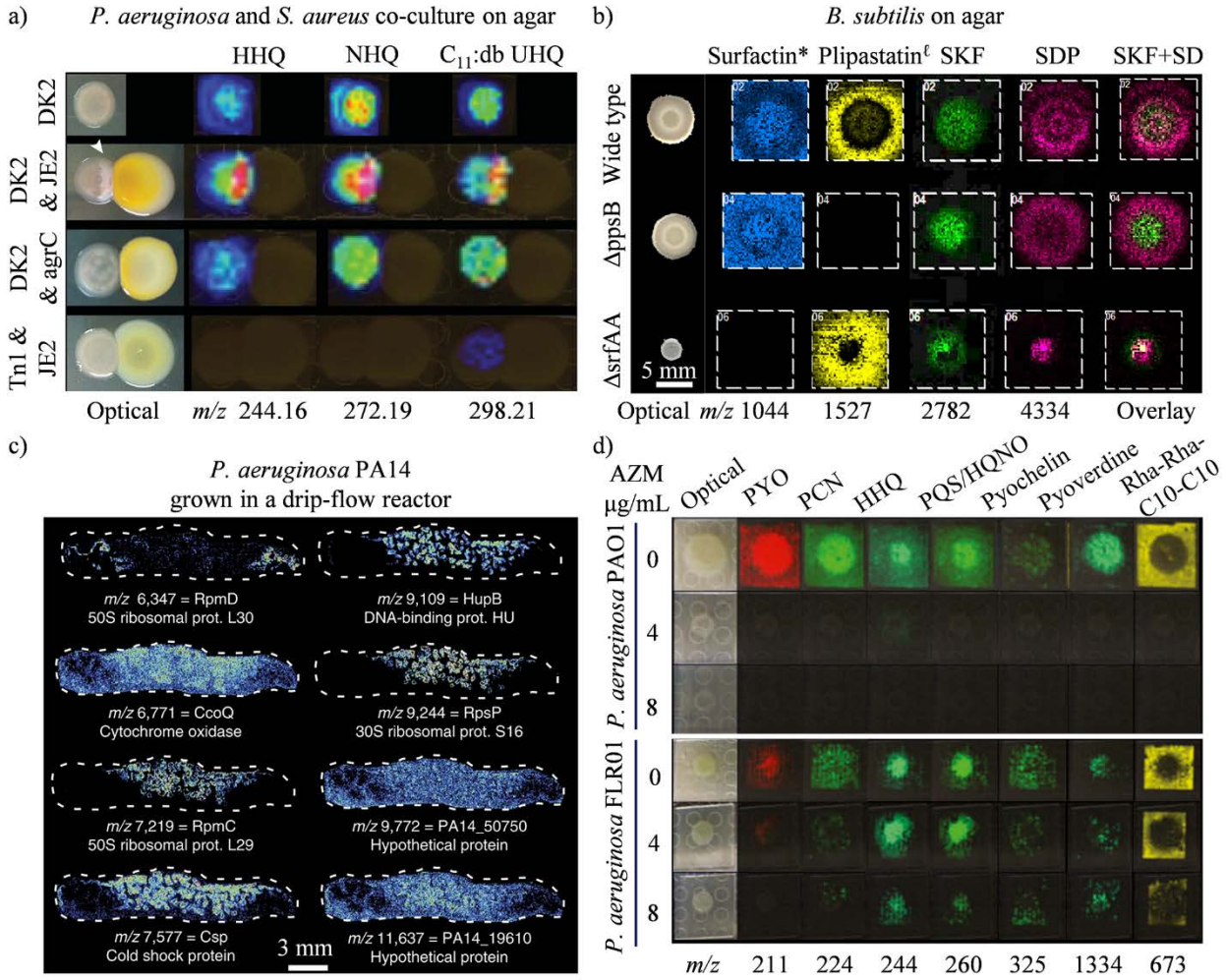

Figure 2.2 Examples of MALDI MSI in microbiology. (a) Alkyl quinolines produced by *P. aeruginosa* in the presence of *S. aureus*. Reprinted with permission from ref 15. Copyright 2016 Macmillan Publishers Ltd. (b) Surfactants and peptides produced by colony biofilms of *B. subtilis.* Adapted from ref 16. Copyright 2016 American Chemical Society. (c) Nutritionally dependent *P. aeruginosa* proteins from a heterogeneous biofilm grown in a drip-flow reactor. Adapted with permission from ref 17. Copyright 2016 Nature Publishing Group under a Creative Commons CC-BY license. (d) Chemical response of two strains of *P. aeruginosa* in the presence of the antibiotic azithromycin. Adapted with permission from ref 18. Copyright 2015 Springer. See the original references for more information on the specific bacterial strains used and the identities of all of the ions. *****, Surfactin-C14; ℓ, Plipastatin-C17-Val.

2.2d).[18] These studies and many others illustrate the potential of MALDI MSI in both fundamental biological discovery and medical research.

Because of their high water content and the propensity for analytes to migrate during handling, microbial samples cultivated on agar are challenging to analyze with MSI. These challenges are often exacerbated by the MALDI matrix application process. One simple method developed specifically for agar-bound microbes is to apply dry matrix to the hydrated colony with a sieve followed by oven drying at 37 °C.[19] Recently, spray-based matrix application to

both hydrated[20] and dry[21] agar samples was shown to provide reproducible ion images. Another challenge with agar is that thick, nonconductive samples can become electrically charged under laser irradiation, potentially leading to signal decay over the duration of an image.[19] This impediment can be overcome by using agar with an ultimate dry thickness of less than 50 μm or potentially by sputter-coating the sample with a few nanometers of a conductive material prior to imaging. These examples illustrate that method optimization is often required when using the unique samples present in microbiology.

Although issues are certain to arise during the adaptation process, many of the traditional methods for applying MALDI matrices to animal tissues are applicable to dehydrated microbial communities. Researchers are also encouraged to look to "matrix-free" methods for laser desorption/ionization (LDI), which primarily utilize UV-absorbing nanoparticles, metal overlays, or nanostructured surfaces.[22] Whether adapting existing approaches or developing entirely new methods, one should take care to perform the appropriate control and replicate experiments. As the title of Richard Goodwin's excellent 2012 review suggests, "Small mistakes [in MSI sample preparation] can lead to big consequences."[23]

2.3.1.2. Secondary Ion Mass Spectrometry

Ion beams can be focused to exceptionally small spot sizes, allowing SIMS to achieve a lateral resolution of better than 50 nm for monatomic and diatomic secondary ions such as C^-, S^-, and CN^-. This approach (dubbed NanoSIMS) is especially powerful when coupled to metabolic function experiments through stable isotope labeling or cytogenetic identification via fluorescence in situ hybridization (FISH). A recent example of NanoSIMS with FISH metabolic labeling is shown in **Figure 2.3a**.[24]

Highly focused ion beams induce molecular fragmentation that limits the observable mass range and causes damage accumulation at or just below the sample surface. To partially alleviate these effects, polyatomic ions (e.g., Bi_3^+ or C_{60}^+) or large gas clusters (e.g., Ar_n^+ or $(H2O)_n^+$) are often employed as projectile sources for biomolecular SIMS imaging. These ion sources have extended the usable mass range of SIMS to above *m/z* 2000 and enabled 3D imaging; however, limitations in primary ion flux and focusing capacity currently restrict the achievable lateral resolution to about 3 μm for lipids.[25]

In principle, SIMS imaging requires little to no sample preparation, but the specimen must be dry and vacuum-stable, and, depending on the ion optics, it may also need to be

conductive and microscopically flat. These limitations have historically prevented direct SIMS imaging of microbial communities on agar—an important growth substrate required for many microbiology experiments. Debois et al.[26] circumvented issues with charging and surface architecture by imprint-transferring surfactants produced by swarming *B. subtilis* onto a silicon wafer (**Figure 2.3b**). Many researchers avoid agar by cultivating samples directly on conductive silicon wafers, which can be dehydrated and analyzed directly.[27-28] **Figure 2.3c** shows a series of

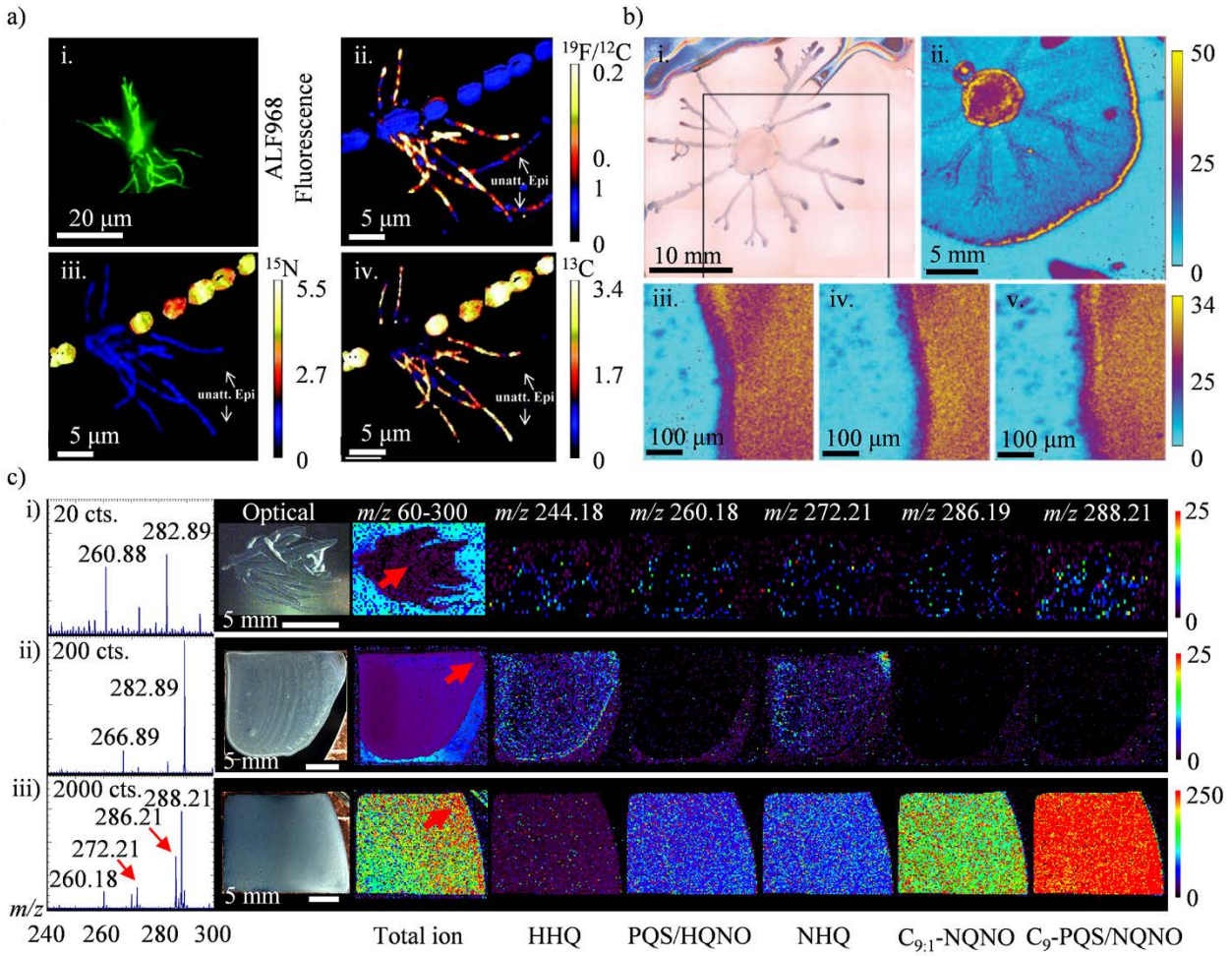

Figure 2.3. Examples of SIMS imaging in microbiology. (a) (i) FISH and (ii–iv) NanoSIMS imaging of the filamentous cyanobacterium *Anabaena sp.* and *Rhizobium sp.* In (ii), *Rhizobium sp.* is labeled with fluorine using ALF968 dye, while in (iii) and (iv) *Anabaena sp*. metabolically incorporates ^{15}N-dinitrogen and ^{13}C-bicarbonate. Adapted with permission from ref 24. Copyright 2008 American Society for Microbiology. (b) Bi_3^+-TOF-SIMS imaging of a *B. subtilis* swarming community imprinted onto a silicon wafer. (i) Microscopy image of the community prior to imprinting. (ii) Low- and (iii–v) high-resolution TOF-SIMS images of the sum of all surfactant ions. Adapted with permission from ref 26. Copyright 2008 John Wiley and Sons. (c) Quinolones and quinolines produced by static (i) *P. aeruginosa* microcolonies, (ii) planktonic culture, and (iii) 7 h biofilms. Mass spectra are averages of four pixels from the regions indicated by the red arrows. Reproduced with permission from ref 28. Copyright 2015 Royal Society of Chemistry.

SIMS images of alkyl quinolone signaling molecules collected from *P. aeruginosa* communities grown on or transferred to silicon wafers.[27] The advent of new SIMS instruments with orthogonal mass analyzers should reduce the impact of topographical variations and conductivity and therefore allow direct SIMS imaging of agar-bound communities.[29]

As with MALDI, there is considerable interest in sample treatments that enhance SIMS ion yields. Because of an overall increase in ion availability, these protocols are also expected to produce improvements in molecular coverage and spatial resolution. Using C_{60}^+-SIMS, our lab demonstrated that a thin layer of gold selectively enhances the yields of quinolone cell-to-cell signaling molecules and rhamnolipid biosurfactants in *P. aeruginosa* bacterial biofilms while simultaneously suppressing background ions from the cell-culture medium,[30] and previously we employed a similar tactic for enhanced ionization with monatomic (Au^+) primary ion beams.[29]

2.3.1.3. Desorption Electrospray Ionization

Although DESI is an ambient ionization method and should therefore be applicable for direct imaging of hydrated (and live) microbial samples, the technique works best on hard, uniform surfaces.[31] This experimental constraint makes it difficult to image many sample types without prior dehydration. As with SIMS and MALDI, imprinting onto an amenable substrate prior to DESI imaging has been shown to be effective. An example of imprint DESI MSI used to visualize interacting communities of *B. subtilis* and *Streptomyces coelicolar* is presented in **Figure 2.4a**.[32] A number of blotting surfaces, such as polytetrafluoroethylene (PTFE), porous Teflon, TLC plates, C-18 beads, and cellulose membranes, have been reported as viable substrates for indirect DESI MSI.[33] The simplest approach to DESI imaging, and the one that is reported to offer the best results, is to image following cultivation on thin agar and vacuum desiccation (**Figure 2.4b**).[34]

Direct MSI of living colonies has been accomplished through the use of "nanospray" DESI, an ionization approach that implements a small liquid microjunction as an extraction probe. NanoDESI has been applied to image living communities of *Shewanella oneidensis, B. subtilis*, and *S. coelicolor* as well as mixed biofilms (**Figure 2.4c).**[35] While topographical irregularities are a complicating factor for all ionization modalities, they can be especially challenging for NanoDESI, as they disrupt the liquid microjunction. This complication can be overcome by way of a feedback mechanism that adjusts the sample-to-microjunction distance on the basis of the local topography.[35]

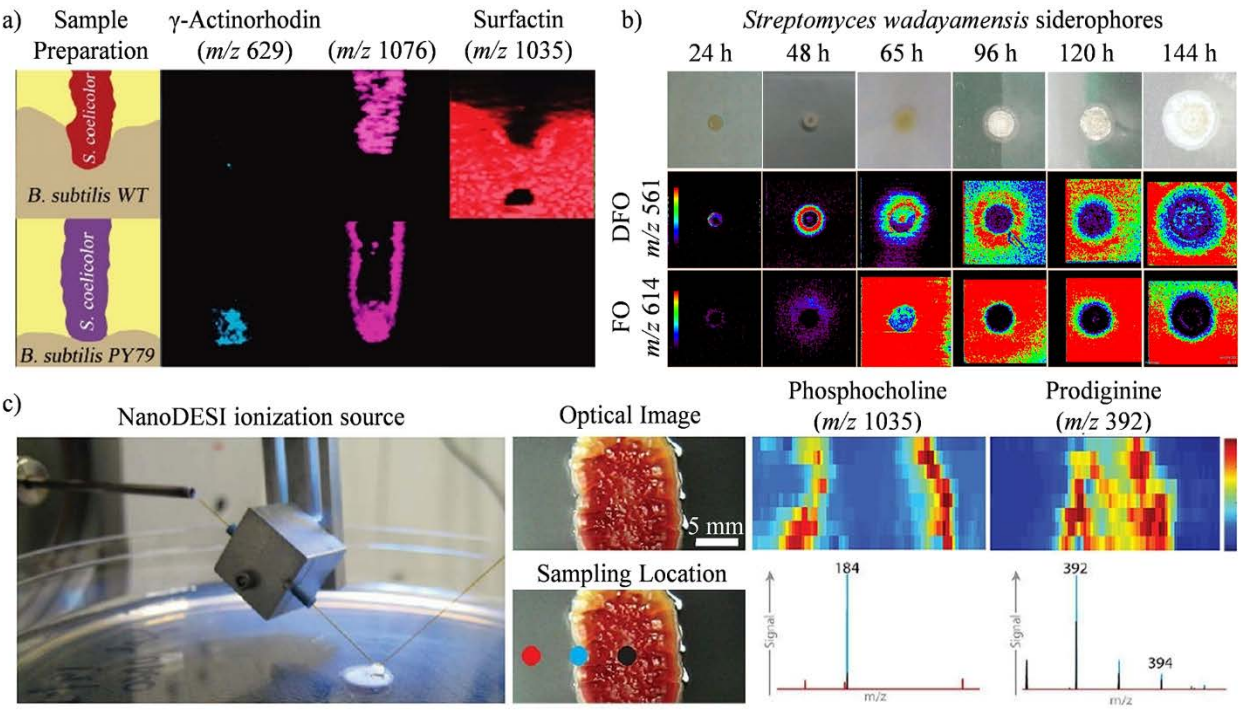

Figure 2.4. Examples of DESI MSI in microbiology. (a) Imprint imaging of interacting communities of *B. subtilis* and *S. coelicolor*. Adapted from ref 32. Copyright 2010 American Chemical Society. (b) Ion images of iron-scavenging siderophores at different times during the growth of *Streptomyces wadayamensis*. Samples were grown on thin agar and vacuum-desiccated prior to imaging. Adapted from ref 34. Copyright 2015 American Chemical Society. (c) NanoDESI liquid microjunction probe design and ion images of living *S. coelicolor* colonies on agar. Adapted from ref 35. Copyright 2013 American Chemical Society.

2.3.2. Mass Analyzers for Microbial MSI

The choice of mass analyzer is as important as the modality of ionization, as this selection will determine the range of detectable ions and the confidence of the chemical assignments. Important considerations include mass accuracy (deviation between the theoretical mass and the measured mass), mass resolving power or resolution (smallest difference between two peaks such that the valley between is discernible by a specified fraction of the peak height), mass range (minimum and maximum detectable *m/z* values), data acquisition speed, and tandem-MS (MS/MS) capabilities, with the details on specific figures of merit being similar to those for other MSI applications.[36]

As is the case for all MS methods, identification of isomers, which share elemental compositions (and therefore *m/z* values), and isobars, which differ by small fractions of an *m/z* value, can be exceptionally challenging. Isobars can be distinguished using instruments with high mass accuracy and high mass resolving power, such as Fourier transform ion cyclotron resonance (FT-ICR) and Orbitrap mass spectrometers, which are capable of differentiating mass

deviations smaller than 1 ppm. Although high-resolving-power analyzers are well-suited for differentiating isobars and for determining elemental composition through isotopic fine structure, they are relatively slow when it comes to acquiring the hundreds of thousands of mass spectra that can be present in a single MS image. For example, to achieve a mass resolving power of 50 000 (full width at half-maximum) at *m/z* 1000, a typical Orbitrap or FT-ICR instrument requires an acquisition time of about 1 s/pixel, while a time-of-flight (TOF) analyzer can achieve a similar resolving power in less than 0.1 s/pixel. Additionally, the large data files arising from images obtained at high mass resolving power can quickly become cumbersome, resulting in images of several terabytes. For these reasons, most commercial imaging instruments are equipped with TOF analyzers, which have the added benefit of compatibility with pulsed microprobes, such as lasers and ion beams.

Identification of isomers is more challenging and often cannot be accomplished with MS alone. MS/MS fragmentation offers some clues, as it allows for comparison of the fragmentation spectrum of the unknown analyte to those from an analytical standard or an online repository, e.g., METLIN (metlin.scripps.edu), KNApSAck (kanaya.naist.jp/KNApSAcK), Lipidomics Gateway (lipidmaps.org), and the RIKEN MSn spectral database (spectra.psc.riken.jp). Many available MSI instruments, including hybrid TOF configurations, such as a quadrupole TOF (QTOF) or a TOF/TOF, are capable of MS/MS. SIMS instrument manufacturers have been slow to adapt to the imperatives of the biological imaging community, and most instruments are made with either magnetic sector or single-stage TOF analyzers, which are relatively low resolution, strongly influenced by topography, and not capable of MS/MS. Promising developments include the release of a novel ion bunching-TOF-SIMS by Ionoptika Ltd., a TOF/TOF-SIMS from Physical Electronics, and an Orbitrap/TOF-SIMS from ionTOF and Thermo Scientific, all of which are equipped with MS/MS capabilities.

Isobars and isomers are particularly challenging for imaging experiments, as a single *m/z* value can arise from different compounds. One approach to resolve this issue is to use MS/MS in conjunction with MSI. In an example relevant to microbiology, our lab applied SIMS MS/MS imaging to map the distribution of two isomeric analyte pairs, *Pseudomonas* quinolone signal (PQS, 2-heptyl-3-hydroxy-4-quinolone) and 4-hydroxy-2-heptylquinoline-*N*-oxide (HQNO) and the nine-carbon variants C_9-PQS and NQNO, across static *P. aeruginosa* biofilms (**Figure 2.5**). MS/MS imaging showed the *N*-oxide species to be localized in high-abundance zones throughout

the sample (visible as high-intensity spots in the MS/MS images for the *m/z* 159.08 peak of NQNO (**Figure 2.5a**) and HQNO (**Figure 2.5b**)), whereas C_9-PQS and PQS were at lower abundance and distributed more evenly.[28]

While MS/MS imaging has obvious utility for isomeric imaging, the technique is limited in terms of throughput, as—with some notable exceptions[37]—only a single precursor ion can be examined with each image collection. One possibility for retaining the multiplexed capabilities of MSI while improving chemical specificity is to incorporate an ion mobility (IM) drift cell into a traditional MSI instrument. In IM-MS, gas-phase ions are separated on the basis of their collisional cross sections prior to MS detection, allowing some isomers and isobars to be differentiated by shape. Commercial IM-MSI instruments have been available for several years, and multiple applications have been demonstrated for tissue imaging.[38] In an example with relevance to microbiology, Li and co-workers[39] complemented MSI with IM-MS to identify and

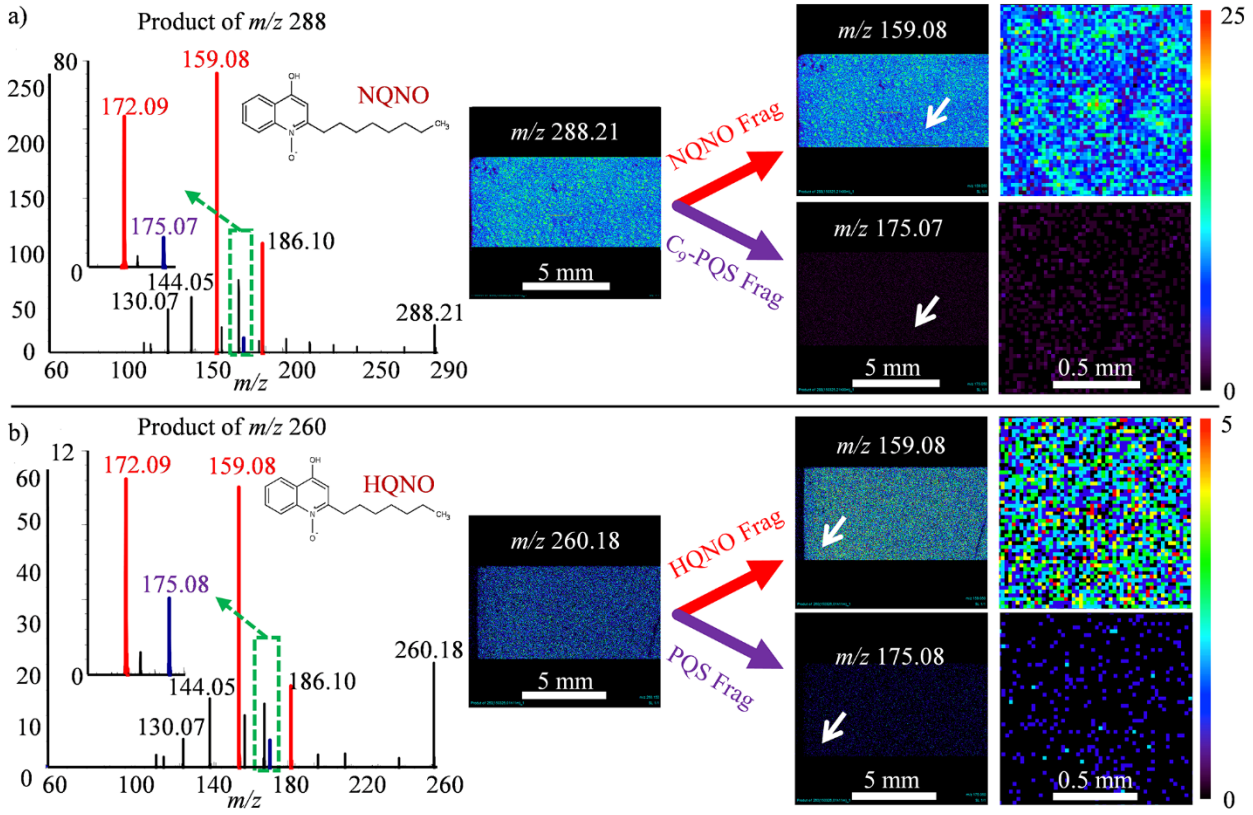

Figure 2.5. C_{60}-SIMS product ion imaging to differentiate the PQS/HQNO and C_9-PQS/NQNO isomeric pairs on two adjacent regions of a *P. aeruginosa* biofilm. (a) Product of *m/z* 288 for C9-PQS and NQNO. (b) Product of *m/z* 260 for PQS and HQNO. Fragments arising from PQS and C_9-PQS are shown in purple, while those arising from $_N$-oxides are shown in red. The white arrows indicate the approximate locations of the subsequent higher-magnification images. Reproduced with permission from ref 28. Copyright 2015 Royal Society of Chemistry.

image molecules related to growth, metabolism, and antibiotic inhibition in bacterial colonies. IM-MSI is a leading technology with potential to alleviate the chemical ambiguity in imaging data.

Another attractive approach for increasing chemical coverage and specificity is to use a combination of several complementary imaging approaches to analyze the same or similar samples. Such combinatorial approaches are commonly termed "correlated" or "multimodal" imaging. For example, when studying multispecies communities with NanoSIMS it is often advantageous to incorporate FISH and/or electron microscopy. This allows accurate pairing of chemical information with cell identity and colony morphology.[24] Our lab has also found it advantageous to image microbial samples with a combination of MS and confocal Raman microscopy, a nondestructive vibrational imaging technique that provides information on the composition of functional groups and is applicable to living communites.[27-28] We anticipate multimodal imaging approaches to become increasingly necessary as biological inquiries grow in complexity.

2.4. Prevailing Challenges for Microbial MSI

Of the tools available to the modern scientist, MSI is uniquely capable of untargeted interrogation of chemically complex systems with a high degree of spatial and chemical specificity. Since its introduction, the utility of MSI has been affirmed by numerous applications and their resulting discoveries. Despite this progress, there remains significant room for improvement in terms of both the technical aspects of the methods and the systems to which these methods can be applied. The following developmental challenges will help overcome many existing barriers in microbial MSI.

Challenge #1: Robust Sampling Protocols and Ionization Methods That Enable Interrogation of Samples in Their Endogenous Chemical and Physical States

Most imaging experiments are currently conducted while the sample is under vacuum, which requires prior desiccation. Nonetheless, a number of promising ionization approaches operate under ambient conditions and should be adaptable to examine living microbial communities. Beyond NanoDESI, several other liquid extraction techniques are in use (as recently reviewed by Laskin and Lanekoff).[40] Ambient SIMS and MALDI have also been demonstrated. TOF-SIMS has been used to examine hydrated *P. aeruginosa* biofilms in a unique vacuum-compatible

microfluidic reactor[41] as well as HeLa cells in their frozen-hydrated state.[42] Another promising method is to use infrared lasers with MALDI, which rely on water as the matrix and therefore allow for hydrated imaging.[43] To be applicable for a broader segment of scientists, these ambient ionization approaches need to become more robust and either be incorporated into commercial instruments or made available as affordable off-the-shelf attachments.

Challenge #2: Relative and Absolute Quantitation

In perhaps what represents the biggest challenge for the MSI community as a whole, it has been repeatedly shown that small sample differences—in terms of morphology, local salt concentration, or hardness—dramatically affect ionization efficiency and, as a result, the observed molecular distribution.[19, 44] Difficulties can also arise when comparing the concentration of one analyte to that of another, as small differences in chemical structure can lead to large variations in ionization efficiency. As an example, the same molecule localized to different nanoenvironments, whether associated with a protein complex inside the cell or within a specific subdomain of the EPS, can exhibit large differences in extraction and ionization yields, and these differences cannot be easily recapitulated with externally applied standards. For these reasons, it is often necessary to combine MSI with other molecular imaging modalities or to follow MSI with localized extraction and quantitative analysis via an established approach such as LC–MS.[18] While it is conceivable to perform secondary verification procedures with every imaging experiment, this process is prohibitively time-consuming and expensive. Thus, there is a substantial need for imaging methods that are inherently quantitative and not reliant on secondary verification. Outside of NanoSIMS, we are aware of no published report on quantitative microbial MSI, but many existing approaches, including those used for tissue imaging[45] and drug penetrance studies,[46] should be adaptable.

Challenge #3: Specialized Sampling Protocols for Low-Abundance or Difficult-to-Access Chemicals or Chemical Classes

In its current state, MSI samples only a tiny fraction of the available chemical information in a microbial community. Although many important compounds can be easily studied using existing approaches, some analytes—particularly those that are low in concentration, labile, or difficult to ionize—require specialized procedures. We expect that these efforts will focus on in situ derivatization to target specific analyte classes and enhance ionization,[47-48] the use of nanomaterials for SIMS and LDI,[22] and the development of novel organic matrices.

Challenge #4: Improving Instrumentation and Sampling Protocols to Enable Routine Access to Chemical Environments across Many Dimensions of Space and Time

The chemical dynamics of microbial ecosystems occurs over many orders of magnitude in both space and time. On one end of the spectrum, microbes interact with their environment on a massive scale, influencing the chemistries of oceans, soils, and our built environments. On the other hand, comprehending microbial communities as a whole often requires understanding the microscopic contributions of individual bacteria on millisecond time scales. Studying these diverse systems will require a collection of innovative analytical approaches. We need to draw on the emerging field of 3D chemical cartography[10] to map the chemical contributions of bacteria across massive environments. We should develop our analytical platforms to improve sensitivity and spatial resolution (which often go hand-in-hand) for routine submicron chemical imaging.

Challenge #5: Developing and Nurturing Collaborations among Scientists from Diverse Fields

Directly addressing the grand challenges within the microbiome requires collaboration among scientists with vastly different expertise. This is even more important when the system under study is composed not only of microbes but also of microbes interacting with some component of their environment, whether it be natural (e.g., soil, plants, animals, decomposing vegetation, minerals) or a human construct (e.g., water pipes, oil pipelines, implanted medical devices, food processing machinery). These collaborations need to be established both among scientists with different analytical skills—such as spectrometrists, spectroscopists, and geneticists—and at a broader intellectual level among physicians, industrial scientists, and academics.

2.5. Concluding Remarks

We expect multiple research areas to gain from microbial MSI in the coming years. There is great potential for fundamental biological discovery and for understanding cellular heterogeneity, cell-to-cell signaling, the general chemical dynamics of single and multispecies microbial communities, and the interactions of the microbiome with its host. As an example, with over two million deaths per year caused by bacterial infections and close to 70% of pathogenic bacteria currently resistant to standard antibiotics, there is a critical need to elucidate

the various mechanisms behind antibiotic resistance in order to develop new treatment strategies.[49]

Similarly, we need to further our understanding of the complex chemical interactions that occur in plant root/microbial communities; the changing environmental challenges impacting agriculture and bioenergy require enhanced approaches to understand these complex ecologies. In addition to bacteria, our understanding of the chemical processes underlying other microbial communities, including yeast, fungi, and archaea, could greatly benefit from the discovery power of MSI. As microbial MSI methods continue to become more rigorous, simpler to implement, and more accepted by a broader audience, the technique will become an essential chemical imaging tool ubiquitously employed by microbiologists in diverse sectors of science and industry.

2.6. References

1. Kato, C.; Li, L.; Nogi, Y.; Nakamura, Y.; Tamaoka, J.; Horikoshi, K., Extremely barophilic bacteria isolated from the Mariana Trench, Challenger Deep, at a depth of 11,000 meters. *Appl. Environ. Microbiol.* **1998,** *64*, 1510.
2. Wainwright, M.; Wickramasinghe, N. C.; Narlikar, J. V.; Rajaratnam, P., Microorganisms cultured from stratospheric air samples obtained at 41 km. *FEMS Microbiol. Lett.* **2003,** *218*, 161.
3. Locey, K. J.; Lennon, J. T., Scaling laws predict global microbial diversity. *Proc. Natl. Acad. Sci. U. S. A.* **2016,** *113*, 5970.
4. Biteen, J. S.; Blainey, P. C.; Cardon, Z. G.; Chun, M.; Church, G. M.; Dorrestein, P. C.; Fraser, S. E.; Gilbert, J. A.; Jansson, J. K.; Knight, R.; Miller, J. F.; Ozcan, A.; Prather, K. A.; Quake, S. R.; Ruby, E. G.; Silver, P. A.; Taha, S.; van den Engh, G.; Weiss, P. S.; Wong, G. C. L.; Wright, A. T.; Young, T. D., Tools for the microbiome: nano and beyond. *ACS Nano* **2016,** *10*, 6.
5. Handelsman, J., FACT SHEET: Announcing the National Microbiome Initiative. White House Office of Science and Technology Policy, Ed. https://obamawhitehouse.archives.gov/blog/2016/05/13/announcing-national-microbiome-initiative, 2016.
6. Miller, M. B.; Bassler, B. L., Quorum sensing in bacteria. *Annu. Rev. Microbiol.* **2001,** *55*, 165.
7. Wagner, V. E.; Bushnell, D.; Passador, L.; Brooks, A. I.; Iglewski, B. H., Microarray analysis of Pseudomonas aeruginosa quorum-sensing regulons: effects of growth phase and environment. *J. Bacteriol.* **2003,** *185*, 2080.
8. Cliff, J. B.; Gaspar, D. J.; Bottomley, P. J.; Myrold, D. D., Exploration of inorganic C and N assimilation by soil microbes with time-of-flight secondary ion mass spectrometry. *Appl. Environ. Microbiol.* **2002,** *68*, 4067.
9. Lechene, C. P.; Luyten, Y.; McMahon, G.; Distel, D. L., Quantitative imaging of nitrogen fixation by individual bacteria within animal cells. *Science* **2007,** *317*, 1563.
10. Bouslimani, A.; Porto, C.; Rath, C. M.; Wang, M.; Guo, Y.; Gonzalez, A.; Berg-Lyon, D.; Ackermann, G.; Moeller Christensen, G. J.; Nakatsuji, T.; Zhang, L.; Borkowski, A. W.; Meehan, M. J.; Dorrestein, K.; Gallo, R. L.; Bandeira, N.; Knight, R.; Alexandrov, T.; Dorrestein, P. C., Molecular cartography of the human skin surface in 3D. *Proc. Natl. Acad. Sci. U. S. A.* **2015,** *112*, E2120.

11. Rubakhin, S. S.; Sweedler, J. V., *Mass Spectrometry Imaging*. 2010.
12. Fang, J.; Dorrestein, P. C., Emerging mass spectrometry techniques for the direct analysis of microbial colonies. *Curr. Opin. Microbiol.* **2014,** *19*, 120.
13. Zavalin, A.; Yang, J.; Hayden, K.; Vestal, M.; Caprioli, R. M., Tissue protein imaging at 1 μm laser spot diameter for high spatial resolution and high imaging speed using transmission geometry MALDI TOF MS. *Anal. Bioanal. Chem.* **2015,** *407*, 2337.
14. Kompauer, M.; Heiles, S.; Spengler, B., Atmospheric pressure MALDI mass spectrometry imaging of tissues and cells at 1.4-μm lateral resolution. *Nat. Methods* **2016**.
15. Frydenlund Michelsen, C.; Hossein Khademi, S. M.; Krogh Johansen, H.; Ingmer, H.; Dorrestein, P. C.; Jelsbak, L., Evolution of metabolic divergence in Pseudomonas aeruginosa during long-term infection facilitates a proto-cooperative interspecies interaction. *ISME J.* **2016,** *10*, 1323.
16. Si, T.; Li, B.; Zhang, K.; Xu, Y.; Zhao, H.; Sweedler, J. V., Characterization of Bacillus subtilis colony biofilms via mass spectrometry and fluorescence imaging. *J. Proteome Res.* **2016,** *15*, 1955.
17. Wakeman, C. A.; Moore, J. L.; Noto, M. J.; Zhang, Y.; Singleton, M. D.; Prentice, B. M.; Gilston, B. A.; Doster, R. S.; Gaddy, J. A.; Chazin, W. J.; Caprioli, R. M.; Skaar, E. P., The innate immune protein calprotectin promotes Pseudomonas aeruginosa and Staphylococcus aureus interaction. *Nat. Commun.* **2016,** *7*, 11951.
18. Phelan, V. V.; Fang, J.; Dorrestein, P. C., Mass spectrometry analysis of Pseudomonas aeruginosa treated with Azithromycin. *J. Am. Soc. Mass Spectrom.* **2015,** *26*, 873.
19. Yang, J. Y.; Phelan, V. V.; Simkovsky, R.; Watrous, J. D.; Trial, R. M.; Fleming, T. C.; Wenter, R.; Moore, B. S.; Golden, S. S.; Pogliano, K.; Dorrestein, P. C., Primer on agar-based microbial imaging mass spectrometry. *J. Bacteriol.* **2012,** *194*, 6023.
20. Li, B.; Comi, T. J.; Si, T.; Dunham, S. J. B.; Sweedler, J. V., A one-step matrix application method for MALDI mass spectrometry imaging of bacterial colony biofilms. *J. Mass Spectrom.* **2016,** *51*, 1030.
21. Hoffmann, T.; Dorrestein, P. C., Homogeneous matrix deposition on dried agar for MALDI imaging mass spectrometry of microbial cultures. *J. Am. Soc. Mass Spectrom.* **2015,** *26*, 1959.
22. Peterson, D. S., Matrix-free methods for laser desorption/ionization mass spectrometry. *Mass Spectrom. Rev.* **2007,** *26*, 19.
23. Goodwin, R. J. A., Sample preparation for mass spectrometry imaging: Small mistakes can lead to big consequences. *J. Proteomics* **2012,** *75*, 4893.
24. Behrens, S.; Lösekann, T.; Pett-Ridge, J.; Weber, P. K.; Ng, W. O.; Stevenson, B. S.; Hutcheon, I. D.; Relman, D. A.; Spormann, A. M., Linking microbial phylogeny to metabolic activity at the single-cell level by using enhanced element labeling-catalyzed reporter deposition fluorescence in situ hybridization (EL-FISH) and NanoSIMS. *Appl. Environ. Microbiol.* **2008,** *74*, 3143.
25. Fletcher, J. S., Latest applications of 3D ToF-SIMS bio-imaging. *Biointerphases* **2015,** *10*, 018902.
26. Debois, D.; Hamze, K.; Guérineau, V.; Le Caër, J. P.; Holland, I. B.; Lopes, P.; Ouazzani, J.; Séror, S. J.; Brunelle, A.; Laprévote, O., In situ localisation and quantification of surfactins in a Bacillus subtilis swarming community by imaging mass spectrometry. *Proteomics* **2008,** *8*, 3682.
27. Lanni, E. J.; Masyuko, R. N.; Driscoll, C. M.; Dunham, S. J. B.; Shrout, J. D.; Bohn, P. W.; Sweedler, J. V., Correlated imaging with C60-SIMS and confocal raman microscopy: visualization of cell-scale molecular distributions in bacterial biofilms. *Anal. Chem.* **2014,** *86*, 10885.
28. Baig, N. F.; Dunham, S. J. B.; Morales-Soto, N.; Shrout, J. D.; Sweedler, J. V.; Bohn, P. W., Multimodal chemical imaging of molecular messengers in emerging Pseudomonas aeruginosa bacterial communities. *Analyst* **2015,** *140*, 6544.
29. Lanni, E. J.; Dunham, S. J. B.; Nemes, P.; Rubakhin, S. S.; Sweedler, J. V., Biomolecular imaging with a C60-SIMS/MALDI dual ion source hybrid mass spectrometer: instrumentation, matrix enhancement, and single cell analysis. *J. Am. Soc. Mass Spectrom.* **2014,** *25*, 1897.
30. Dunham, S. J. B.; Comi, T. J.; Ko, K.; Li, B.; Baig, N. F.; Morales-Soto, N.; Shrout, J. D.; Bohn, P. W.; Sweedler, J. V., Metal-assisted polyatomic SIMS and laser desorption/ionization for enhanced small molecule imaging of bacterial biofilms. *Biointerphases* **2016,** *11*, 02A325.

31. Venter, A.; Sojka, P. E.; Cooks, R. G., Droplet dynamics and ionization mechanisms in desorption electrospray ionization mass spectrometry. *Anal. Chem.* **2006,** *78*, 8549.
32. Watrous, J.; Hendricks, N.; Meehan, M.; Dorrestein, P. C., Capturing bacterial metabolic exchange using thin film desorption electrospray ionization-imaging mass spectrometry. *Anal. Chem.* **2010,** *82*, 1598.
33. Cabral, E. C.; Mirabelli, M. F.; Perez, C. J.; Ifa, D. R., Blotting assisted by heating and solvent extraction for DESI-MS imaging. *J. Am. Soc. Mass Spectrom.* **2013,** *24*, 956.
34. Angolini, C. F. F.; Vendramini, P. H.; Araújo, F. D. S.; Araújo, W. L.; Augusti, R.; Eberlin, M. N.; de Oliveira, L. G., Direct protocol for ambient mass spectrometry imaging on agar culture. *Anal. Chem.* **2015,** *87*, 6925.
35. Watrous, J.; Roach, P.; Heath, B.; Alexandrov, T.; Laskin, J.; Dorrestein, P. C., Metabolic profiling directly from the Petri dish using nanospray desorption electrospray ionization imaging mass spectrometry. *Anal. Chem.* **2013,** *85*, 10385.
36. de Hoffmann, E.; Stroobant, V., *Mass Spectrometry: Principles and Applications*. 2007.
37. Feenstra, A. D.; Hansen, R. L.; Lee, Y. J., Multi-matrix, dual polarity, tandem mass spectrometry imaging strategy applied to a germinated maize seed: toward mass spectrometry imaging of an untargeted metabolome. *Analyst* **2015,** *140*, 7293.
38. Trim, P. J.; Henson, C. M.; Avery, J. L.; McEwen, A.; Snel, M. F.; Claude, E.; Marshall, P. S.; West, A.; Princivalle, A. P.; Clench, M. R., Matrix-assisted laser desorption/ionization-ion mobility separation-mass spectrometry imaging of Vinblastine in whole body tissue sections. *Anal. Chem.* **2008,** *80*, 8628.
39. Li, H.; Balan, P.; Vertes, A., Molecular imaging of growth, metabolism, and antibiotic inhibition in bacterial colonies by laser ablation electrospray ionization mass spectrometry. *Angew. Chem.* **2016,** *128*, 15259.
40. Laskin, J.; Lanekoff, I., Ambient mass spectrometry imaging using direct liquid extraction techniques. *Anal. Chem.* **2016,** *88*, 52.
41. Hua, X.; Yu, X. Y.; Wang, Z.; Yang, L.; Liu, B.; Zhu, Z.; Tucker, A. E.; Chrisler, W. B.; Hill, E. A.; Thevuthasan, T.; Lin, Y.; Liu, S.; Marshall, M. J., In situ molecular imaging of a hydrated biofilm in a microfluidic reactor by ToF-SIMS. *Analyst* **2014,** *139*, 1609.
42. Piwowar, A. M.; Keskin, S.; Delgado, M. O.; Shen, K.; Hue, J. J.; Lanekoff, I.; Ewing, A. G.; Winograd, N., C60-ToF SIMS imaging of frozen hydrated HeLa cells. *Surf. Interface Anal.* **2013,** *45*, 302.
43. Berkenkamp, S.; Karas, M.; Hillenkamp, F., Ice as a matrix for IR-matrix-assisted laser desorption/ionization: mass spectra from a protein single crystal. *Proc. Natl. Acad. Sci. U. S. A.* **1996,** *93*, 7003.
44. Lanekoff, I.; Stevens, S. L.; Stenzel-Poore, M. P.; Laskin, J., Matrix effects in biological mass spectrometry imaging: identification and compensation. *Analyst* **2014,** *139*, 3528.
45. Groseclose, M. R.; Castellino, S., A mimetic tissue model for the quantification of drug distributions by MALDI imaging mass spectrometry. *Anal. Chem.* **2013,** *85*, 10099.
46. Prideaux, B.; Dartois, V.; Staab, D.; Weiner, D. M.; Goh, A.; Via, L. E.; Barry Iii, C. E.; Stoeckli, M., High-sensitivity MALDI-MRM-MS imaging of Moxifloxacin distribution in tuberculosis-infected rabbit lungs and Granulomatous lesions. *Anal. Chem.* **2011,** *83*, 2112.
47. Shariatgorji, M.; Strittmatter, N.; Nilsson, A.; Källback, P.; Alvarsson, A.; Zhang, X.; Vallianatou, T.; Svenningsson, P.; Goodwin, R. J. A.; Andren, P. E., Simultaneous imaging of multiple neurotransmitters and neuroactive substances in the brain by desorption electrospray ionization mass spectrometry. *NeuroImage* **2016,** *136*, 129.
48. Wu, Q.; Comi, T. J.; Li, B.; Rubakhin, S. S.; Sweedler, J. V., On-tissue derivatization via electrospray deposition for matrix-assisted laser desorption/ionization mass spectrometry imaging of endogenous fatty acids in rat brain tissues. *Anal. Chem.* **2016,** *88*, 5988.
49. Berdy, J., Thoughts and facts about antibiotics: where we are now and where we are heading. *J. Antibiot.* **2012,** *65*, 441.

CHAPTER 3

Multimodal Chemical Imaging of Molecular Messengers in Emerging *Pseudomonas aeruginosa* Bacterial Communities

3.1. Acknowledgements

This chapter was originally published as a research article in *Analyst* **2015**, (140) 6544-6552, and has been adapted here with permission from the Royal Society of Chemistry, copyright 2015. Co-authors include Nameera F. Baig, Sage J. B. Dunham, Nydia Morales-Soto, Joshua D. Shrout, Jonathan V. Sweedler, and Paul W. Bohn. SJBD performed all mass spectrometry and electron microscopy experiments as well as the associated data analysis and interpretation, wrote much of the manuscript, and helped to plan the experiments. NFB performed all Raman measurements and the associated data analysis, helped to plan experiments, cultivated most the biofilms and planktonic culture, and wrote a large portion of the manuscript. NMS cultivated the swarm samples, helped to plan experiments, and assisted with writing. JDS, JVS, and PWB helped to plan experiments and assisted with manuscript writing. Financial support was provided by the National Institute of Health grant 1R01AI113219-01, and the Department of Energy grant DE SC-0006642. The authors would like to thank Bin Li and Eric Lanni for helpful MSI discussion, as well as Scott Robinson and Cate Wallace in the Beckman Institute Imaging Technology Group, which is partially supported by the National Science Foundation grant DBI-9871103.

3.2. Introduction

Mass spectrometry imaging (MSI) and confocal Raman microscopy (CRM) are powerful analytical platforms for studying complex biological systems in situ at the molecular level. CRM enables non-destructive characterization of biomolecules based upon their vibrational fingerprints, while MSI uses a focused microprobe to generate position-specific ion maps for identification and characterization through mass-to-charge (*m/z*) and fragmentation profiles.[1-2] Unlike many conventional chemical imaging modalities, such as fluorescence microscopy and positron emission tomography, MSI and CRM require no a priori knowledge about chemical composition, and sample perturbations engendered by staining or genetic label incorporation are avoided.[3-4] Multimodal imaging approaches that combine MSI and CRM have proven advantageous for study

of biological systems, generating information that is difficult or impossible to obtain with a single technique alone.[5-6] Our laboratories have employed time-of-flight (ToF) secondary ion mass spectrometry (SIMS) and CRM to study lignin and cellulose distributions in the perennial grass *Miscanthus giganteus*,[7] and matrix assisted laser desorption ionization (MALDI) and CRM to characterize the distribution of lipids and peptides across 3-D cell cultures,[8] while Zenobi and coworkers have successfully correlated Raman and MALDI to study isolated algal cells.[9]

We have previously employed correlated CRM and MSI to study the environmentally ubiquitous gram-negative bacterium *Pseudomonas aeruginosa*.[10] *P. aeruginosa* is an opportunistic pathogen for both plants and humans and is responsible for approximately 8% of the healthcare associated infections each year.[11] Among the commonly infected are burn victims and the immuno-compromised, such as cystic fibrosis patients.[12] Once an infection is established it is difficult to eradicate, as *P. aeruginosa* is highly resistant to both antibiotics and the body's natural immune response.[13-15] The prevalence and resilience of *P. aeruginosa* is largely a result of its complex lifecycle. Under many conditions, these organisms cooperate to remodel their environment, resulting in the secretion of a protective scaffolding of DNA, proteins, polysaccharides, small molecule metabolites, and other extracellular polymeric substances (EPS) termed a biofilm.[16-17]

Cooperative behavior, and biofilm formation itself, are largely dependent upon an intercellular communication system, called quorum sensing (QS), in which individual cells differentially produce and sequester a diverse array of molecules.[18-19] Achieving a threshold concentration of QS molecules results in the up- or down-regulation of target genes, leading to phenotypical differentiation and the manifestation of specific behavioral patterns such as flagella driven surface motility and surface colonization. Particularly prominent among the molecules involved in the *P. aeruginosa* QS system are the quinolone class of small-molecule secondary metabolites, which have been implicated in a wide array of biological functions including virulence and biofilm formation.[17-18]

The vast majority of the information about the role of chemical messengers in microbial organization has been obtained from spatially integrated studies of secreted and diffused components and genetic level manipulations. In contrast, here we apply CRM and SIMS imaging to study the spatial and temporal organization of quinolones in emerging *P. aeruginosa* microbial communities, with a specific focus on three modes of growth: colonies on agar plates, free-floating

planktonic cells, and static biofilms. We show here for the first time the use of tandem MS SIMS imaging to image quinolone isomers, we have created enhanced statistical approaches to identify specific quinolones in the CRM data, and we combined these approaches to perform in situ studies of co-localized isomeric analytes in dynamic biological systems. Our CRM and tandem MSI results show a high abundance of distinctly localized *N*-oxide quinolines in the early biofilms and swarm samples, indicating their potential importance in the development of these surface-attached communities of bacteria. Furthermore, we show how CRM, a non-invasive analytical technique, can be used to guide MS analysis, especially for in situ studies of isomeric analytes, which are difficult or impossible to differentiate with either CRM or MS alone. Our studies demonstrate how the combination of MSI and CRM can provide unambiguous spatially resolved chemical characterization of complex systems and generate information important to the understanding of the collective microbiology of these organisms in biomedically-relevant settings.

3.3. Materials and Methods

3.3.1. Materials

Silicon substrates were purchased from WRS Materials (San Jose, CA) as 3 in diameter (100) Si wafers, and they were scored and broken into 2 cm × 2 cm tiles before use. Quinolone standards, 2-heptyl-3-hydroxy-4(1H)-quinolone (Pseudomonas quinolone signal, PQS) and 2-heptyl-4-quinolone (HHQ), were purchased from Sigma-Aldrich (St Louis, MO), while 4-hydroxy-2-heptylquinoline-*N*-oxide (HQNO) was purchased from Enzo Life Sciences (Farmingdale, NY) and Cayman Chemicals (Ann Arbor, MI). The standards were dissolved in either HPLC-grade ethanol or methanol (Sigma-Aldrich), then deposited and air-dried on clean Si wafers for SIMS and CRM measurements.

3.3.2. Static Biofilm and Swarm Plate Assays

Pseudomonas aeruginosa strain PAO1C was used in all experiments. Bacterial colonies were grown on Lysogeny Broth (LB) agar plates by inoculating the plate with bacterial cells from a glycerol stock. The cells were gently streaked on the LB agar plates using a sterile inoculation loop. The inoculated plates were incubated for 18 hours at 37 °C. Cell cultures were grown overnight at 37 °C with shaking at 240 rpm in modified fastidious anaerobe broth (FAB) culture medium supplemented with 30 mM filter sterilized glucose solution as the carbon source. To grow static biofilms, 200 μL of overnight broth culture (OD = 1 at 600 nm) was pipetted onto a 2 cm ×

2 cm sterilized Si tile placed in a Petri dish (each Petri dish holding three tiles). After allowing 10–15 min for bacterial attachment, the inoculated Si tiles were immersed in 18 mL of fresh FAB medium containing 450 μL of 1.2 M glucose and incubated at 37 °C until the desired growth time had elapsed. The tiles containing bacterial growth were carefully removed from the petri dish with sterile tweezers and allowed to dry for ∼1 h in a hood. When indicated, *P. aeruginosa* overnight broth culture (source of planktonic cells) and colonies from LB agar plates were transferred to sterile Si tiles and dried prior to analysis. Both dried and hydrated static biofilm samples were analyzed in parallel with CRM to ensure that the observed analyte morphology is not due to sample drying effects, while MSI was conducted exclusively on dried samples. No notable differences in analyte morphology or distribution were observed between dried and hydrated samples.

For CRM imaging under swarm motility conditions, 0.9 g of noble agar was added to 200 mL of FAB media containing 2 g L^{-1} (NH4)2SO4. The FAB–agar mixture was autoclaved, cooled to 50 °C, and 2 mL of sterile 1.2 M glucose was added while stirring at room temperature. Sterile medium (7.5 mL) was gently pipetted into 60 mm polystyrene Petri dishes and allowed to cure for 30 min. After drying, the plates were stab-inoculated with an overnight FAB-glucose broth culture (OD = 1 at 600 nm) and incubated at 30 °C for 48 h.[20]

3.3.3. Confocal Raman Microscopy (CRM)

Raman imaging was performed using a confocal Raman microscope (Alpha 300R, WITec, GMBH, Germany), equipped with a 532 nm doubled Nd:YAG excitation laser. The laser radiation was delivered to the microscope using a polarization preserving single-mode optical fiber, deflected through a dichroic beam-splitter and focused onto the sample through the microscope objective. The Raman scattered radiation was collected using the same objective and delivered through a 50 μm diameter multi-mode fiber to a UHTS 300 spectrometer equipped with a 600 groove mm^{-1} grating and a back-illuminated CCD camera (Newton DU970 N-BV, Andor Inc., cooled to −60 °C). Raman images from biofilms were acquired using a coverslip corrected Nikon water immersion 60× objective (NA = 1) while a 40× air objective (NA = 0.6) was used to image swarm plates. Images were obtained by acquiring a full Raman spectrum from each image pixel (100 × 100 or 80 × 80 pixels) over a desired region on the sample with an integration time of 100 ms per spectrum. Data processing software WITec Project 2.10 was used to remove cosmic ray spikes from Raman images. Principal component analysis was performed on the Raman images in MATLAB using previously established procedures.

3.3.4. Secondary Ion Mass Spectrometry (SIMS)

The dried samples were subjected to mass-to-charge (*m/z*) analysis using a custom hybrid MALDI/C60-SIMS Q-TOF mass spectrometer, which has been described in detail elsewhere.[21] Briefly, this instrument is a modified QTOF XL (AB SCIEX, Framingham, MA) equipped with a 20 kV DC Buckminsterfullerene (C_{60}) primary ion beam and a UV laser for C60-SIMS and MALDI, respectively. All experiments described in this manuscript were conducted using the singly charged C60+ ion beam with a sample current of either 300 pA (40 μm diameter spot) for whole film imaging or 100 pA (15 μm diameter spot) for targeted imaging. Whole film imaging was conducted in raster mode with a 200 μm × 200 μm pixel size and a collection time of 656 ms per pixel, while targeted imaging utilized a 21 μm × 21 μm pixel size and a collection time of 101 ms per pixel. For both operating conditions the spectrometer was set to measure positive secondary ions from *m/z* 60–300 with a Q1 transmission bias of 15% at *m/z* 60, 35% at *m/z* 120, and 50% at *m/z* 200. Mass calibration was performed using In1–7+ ions. Data were acquired using Analyst v1.2 and oMALDI Server v5.1 (AB SCIEX) and converted from wiff to img format at 20 data points per *m/z* value. Post conversion analysis of the TIC normalized or raw images (as indicated in the text) was performed in BioMap (Novartis, Switzerland) with voxelated rainbow color map intensities manually chosen to accentuate inter- and intra-film intensity differences. In situ tandem MS and targeted tandem MSI was performed at unit resolution with 15–30 eV in argon collision gas, and molecular assignments were made by fragmentation comparison to analytical standards (where available) and published literature.

3.3.5. Secondary Electron Microscopy (SEM)

Dry samples were sputter coated (Desk II TSC Turbo Sputter Coater, Denton Vacuum, Morristown, NJ, USA) in Au/Pd for 70 s at 40% power (estimated thickness of 7 nm). SEM (Philips XL30 ESEM-FEG, FEI Company, Amsterdam, Netherlands) images were acquired with a 5 kV electron beam energy and a 5 mm working distance.

3.4. Results and Discussion

3.4.1. Survey of Quinolones

Four conditions were chosen to characterize microbial community development, namely bacterial plate micro-colonies, planktonic cells, 7 h and 48 h biofilms, and each sample was subjected to analysis by both SIMS and CRM imaging. Manually probing the cells with SIMS revealed that the

7 h biofilm mass spectrum exhibits prominent peaks at *m/z* 244.18, 260.18, 270.20, 272.21, 286.19, 288.21, and 298.23, which have been previously assigned to 2-alkyl-4-(1H) quinolines (AQ) MH^+ ions and are confirmed here with tandem MS (**Table 1** and **Figure 3.1**).[10, 22-23] The observed ions fall into three molecular classes, specifically 2-heptyl-4-quinoline (HHQ)-derived (*m/z* 244.18, 270.20, and 272.21), 2-heptyl-3-hydroxyquinolone (PQS)-derived (*m/z* 260.18 and 288.21), and 4-hydroxy-2-heptylquinoline-*N*-oxide (HQNO)-derived (*m/z* 260.18, 286.19 and 288.21) ions. Among these compounds, the isomeric pairs PQS/HQNO and C9-PQS/NQNO both appear in the 7 h biofilm based upon tandem-MS fragmentation patterns (**Figure 3.1**). The 48 h biofilm showed a nearly identical set of tandem-MS spectra for the AQ ions (data not shown), while AQ ion intensities from the LB micro-colonies and FAB overnight broth culture were too low to characterize using tandem-MS fragmentation.

Table 3.1. 4-Hydroxy-2-alkylquinolines observed in 7 h *P. aeruginosa* biofilms.

Compound ID	Molecular formula	$[M+H]^+$ expected	$[M+H]^+$ observed	*In situ* tandem MS fragments expected	*In situ* tandem MS fragments observed
HHQ (2-heptyl-4-quinoline)	$C_{16}H_{21}NO$	244.17	244.17	159.07, 172.08	159.08, 172.09
PQS (2-heptyl-3-hydroxyquinolone)*	$C_{16}H_{21}NO_2$	260.17	260.18	175.06, 188.07	175.08, 188.09
HQNO (4-hydroxy-2-heptylquinoline-*N*-oxide)	$C_{16}H_{21}NO_2$	260.17	260.18	159.07, 172.08, 186.09	159.08, 172.08, 186.10
$C_{9:1}$-NHQ (2-nonenyl-4-quinoline)	$C_{18}H_{23}NO$	270.19	270.20	159.07, 172.08, 184.07	159.07, 172.08, 184.08
NHQ (2-nonyl-4-quinoline)	$C_{18}H_{25}NO$	272.20	272.21	159.07, 172.08	159.07, 172.08
$C_{9:1}$-NQNO (4-hydroxy-2-nonenylquinoline-*N*-oxide)	$C_{18}H_{23}NO_2$	286.18	286.19	159.07, 172.08, 184.07, 198.07	159.07, 172.08, 184.08, 198.10
C_9-PQS (2-nonyl-hydroxyquinolone)*	$C_{18}H_{25}NO_2$	288.20	288.21	175.06, 188.07	175.08, 188.09
C_9-NQNO (4-hydroxy-2-nonylquinoline-*N*-oxide)	$C_{18}H_{25}NO_2$	288.20	288.21	159.07, 172.08, 186.09	159.08, 172.08, 186.10
$C_{11:1}$-UHQ (2-undecenyl-4-quinoline)	$C_{20}H_{27}NO$	298.22	298.23	159.07, 172.08, 184.07	159.07, 172.08, 184.08

*Low abundance/minor component of spectrum

3.4.2. Global SIMS Imaging of *P. aeruginosa*

The microbial communities were further imaged by C60-SIMS, the results of which are displayed in the false-color ion maps of **Figure 3.2.** The microcolony mass spectrum, **Figure 3.2a** is low in abundance (20 counts) and dominated by background ions from the LB medium (*m/z* 260.88 and

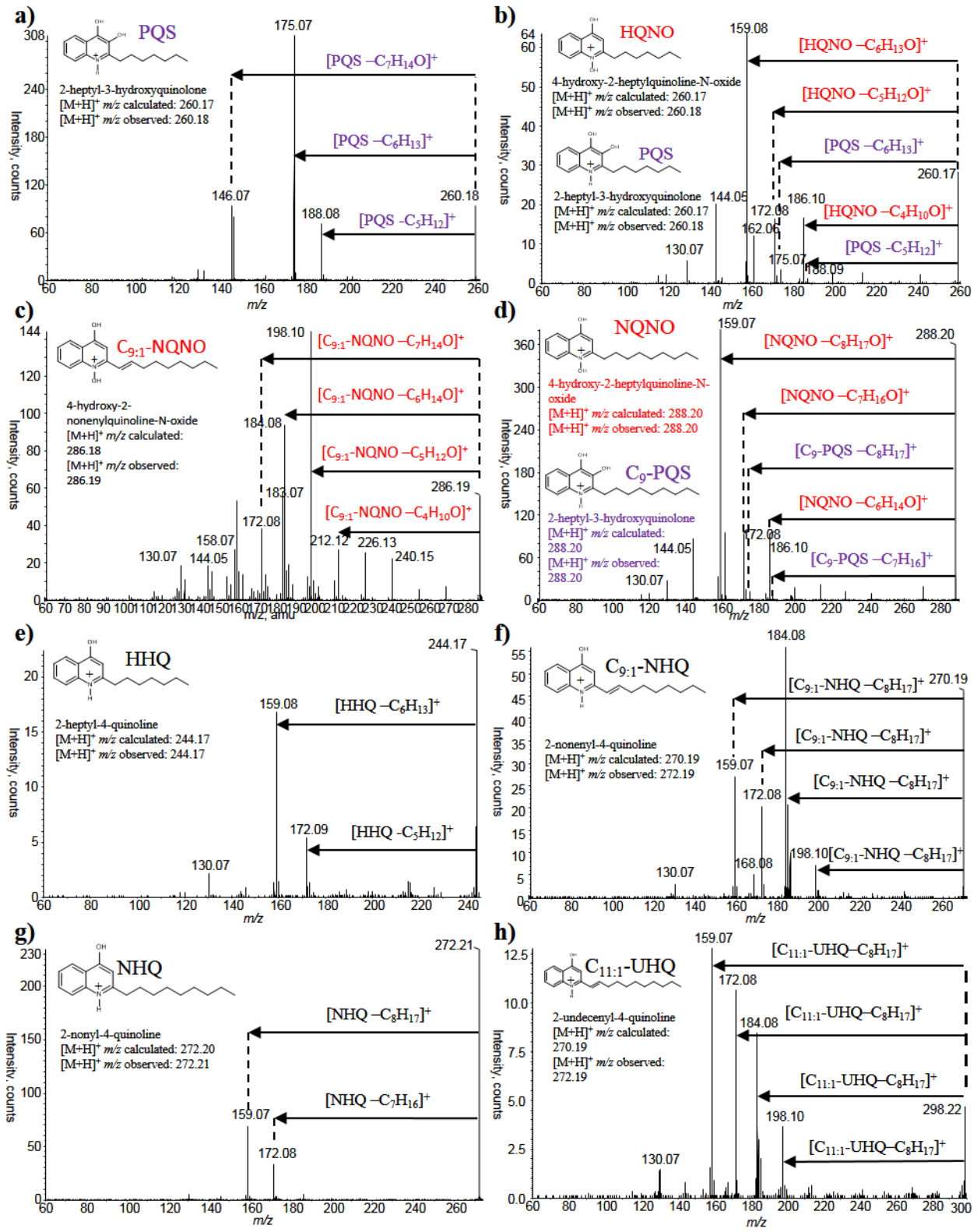

Figure 3.1. SIMS tandem MS spectra of alkyl quinolones in a 7-hr PAO1C biofilm. (**a**) PQS standard; (**b**) endogenous PQS and HQNO; (**c**) endogenous C9:1-NQNO; (**d**) endogenous C9-PQS and NQNO; (**e**) endogenous HHQ; (**f**) endogenous C9:1-NHQ; (**g**) endogenous NHQ; and (**h**) endogenous C11:1-UHQ.

282.89), and the corresponding AQ ion image intensities are near the detection threshold. The prominent ions observed in the overnight culture (*m/z* 266.89 and 282.89, **Figure 3.2b**) arise from the culture medium, while ion images reveal that HHQ (*m/z* 244.18) and NHQ (*m/z* 272.21) are present in low amounts. Overnight culture ions *m/z* 244.18 and 272.21 are beneath the threshold for tandem-MS fragmentation analysis; therefore their presence is confirmed by mass-match alone. The 7 h biofilm SIMS spectrum, **Figure 3.2c**, is dominated by AQs in the *m/z* 240–300 range, with an approximate 100-fold and 10-fold increase in ion count over the LB micro-colonies and FAB overnight broth culture, respectively. Ion images reveal a macroscopically uniform distribution of observed AQs, with the highest abundance for the *N*-oxide quinoline C9:1-NQNO and the C9-PQS/NQNO isomers. In agreement with previous studies of 72 h biofilms, the 48 h biofilms exhibit a quinolone profile with aggregation primarily localized near the biofilm edge.[10] The microcolony images in **Figure 3.2a** show a diffuse ion distribution with AQ ion abundances comparable to those observed on bare silicon, suggesting that the low abundance ions are at, or below, the limit of detection (LOD). Taken together, these data suggest that initial biofilm formation is marked by a dramatic increase in the production of select AQs, with a preferential accumulation of those with a 9-carbon side-chain.

The development-based variability in AQ expression may be the result of a number of factors, including changes in phenotypical expression and variations in the nutrient suply.[24] Over

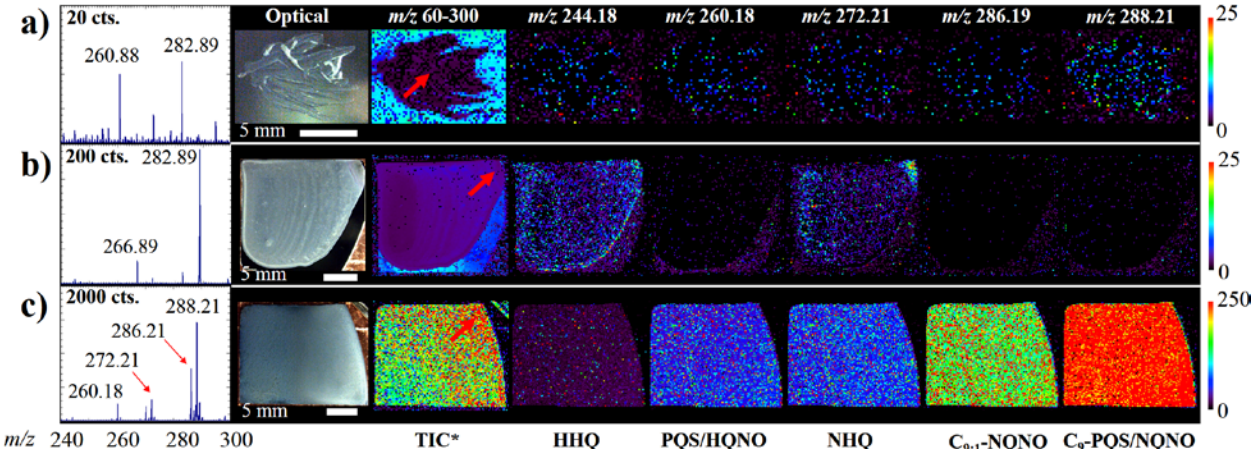

Figure 3.2. Secondary ion mass spectrometry reveals dramatic differences in 4-hydroxy-2-alkylquinoline (AQ) abundance in different states of *P. aeruginosa* organization; (**a**) micro-colonies on LB, (**b**) planktonic cell culture, and (**c**) biofilm grown for 7 h. The mass spectra are drawn from an average of four pixels from representative regions of the samples (as indicated by the red arrows), AQs are observed as protonated $[M + H]^+$ ions, and ion images are normalized to the total ion count (TIC). The TIC images include values in the *m/z* 60–300 range, scaled from 0 to 5 counts, while the individual ion images are scaled as indicated by color bars to the right of each row.

50 AQs, including those examined here, have been observed in bulk studies of *P. aeruginosa* PA14 cell culture using LC-MS,[23] therefore the AQ molecules detected here with SIMS are likely only those that are sufficiently spatially accumulated to rise above the C_{60}-SIMS LOD. Ion images for C9:1-NHQ and C11:1-UHQ (not displayed) show similar global distributions.

3.4.3. CRM and Targeted SIMS Imaging of Static Biofilms

In 7 h biofilms, a high abundance of morphologically distinct structures are observed with bright field microscopy, one of which can be seen in image (**i**) of **Figure 3.3a**. In agreement with the SIMS results of **Figure 3.3b**, Raman spectra acquired from these regions exhibit a strong band at 1357 cm^{-1}, which is attributed to the quinolone ring stretch.[25] Other observed vibrations are related to the quinolone ring, including –CH bending/twisting and C–O stretching centered at ~1205 cm^{-1}, pyridine ring stretch vibrations in the 1550–1600 cm^{-1} region, as well as the symmetric ring breathing vibrations of the aromatic ring at ~715 cm^{-1}.[26-27] Raman image (**ii**) was generated from a region within (**i**) and integrated over the 1338–1376 cm^{-1} window which includes the quinolone ring stretch. Principal component analysis (PCA) was performed on this region, and the first chemically significant principal component, PC3, exhibits high z-score features at 679, 715, 1205,

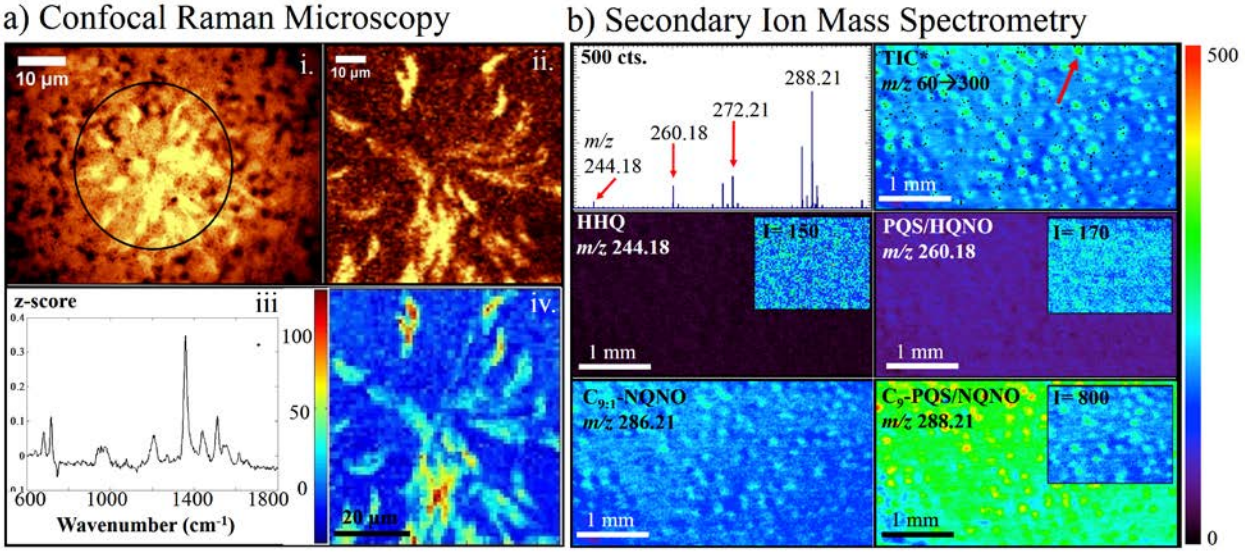

Figure 3.3. (**a**) Bright field microscopy and CRM, and (**b**) targeted SIMS imaging and microspectroscopy of a 7 h *P. aeruginosa* biofilm. (**a**) (i) Bright field microscopy of a quinoline rich region found in 7 h static biofilms; (ii) Raman image acquired from the circled region in (i) and integrated over 1338–1376 cm^{-1}; (iii) PC3 from the Raman image; (iv) heat map showing the spatial distribution and magnitude of PC3. (b) SIMS imaging of regions of high AQ abundance. Inset regions with variable color map intensity show that patterning is present for most AQs, however the intensity differences are most pronounced for the isomeric C9-PQS/NQNO ion at *m/z* 288.21. The mass spectrum is an average of four pixels from a representative high-intensity region of the TIC image (as indicated by the red arrow). The TIC images include values in the *m/z* 60–300 range, scaled from 0 to 2 counts, while the individual ion images are scaled as indicated by the color bar on the right.

1357, 1435, and 1511 cm^{-1} in the loading plot (**iii**), a pattern of features that strongly resembles the bands in the spectrum of HQNO standard (**Figure 3.4**). The congruence between the HQNO standard spectrum and the PC3 loading plot from the in situ image indicates that the distinct structures, as seen in image (**iv**), in 7 h biofilms arise from *N*-oxide quinolines.

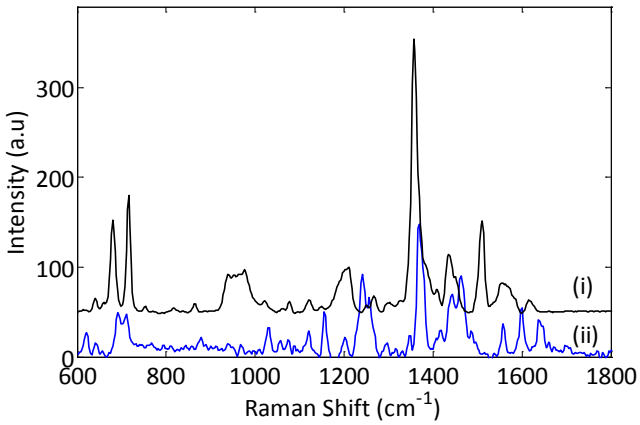

Figure 3.4. Raman spectra of quinolone standards (i) HQNO and (ii) PQS.

While HQNO and PQS standard spectra are used to assign an identity to the secreted components present in these quinolone/*N*-oxide quinoline rich regions, it is not possible to distinguish between AQs possessing the same functional group, but with alkyl chains of different lengths or degree of unsaturation, e.g. PQS and C9-PQS, from CRM data alone. Images displaying these AQs require mass spectrometric data for a definitive assignment. Thus, guided by the microscopic spatial heterogeneity in AQ abundances observed by CRM, 7 h *P. aeruginosa* biofilms were subjected to targeted analysis with C_{60}-SIMS. As can be seen in the representative ion images of **Figure 3.3b**, a series of high intensity regions are found distributed across the entire colony surface. The mass spectra of these regions are predominantly composed of AQ MH^+ ions, and although all detected quinolones appear to be enriched to some degree, *m/z* 288.21 (C9-PQS/NQNO) and *m/z* 286.21 (C9:1-NQNO) are the predominant contributors. The ion images also reveal that AQs are present in the interstitial areas, albeit at lower abundance. For example, a line scan across six of the rich regions shows that the intensity of *m/z* 288.21 changes from 440 (± 2% standard deviation) to 280 (± 7%), or 36 (± 1%) between peak and trough (**Figure 3.5**).

Similar CRM analysis of quinolone accumulations in 48 h static biofilms, **Figure 3.6a**, reveals that, in addition to *N*-oxide quinolines from the HQNO family, co-localized quinolones from the PQS family are also present in visually and spectrally distinct regions near the film edge. For example, PC2 (**Figure 3.6a-ii**) contains features with peaks at 1369, 1461, 1556, and 1591 cm^{-1} that strongly correlate with bands from the spectrum of PQS standard (**Figure 3.4**) while PC3 (**Figure 3.6a-iii**) exhibits features with peaks at 679, 715, 1205, 1357, 1435, and 1511 cm^{-1}, that match bands from the standard spectrum of HQNO. The most distinct difference between the

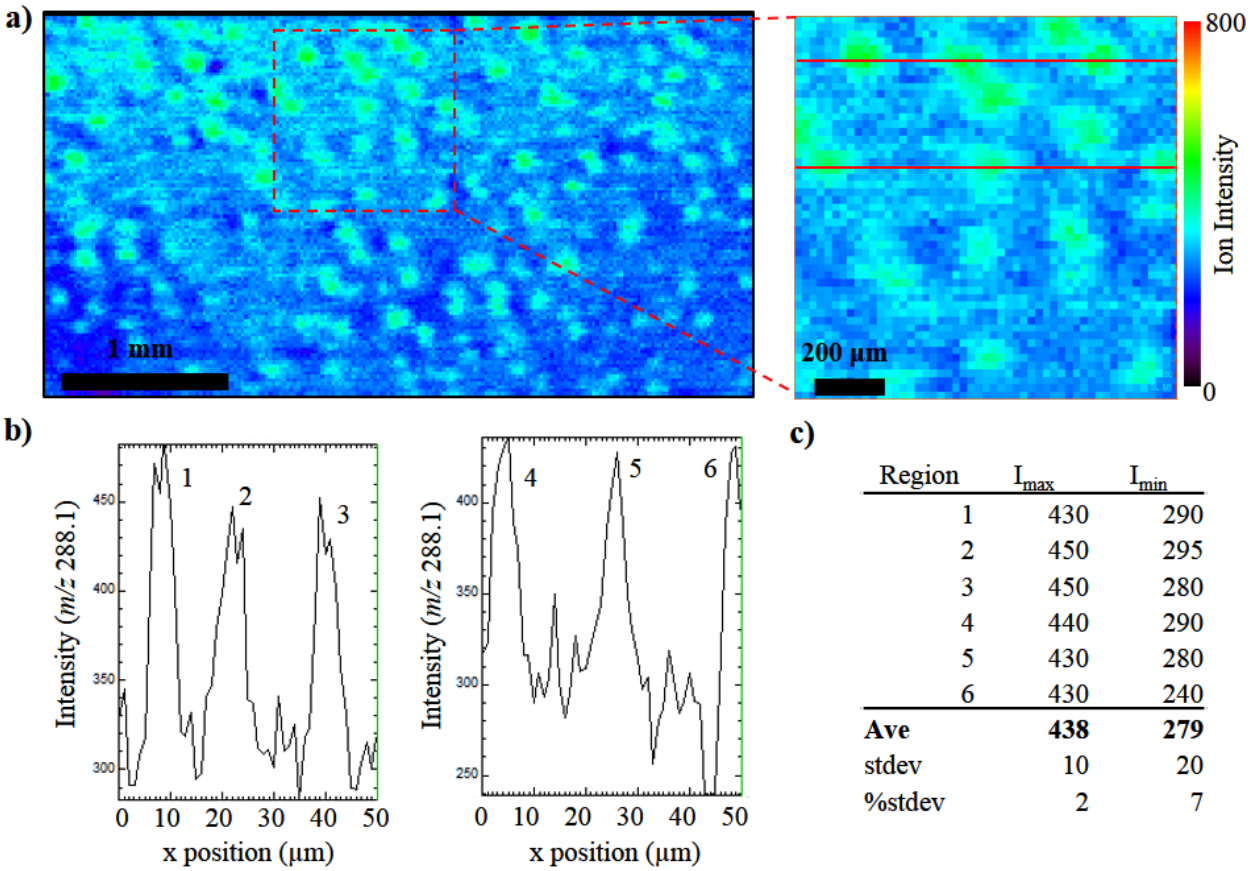

Region	I_{max}	I_{min}
1	430	290
2	450	295
3	450	280
4	440	290
5	430	280
6	430	240
Ave	**438**	**279**
stdev	10	20
%stdev	2	7

Figure 3.5. Line-scan measurements of the *m/z* 288.21 ion image from the 7 h biofilm shown in **Figure 3.3**. (**a**) Ion image for NQNO (*m/z* 288.21) with red box indicating magnified area; (**b**) line-scans across the two regions indicated by the red bars in (**a**); and (**c**) ion intensity measurements for the peaks and troughs of the line-scans.

spectra of HQNO and PQS is the quinolone ring stretch, which occurs at ~1357 cm^{-1} in HQNO, while in PQS this band is shifted to ~1369 cm^{-1}. The two secreted components are clearly differentiated by the distinct features in the loading plots, **Figure 3.6a-ii** and **iii**, which correspond to vibrational bands in the respective Raman spectra of the standard compounds and by the anti-correlated intensities in the heat maps of PC2 and PC3, cf. **Figure 3.6a-iv** and **v**.

Subsequent SIMS analysis of a similar region near the edge of the 48 h biofilm, **Figure 3.6b**, shows a ~10-fold reduction in AQ ion intensity when compared to the 7 h biofilm, **Figure 3.3b**. Although the C9-PQS/HQNO isomer is still the most abundant ion, the PQS/HQNO ion at *m/z* 260.18 is observed with a much higher relative abundance than in the 7 h film. Furthermore, the center of the film is all-but devoid of AQs, which are primarily confined to the film boundary. The appearance of high intensity ions near the colony edge in the low resolution SIMS images generally correlates with a thinner biofilm and may reflect either analyte migration during the drying process or natural variability in EPS composition.

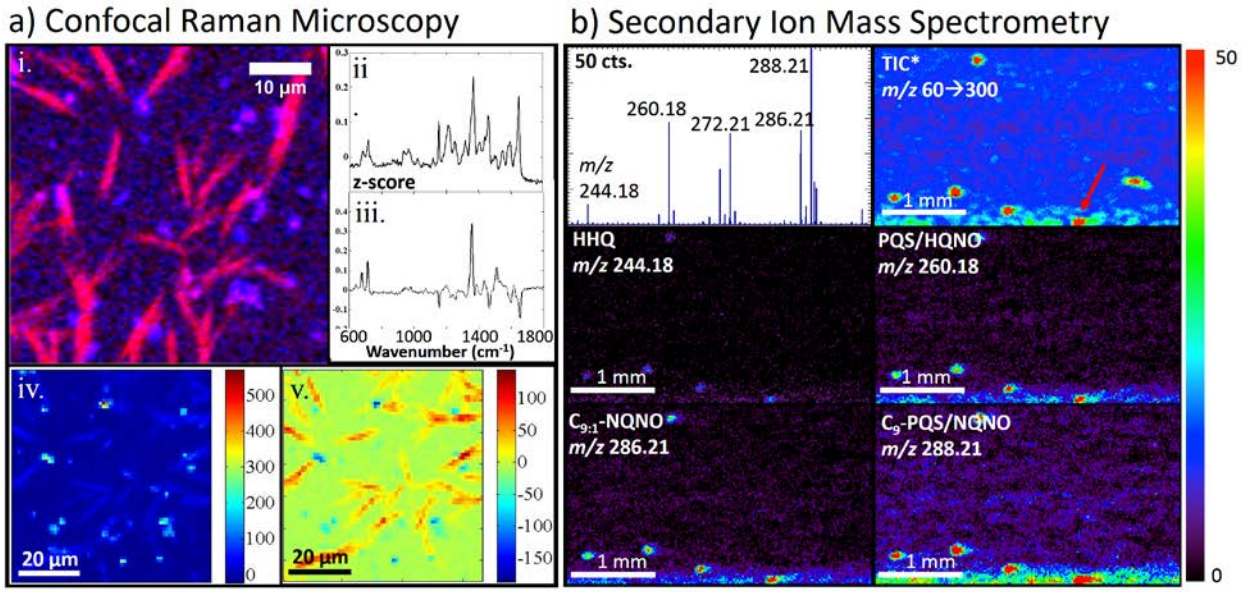

Figure 3.6. CRM (**a**) and targeted SIMS (**b**) imaging and microspectroscopy of a representative region of a 48-hour *P. aeruginosa* biofilm. (**a**) (i) Composite Raman image acquired from the edge of a 48 h static biofilm constructed from images integrated over 1338–1376 cm^{-1} (pink) and 1638–1676 cm^{-1} (blue) show the co-location of two distinct chemical entities within the same region; (ii) PC2 and (iii) PC3 contain features resembling bands of PQS and HQNO standards, respectively; heat maps of PC2 (iv) and PC3 (v). (**b**) SIMS images at lower resolution reveal that the central regions of the 48 h films are mostly devoid of the high intensity regions, with the AQs primarily confined to the colony boundary. The mass spectrum is an average of four pixels from a high-intensity region of the biofilm (as indicated by the red arrow). The TIC images include values in the *m/z* 60–300 range, scaled from 0 to 2 counts, while the individual ion images are scaled as indicated by the color bar on the right.

3.4.4. SIMS Imaging of Isomeric Species

The surprising observation of discrete regions of high *N*-oxide quinoline abundance by CRM in the 7 h biofilm inspired the development of tandem MSI methods targeting the PQS/HQNO and C9-PQS/NQNO isomeric pairs at *m/z* 260.18 and *m/z* 288.21 respectively. Tandem MSI methods were employed to examine adjacent regions of the microbial community to probe for the parent ions ion as well as characteristic fragments of the PQS (*m/z* 175.08, and 188.10) and *N*-oxide (*m/z* 159.08 and *m/z* 172.09) families, **Figure 3.7**. Ion images for the C9-PQS/NQNO precursor ion at *m/z* 288.21, **Figure3.7a**, shows the same microscopic pattern as in the MSI of **Figure 3.3**, as do the images from the NQNO fragment at *m/z* 159.08. This is in contrast to the most abundant C9-PQS fragment at *m/z* 175.07, which is near the lower abundance limit of our imaging capabilities and shows no discernable microscopic patterning. This results is in agreement with the product ion images acquired through fragmentation of *m/z* 260.18, **Figure 3.7b**, which shows microscopic patterning for *m/z* 260.18 and the HQNO specific fragment at 159.08 and low abundance for the PQS specific fragment at 175.08. These results support the tentative conclusions based on the

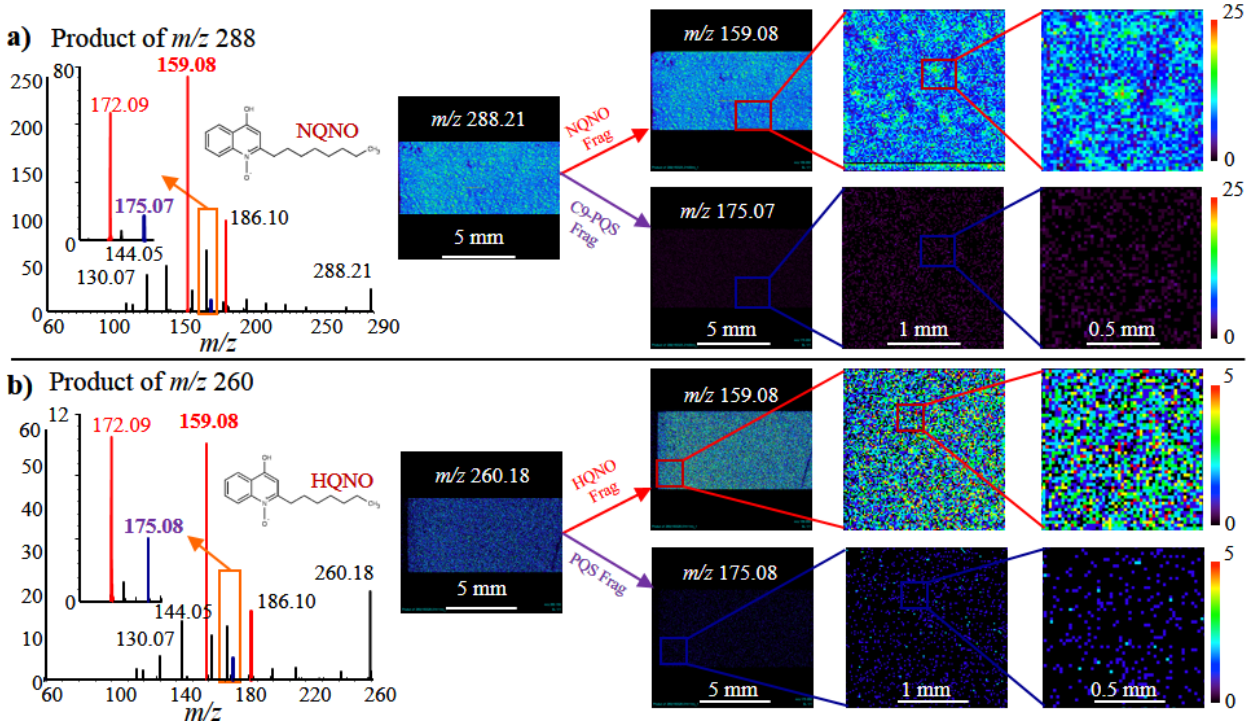

Figure 3.7. SIMS product ion spectra and images near the edge of a 7 h biofilm. (**a**) Tandem MS of *m/z* 288 reveals prominent fragments at *m/z* 159.08, 172.09, and 186.10 (red), which correspond to alkyl chain loss and rearrangement from the protonated *N*-oxide quinoline precursor, NQNO. Characteristic fragments for C9-PQS (blue) are also observable at *m/z* 175.07 and 188.08, although at a much lower intensity. Product ion images for the NQNO fragment (*m/z* 159.08) reveal microscopic patterning, while those for C9-PQS do not. (**b**) Tandem MS of *m/z* 260 reveals a similar fragmentation pattern, with prominent HQNO fragments (red) observable at *m/z* 159.08, 172.09, and *m/z* 186.10, and minor contributions from the PQS fragments (blue) at *m/z* 175.07 and 188.08. Microscopic patterning is observed for the NQNO fragment, but not the PQS fragment.

CRM analysis above, indicating that although all four analytes are present, the primary contributions to the early biofilm SIMS spectrum at *m/z* 260.18 and *m/z* 288.21 are the *N*-oxide constituents of the PQS/HQNO and C9-PQS/NQNO isomeric pairs.

3.4.5. Secondary Electron Microscopy for EPS Characterization

The distinct spatial heterogeneity in AQ distribution observed with CRM and SIMS, especially in the 7 h biofilms, raises obvious questions about the correlation between morphological and chemical features in the biofilms. Therefore, a 7 h biofilm was studied by scanning electron microscopy, which revealed that regions of high AQ abundance are morphologically distinct from the adjacent low intensity regions. **Figure 3.8a** shows that SEM micrographs of the 7 h biofilms exhibit a pattern of dark areas across the colony surface, the size and shape of which match the quinolone localization profiles observed with SIMS and CRM. Upon closer inspection, **Figures 3.8b** and **3.8c**, the cells in the dark regions of the film are encased in a thick material (left side of

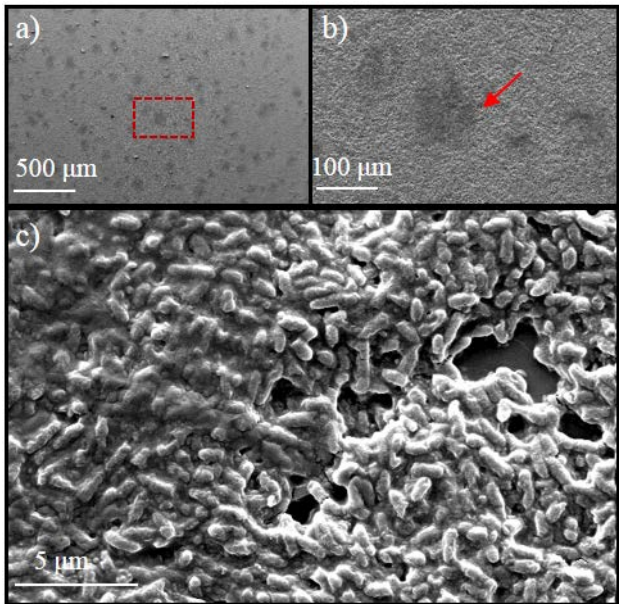

Figure 3.8. Scanning electron microscopy of early biofilms shows morphological patterning of the EPS across the colony surface. The rod-shapes are individual *P. aeruginosa* cells. The box in (**a**) and the arrow in (**b**) indicates the location of images **b** and **c**, respectively. Scale bars are 500, 100, and 5 µm for **a**, **b** and **c**.

Figure 3.8c), while the surrounding regions are relatively barren and more exposed to the surrounding environment. Dark and light regions in the SEM micrograph indicate regions of low and high electron emission, respectively, which further supports an interpretation of the CRM and SIMS images in terms of a heterogeneous chemical distribution.[28] It is possible that these regions represent nucleation sites for the local onset of biofilm attachment or EPS production.

3.4.6. CRM Imaging of Swarm Zones

Moving beyond the inoculated Si wafer constructs, high density aggregations of quinolones and *N*-oxide quinolines were also observed within surface motile communities of swarming *P. aeruginosa* after 48 h. PC analysis of the full dataset used to produce the Raman image in **Figure 3.9a** generated a PC1 loading plot, **Figure 3.9b** that contains features resembling bands of both PQS and HQNO. Features at 682 and 718 cm^{-1} are at the same position as bands from the spectrum of HQNO standard, while features with peaks at 1553 and 1654 cm^{-1} match bands from the spectrum of the PQS standard. The broad feature at ~1359 cm^{-1} appears to be a combination of closely spaced features in the 1350–1400 cm^{-1} regime, which is tentatively assigned to contributions from the quinolone ring vibration of both *N*-oxide quinolines and 3-hydroxy-4-quinolones, indicating that these analytes are highly co-localized and thus contribute to the same principal component, PC1. The observation that similar quinolone accumulations occur both in static biofilms and within swarm zones highlights the dichotomy between surface motility and biofilm formation. The quinolones and quinolines tend to accumulate in regions where the cells have colonized the surface and may have begun forming stationary biofilms, as opposed to the advancing swarm edge where the cells are actively motile.[29-30]

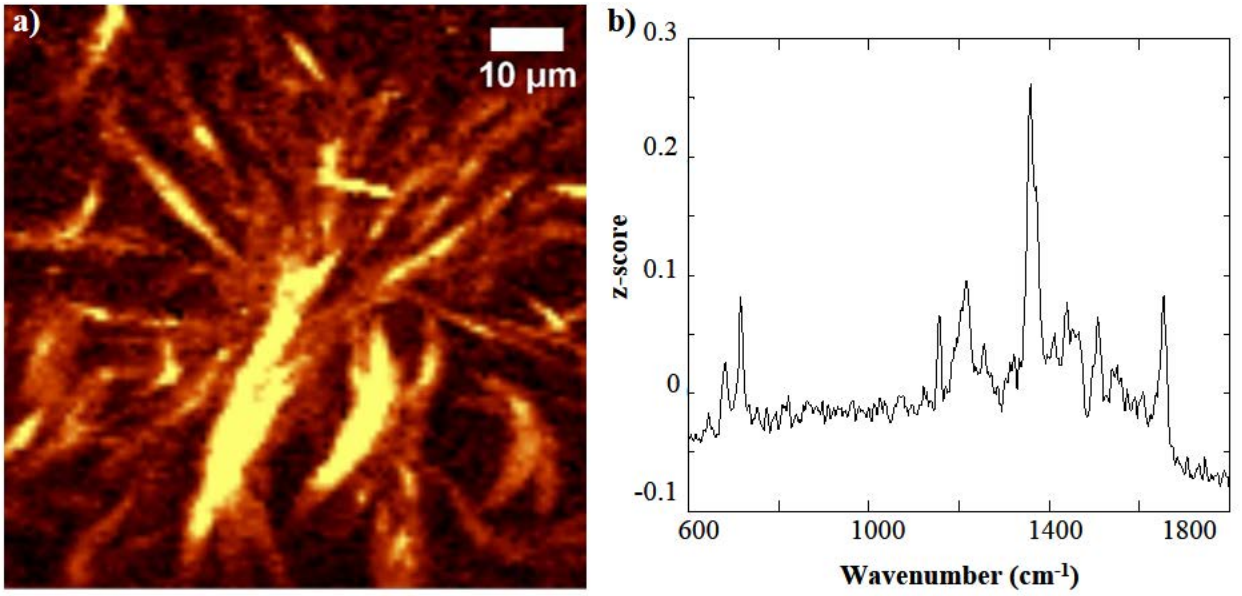

Figure 3.9. Raman imaging of AQ aggregates in a *P aeruginosa* swarm. (**a**) Raman image acquired from a 48 h swarm plate constructed from a 1338–1376 cm^{-1} filter to include the marker band for quinolones/quinolines; (**b**) loading plot of PC1 generated from analysis of the Raman image of the 48 h swarm plate. PC1 contains features that correspond to bands from both PQS and HQNO standard spectra.

3.5. Conclusions

In this work a combination of SIMS and CRM imaging was used to characterize the spatial distribution of several quinolone quorum sensing molecules and quinoline secondary metabolites across the surface of *P. aeruginosa* throughout various states of organization. CRM in conjunction with PCA was first used to identify broad molecular classes, e.g. quinolones and quinolines, and this information was used to guide mass spectrometric analysis. This multimodal approach allowed for the conclusion that the primary AQs belong to the *N*-oxide family as opposed to the isomeric PQS family at 7 h of biofilm growth. This is in contrast with 48 h biofilms, which are marked by a dramatic decrease in the quantity of all AQs and a shift from the *N*-oxide family towards the PQS family, with co-localization of the two species. These combined CRM/MSI experiments demonstrate how molecular information was obtained across several orders of magnitude in length, with distinct chemical distributions observed at length scales from a few micrometers to centimeters.

Our results demonstrate the efficacy of a combined MSI/CRM approach for characterization of complex biological systems and suggest an important role for *N*-oxide quinolines in early biofilm formation. We show that the transition from the planktonic state to the

formation of a biofilm is marked by a dramatic increase in the presence of the *N*-oxide family of quinolines, and chemical similarities between swarming motility and early biofilms indicate conserved chemical expression across multiple phenotypical states. Furthermore, CRM and SIMS imaging in conjunction with electron microscopy reveal a dramatic patterning of highly localized biomolecules across the surface of 7 h biofilms, which correspond to areas of thick matrix composition.

3.6. References

1. Rubakhin, S. S.; Sweedler, J. V., *Mass spectrometry imaging: Principles and protocols*. Humana Press New York:: 2010.
2. Huang, W. E.; Li, M.; Jarvis, R. M.; Goodacre, R.; Banwart, S. A., Chapter 5 - Shining Light on the Microbial World: The Application of Raman Microspectroscopy. In *Advances in Applied Microbiology*, Allen, I. L.; Sima, S.; Geoffrey, M. G., Eds. Academic Press: 2010; Vol. Volume 70, pp 153-186.
3. McDonnell, L. A.; Heeren, R. M. A., Imaging mass spectrometry. *Mass Spectrometry Reviews* **2007,** *26* (4), 606-643.
4. Petry, R.; Schmitt, M.; Popp, J., Raman Spectroscopy—A Prospective Tool in the Life Sciences. *ChemPhysChem* **2003,** *4* (1), 14-30.
5. Ilin, Y.; Kraft, M. L., Secondary ion mass spectrometry and Raman spectroscopy for tissue engineering applications. *Current Opinion in Biotechnology* **2015,** *31* (0), 108-116.
6. Masyuko, R.; Lanni, E. J.; Sweedler, J. V.; Bohn, P. W., Correlated imaging - a grand challenge in chemical analysis. *Analyst* **2013,** *138* (7), 1924-1939.
7. Li, Z.; Chu, L.-Q.; Sweedler, J. V.; Bohn, P. W., Spatial Correlation of Confocal Raman Scattering and Secondary Ion Mass Spectrometric Molecular Images of Lignocellulosic Materials. *Analytical Chemistry* **2010,** *82* (7), 2608-2611.
8. Ahlf, D. R.; Masyuko, R. N.; Hummon, A. B.; Bohn, P. W., Correlated mass spectrometry imaging and confocal Raman microscopy for studies of three-dimensional cell culture sections. *Analyst* **2014,** *139* (18), 4578-4585.
9. Fagerer, S. R.; Schmid, T.; Ibanez, A. J.; Pabst, M.; Steinhoff, R.; Jefimovs, K.; Urban, P. L.; Zenobi, R., Analysis of single algal cells by combining mass spectrometry with Raman and fluorescence mapping. *Analyst* **2013,** *138* (22), 6732-6736.
10. Lanni, E. J.; Masyuko, R. N.; Driscoll, C. M.; Dunham, S. J. B.; Shrout, J. D.; Bohn, P. W.; Sweedler, J. V., Correlated Imaging with C60-SIMS and Confocal Raman Microscopy: Visualization of Cell-Scale Molecular Distributions in Bacterial Biofilms. *Analytical Chemistry* **2014,** *86* (21), 10885-10891.
11. CDC. *Pseudomonas aeruginosa* in Healthcare Settings 2014. (accessed 05/04/2015).
12. Lyczak, J. B.; Cannon, C. L.; Pier, G. B., Lung Infections Associated with Cystic Fibrosis. *Clinical Microbiology Reviews* **2002,** *15* (2), 194-222.
13. Stewart, P. S.; William Costerton, J., Antibiotic resistance of bacteria in biofilms. *The Lancet* **2001,** *358* (9276), 135-138.
14. Høiby, N.; Ciofu, O.; Bjarnsholt, T., *Pseudomonas aeruginosa* biofilms in cystic fibrosis. *Future Microbiology* **2010,** *5* (11), 1663-1674.
15. Prevention, C. f. D. C. a., Antibiotic Resistance Threates in the United States. Prevention, C. f. D. C. a., Ed. Atlanta, GA, 2013.
16. Singh, P. K.; Schaefer, A. L.; Parsek, M. R.; Moninger, T. O.; Welsh, M. J.; Greenberg, E. P., Quorum-sensing signals indicate that cystic fibrosis lungs are infected with bacterial biofilms. *Nature* **2000,** *407* (6805), 762-764.

17. Dubern, J.-F.; Diggle, S. P., Quorum sensing by 2-alkyl-4-quinolones in *Pseudomonas aeruginosa* and other bacterial species. *Molecular BioSystems* **2008,** *4* (9), 882-888.
18. Reen, F. J.; Mooij, M. J.; Holcombe, L. J.; McSweeney, C. M.; McGlacken, G. P.; Morrissey, J. P.; O'Gara, F., The Pseudomonas quinolone signal (PQS), and its precursor HHQ, modulate interspecies and interkingdom behaviour. *FEMS Microbiology Ecology* **2011,** *77* (2), 413-428.
19. De Kievit, T. R., Quorum sensing in *Pseudomonas aeruginosa* biofilms. *Environmental Microbiology* **2009,** *11* (2), 279-288.
20. Morales-Soto, N.; Anyan, M. E.; Mattingly, A. E.; Madukoma, C. S.; Harvey, C. W.; Alber, M.; ziel, E.; Kearns, D. B.; Shrout, J. D., Preparation, Imaging, and Quantification of Bacterial Surface Motility Assays. **2015,** (98), e52338.
21. Lanni, E.; Dunham, S. B.; Nemes, P.; Rubakhin, S.; Sweedler, J., Biomolecular Imaging with a C60-SIMS/MALDI Dual Ion Source Hybrid Mass Spectrometer: Instrumentation, Matrix Enhancement, and Single Cell Analysis. *J. Am. Soc. Mass Spectrom.* **2014,** *25* (11), 1897-1907.
22. Lanni, E. J.; Masyuko, R. N.; Driscoll, C. M.; Aerts, J. T.; Shrout, J. D.; Bohn, P. W.; Sweedler, J. V., MALDI-guided SIMS: Multiscale Imaging of Metabolites in Bacterial Biofilms. *Analytical Chemistry* **2014,** *86* (18), 9139-9145.
23. Lépine, F.; Milot, S.; Déziel, E.; He, J.; Rahme, L., Electrospray/mass spectrometric identification and analysis of 4-hydroxy-2-alkylquinolines (HAQs) produced by *Pseudomonas aeruginosa*. *J. Am. Soc. Mass Spectrom.* **2004,** *15* (6), 862-869.
24. Heeb, S.; Fletcher, M. P.; Chhabra, S. R.; Diggle, S. P.; Williams, P.; Cámara, M., Quinolones: from antibiotics to autoinducers. *FEMS Microbiology Reviews* **2011,** *35* (2), 247-274.
25. Neugebauer, U.; Szeghalmi, A.; Schmitt, M.; Kiefer, W.; Popp, J.; Holzgrabe, U., Vibrational spectroscopic characterization of fluoroquinolones. *Spectrochimica Acta Part A: Molecular and Biomolecular Spectroscopy* **2005,** *61* (7), 1505-1517.
26. Wang, Y.; Yu, K.; Wang, S., Vibrational spectra study on quinolones antibiotics. *Spectrochimica Acta Part A: Molecular and Biomolecular Spectroscopy* **2006,** *65* (1), 159-163.
27. Frosch, T.; Popp, J., Relationship between molecular structure and Raman spectra of quinolines. *Journal of Molecular Structure* **2009,** *924–926* (0), 301-308.
28. Reimer, L., Image Contrast and Signal Processing. In *Scanning Electron Microscopy*, Springer Berlin Heidelberg: 1998; Vol. 45, pp 207-251.
29. Shrout, J. D.; Chopp, D. L.; Just, C. L.; Hentzer, M.; Givskov, M.; Parsek, M. R., The impact of quorum sensing and swarming motility on *Pseudomonas aeruginosa* biofilm formation is nutritionally conditional. *Molecular microbiology* **2006,** *62* (5), 1264-77.
30. Verstraeten, N.; Braeken, K.; Debkumari, B.; Fauvart, M.; Fransaer, J.; Vermant, J.; Michiels, J., Living on a surface: swarming and biofilm formation. *Trends Microbiol* **2008,** *16* (10), 496-506.

CHAPTER 4

Metal-Assisted Polyatomic SIMS and Laser Desorption/Ionization for Enhanced Small Molecule Imaging of Bacterial Biofilms

4.1. Acknowledgements

This chapter was originally published as an original research article in a special issue of *Biointerphases* dedicated to the 20th Annual Conference in Secondary Ion Mass Spectrometry (*Biointerphases* **2016**, 11 (2), 02A325). It has been reprinted with permission from *Biointerphases*. Copyright 2016, American Vacuum Society. The manuscript was co-authored by Sage J. B. Dunham, Troy J. Comi, Kyungwon Ko, Bin Li, Nameera F. Baig, Nydia Morales-Soto, Joshua D. Shrout, Paul W. Bohn, and Jonathan V. Sweedler. SJBD planned and performed most of the experiments, developed all original methods, and wrote most of the manuscript. TJC helped with the statistical analysis, experimental planning, and manuscript composition. KK performed many of the tandem mass spectrometry experiments and helped to write the manuscript. BL helped to plan experiments, interpret results, and write the manuscript. NFB cultured the biological samples, helped to plan experiments, and assisted with manuscript writing. NMS, JDS, PWB, and JVS helped to plan experiments, interpret results, and write the manuscript. Expert assistance with AFM and SEM was provided by Drs. Leilei Yin, Catherine Wallace, and Scott Robinson from the Beckman Institute Imaging Technology Group, which is partially supported by the National Science Foundation Award Number DBI-9871103. Research reported in this chapter was supported by the National Institute of Allergy and Infectious Diseases of the National Institutes of Health under Award Number R01AI113219, and the Department of Energy under Award Number DE SC-0006642.

4.2. Introduction

Bacterial biofilms are one of the oldest and most prolific communal ecosystems on Earth. These amalgamations of cells, extracellular DNA, proteins, polysaccharides, lipids, and various secondary metabolites present a unique analytical challenge that requires both the application of existing analytical techniques and the invention of novel approaches.[1-3] One of the most promising methodologies for studying the chemical composition and distribution of biofilm ecosystems is

microprobe mass spectrometry imaging (MSI), which uses a focused beam of ions, photons, or solvent to desorb molecules from a sample for subsequent spatially resolved spectrometric analysis. Over the previous two decades MSI has emerged as a vital tool for *in situ* chemical imaging of many biological systems, including biofilms,[4-6] cultured neurons and neural networks,[7-8] and subcellular structures.[9-10]

Owing to its broad commercial availability and unparalleled mass range, matrix-assisted laser desorption / ionization (MALDI) is the most widely applied MSI ionization method for many sample types, including biofilms.[11-12] While versatile, MALDI is limited by the effects of matrix interference in the low mass range ($m/z < 500$). The application of solvated organic matrix can also induce analyte migration, thereby altering native molecular distributions and limiting the effective spatial resolution.[13-14] One means for overcoming the challenges associated with organic matrices is to use "matrix-free" methods for laser desorption / ionization (LDI); a broad assortment of sample preparation strategies, such as the application of metal films and nanoparticles,[15-18] or the use of patterned surfaces and clathrate nanostructures,[19-20] among other approaches.[21-22]

Requiring no sample preparation beyond what is necessary for high vacuum compatibility, secondary ion mass spectrometry (SIMS) offers a small molecule imaging approach that is complementary to MALDI. The principal advantages of SIMS include spatial resolution—with many commercial instruments offering a lateral resolution better than 500 nm—and the capability to examine unadulterated samples, thus eliminating matrix interference and mitigating analyte migration. SIMS has been successfully applied to image many biological systems, including biofilms, tissues, and cells.[23] The SIMS ion bombardment process is highly energetic, making it most suited for imaging small molecular ions and characteristic molecular fragments ($m/z < \sim 500$). Energetic ion bombardment also produces surface and subsurface damage that confines analysis to a fraction (typically < 1%) of the uppermost layer of the sample surface, thereby reducing the quantity of accessible analyte.[23] Researchers have expended great effort on both sample preparation and instrument design, with the intention of expanding molecular coverage and sensitivity.

One important instrumental innovation has been the introduction of cluster and polyatomic primary ion sources, which are now commonly used for biomolecular imaging. These sources spread the kinetic energy of the primary ion impact among many atoms in the projectile, resulting in reduced analyte fragmentation, more efficient molecular ionization, and less subsurface

damage.[24] Cluster sources have expanded the practical mass range for SIMS above *m/z* 1000 while allowing analysis of greater portions of the surface and subsurface regions.[23, 25]

On the other end of SIMS inquiry, researchers have focused on developing novel sample treatment strategies broadly aimed at improving ionization. Innovations have included exposure to reactive vapor,[26] and application of traditional MALDI matrices,[27-28] metal films,[16, 29] or nanoparticles.[30] Applying a thin layer of gold or silver to the sample is particularly appealing due to the wide availability of conventional sputter-coating devices for electron microscopy. Metallization has been investigated for its ability to improve SIMS sensitivity and image quality for samples as diverse as tissue and cells,[29, 31-32] polymers,[33-38] and small organic molecules or molecular mixtures.[34, 37-43] Unfortunately, the effort to combine the benefits of cluster ionization with metallization has thus far been unsuccessful, with several researchers reporting decreased molecular ion yields for metallized samples when a large polyatomic or cluster source is employed.[37, 39] To date, most fundamental MetA-SIMS studies have been conducted using spin-cast organic standards or organic polymers on hard surfaces, and we hypothesized that the effects of surface metallization might be very different in soft and architecturally complex samples. In this work we utilize a hybrid imaging mass spectrometer, equipped with both a 20 kV Buckminsterfullerene (C_{60}^+) ion beam and a UV laser, to examine the effect of surface metallization upon the ionization of small molecule secondary metabolites in *Pseudomonas aeruginosa* (*P. aeruginosa*) biofilms, a biological system with a complex molecular composition and surface architecture. We further exploit the hybrid nature of the instrument to compare C_{60}-SIMS, metal-assisted (MetA)-C_{60}-SIMS, and MetA-LDI.

The gram-negative bacterium and opportunistic pathogen *P. aeruginosa* offers an excellent model for biofilm biology, as the organism readily forms intricate microbial communities that utilize a diverse collection of small molecules to coordinate behaviors, including colony formation, virulence, and cell death.[44] We have previously developed methods for the analysis of biofilms using both MetA-LDI and monatomic (Au^+ primary ion beam) MetA-SIMS, and found that coating the biofilm surface with a few nanometers of gold improved sensitivity for lipids and small molecule secondary metabolites in LDI and monatomic SIMS.[16] In separate work we created methods that correlate C_{60}-SIMS imaging with confocal Raman microscopy, and applied them to image several small molecule secondary metabolites in the same biofilm model.[5, 27]

In the present study, we have found that while C_{60}-SIMS, MetA-C_{60}-SIMS and MetA-LDI are applicable for imaging small molecules in *P. aeruginosa* biofilms, each presents its own unique advantages. Our results show that, in comparison to an untreated biofilm, a 2.5 nm layer of gold selectively improves C_{60}-SIMS ionization efficiency for several analyte classes, including rhamnolipids (RHLs) and 2-alkyl-4-quinolones (AQs). Remarkably, the enhancement was not observed for standard solutions deposited on a bare silicon wafer, supporting the hypothesis that surface hardness and projectile penetration substantially influence biomolecular fragmentation and ionization efficiency.[36, 43] Furthermore, in MetA-C_{60}-SIMS, high-intensity background ions derived from the cell culture medium are selectively suppressed, thereby dramatically improving spectral quality. These findings have potential application to biomolecular SIMS imaging of samples of diverse origin.

4.3. Materials, Reagents, and Methods

4.3.1. Materials and Reagents

Silicon tiles were purchased from University Wafer (South Boston, MA) and stainless steel sample plates used throughout all MSI experiments were designed in-house and manufactured in the University of Illinois at Urbana-Champaign School of Chemical Sciences Machine Shop. Analytical standards, including 2-heptyl-3-hydroxy-4(1*H*)-quinolone (*Pseudomonas* quinolone signal, PQS), 2-heptyl-4-quinolone (HHQ), and R95 rhamnolipid, were purchased from Sigma-Aldrich (St Louis, MO), while 4-hydroxy-2-heptylquinoline-*N*-oxide (HQNO) was purchased from Cayman Chemicals (Ann Arbor, MI). All standards were used as received without further purification.

4.3.2. Cell Culture and Biofilm Formation

Pseudomonas aeruginosa (PAO1C) was grown overnight at 37 ºC with 240 rpm agitation in a chemically defined, phosphate-buffered, minimal culture medium containing 30 mM sterilized glucose.[45] Aliquots (200 µL each) of the resulting culture (OD_{600} = 1) were transferred to 2 cm × 2 cm sterilized silicon shards in a Petri dish. Following 10–15 min of incubation, 18 mL of fresh culture medium with 30 mM glucose was gently added and the bacteria were allowed to grow at 37 ºC for 24 h. The liquid medium then was carefully removed from the dish, and the resulting colonies were allowed to dry for 1 h in a sterile hood. While care was taken to generate samples with similar morphology, biofilms are inherently heterogeneous and it is therefore difficult, and

possibly undesirable, to cultivate identical biological replicates. In this case, two of the samples prepared for this study were morphologically and chemically similar, while a third contained a central region with low cell density. Control samples were generated by depositing 10 μL of culture medium onto clean silicon shards and drying the resulting spot under a gentle stream of N_2. Samples were stored in a positive-pressure nitrogen dry box until analysis.

4.3.3. Gold Sputter Coating and Morphological Evaluation

Gold sputter coating was performed as previously described[16] using a Desk II TSC sputter coater (Denton Vacuum, Moorestown, NJ) with 64 mTorr Ar and a 40 mA current. The thickness and morphology of the gold layer were evaluated via atomic force microscopy (AFM) using a Multimode NanoScope IIIa (Veeco Metrology Inc., Santa Barbara, CA) equipped with a silicon nitride cantilever (ScanAsyst-Air, Bruker AXC Inc., Madison, WI) with a tip radius of 10–20 nm. Sputtering for 5–6 s resulted in the application of 2.5 nm of gold on silicon (see Section **3c**), which was initially optimized for MetA-C_{60}-SIMS and used throughout all experiments. It is important to note that the optimal overlay thickness is dependent upon many variables, including the analyte of interest, the surface composition, and the choice of microprobe (e.g., projectile mass, laser energy, etc.). For example, previous work has shown that a thicker coating of ~6 nm is optimal for MetA-UV-LDI[29] and that 0.2–2 nm is optimal for monatomic SIMS with Xe^+, Bi^+, Ar^+, and Ga^+ bombardment of single-component organic standards.[34]

Biofilm morphology was evaluated with both AFM (as described above) and scanning electron microscopy (SEM). For SEM, a gold-treated sample was examined using a field-emission environmental scanning electron microscope (Philips XL30 ESEM-FEG, FEI Company, Hillsboro, OR) operated with 5 kV and a working distance of 6.2 mm.

4.3.4. Sequential MSI and Tandem MS

Sequential imaging experiments were performed with a hybrid MALDI/C_{60}-SIMS time-of-flight (ToF) imaging mass spectrometer, which is a modified QSTAR-XL (AB SCIEX, Framingham, MA) described in detail elsewhere.[27] Positive-mode imaging was conducted at a raster size of 300 μm × 300 μm with 1.5 s of total acquisition time per pixel. The mass range was confined to *m/z* 100–1000, with a Q_1 ion guide transmission bias of 10, 20, 30, and 40% at *m/z* 120, 240, 440, and 600, respectively. $In_{1\text{-}7}^+$ cluster ions were used for external calibration. Images were collected in Analyst 1.1 and oMALDI Server 5.1 (AB SCIEX), converted from wiff to img format at 20 data points per mass unit, and processed with BioMap (Novartis, Basel, Switzerland).

SIMS imaging with neat or metallized samples was performed using a 20 keV continuous C_{60}^+ beam (Ionoptika Ltd., Hampshire, UK) operated with a 80-µm spot size and a 1300 pA sample current for a total ion dose of 5.1×10^{13} ions/cm^2. For MetA-LDI, a 337 nm Spectra Physics (Santa Clara, CA) VLS-335 pulsed nitrogen laser (oblong spot size of 100 µm × 200 µm) was operated at 40 Hz and 90 µJ. As illustrated in **Scheme 4.1**, biofilms were (1) imaged directly by C_{60}-SIMS, (2) coated in 1–2 nm of Au and imaged by MetA-C_{60}-SIMS, and (3) imaged by MetA-LDI. Between each image collection, the analysis region was offset by 100 µm to enable examination of an unperturbed region. It is important to note that the laser spot is larger than the ~120 µm of unperturbed area; therefore the peripheries of the LDI rows may have been influenced by the prior SIMS acquisitions. Tandem-MS (MS^2) was performed directly from the sample surface using the spectrometer and microprobe settings described above, argon collision gas, and 20–50 eV CID as needed.

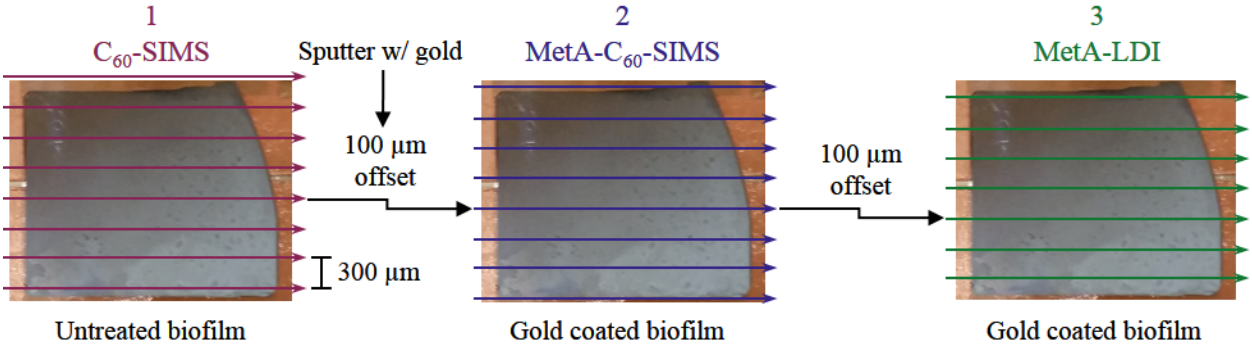

Scheme 4.1. Experimental design for the sequential imaging experiments. The 100 µm offset provided an unperturbed region for each subsequent ionization modality; 2–3 nm of gold was applied between images 1 and 2.

4.3.5. Statistical Evaluation of the Sequential Imaging Results

To quantitatively investigate the spectral changes associated with gold coating, MSI data were analyzed with several custom MATLAB scripts (MathWorks, Natick, MA). AB SCIEX wiff files were converted to mzML with the ProteoWizard msconvert function,[46] and the resulting mzML files were further converted to imzML with the imzMLConverter program[47] and read into MATLAB with a modified version of loadimzMLfile from MSiReader.[48] The raw spectra were binned at 0.1 *m/z* for non-targeted analysis, and a total ion count (TIC)-normalized average spectrum was calculated for each image row. For principal component analysis (PCA), the image matrices were concatenated and analyzed with the pca functions in MATLAB. Score plots depict the score of each averaged row of the image. The data were further analyzed with targeted *m/z* values corresponding to potential analytes of interest (**Table 4.1**). The TIC-normalized, maximum

intensity within 250 ppm of each *m/z* value was extracted and averaged by row as before. In addition to PCA, the relative change of absolute intensity was also calculated as the pair-wise difference between corresponding rows of the images.

Table 4.1. Ions used for targeted principal component analysis.

AQ fragments		**AQs**		**Rhamnolipids**	
Name	*m/z*	Name	*m/z*	Name	*m/z*
C_9H_6NO	144.04	C7:1 HHQ [+H]	242.16	R-C8 [+2Na-H]	351.14
C_9H_8NO	146.06	HHQ [+H]	244.17	R-C10 [+Na]	357.19
$C_{10}H_9NO$	159.07	C7:1 PQS/HQNO [+H]	258.15	R-C10 [+2Na-H]	379.17
$C_{11}H_{10}NO$	172.08	PQS/HQNO [+H]	260.17	R-C12:2 [+Na]	381.19
$C_{10}H_9NO_2$	175.06	C9:1 NHQ [+H]	270.19	R-C17:2 [+K]	467.24
$C_{12}H_{10}NO$	184.08	NHQ [+H]	272.20	R-R-C8 [+2Na-H]	497.20
$C_{12}H_{12}NO$	186.09	C9:1 PQS/NQNO [+H]	286.18	R-R-C10 [+Na]	503.25
$C_{11}H_{10}NO_2$	188.07	C9 PQS/NQNO [+H]	288.20	R-R-C10 [+2Na-H]	525.23
$C_{13}H_{10}NO$	196.08	C11:1 UHQ [+H]	298.22	R-C10-C10 [+Na]	527.32
		UHQ [+H]	300.23	R-C10-C10 [+2Na-H]	549.30
		C10:1 PQS/DQNO [+H]	300.20	R-R-C10-C10:1 [+H]	649.38
		C10 PQS/DQNO [+H]	302.21	R-R-C8-C10 [+2Na-H]	667.33
		C12:2 HDQ [+H]	310.22	R-R-C10-C10 [+Na]	673.38
		C11:2 UQNO [+H]	312.20	R-R-C10-C10 [+2Na-H]	695.36
		C11:1 UQNO [+H]	314.21		
		UQNO [+H]	316.21		
		C13:2 TQNO [+H]	340.23		
		C13:1 TQNO [+H]	342.24		

4.4. Results and Discussion

4.4.1. Application of a Thin Gold Film Reduces Fragmentation and Ionization of Media-Specific Compounds

Three separate *P. aeruginosa* biofilms were sequentially imaged, as described in the **Methods** section. The growth across two of these samples was macroscopically uniform, while the center of the third sample had a region of visibly thin growth (**Figure 4.1).** Representative spectra for the three imaging modalities are displayed in **Figure 4.2a**. Each spectrum was generated by averaging the pixels contained within an imaging row, and was drawn from adjacent regions on the same

biofilm to diminish intra- and inter-sample variability. While the three methods generated ions across the entire mass range, the C_{60}-SIMS spectrum contains multiple peaks that are either substantially higher in absolute intensity or exclusive to this ionization mode. Comparison of the C_{60}-SIMS spectra from Biofilm 2 to those obtained from the culture media control (**Figure 4.3b**) shows that the overwhelming majority of the high intensity ions from the biofilm are also present in the media control, suggesting that the high intensity C_{60}-SIMS ions are derived from constituents of the culture medium, rather than bacteria-specific biomolecules. Following the application of gold, media-specific ion intensities are substantially diminished and the Au^+, Au_3^+, and Au_5^+ ions (*m/z* 196.97, 590.91, and 984.80, respectively) are predominant. The MetA-LDI spectrum is also free of the most intense C_{60}-SIMS constituents, and several ions arise in the *m/z* range corresponding to lipids (e.g., *m/z* 500–800).

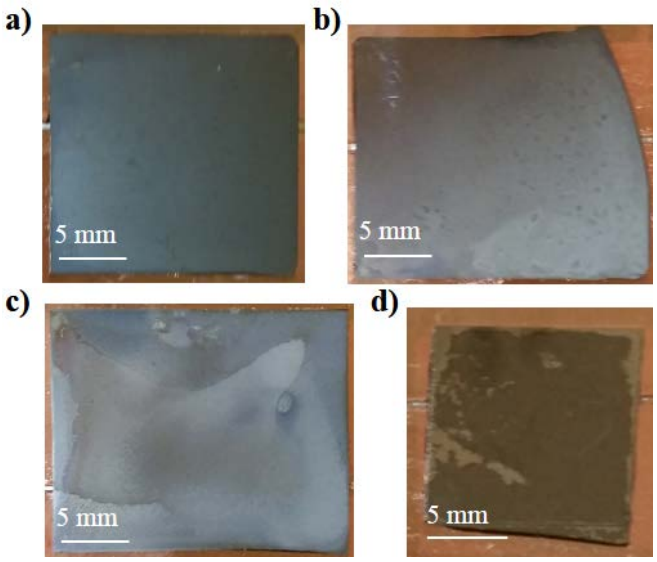

Figure 4.1. *P. aeruginosa* biofilms used for the experiments described in this paper: (**a-c**) Biofilms 1-3, (**d**) media control.

The three images from each sample and the media control were deconstructed into individual rows, the pixels contained within each row were averaged together to create a collection of 780 spectra from 12 images, and non-targeted PCA was performed to evaluate the major differences between samples and between ionization methods. The scores and loadings plots for the first two principal components **Figure 4.3** show two levels of clustering, with the mode of ionization providing primary clustering, and the sample origin providing secondary clustering. Those spectra affiliated with C_{60}-SIMS (red) largely group at positive values of PC1 (44% of the total variance in the data set), which are heavily influenced by media-specific background ions (e.g., *m/z* 288.9, 554.7, 390.8, 186.9, etc.), and towards the null point of PC2 (23% of the variance). This is in contrast with the MetA-C_{60}-SIMS spectra (blue), which separate to positive values of PC2 and the null point of PC1. The positive direction of PC2 is heavily weighted by the $Au_{1\text{-}3}^+$ cluster ions and unidentified peaks at *m/z* 608.8 and 626.9, which are most prominent in the MetA-

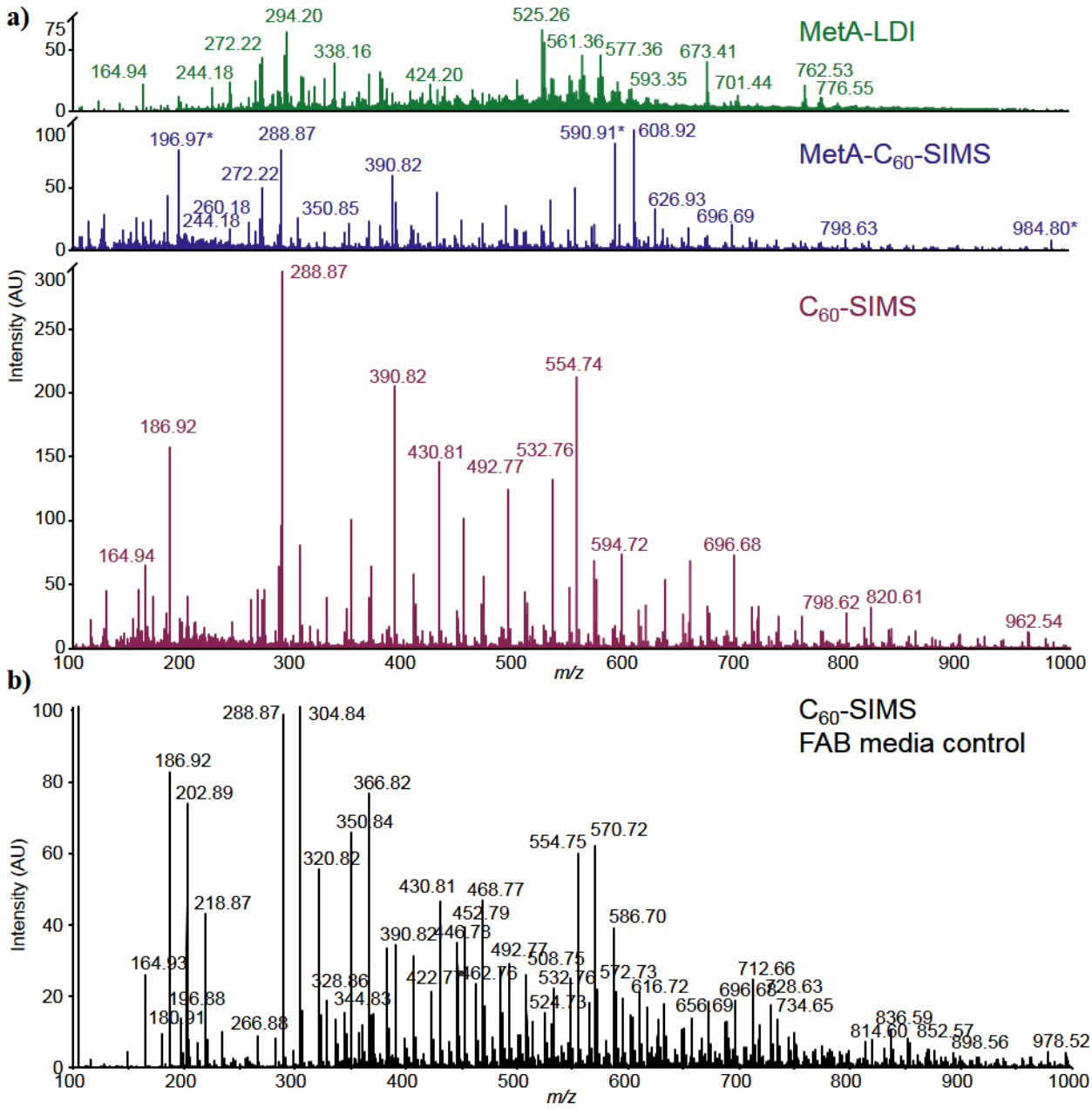

Figure 4.2. Spectral comparison between MetA-LDI, MetA-C_{60}-SIMS, and C_{60}-SIMS of the same sample. (**a**) Representative mass spectra for MetA-LDI (green), MetA-C_{60}-SIMS (blue), and C_{60}-SIMS (red), generated by averaging pixels across adjacent imaging rows in biofilm 2; and (**b**) representative C_{60}-SIMS spectra from a FAB media control, which shows many peaks in common with the uncoated biofilm. The gold cluster ions are marked with an asterisk (*) in the MetA-C_{60}-SIMS spectrum of panel (**a**).

C_{60}-SIMS spectra. Also of note, many of the C_{60}-SIMS and MetA-C60-SIMS spectra are roughly distributed along lines in the scores plot. This distribution is generally indicative of a sample with roughly constant ratios for ions along a given vector, but that differ in absolute intensity. In this case, the spectra partition along PC1, which is heavily influenced by background ions arising from

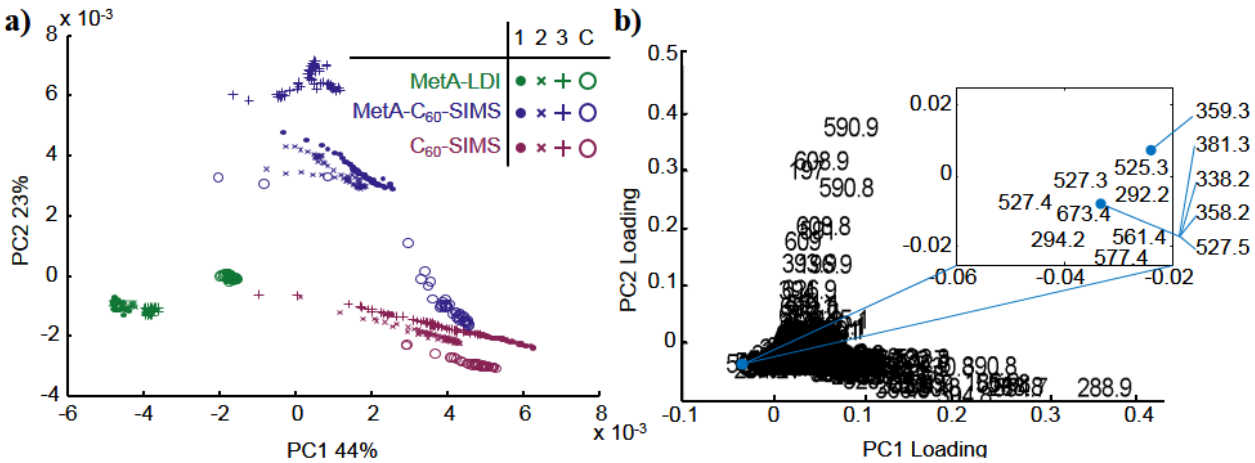

Figure 4.3. Principal component analyses of the three biofilms and media control from **Figure 1**. (**a**) scores plot and (**b**) loadings plot from unsupervised PCA of 780 average row spectra from Biofilms 1 (•), 2 (x), and 3 (+), and the media control C (O).

the cell culture medium. It therefore appears that the spectral distribution reflects a proportional scaling of media-specific ions.

The MetA-LDI spectra (green) are found at negative values of PC1 and PC2, a space influenced by high intensity ions in the lipid mass range (e.g., *m/z* 525.3, 527.4, 673.4, 577.4, etc.), and by a few prominent low-mass ions at *m/z* 294.2 and 292.2. MS^2 results reveal that *m/z* 292.2 and 294.2 are similar in structure to compounds from the 2-alkyl-4-quinolone class. Analogous MS^2 evaluation of the high mass ions clustering towards negative PC1 and PC2 reveals that these ions correspond to RHL biosurfactants (**Table 4.2**). For a more complete discussion of the relevant biomolecules please see section **4.2**.

Interestingly, the MetA-C_{60}-SIMS and MetA-LDI spectra from the media control (open circles) cluster together with biofilm spectra obtained with C_{60}-SIMS. This distribution across PC1 most likely arises because the control is deficient in compounds produced by *P. aeruginosa* and contains only the background ions that dominate the C_{60}-SIMS spectra. Consistent with the trends observed in the representative spectra of **Figure 4.2a**, MetA-C_{60}-SIMS primarily separates across PC2 because of the strong $Au_{1\text{-}3}^+$ cluster ion signals, MetA-LDI separates in PC1 based upon abundant ions in the lipid range, and C_{60}-SIMS separates based upon the prevalence of background ions from the cell culture medium.

In situ MS^2 of the more massive ions from the biofilm and media control reveals that many of the high-intensity ions observed with C_{60}-SIMS are fragments of larger ions. For example, MS^2 of *m/z* 594.8 (**Figure 4.4a**) produced the successive loss of 101.95 to generate *m/z* 492.77, 390.83,

Table 4.2. *In situ* C_{60}-SIMS MS^2 of AQs and RHLs acquired from a neat biofilm.

AQs	Molecular formula	$[M+H]^+$ Expected	$[M+H]^+$ Observed	*In situ* tandem MS fragments Expected					Observed				
HHQ (2-heptyl-4-quinolone)	$[C16H22NO]^+$	244.17	244.17	130.07	159.07	172.08			130.06	159.06	172.07	186.09	200.13
C9:1-NHQ (DB-2-nonyl-4-quinolone)	$[C18H24NO]^+$	270.19	270.20	130.07	159.07	172.08	184.08	198.09	130.07	159.08	172.08	184.08	198.09
NHQ (2-nonyl-4-quinolone)	$[C18H26NO]^+$	272.20	272.21	130.07	159.07	172.08			130.07	159.08	172.08	186.09	200.10
C11:1-UHQ (DB-2-undecyl-4-quinolone)	$[C20H28NO]^+$	298.22	298.23	130.07	159.07	172.08	184.08	198.09	130.06	159.07	172.07	184.07	198.09
UHQ (2-undecyl-4-quinolone)	$[C20H30NO]^+$	300.23	300.22	130.07	159.07	172.08			130.07	159.08	172.08	186.08	200.07
PQS/HQNO (2-heptyl-3-hydroxy-4-quinolone/ 2-heptyl-4quinoline-N-oxide)	$[C16H22NO2]^+$	260.16	260.17	130.07	175.06 159.07	188.11 172.08	186.09	200.06	130.07	159.07 175.07	172.08 188.07	186.09	200.07
C9:1-NQNO (DB-2-nonyl-4quinoline-N-oxide)	$[C18H24NO2]^+$	286.18	286.20	130.07	159.07	172.08	184.08	198.09	130.07	159.06	172.07	184.07	198.10
C9-PQS/NQNO (2-nonyl-3-hydroxy-4-quinolone/ 2-nonyl-4quinoline-N-oxide)	$[C18H26NO2]^+$	288.20	288.21	130.07	175.06 159.07	188.11 172.08	186.09	200.06	130.07	175.07 159.08	188.08 172.08	186.10	200.12
C11:1-PQS/C11:1-UQNO (DB-2-undecyl-3-hydroxy-4-quinolone/ DB-2-undecyl-4quinoline-N-oxide)	$[C20H28NO2]^+$	314.21	314.11	130.07	175.06 159.07	188.11 172.08	184.08	198.09	130.07	175.05 159.08	188.06 172.07	184.08	198.09
C11-PQS/UQNO (2-undecyl-3-hydroxy-4-quinolone/ 2-undecyl-4quinoline-N-oxide)	$[C20H30NO2]^+$	316.23	316.20	130.07	175.06 159.07	188.11 172.08	186.09	200.06	130.06	175.05 159.07	188.05 172.09	186.09	200.11

Rhamnolipids	Molecular formula	$[M+Na]^+$ Expected	$[M+Na]^+$ Observed	$[M+2Na-H]^+$ Expected	$[M+2Na-H]^+$ Observed	*In situ* tandem MS fragments Expected					Observed				
Rha-C10 $[M+Na]^+$	$[C16H30NaO7]^+$	357.19	357.15			127.03	169.04	211.14	329.11		169.04	211.14	329.11		
Rha-C10 $[M+2Na-H]^+$	$[C16H29Na2O7]^+$			379.17	379.18	104.99	149.02	233.11	215.10		149.02	215.10	233.12		
Rha-C10-C10 $[M+Na]^+$	$[C26H48NaO9]^+$	527.32	527.34			211.13	357.19	381.26			211.12	357.17	381.23		
Rha-C10-C10 $[M+2Na-H]^+$	$[C26H47Na2O9]^+$			549.30	549.33	104.99	149.02	215.07	233.11	379.17	149.02	215.07	233.11	379.15	521.21
Rha-Rha-C8 $[M+2Na-H]^+$	$[C20H35Na2O11]^+$			497.20	497.23	104.99	177.05	205.08	251.09	351.14	205.07	251.06	351.13		
Rha-Rha-C10 $[M+Na]^+$	$[C22H40NaO11]^+$	503.25	503.27			169.04	211.13	315.14	333.12	357.19	169.04	211.14	315.10	333.11	357.22
Rha-Rha-C10 $[M+2Na-H]^+$	$[C22H39Na2O11]^+$			525.23	525.24	104.99	177.05	233.11	251.09	349.17	177.02	233.12	251.05	379.16	
Rha-Rha-C10-C8/ Rha-Rha-C8-C10 $[M+2Na-H]^+$	$[C30H53Na2O13]^+$			667.33	667.28	375.19	497.20	521.27	525.23		251.05	375.03	525.19 497.17	521.15	
Rha-Rha-C10-C10 $[M+Na]^+$	$[C32H58NaO13]^+$	673.38	673.39			315.12	357.19	381.26	527.32	503.25	211.12	315.11	381.27	503.23	527.29
Rha-Rha-C10-C10 $[M+2Na-H]^+$	$[C32H57Na2O13]^+$			695.36	695.38	177.01	233.11	251.09	379.17	525.23	177.01	233.10	251.04	379.17	525.22

288.89, and 186.94, which are present at high abundance in MS^1. Similar peak series are observed for many components of the C_{60}-SIMS spectra; starting with a given low mass ion (e.g., *m/z* 164.90, 186.91, or 202.85, among others) and successively adding *m/z* 101.95 results in many of the other high-abundance peaks. The presence of many of the same ions in both MS^1 and MS^2, and the regular pattern of fragmentation, suggests that these constituents arise from in-source fragmentation of higher molecular weight polymer

Remarkably, ionization of these high-abundance polymeric fragments is substantially diminished following metallization. For example, ion images of the *m/z* 186.91–594.27 sequence in Biofilm 2 (**Figure 4.4b**)—which are broadly representative of the media-specific ions as a whole—are substantially lower in intensity with MetA-C_{60}-SIMS and MetA-LDI than with C_{60}-SIMS. This phenomenon was quantitatively explored through pairwise comparison of the three imaging modalities (**Figure 4.4c**). Calculating the change in abundance of MetA-C_{60}-SIMS and MetA-LDI relative to C_{60}-SIMS reveals that ionization of media-specific compounds decreases by an average of 65% for MetA-SIMS and 89% for Meta-LDI. Taken together, these results suggest that the gold treatment facilitates a reduction in C_{60}-SIMS in-source fragmentation.

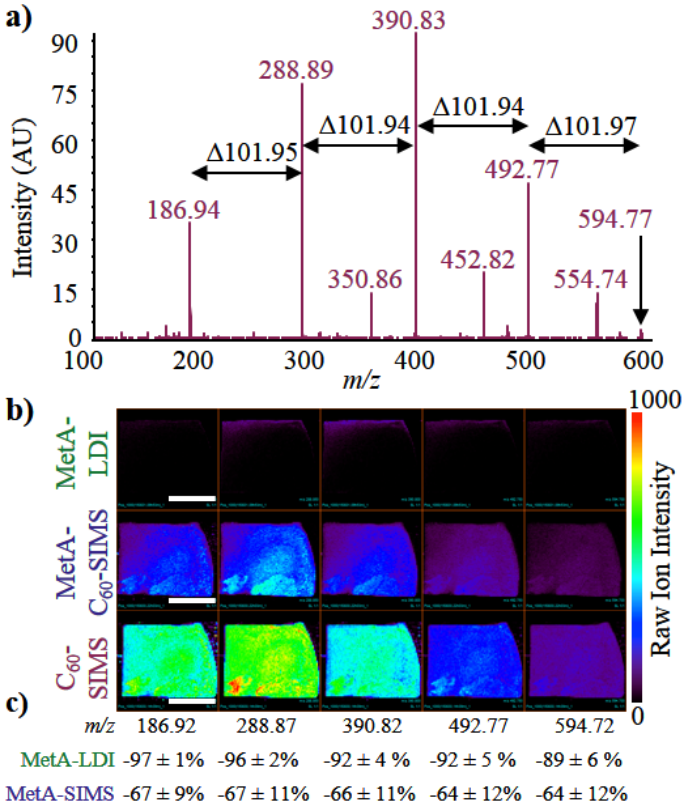

Figure 4.4. (**a**) *In situ* C_{60}-SIMS MS^2 of a representative media-specific ion, *m/z* 594.8, produces the successive loss of 101.95 to generate several high-abundance ions that are also found in the MS^1 spectra; (**b**) MS^1 images of the *m/z* 186.92–594.77 ion sequence in Biofilm 2; and (**c**) relative abundance change between C_{60}-SIMS and the other two ionization modalities. The white scale bars in (**b**) represent 1 cm, and the error in (**c**) was calculated as the relative standard deviation between biofilms with n = 3.

4.4.2. Gold Treatment Exhibits a Variable Influence on Small Molecule Ion Yield

The community-scale coordination of biofilm-bound *P. aeruginosa* is dependent upon the production and utilization of a wide assortment of small molecule secondary metabolites. Important classes include AQs, of which several have been identified as intercellular signaling

molecules,[49] and RHLs, which are biosurfactants important for colony morphology and nutrient uptake (see **Figure 4.5**).[50] Both compound classes are structurally diverse, with variations in the length, number, and saturation of the aliphatic side-chains, as well as the position of the hydroxyl group in AQs and the number of rhamnose groups in RHLs. It is unclear whether the diversity in structure is matched by a similar diversity in function, as only a few of the over 50 AQs found in *P. aeruginosa* have assigned functions.[51]

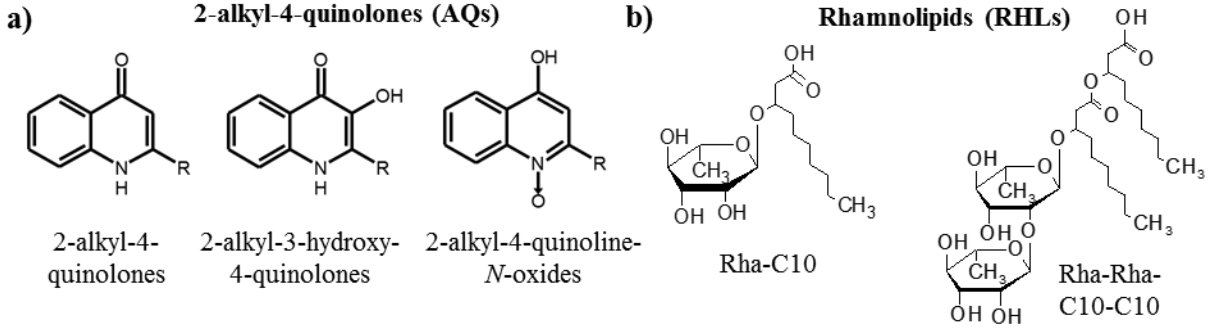

Figure 4.5. (**a**) 2-alkyl-4-quinolones (AQs) and (**b**) rhamnolipids (RHAs) produced by P. aeruginosa. Intra-class heterogeneity arises from the length and saturation of the aliphatic sidechain (R), as well as the presence and location of the hydroxyl group in AQs and the number of rhamnose (Rha) and R groups in RHLs. Please consult **Table S1** for more information on the specific analytes observed in this study.

Both AQs and RHLs are abundantly expressed in the bacterial communities examined here, and are readily observable with all three imaging modalities. The spectra displayed in **Figure 4.6a** show protonated molecular ions for several AQs, including 7, 9 and 11 carbon variants of each of the three major subclasses—e.g., 2-alkyl-4-quinolones (observed at *m/z* 244.18, 270.17, 272.21, 298.23, and 300.21), 2-alkyl-3-hydroxy-4-quinolones (observed at *m/z* 260.18, 286.19, 288.20, 314.23, and 316.23), and 2-alkyl-4-quinoline-*N*-oxides (which are isomeric with 2-alkyl-3-hydroxy-4-quinolones). Several of these ions have been previously assigned via MS^2,[5, 52] and they are similarly characterized in this work (**Table 4.2**). Also observable in the spectra presented in **Figure 4.6a** are AQ fragments (e.g., *m/z* 159.08, 172.09, 196.09, and 210.10), Au^+ at *m/z* 196.97, and background ions from the cell culture medium (as indicated by asterisks). Several RHLs are also present in both the sodiated ($[M + Na]^+$) and di-sodiated ($[M + 2Na-H]^+$) forms; however, with the exception of Rha-C10 at *m/z* 379.19, most are not observable in the *m/z* range shown in **Figure 4.6a** and can instead be seen in **Figure 4.2a**. Abundant RHLs include Rha-C10 (*m/z* 379.17), Rha-C8 (*m/z* 497.20), Rha-Rha-C10 (*m/z* 525.26), Rha-C10-C10 (*m/z* 527.33), and Rha-Rha-C10-C10 (*m/z* 673.41).

To investigate the intensity changes of AQs and RHLs independent of the media background, targeted PCA was performed by selecting only ions derived from either AQs, AQ fragments, or RHLs. A full list of the ions used for targeted PCA is presented in **Table 4.1**. As can be seen in the scores and loadings plots for the first two principal components (**Figure 4.6b** and **4.6c**), the spectra again cluster with others derived from the same ionization modality, and separate across PC1 (48% of the variance) and PC2 (40% of the variance) following the different compound classes.

The spectra affiliated with C_{60}-SIMS (red) segregate to positive values of PC2 and are heavily influenced by AQ fragments (gray ions) and isomeric ion pairs from the 2-alkyl-3-hydroxy-4-quinolone and 2-alkyl-4-quinoline-*N*-oxide subclasses (red ions at *m/z* 288.20, 286.18, and 260.17). The MetA-LDI spectra (green) principally separate to positive values of PC1, which

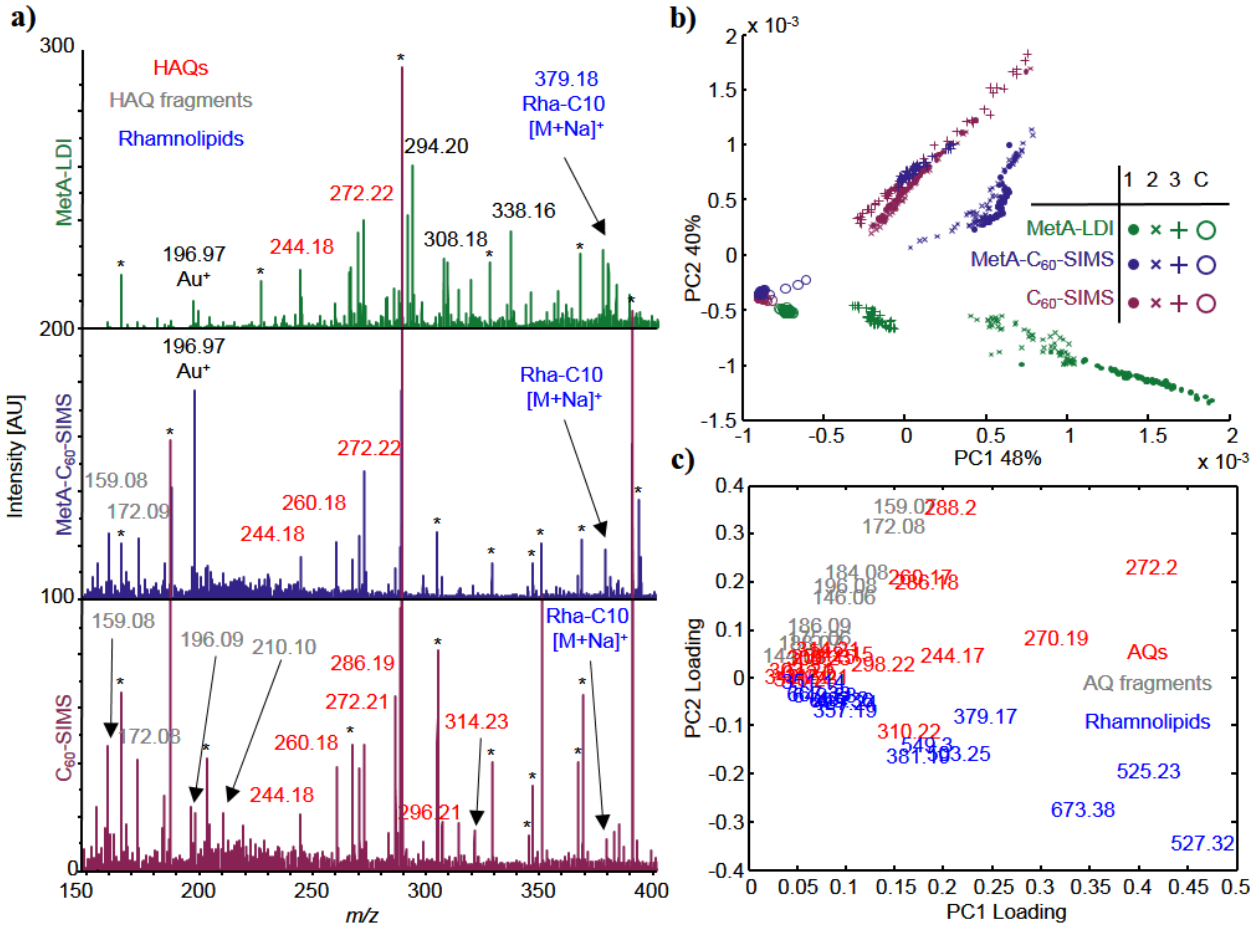

Figure 4.6. (**a**) Representative spectra for MetA-LDI (green), MetA-C_{60}-SIMS (blue), and C_{60}-SIMS (red) generated by averaging pixels across adjacent imaging rows in Biofilm 2; (**b**) scores plot and (**c**) loadings plot from targeted PCA of 780 average row spectra from three Biofilms 1 (•), 2 (x), and 3 (+), and the media control C (O). Ions marked by an asterisk (*) in (**a**) are also found in the control sample.

is dominated by the most abundant RHLs (Rha-Rha-C10, Rha-C10-C10, and Rha-Rha-C10-C10, at *m/z* 525.23, 527.32, and 573.38, respectively), and by high-abundance AQs from the 2-alkyl-4-quinolone subclass (red ions at *m/z* 244.17, 270.19, and 272.2). MetA-LDI spectra also separate to negative values of PC2. The negative loading of RHLs in PC2 indicates that this compound class is responsible for the majority of the separation between spectra from MetA-LDI and those from the other modes of ionization.

Spectra arising from MetA-C_{60}-SIMS (blue) are found between those derived from the other two ionization modalities, with localization at positive values of PC1 and PC2. This grouping appears to be heavily influenced by variable ionization of the AQ subclasses, different amounts of AQ fragmentation, and differences in RHL abundance. AQs from the 2-alkyl-4-quinolone subclass, which is found at the null point of PC2 and positive values of PC1 on the loadings plot, influence the separation between neat C_{60}-SIMS and MetA-C_{60}-SIMS.

The media controls from all three ionization modalities separate to the zero value for PC2 and negative values of PC1, most likely because these spectra have below-average intensities for all analytes. Also of note, Biofilm 3 is an outlier, with its spectra clustered towards more negative values of PC1 then the other spectra from similar ionization methods. Examination of the optical images (**Figure 4.1c**) reveals that the center of Biofilm 3 is largely devoid of the structure associated with the other two samples, and therefore the observed clustering of this sample most likely arises because a substantial region lacks the target analytes and has a chemical composition more resembling the control.

The variation in C_{60}-SIMS AQ ionization was further explored both qualitatively and quantitatively (**Figure 4.7**). Ion images of the 2-alkyl-4-quinolones (**Figure 4.7a**) show substantially higher sensitivity following the application of gold, with the 9-carbon variant (2-nonyl-4-quinolone, or NHQ, *m/z* 272.21) showing the largest enhancement of 120 ± 20% (mean ± S.D. for biofilms, n = 3). Also notable is the enhanced SIMS sensitivity for the 11 carbon variant (2-undecyl-4-quinolone, or UHQ, *m/z* 300.21), which is nearly undetectable with C_{60}-SIMS but well within the detection limit for MetA-C_{60}-SIMS. Quantitative comparisons (calculated as the percent change in SIMS signal intensity before and after metallization) of the 2-alkyl-4-quinolone intensities show this same trend, with all analytes from this subclass enhanced by more than 46% following the application of gold (**Figure 4.7b**). Variation between specific analytes is substantial, with NHQ and UHQ showing the most improvement (141 ± 7% and 117 ± 6%, respectively, in

Biofilm 2, mean ± standard error of the mean), and the double-bonded variant of NHQ (db:NHQ) showing the least improvement (33 ± 7% in Biofilm 3).

Similar evaluation of the isomeric AQs at *m/z* 286.19 (db:C9), 288.20 (C9), 314.23 (db:C11), and 316.23 (C11), shows the opposite trend, with a near universal signal depression of ~ 44% following gold application (**Figure 4.7c** and **4.7d**). The notable exception is *m/z* 260.18, which corresponds to the protonated molecular ions of 2-alkyl-3-heptyl-4-quinolone (also known as *Pseudomonas* quinolone signal, or PQS) and 2-heptyl-4-quinoline-*N*-oxide (HQNO). The PQS / HQNO isomeric pair shows an enhancement of 26 ± 2.5, 19 ± 3, and 28 ± 8%, with Biofilms 1, 2, and 3, respectively.

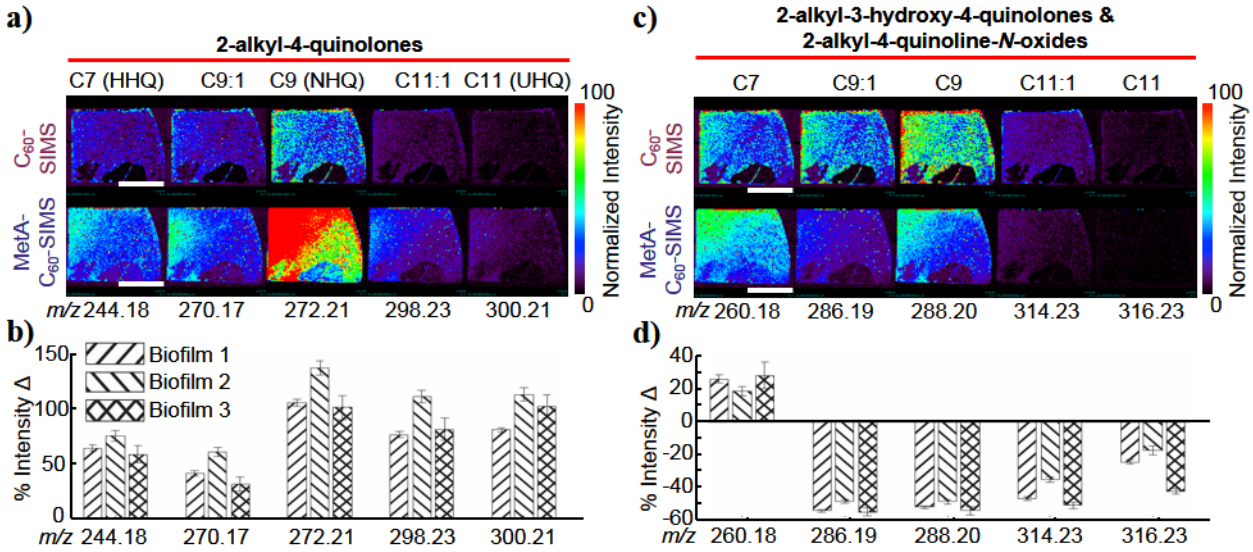

Figure 4.7. C_{60}-SIMS ion images for AQs in Biofilm 2 and relative intensity changes observed for the three samples before and after the application of gold. (**a, b**) 2-alkyl-4-quinolones, (**c, d**) combined 2-alkyl-3-hydroxy-4-quinolones and 2-alkyl-4-quinoline-*N*-oxides. Each bar on the graph depicts the intensity change for a single ion over a biofilm and the error was calculated as standard error of the mean with n = 61, 58, and 56 for Biofilms 1, 2, and 3, respectively. The white scale bar represents 1 cm.

The change in intensity of the isomeric AQ pairs at *m/z* 260.18, 286.19, and 288.19 was further investigated through MS^2 of PQS and HQNO standards (**Figure 4.8**). The most abundant fragments for HQNO and its analogs result from the loss of the *N*-oxide oxygen and fragmentation of the aliphatic sidechain in either the α- (*m/z* 159.08) or β-position (*m/z* 172.09) relative to the quinolone ring. This is in contrast to AQs from the PQS family, which retain the hydroxyl group and undergo aliphatic sidechain fragmentation to produce *m/z* 175.08 and 188.09 (**Figure 4.8a**).[52] MS^2 of a dried droplet containing both PQS and HQNO standards before the application of gold (**Figure 4.8b**) shows fragments for both compounds, with *m/z* 159.08 as the most intense peak.

Following the application of gold, the abundance of the HQNO product ions decrease, while the PQS fragment at *m/z* 175.08 becomes the most abundant product ion in the MetA-C_{60}-SIMS spectrum. The same trend is observed for MS^2 of the isomeric pairs at *m/z* 260.18 (**Figure 4.8c**) and 288.21**(Figure 4.8d**) in the biofilm sample. While analysis of the MetA-LDI was left out of **Figure 4.8**, the *N*-oxide AQs are largely absent from these spectra, and the overall trends in ionization more closely resemble MetA-C_{60}-SIMS than C_{60}-SIMS. Taken together with the ion images in **Figure 4.7**, these data suggest that the gold coating leads to selective enhancement of

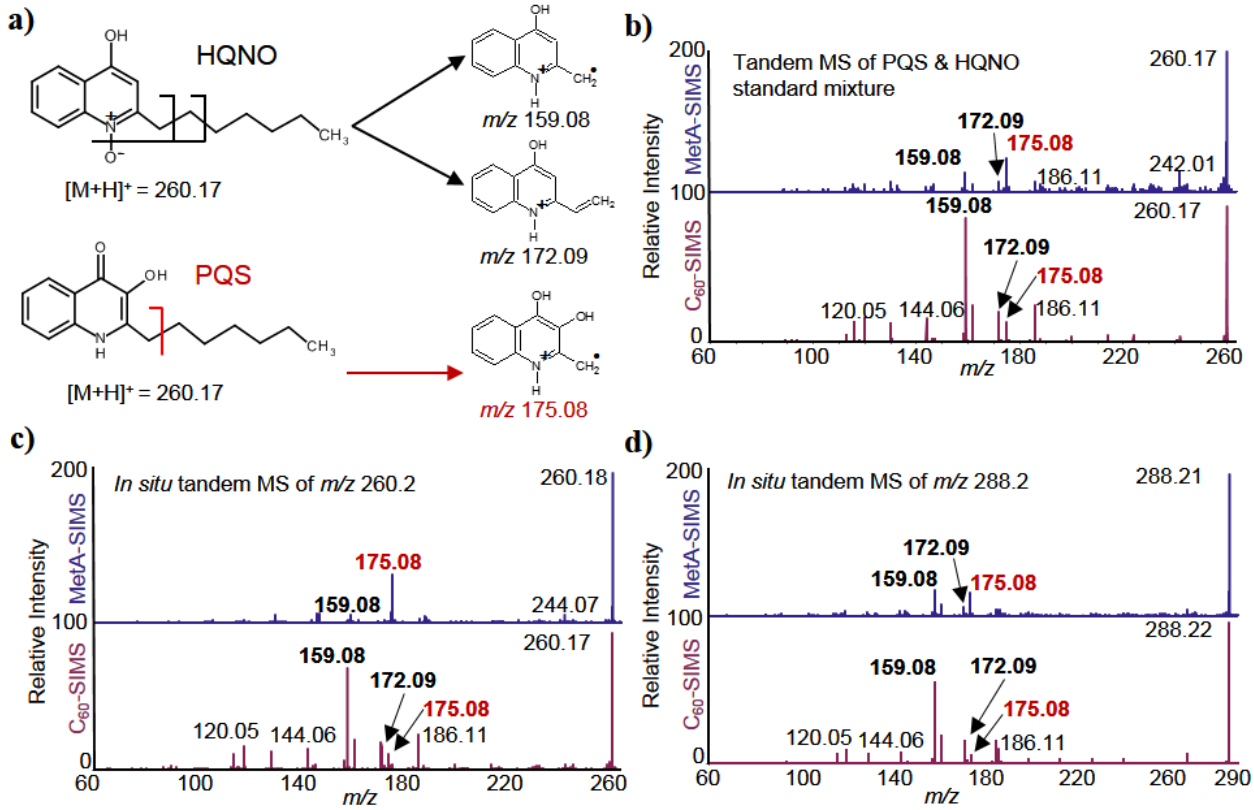

Figure 4.8. (**a**) Predicted fragmentation patterns for the isomeric AQ pairs; (**b**) tandem MS of *m/z* 260.2 in an equimolar mixture of PQS and HQNO before and after metallization of; (**c**) *m/z* 260.2 from the biofilm surface; and (**d**) *m/z* 288.2 from the biofilm surface. These data show that ionization of *N*-oxide AQs is preferentially suppressed following metallization.

PQS and HHQ-type AQs, whereas ionization of the *N*-oxide AQs is suppressed.

The ionization of RHLs is also substantially enhanced (**Figure 4.9**), however the effect is highly variable between samples. Biofilms 1 and 2 show a 45–300% improvement in RHL ionization following the application of gold, while Biofilm 3 shows either no change or a decrease in ion abundance (**Figure 4.9b**). It is likely that this incongruence arises from the distinctive morphology (**Figure 4.1c**), as the center of the sample is devoid of a thick biofilm matrix.

4.4.3. Evaluation of the Gold Coating and Biofilm Morphology

To evaluate the morphology and thickness of the gold coating, a bare silicon wafer was half-masked with clear tape, sputtered with gold, and examined with atomic force microscopy (AFM, **Figure 4.10a** and **b**). After 6 s of sputtering, the average height change across the Au / Si interface was found to be 2.6 nm (± 25% S.D. for n = 4 line scans). R_a values (mean of the absolute height value) were found to be 2.8 Å ± 7% and 1.3 Å ± 8% S.D. for the gold-coated and bare silicon surfaces, respectively (**Figure 4.10a** and **b**). These results are in agreement with previous scanning and transmission electron microscopy observations.[37, 39]

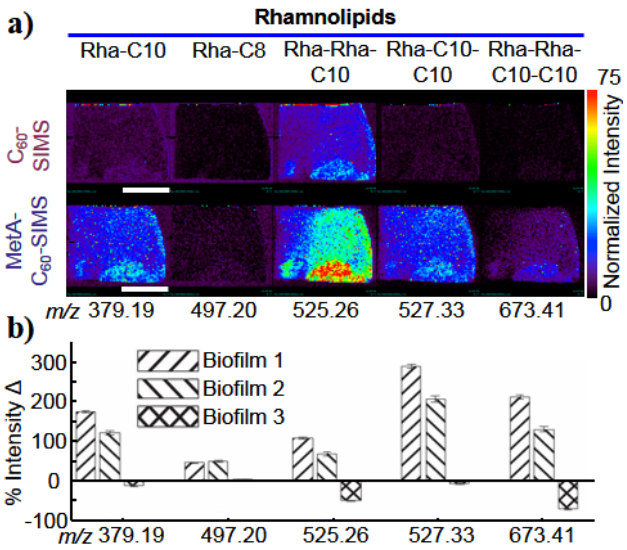

Figure 4.9. (**a**) RHL ion images for biofilm 2 before and after the application of 2–3 nm gold, and (**b**) relative abundance change for all three biofilms before and after gold application. Each bar on the graph depicts the intensity change for a single ion in a single biofilm and the error was calculated as standard error of the mean with n = 61, 58, and 56 for biofilms 1, 2, and 3, respectively. The white scale bar in (**a**) represents 1 cm.

Analogous evaluation of the gold-treated biofilms was hindered by the surface heterogeneity; both SEM and AFM showed dramatic height variations, with a deviation of more than 1 µm observed across a lateral distance of 5 µm (**Figure 4.11a** and **b**). Even with relatively simple organic samples, other authors have reported that variations in surface cohesion result in the formation of 20–100 nm gold islets separated by bare regions of sample; therefore, it is exceedingly unlikely that the biofilm is coated in a uniform layer of gold.[29, 34] Furthermore, a detailed examination of the deposition of metals onto multilayers of benzene revealed that metals penetrate into the surface of the sample and form subsurface clusters.[53] Thus, it probable that much of the sputtered gold penetrates the biofilm surface to form subsurface structures.

4.4.4. Insights into the Mechanism of MetA-C_{60}-SIMS

The mechanism behind MetA-SIMS ionization enhancement is still under debate; nevertheless, several credible hypotheses have been proposed. It has been suggested that metallization can induce changes in the local band structure and work function of the surface, leading to preferential ionization even in instances when sputtering efficiency remains unchanged.[18, 38-39] The increase in

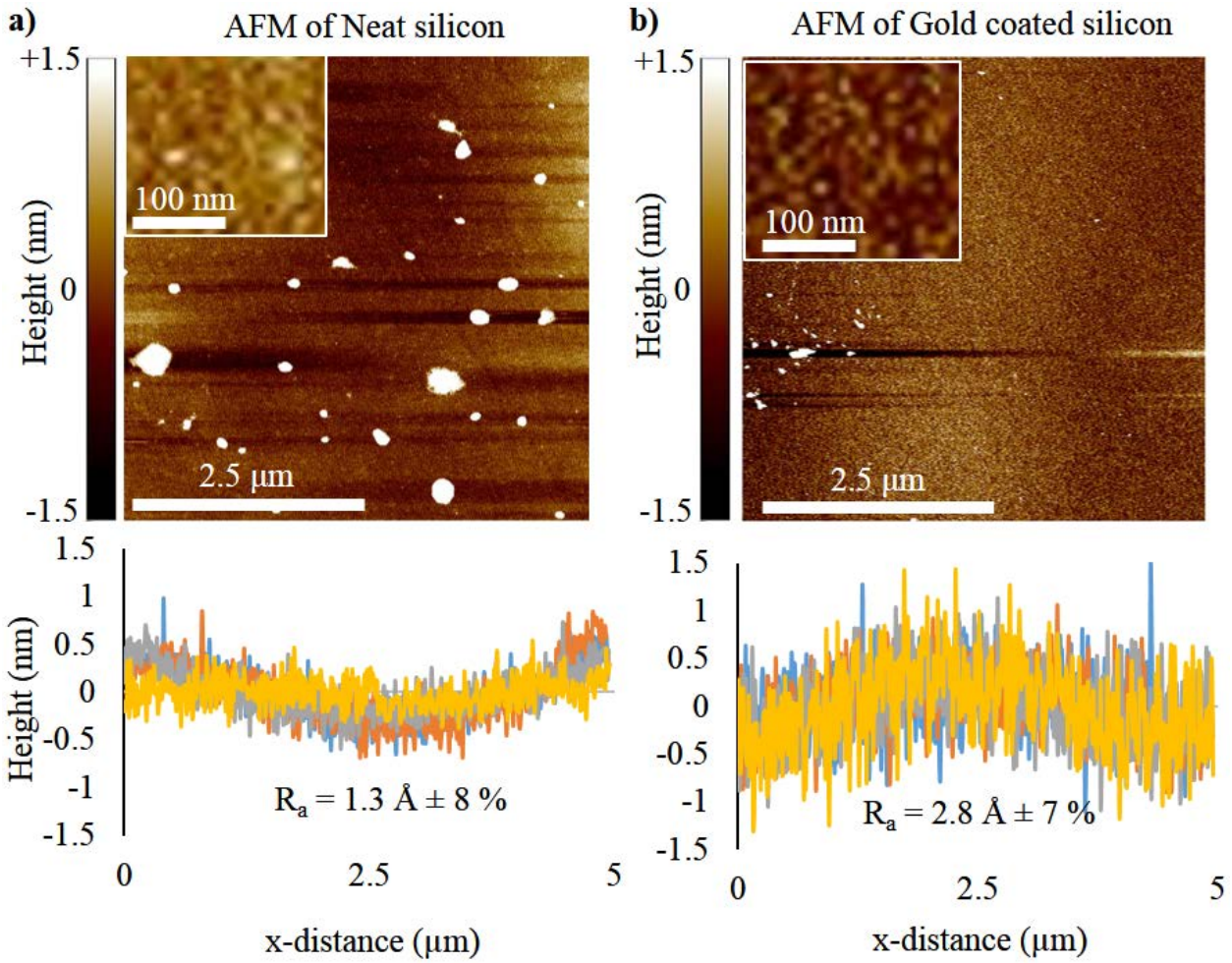

Figure 4.10. AFM Images and line scans for silicon wafer (a) neat and (b) sputtered with gold for 6 s. The white specs (high regions of the AFM images) are attributed to dust particles. The roughness values were calculated as the mean of the absolute value of the height for n = 4 mean centered and median filtered line scans with a block size of 100.

small molecule ion yields may also arise from a mitigation of matrix effects, as was initially shown by Inoue and Murase[40] using a simple mixture of Irganox 1010 and silicon oil. Another intriguing theory is that a combination of analyte migration and increased sputtering efficiency through surface hardening are responsible for the enhancement effect. Using both Ga^+ and SF_5^+ primary ions to analyze a series of organic dyes, Adriaensen *et al.*[41] showed that protonated molecular ions and characteristic fragments increase in intensity following gold and silver application. As the sample aged, the protonated molecular ions generally decreased in intensity while the characteristic fragment ions increased in intensity. This result, as well as the observation that ionization of larger polymers—which would presumably be tangled together with other analytes and therefore less mobile—is depressed following metal application, suggests that endogenous

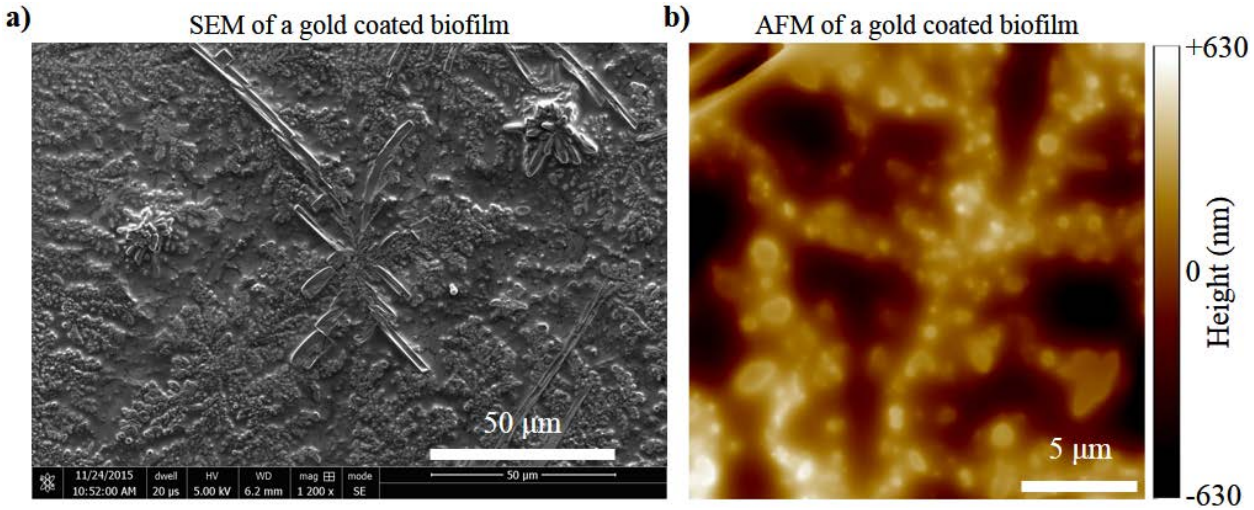

Figure 4.11. (**a**) SEM and (**b**) AFM of a gold coated *P. aeruginosa* biofilm. The surface morphology was too variable to assess the thickness or structure of gold coating on the biofilm.

small molecules migrate onto the top of the gold islands and become more accessible to the primary ion beam.[38]

Augmenting molecular migration is the idea of surface stopping power; an increase in the hardness of a surface leads to the deposition of a higher proportion of the primary ion beam energy in the near-surface region of the sample and accordingly, an increase in sputtering yield for intact secondary ions. For monatomic ion beams this hypothesis has been widely supported empirically and theoretically.[34-37, 39, 54-55] In a pair of studies, Heile *et al.*[36, 43] investigated the relationship between the primary ion beam composition and surface hardness and showed that as the effective thickness of the metal layer increases, there is a tradeoff between an accessible surface (i.e., uncoated area) and hardness. These findings partially explain the previous observation that metallization reduces ionization when polyatomic projectiles are used. Even on neat organic samples, polyatomic projectiles produce shallow impact craters with minimal subsurface damage; therefore, the metal coating reduces the accessible area without providing the benefit of reduced surface penetration.[36] In agreement with previous observations on hard surfaces, examination of AQ standards on a Si wafer before and after the application of gold (**Figure 4.12**) shows a substantial reduction in ion yield (68, 32 and 90% reduction for HHQ, PQS and HQNO, respectively.

In contrast with the samples routinely studied by the SIMS imaging community (e.g., single and few component polymers, spin-cast organic standards, and even cell culture or tissue slices), bacterial biofilms present a heterogeneous surface both with respect to hardness and overall

architecture. Taking these considerations into account, it is likely that the observed signal enhancement is the result of several different effects including: (1) a reduction in the fragmentation and ionization of high molecular weight background polymers from the cell culture medium, and thus, a reduction in matrix effects; (2) a more efficient collision cascade and molecular ejection event; (3) reduced fragmentation of larger biomolecules (e.g., RHLs) and therefore, increased ionization of intact molecular ions; and (4) chemical phenomena, such as differential molecular diffusion onto the top of the gold or alterations in the chemical properties of the surface. The ionization differences between AQ subclasses might arise from differences in depth, preferential migration, or a chemical reaction that produces a secondary byproduct unobservable by MSI.

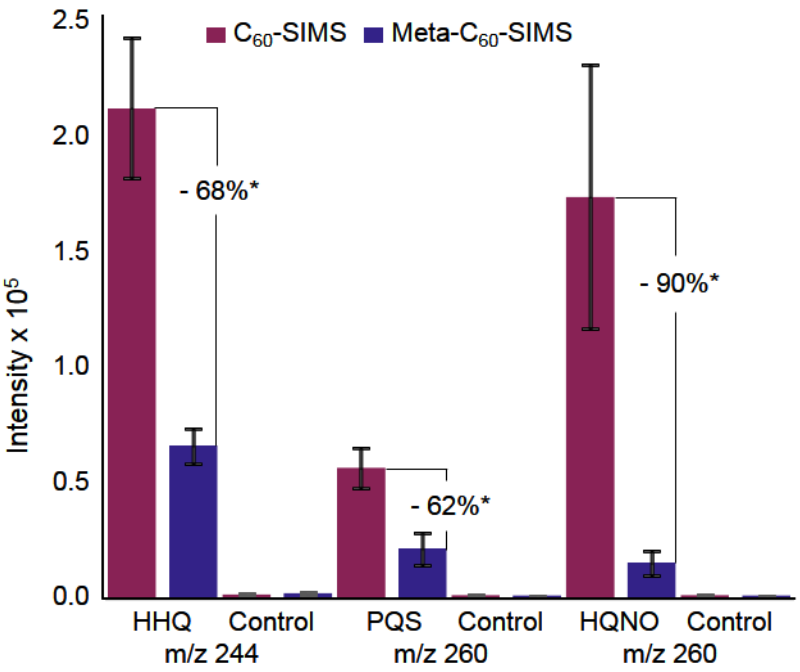

Figure 4.12. C_{60}-SIMS intensity of HHQ (*m/z* 244.17), PQS (*m/z* 260.17), and HQNO (*m/z* 260.17) deposited on a silicon wafer and examined before and after gold coating. The measurement was obtained with n = 5, the control sample was a neat FAB media, and the error bars represent the standard deviation. *p values < 0.001 calculated via the independent two-tailed, two-sample t-test for equal sample sizes and equal variance.

4.5. Conclusions

In this work, we compare the small molecule imaging capabilities of MetA-C_{60}-SIMS to both C_{60}-SIMS and MetA-LDI, and show metallization to be a promising sample treatment for small molecule imaging of complex biological systems. A combination of qualitative image comparison and quantitative statistical analysis shows that sputtering the biofilm surface with an effective 2.5 nm layer of gold provides increased sensitivity and improves spectral purity through reduced ionization of background ions from the cell culture medium. In contrast to standards (**Figure 4.12**) and previous studies reporting universal signal depression, we find that metallization improves *in*

situ C_{60}-SIMS ionization for several molecular classes, including 2-alkyl-4-quinolones and RHLs, by up to 300%. The dramatic reduction of background following the application of gold highlights the utility of MetA-C_{60}-SIMS in cases when the study is afflicted by interference from endogenous background components. When it is necessary to examine intact molecular ions and a premium is placed on high spatial resolution, MetA-C_{60}-SIMS may be the best available option.

The success and degree of the enhancement appears to be dependent upon both the analyte class and the surface composition, suggesting that MetA-SIMS ionization relies upon the interplay between the chemical and physical properties of both the sample and the analytes themselves. While we anticipate that these methods will be broadly applied for polyatomic MetA-SIMS analysis of a diverse assortment sample types, the heterogeneous nature of the enhancement most likely dictates rigorous optimization for each sample under investigation. It is further likely that additional tuning of the thickness and composition of the metal overlay will lead to even greater enhancements than those observed in the present study.

4.6. References

1. Branda, S. S.; Vik, Å.; Friedman, L.; Kolter, R., Biofilms: the matrix revisited. *Trends in Microbiology* **2005,** *13* (1), 20-26.
2. Flemming, H.-C.; Wingender, J., The biofilm matrix. *Nat. Rev. Micro.* **2010,** *8* (9), 623-633.
3. Normark, S., Introducing npj Biofilms and Microbiomes. *NPJ Biofilms Microbiomes* **2015,** *1*, 15004.
4. Vaidyanathan, S.; Fletcher, J. S.; Goodacre, R.; Lockyer, N. P.; Micklefield, J.; Vickerman, J. C., Subsurface Biomolecular Imaging of Streptomyces coelicolor Using Secondary Ion Mass Spectrometry. *Analytical Chemistry* **2008,** *80* (6), 1942-1951.
5. Baig, N. F.; Dunham, S. J. B.; Morales-Soto, N.; Shrout, J. D.; Sweedler, J. V.; Bohn, P. W., Multimodal Chemical Imaging of Molecular Messengers in Emerging Pseudomonas aeruginosa Bacterial Communities. *Analyst* **2015,** *140*, 6544.
6. Brauer, J. I.; Makama, Z.; Bonifay, V.; Aydin, E.; Kaufman, E. D.; Beech, I. B.; Sunner, J., Mass spectrometric metabolomic imaging of biofilms on corroding steel surfaces using laser ablation and solvent capture by aspiration. *Biointerphases* **2015,** *10* (1), 019003.
7. Rubakhin, S. S.; Greenough, W. T.; Sweedler, J. V., Spatial Profiling with MALDI MS: Distribution of Neuropeptides within Single Neurons. *Analytical Chemistry* **2003,** *75* (20), 5374-5380.
8. Tucker, K.; Li, Z.; Rubakhin, S.; Sweedler, J., Secondary Ion Mass Spectrometry Imaging of Molecular Distributions in Cultured Neurons and Their Processes: Comparative Analysis of Sample Preparation. *Journal of The American Society for Mass Spectrometry* **2012,** *23* (11), 1931-1938.
9. Monroe, E. B.; Jurchen, J. C.; Lee, J.; Rubakhin, S. S.; Sweedler, J. V., Vitamin E Imaging and Localization in the Neuronal Membrane. *Journal of the American Chemical Society* **2005,** *127* (35), 12152-12153.
10. Ghosal, S.; Fallon, S. J.; Leighton, T. J.; Wheeler, K. E.; Kristo, M. J.; Hutcheon, I. D.; Weber, P. K., Imaging and 3D Elemental Characterization of Intact Bacterial Spores by High-Resolution Secondary Ion Mass Spectrometry. *Analytical Chemistry* **2008,** *80* (15), 5986-5992.
11. Amstalden van Hove, E. R.; Smith, D. F.; Heeren, R. M. A., A concise review of mass spectrometry imaging. *Journal of Chromatography A* **2010,** *1217* (25), 3946-3954.

12. Watrous, J. D.; Dorrestein, P. C., Imaging mass spectrometry in microbiology. *Nat. Rev. Micro.* **2011,** *9* (9), 683-694.
13. Zhang, S.; Liu, J. a.; Chen, Y.; Xiong, S.; Wang, G.; Chen, J.; Yang, G., A Novel Strategy for MALDI-TOF MS Analysis of Small Molecules. *Journal of the American Society for Mass Spectrometry* **2010,** *21* (1), 154-160.
14. Gemperline, E.; Rawson, S.; Li, L., Optimization and Comparison of Multiple MALDI Matrix Application Methods for Small Molecule Mass Spectrometric Imaging. *Analytical Chemistry* **2014,** *86* (20), 10030-10035.
15. Kurczy, M. E.; Zhu, Z.-J.; Ivanisevic, J.; Schuyler, A. M.; Lalwani, K.; Santidrian, A. F.; David, J. M.; Giddabasappa, A.; Roberts, A. J.; Olivos, H. J.; O'Brien, P. J.; Franco, L.; Fields, M. W.; Paris, L. P.; Friedlander, M.; Johnson, C. H.; Epstein, A. A.; Gendelman, H. E.; Wood, M. R.; Felding, B. H.; Patti, G. J.; Spilker, M. E.; Siuzdak, G., Comprehensive bioimaging with fluorinated nanoparticles using breathable liquids. *Nat. Comm.* **2015,** *6*, 5998.
16. Lanni, E. J.; Masyuko, R. N.; Driscoll, C. M.; Aerts, J. T.; Shrout, J. D.; Bohn, P. W.; Sweedler, J. V., MALDI-guided SIMS: Multiscale imaging of metabolites in bacterial biofilms. *Analytical Chemistry* **2014,** *86* (18), 9139-9145.
17. Amendola, V.; Litti, L.; Meneghetti, M., LDI-MS Assisted by Chemical-Free Gold Nanoparticles: Enhanced Sensitivity and Reduced Background in the Low-Mass Region. *Analytical Chemistry* **2013,** *85* (24), 11747-11754.
18. Prabhakaran, A.; Yin, J.; Nysten, B.; Degand, H.; Morsomme, P.; Mouhib, T.; Yunus, S.; Bertrand, P.; Delcorte, A., Metal condensates for low-molecular-weight matrix-free laser desorption/ionization. *International Journal of Mass Spectrometry* **2012,** *315*, 22-30.
19. Woo, H.-K.; Northen, T. R.; Yanes, O.; Siuzdak, G., Nanostructure-initiator mass spectrometry: a protocol for preparing and applying NIMS surfaces for high-sensitivity mass analysis. *Nat. Protocols* **2008,** *3* (8), 1341-1349.
20. Wei, J.; Buriak, J. M.; Siuzdak, G., Desorption-ionization mass spectrometry on porous silicon. *Nature* **1999,** *399* (6733), 243-246.
21. Peterson, D. S., Matrix-free methods for laser desorption/ionization mass spectrometry. *Mass Spectrometry Reviews* **2007,** *26* (1), 19-34.
22. Wang, F.; Hong, M.; Xu, L.; Geng, Z., Nanomaterial-based surface-assisted laser desorption ionization mass spectroscopy. *Prog. Chem.* **2015,** *27* (5), 571-584.
23. Vickerman, J. C.; Winograd, N., SIMS—A precursor and partner to contemporary mass spectrometry. *Int. J. Mass Spectrom.* **2015,** *377*, 568-579.
24. Brenes, D. A.; Postawa, Z.; Wucher, A.; Blenkinsopp, P.; Garrison, B. J.; Winograd, N., Fluid Flow and Effusive Desorption: Dominant Mechanisms of Energy Dissipation after Energetic Cluster Bombardment of Molecular Solids. *journal of physical chemistry letters* **2011,** *2* (16), 2009-2014.
25. Fearn, S., Characterisation of biological material with ToF-SIMS: a review. *Materials Science and Technology* **2014,** *31* (2), 148-161.
26. Angerer, T. B.; Dowlatshahi Pour, M.; Malmberg, P.; Fletcher, J. S., Improved Molecular Imaging in Rodent Brain with Time-of-Flight-Secondary Ion Mass Spectrometry Using Gas Cluster Ion Beams and Reactive Vapor Exposure. *Analytical Chemistry* **2015,** *87* (8), 4305-4313.
27. Lanni, E. J.; Dunham, S. J. B.; Nemes, P.; Rubakhin, S. S.; Sweedler, J. V., Biomolecular imaging with a C60-SIMS/MALDI dual ion source hybrid mass spectrometer: Instrumentation, matrix enhancement, and single cell analysis. *Journal of the American Society for Mass Spectrometry* **2014,** *25* (11), 1897-1907.
28. Locklear, J. E.; Guillermier, C.; Verkhoturov, S. V.; Schweikert, E. A., Matrix-enhanced cluster-SIMS. *Applied Surface Science* **2006,** *252* (19), 6624-6627.
29. Altelaar, A. F. M.; Klinkert, I.; Jalink, K.; de Lange, R. P. J.; Adan, R. A. H.; Heeren, R. M. A.; Piersma, S. R., Gold-Enhanced Biomolecular Surface Imaging of Cells and Tissue by SIMS and MALDI Mass Spectrometry. *Analytical Chemistry* **2006,** *78* (3), 734-742.

30. Mohammadi, A. S.; Fletcher, J. S.; Malmberg, P.; Ewing, A. G., Gold and silver nanoparticle-assisted laser desorption ionization mass spectrometry compatible with secondary ion mass spectrometry for lipid analysis. *Surface and Interface Analysis* **2014,** *46* (S1), 379-382.
31. Nygren, H.; Malmberg, P., Silver deposition on freeze-dried cells allows subcellular localization of cholesterol with imaging TOF-SIMS. *Journal of Microscopy* **2004,** *215* (2), 156-161.
32. McDonnell, L. A.; Heeren, R. M. A.; de Lange, R. P. J.; Fletcher, I. W., Higher Sensitivity Secondary Ion Mass Spectrometry of Biological Molecules for High Resolution, Chemically Specific Imaging. *Journal of the American Society for Mass Spectrometry* **2006,** *17* (9), 1195-1202.
33. Nittler, L.; Delcorte, A.; Bertrand, P.; Migeon, H. N., Insights into the yield enhancement and ion emission process in metal-assisted SIMS. *Surface and Interface Analysis* **2013,** *45* (1), 18-21.
34. Heile, A.; Lipinsky, D.; Wehbe, N.; Delcorte, A.; Bertrand, P.; Felten, A.; Houssiau, L.; Pireaux, J. J.; De Mondt, R.; Van Royen, P.; Van Vaeck, L.; Arlinghaus, H. F., Investigation of methods to enhance the secondary ion yields in TOF-SIMS of organic samples. *Surface and Interface Analysis* **2008,** *40* (3-4), 538-542.
35. Restrepo, O.; Prabhakaran, A.; Hamraoui, K.; Wehbe, N.; Yunus, S.; Bertrand, P.; Delcorte, A., Mechanisms of metal-assisted secondary ion mass spectrometry: a mixed theoretical and experimental study. *Surface and Interface Analysis* **2010,** *42* (6-7), 1030-1034.
36. Heile, A.; Muhmann, C.; Lipinsky, D.; Arlinghaus, H. F., Investigations of secondary ion yield-enhancing methods in combination. *Surface and Interface Analysis* **2011,** *43* (1-2), 20-23.
37. Delcorte, A.; Yunus, S.; Wehbe, N.; Nieuwjaer, N.; Poleunis, C.; Felten, A.; Houssiau, L.; Pireaux, J. J.; Bertrand, P., Metal-Assisted Secondary Ion Mass Spectrometry Using Atomic (Ga+, In+) and Fullerene Projectiles. *Analytical Chemistry* **2007,** *79* (10), 3673-3689.
38. Delcorte, A.; Médard, N.; Bertrand, P., Organic Secondary Ion Mass Spectrometry: Sensitivity Enhancement by Gold Deposition. *Analytical Chemistry* **2002,** *74* (19), 4955-4968.
39. Wehbe, N.; Heile, A.; Arlinghaus, H. F.; Bertrand, P.; Delcorte, A., Effects of Metal Nanoparticles on the Secondary Ion Yields of a Model Alkane Molecule upon Atomic and Polyatomic Projectiles in Secondary Ion Mass Spectrometry. *Analytical Chemistry* **2008,** *80* (16), 6235-6244.
40. Inoue, M.; Murase, A., Reduction of matrix effects in TOF-SIMS analysis by metal-assisted SIMS (MetA-SIMS). *Surface and Interface Analysis* **2005,** *37* (12), 1111-1114.
41. Adriaensen, L.; Vangaever, F.; Gijbels, R., Metal-Assisted Secondary Ion Mass Spectrometry: Influence of Ag and Au Deposition on Molecular Ion Yields. *Analytical Chemistry* **2004,** *76* (22), 6777-6785.
42. Keune, K.; Boon, J. J., Enhancement of the static SIMS secondary ion yields of lipid moieties by ultrathin gold coating of aged oil paint surfaces. *Surface and Interface Analysis* **2004,** *36* (13), 1620-1628.
43. Heile, A.; Muhmann, C.; Lipinsky, D.; Arlinghaus, H. F., Correlation between molecular secondary ion yield and cluster ion sputtering for samples with different stopping powers. *Applied Surface Science* **2012,** *258* (18), 6993-6999.
44. Steinberg, N.; Kolodkin-Gal, I., The Matrix Reloaded: How Sensing the Extracellular Matrix Synchronizes Bacterial Communities. *Journal of Bacteriology* **2015,** *197* (13), 2092-2103.
45. Morales-Soto, N.; Anyan, M. E.; Mattingly, A. E.; Madukoma, C. S.; Harvey, C. W.; Alber, M.; Deziel, E.; Kearns, D. B.; Shrout, J. D., Preparation, imaging, and quantification of bacterial surface motility assays. *J. Vis. Exp.* **2015,** *98*, 52338.
46. Chambers, M. C.; Maclean, B.; Burke, R.; Amodei, D.; Ruderman, D. L.; Neumann, S.; Gatto, L.; Fischer, B.; Pratt, B.; Egertson, J.; Hoff, K.; Kessner, D.; Tasman, N.; Shulman, N.; Frewen, B.; Baker, T. A.; Brusniak, M.-Y.; Paulse, C.; Creasy, D.; Flashner, L.; Kani, K.; Moulding, C.; Seymour, S. L.; Nuwaysir, L. M.; Lefebvre, B.; Kuhlmann, F.; Roark, J.; Rainer, P.; Detlev, S.; Hemenway, T.; Huhmer, A.; Langridge, J.; Connolly, B.; Chadick, T.; Holly, K.; Eckels, J.; Deutsch, E. W.; Moritz, R. L.; Katz, J. E.; Agus, D. B.; MacCoss, M.; Tabb, D. L.; Mallick, P., A cross-platform toolkit for mass spectrometry and proteomics. *Nature Biotechnology* **2012,** *30* (10), 918-920.

47. Race, A. M.; Styles, I. B.; Bunch, J., Inclusive sharing of mass spectrometry imaging data requires a converter for all. *Journal of Proteomics* **2012,** *75* (16), 5111-5112.
48. Robichaud, G.; Garrard, K.; Barry, J.; Muddiman, D., MSiReader: An Open-Source Interface to View and Analyze High Resolving Power MS Imaging Files on Matlab Platform. *Journal of The American Society for Mass Spectrometry* **2013,** *24* (5), 718-721.
49. Huse, H.; Whiteley, M., 4-Quinolones: Smart Phones of the Microbial World. *Chemical reviews* **2011,** *111* (1), 152-159.
50. Abdel-Mawgoud, A. M.; Lépine, F.; Déziel, E., Rhamnolipids: diversity of structures, microbial origins and roles. *Applied Microbiology and Biotechnology* **2010,** *86* (5), 1323-1336.
51. Heeb, S.; Fletcher, M. P.; Chhabra, S. R.; Diggle, S. P.; Williams, P.; Cámara, M., Quinolones: from antibiotics to autoinducers. *FEMS Microbiology Reviews* **2011,** *35* (2), 247-274.
52. Lépine, F.; Milot, S.; Déziel, E.; He, J.; Rahme, L., Electrospray/mass spectrometric identification and analysis of 4-hydroxy-2-alkylquinolines (HAQs) produced by Pseudomonas aeruginosa. *Journal of the American Society for Mass Spectrometry* **2004,** *15* (6), 862-869.
53. Whitten, J. E.; Gomer, R., Deposition of Ni and Ag on Benzene Multilayers Adsorbed on W(110). *Journal of Physical Chemistry* **1996,** *100* (6), 2255-2259.
54. Restrepo, O. A.; Gonze, X.; Bertrand, P.; Delcorte, A., Computer simulations of cluster impacts: effects of the atomic masses of the projectile and target. *Physical Chemistry Chemical Physics* **2013,** *15* (20), 7621-7627.
55. Restrepo, O. A.; Prabhakaran, A.; Delcorte, A., Interaction of energetic clusters (Au3, Au400 and C60) with organic material and adsorbed gold nanoparticles. *Nucl. Instrum. Methods Phys. Res. B* **2011,** *269* (14), 1595-1599.

CHAPTER 5

Quantitative SIMS Imaging of Agar-Based Microbial Communities

5.1. Acknowledgements

This chapter has been reproduced in part with permission from Analytical Chemistry, 2018. Article in press, copyright 2018 American Chemical Society. Co-authors include Sage J. B. Dunham, Joseph F. Ellis, Nameera F. Baig, Nydia Morales-Soto, Tianyuan Cao, Joshua D. Shrout, Paul W. Bohn, and Jonathan V. Sweedler. SJBD performed most of the experimental planning, method development, SIMS imaging, data analysis, and manuscript composition. JFE helped to plan experiments, performed most of the chemical inkjet printing and 3D confocal fluorescence microscopy experiments, and performed some of the SIMS imaging and data analysis. NFB and NMS cultivated the microbial samples, helped develop the biofilm dehydration methods, and helped with experimental planning. TC helped to prepare samples. JDS, PWB, and JVS helped to plan experiments and compose the manuscript. The authors acknowledge intellectual contributions of Dr. Troy Comi, Dr. Bin Li, Kyungwon Ko, Amit Patel, and Kisurb Choe, thank Robert Mowery and Stephanie Lozano for their assistance with data analysis, and acknowledge Dr. Mizuki Endo for his help with confocal fluorescence microscopy. Research funding was provided through the National Institutes of Health under Award No. R01AI113219.

5.2. Introduction

Simultaneous improvements to primary ion sources and mass spectrometers have facilitated the emergence of secondary ion mass spectrometry (SIMS) as a viable tool for small-molecule imaging in biology.[1] The introduction and wide-scale incorporation of polyatomic and cluster ion sources has improved ionization efficiencies for intact molecular ions and extended the upper mass detection limit above *m/z* 1000.[2-3] Academic work[4-6] inspired instrument manufacturers to incorporate tandem MS (MS^2)-capable mass analyzers into commercial SIMS instruments,[7-8] an essential development that enables the differentiation of isomers, which are pervasive in biological systems. Among other examples, biomolecular SIMS imaging has been applied to examine single cells,[9-11] neurons,[6, 12-13] bacterial biofilms,[14-20] and brain tissue from songbirds,[7, 21] rodents,[22-23] and *Drosophila*.[24-26]

As evidenced by the 2016 announcement of the National Microbiome Initiative, the need for tools and workflows that reveal microbial chemistry is increasingly urgent.[27-28] Characterizing the role of small molecules in bacterial life is essential for not only understanding the microorganisms themselves, but also the ecosystems that they inhabit and influence. In a process termed quorum sensing, collaborative communities of bacteria produce and sense small molecules, (e.g., acyl homoserine lactones, cyclic peptides, and quinolones) to communicate with one another and coordinate collective behavior.[29] Beyond signaling, bacterial communities utilize small molecules to cohesively modify their local environment, enhance nutrient uptake, colonize new territory, and defend themselves against competing organisms. Because of the simple sample preparation requirements, and an innate capability for two- and in some cases three-dimensional small molecule imaging, SIMS is wonderfully positioned to facilitate the exploration of microbial chemistry.

As discussed in a recent Account,[30] the large variations in both chemical composition and surface architecture make microbial communities exceptionally challenging to study with mass spectrometry imaging (MSI). Further complexity arises from the cultivation requirements; biofilms and other microbial communities are often grown on semi-solid agar, which must be dehydrated prior to introduction to the vacuum environment of the instrument sample chamber. The agar dehydration process can introduce artifacts in biofilm morphology and chemical distribution. Although there have been several excellent applications of matrix-assisted laser desorption/ionization (MALDI)[31-35] and desorption electrospray ionization (DESI)[36-38] to study agar-based microbial samples, to our knowledge there are no reports describing the direct application of SIMS imaging to microbial communities while they are still affixed to the agar substrate. Other successful examples of microbial SIMS imaging include analysis of imprint-transferred surfactants from *Bacillus* swarming communities grown on agar,[18] imaging of quinolone signaling molecules and rhamnolipid surfactants produced by *Pseudomonas aeruginosa* biofilms grown on silicon wafers,[14-17] *in situ* examination of liquid biofilms through a SiN membrane,[20, 39] and ultra-high-resolution NanoSIMS imaging of nitrogen fixation by cyanobacteria.[40-41] Another example of note is the use of SIMS to image quinolones and xenobiotics in *P. aeruginosa* biofilms cultivated on indium-tin oxide-coated glass slides and inside of an *ex vivo* pig lung model.[19]

As with other MS sampling modalities, the information generated by SIMS depends on both the properties and settings of the instrument, as well as the molecular properties of the analyte, such as gas-phase basicity and size. Furthermore, despite substantial improvements in modern cluster and polyatomic ion sources, SIMS remains a highly energetic ionization process, leading to hard ionization that can fragment biomolecules into smaller ions prior to detection. These factors prohibit direct comparison of the distribution or intensity of one analyte to that of another. Therefore, most SIMS experiments generate qualitative rather than quantitative information.

Several clever methods for quantitative MSI have been demonstrated. These include the use of a mimetic tissue model for brain imaging with MALDI,[42] the addition of a standard into the DESI solvent,[43] and the metabolic incorporation of isotopically labeled internal standards into bacterial and mammalian cells.[40, 44] Application of an isotopically labeled internal standard on top or beneath a sample has also been successfully employed for quantitative MALDI imaging of tissue.[45-46] In comparison to other ionization modalities, the challenges associated with quantitative MSI are even more prominent for SIMS. In static SIMS, the primary ion beam only accesses the first few molecular layers of the sample, therefore an exogenously applied external standard is liable to influence or obscure the native surface composition.

Here we develop a workflow for quantitative SIMS imaging with a focus on 2-alkyl-4(1H)-quinolone (AQ) and 2-alkyl-4-hydroxyquinoline *N*-oxide (AQNO) structural isomers in static *P. aeruginosa* colony biofilms. In a process similar to the initial steps demonstrated for DESI[37] and MALDI,[34] we cultivate the microbial communities on thin agar and dry them under a gentle stream of nitrogen. The microbial samples, and a series of external calibration samples, are examined using SIMS product ion imaging. Quadratic calibration with an adjustment for common (interfering) fragmentation provides the surface density of each analyte on a pixel-by-pixel basis, enabling quantitative comparisons within and between samples. Our results indicate that the described methodology for quantitative SIMS imaging could be extended to examine small molecules in biological samples of diverse composition and origin.

5.3. Experimental

5.3.1. Materials and Reagents

LC-MS grade methanol, ethanol, fluorescein sodium salt, HHQ (2-heptyl-4-quinolone), and PQS

("*Pseudomonas* quinolone signal"; 2-heptyl-3-hydroxy-4(1H)-quinolone) were purchased from Sigma-Aldrich (St Louis, MO). HQNO (2-heptyl-4-hydroxyquinoline *N*-oxide), NQNO (2-alkyl-4-nonylquinoline-*N*-oxide2-nonyl-4-hydroxyquinoline *N*-oxide), NHQ (2-nonyl-4-quinolone), and C9-PQS (2-nonyl-3-hydroxy-4(1H)-quinolone) were purchased from Cayman Chemical (Ann Arbor, MI). All standards were acquired at 96% purity or better and used without further purification.

Custom aluminum SIMS sample plates were machined by the expert craftsman in the University of Illinois School of Chemical Sciences' Machine Shop. Double sided conductive copper tape, 3M 1182, was purchased from Ted Pella, Inc. (Redding, CA) and Structure Probe, Inc. (West Chester, PA).

5.3.2. Colony Biofilm Cultivation

Two *P. aeruginosa* strains, PAO1C ("wild-type" lab strain) and FRD1 (alginate overproducing cystic fibrosis lung isolate),[47] were used in this study. Cell cultures were grown for 18 h at 37 °C with shaking at 240 rpm in modified fastidious anaerobe broth (FAB) culture medium supplemented with 30 mM filter-sterilized glucose as the source of carbon. Growth plates were prepared by aliquoting 7.5 mL of sterile FAB-noble agar (1% agar supplemented with 12 mM glucose) into 60 mm diameter Petri dishes. The agar plates were inoculated with 5 µL cell culture (OD_{600} = 1) and incubated at 37 °C for 72 h. More than 25 single and co-culture colony biofilms were used for optimization and verification of the methods developed here. Culture handling and manipulation were performed in accordance with institutional and CDC laboratory and biological safety guidelines, and included the use of aseptic techniques, personal protective equipment, and disinfection and sterilization procedures specific to the biosafety level of the organism.[48]

5.3.3. Optical Imaging and Analysis

Macroscopic optical images of the hydrated and dried samples were obtained using a Nikon D3300 camera equipped with a Nikon AF-S DX NIKKOR (18–55 mm 1:3.5–5.6 VR II, ∞-0.28m/0.92ft ø52) (Nikon, Melville, NY). Images were processed using either MATLAB (MathWorks, Natick, MA) or ImageJ (64 bit) as previously described.[49] Microscopy images of AQ aggregates within the colony biofilms were acquired using a Nikon Eclipse 90i confocal microscope equipped with a 10× objective, and the images processed with the NIS-Elements AR Imaging Software (Nikon).

5.3.4. Chemical Printing

Two pooled solutions were prepared in 50% ethanol (50% water, v/v) containing equimolar quantities of HHQ, PQS, and NQNO, or NHQ, C9-PQS, and HQNO. Direct dilutions were made into 50% ethanol to create a series of nine of each of the two pooled solutions ranging in concentration from 1.0–200 μM. The solutions were deposited on dry FAB agar using a chemical inkjet printer (CHIP 1000, Shimadzu Corp., Kyoto, Japan) in multi-pass iterative mode. Before printing and between solutions, the CHIP was rinsed with 250 μL isopropyl alcohol followed by 250 μL 50% ethanol. Dwell voltages and dwell times were initially set to 25 V and 35 μs, respectively, and adjusted as needed throughout printing to obtain uniform droplets. Each deposition area was constructed with two parallel lines containing 10 spots each, with an intraspot spacing of 200 μm, to form uniform regions of approximately 2.2 mm × 0.6 mm. Four iterative passes of 500 pL per droplet (2 s pause between each pass) resulted in a total deposition quantity of 40–8000 fmol of each analyte at a surface density range of 3.0–610 pmol/cm^2.

For confocal fluorescence microscopy control experiments, solutions containing either 20 μM fluorescein or 20 μM fluorescein and 100 μM each of HHQ, PQS, and NQNO was deposited onto agar using the CHIP 1000 in spot-mode. Each deposition spot was composed of 10, 100 pL drops for a total deposition quantity of 20 fmol fluorescein and 100 fmol HHQ, PQS, and NQNO. The dwell voltage and dwell time were set to 35 V and 35 μs respectively. Prior to solution deposition, the agar was prepared by dehydrating 1 cm x 1 cm squares on glass microscopy slides.

5.3.5. Confocal Fluorescence Microscopy

Fluorescein and AQ spots were examined using a Leica SP8 fluorescence confocal microscope (Buffalo Grove, IL) with a 10× dry objective (NA = 0.4). Both transmission and fluorescence channels were used with a Z-stacking range confined to the observable fluorescence signal. A stage step-size of 2.41 μm was used for the Z-stacking, and the field of view was set to 512 × 512 pixels. The Ar laser excitation wavelength was 488 nm and emission was collected from 494-618 nm. The resulting data were processed in ImageJ using the Bio Formats toolbox.[50-51] Fluorescent spots were selected with the ROI selection tool and the average intensity values of each Z-stack were exported into MATLAB for further analysis.

5.3.6. Scanning Electron Microscopy

Dehydrated samples were sputter coated in Au/Pd using a Denton Vacuum Desk II (Moorestown, NJ) operated with 64 mTorr Ar and 40 mA current for 70 s. Scanning electron microscopy (SEM)

was performed on dehydrated samples using a Philips XL30 ESEM-FEG (Hillsboro, OR) operated under high-vacuum conditions at 5 kV and an approximate working distance of 10 mm.

5.3.7. SIMS Imaging

Mass spectrometric measurements were performed with a modified quadrupole time-of-flight (qTOF) mass spectrometer, described in detail elsewhere.[6] The instrument is a QSTAR XL (AB SCIEX, Framingham, MA) equipped with a Buckminsterfullerene (C_{60}) ion source (Ionoptika Ltd., Hampshire, UK) for SIMS. The ion source was adjusted to produce a continuous beam of 20 keV C_{60}^{+} primary ions at a 35 μm spot size with 500 pA sample current. The approximate primary ion dose was held to 5×10^{13} ions/cm^2, which exceeds the static limit of 1×10^{13} primary ions/cm^2, and represents an estimated sampling depth of 40 nm based on measurements from 20 keV C_{60}^{2+} bombardment of HeLa cells.[9] SIMS sputtering rates depend on both chemical composition[52] and surface morphology,[53] and biofilms are both morphologically and chemical heterogeneous. Therefore the actual sampling depth will fluctuate from pixel-to-pixel.

Each sample was raster imaged three times with a 25 μm vertical offset between images to present a predominantly unperturbed sampling region for each acquisition. The first image produced secondary ions from *m/z* 60–850 with a pixel size of 100 μm × 100 μm and a sputtering time of 500 ms/pixel. The quadrupole bias was set to 15%, 25%, and 60% at *m/z* 100, 200, and 400, respectively. The second and third images were collected in product ion mode with a unit resolution precursor mass transmission for product of *m/z* 288 and *m/z* 260, 30 eV argon CID (collision induced dissociation), and “Enhance All” mode activated to selectively enhance transmission of product ions in the low mass range. The quadrupole bias was set to 5%, 47.5%, and 47.5% at *m/z* 40, 90, and 180, respectively; the pixel size was 200 μm × 200 μm, and the sputtering time was 1 s/pixel.

5.3.8. SIMS Data Analysis

AB SCIEX wiff data files produced by Analyst v1.2 and oMALDI Server v5.1 (AB SCIEX) were converted to mzML with the ProteoWizard msconvert function,[54] to imzML using imzMLConverter,[55] and imported into MSiReader v0.09.[56] For standard curve creation and quantitation, the *m/z* intensity data for each sample or region of interest was exported to Excel using the MSiReader ROI tool (‘sum of window’ over 0.1 Da). Further processing, which was performed using either Excel or MATLAB, is detailed in the Results and Discussion section.

5.4. Results and Discussion

5.4.1. Dehydration Causes Agar Contraction but Preserves the Overall Morphology of the Colony Biofilm

The dehydration-induced changes in sample morphology and analyte distribution were assessed by evaluating optical images of biofilms before and after desiccation. Images from one representative sample, a 72 h co-culture of two *P. aeruginosa* strains, are provided in **Figure 5.1**. These two strains were chosen because of their differing attributes: PAO1C (left) is a common laboratory strain that readily spreads in motility agar assays,[57] whereas FRD1 (right) is a mucoid cystic fibrosis isolate strain with limited motility that produces the exopolysaccharide alginate in great abundance.[47]

The biofilms were cultivated on thin agar (**Figure 5.1a**), transferred to a 250 μm recessed aluminum SIMS sample plate covered with 88 μm thick double-sided conductive coper tape (**Figure 5.1b**), and dehydrated under a gentle stream of nitrogen (**Figure 5.1c**). An overlay of the hydrated (green) and dehydrated sample (blue) shows a slight contraction of the agar during dehydration (**Figure 5.1d**), and measurements of four independent biofilms show that the agar area is reduced by 26% ± 2 (standard deviation) during dehydration.

Changes in sample morphology were also evaluated in a spatially resolved fashion. Images of biofilms acquired before and after dehydration were overlaid and registered using an affine transformation to account for variance in angle, distance, and camera position. Approximately 50 teach points present on both images were utilized to perform a non-affine polynomial transform to dynamically “stretch” the dehydrated sample to match the shape of its hydrated counterpart. The magnitude of contraction was calculated for an equally spaced array, and is represented as a rainbow quiver plot (**Figure 5.1e** and **5.1f**). The magnitude of distortion at a given point on the quiver plot is represented both by the length of the vector and its color, with long yellow vectors indicating regions of greater contraction, and short blue vectors indicating regions with less contraction. The inset image (**Figure 5.1f**) shows that the sample contracts by over 2 mm at the agar edge and converges to a point of zero contraction near the intersection of the two biofilms. We surmise that the point of least contraction is shifted slightly towards the FRD1 biofilm due to the thicker biofilm structure, which results in slower drying for the underlying agar.

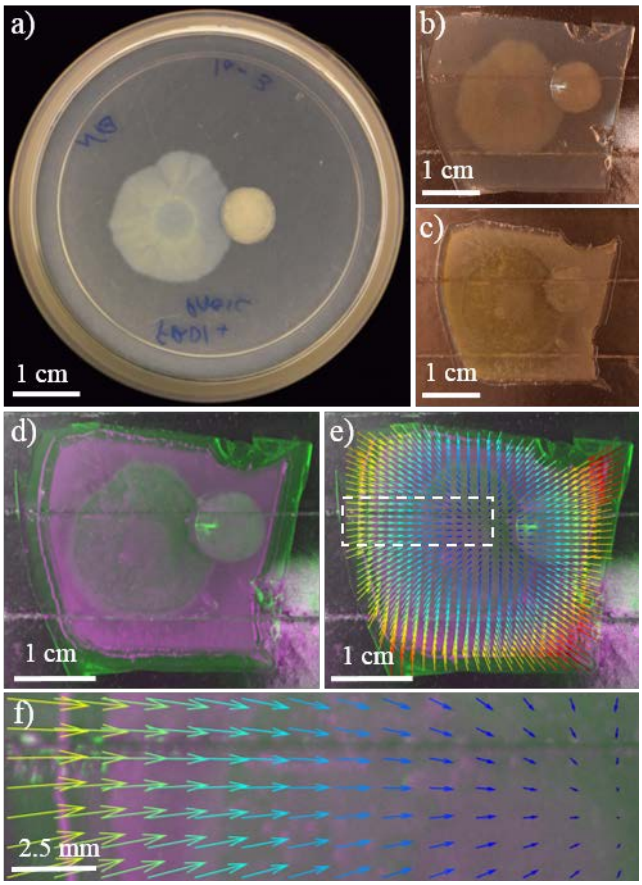

Figure 5.1. Evaluation of biofilm dehydration in preparation for SIMS imaging. A 72 h *P. aeruginosa* PAO1C (left) and FRD1 (right) co-culture colony biofilm: (**a**) as cultivated in a Petri dish; (**b**) excised and transferred to a SIMS sample plate with double-sided copper tape; (**c**) after dehydration with N_2; (**d**) overlay of the same sample before (green) and after (purple) dehydration; (**e**) quiver plot with vector length and color showing the magnitude and direction of dehydration-induced contraction; and (**f**) inset of the quiver plot shown in **e**. The scale bars represent 1 cm in **a–d** and 2.5 cm in **f**.

Overall these results indicate that although the agar contracts during drying, it does so in a uniform and predictable manner, with the greatest contraction occurring near the agar edges. The macroscopic biofilm morphology remains intact and suitable for follow-up analysis. In our experience, the best results are obtained by starting with a thin agar of uniform thickness and unfurling it gradually onto the SIMS substrate with a steel spatula or a razor blade. Care must be taken to avoid distorting the agar or trapping air bubbles during the transfer process. We initially experimented with several different preservation procedures, including vacuum desiccation, freeze-drying, and oven drying, however we found that a simple nitrogen-assisted dehydration provided the best retention of biofilm morphology and the most consistent results. Attempts were also made to deposit the agar directly onto aluminum sample plates or onto silicon wafers, thus avoiding the use of copper tape and the possible introduction of chemical contaminants, but the agar tended to separate from the substrate during dehydration so the tape was found to be essential for adhesion.

To evaluate changes in analyte distribution, endogenous aggregates in the hydrated and dried samples were visualized with optical microscopy (**Figure 5.2**). Previous Raman microscopy investigations into aggregates of this shape in *P. aeruginosa* biofilms revealed that they contain both AQs and AQNOs,[14, 58] which are the primary analytes of interest for this study. Representative microscopy images acquired near the center of the PAO1C biofilm show that the overall shape and

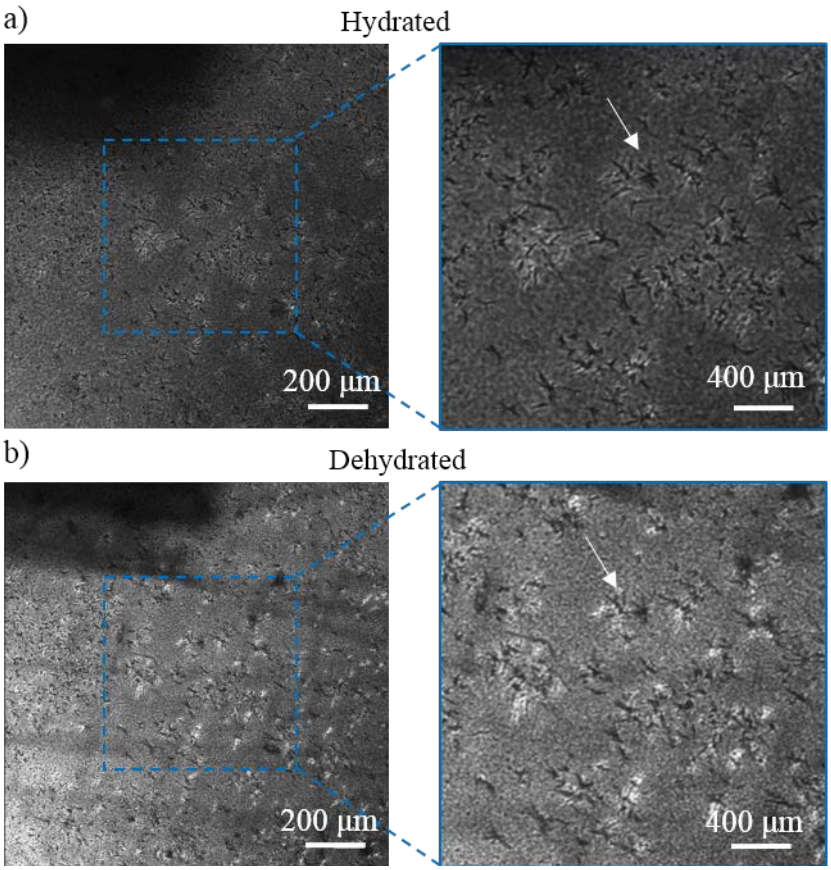

Figure 5.2. Microscopic evaluation of AQ distribution before and after preparation of a *P. aeruginosa* PAO1C biofilm for SIMS imaging. The same aggregates are visible in both hydrated (**a**) and (**b**) dehydrated samples and remain stationary with respect to one another during drying. The insets are magnified by 2x with respect to the original image, and the white arrow indicates an example AQ crystal.

distribution of the AQ and AQNO aggregates are largely retained during dehydration (**Figure 5.2**). These investigations suggest that the sample preservation was not a limiting factor in the ultimate imaging resolution, which was confined to 100 µm or greater in the current work.

Notably, this analysis does not account for hydrophilic analytes, which may partially absorb into the agar and migrate throughout the sample, or amphiphilic rhamnolipid biosurfactants, which could diffuse laterally during drying.[59] The solubility of AQs and AQNOs is improved by the presence of rhamnolipids, so it is possible that these analytes can be distributed more widely across the surface if substantial rhamnolipid diffusion occurs.[60]

5.4.2. Optimization and Evaluation of Standard Deposition

The experiments described in this manuscript largely focus on **t**wo AQs and two AQNOs reported to be most abundant in *P. aeruginosa*,[61] namely the saturated 7- and 9-carbon variants of the major subclass (i.e., PQS, C9-PQS, HQNO, and NQNO). In *P. aeruginosa,* PQS is a known cell-to-cell signaling molecule,[62] and both HQNO[63] and NQNO[64] are active against *Staphylococcus aureus*. The functional roles of C9-PQS and most of the other AQs and AQNOs produced by *P. aeruginosa* are currently unknown.[65] Differing only by the location of a hydroxyl group, PQS and HQNO both produce a protonated molecular ion at *m/z* 260.1650. Similarly, the 9-carbon variants of these two molecules (i.e., C9-PQS and NQNO) are both found at *m/z* 288.1963. Differentiation of these

analytes with mass spectrometry therefore requires fragmentation-based MS^2 analysis. As previously reported, the two AQNOs (HQNO and NQNO) fragment under CID to yield a base peak of *m/z* 159.07 (**Figure 5.3b** and **5.3d** respectively), while AQs produce a base peak of *m/z* 175.07 (**Figure 5.3a** and **5.3b** respectively), which, along with several other distinguishing fragments, enables this differentiation (**Figure 5.3a** and **Figure 5.3c**).[61] However, closer inspection reveals that each of these analytes also produces a competing product ion signal that directly interferes with the isomeric counterpart. In fact, for MS^2 analysis of both *m/z* 260 and *m/z* 288, no single product ion can be used to completely separate the signal arising from either compound. Because of these complications, the standards were separated into two separate multicomponent dilution series, one containing HHQ, PQS and NQNO, and another contained NHQ, C9-PQS, and HQNO (HHQ and NHQ were included as part of the original study design but were not used for quantitation and therefore will not be discussed further).

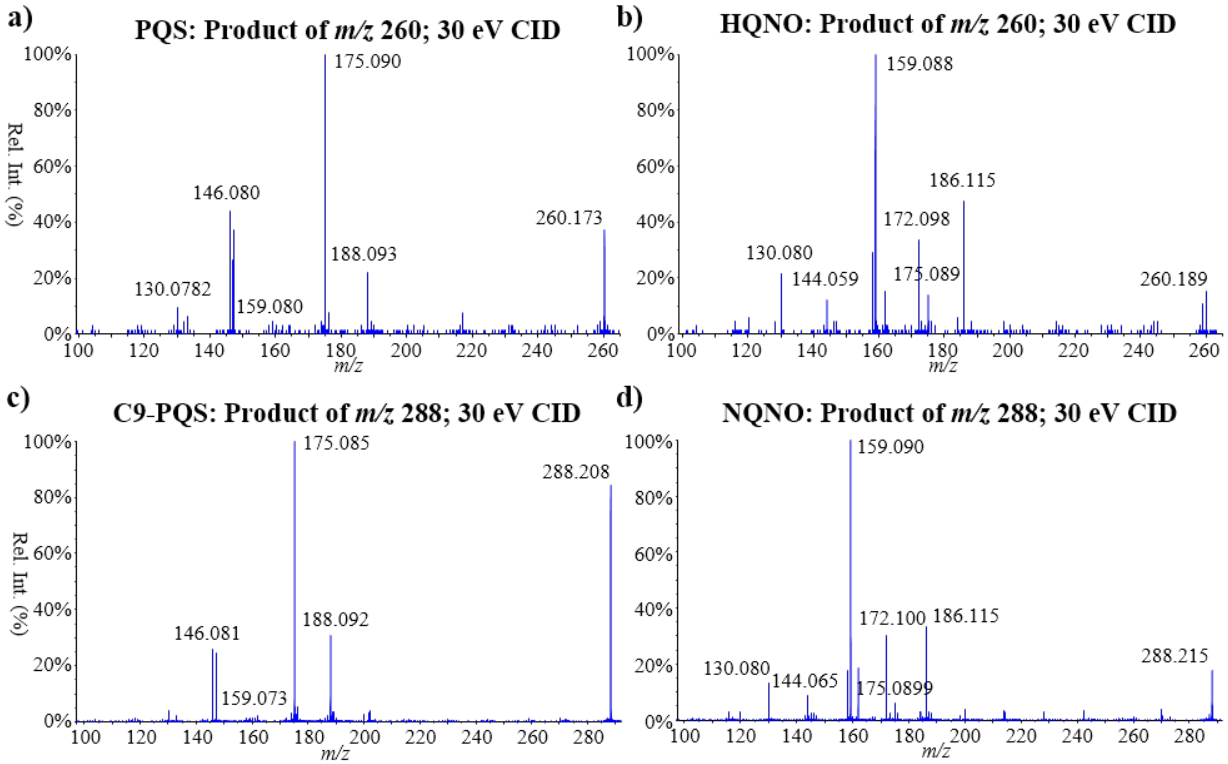

Figure 5.3. C_{60}-SIMS product ion spectra for (**a**) PQS, (**b**) HQNO, (**c**) C9-PQS, and (**d**) NQNO. Notice that despite a strong base peak of *m/z* 159.07 for both HQNO and NQNO, and *m/z* 175.07 for PQS and C9-PQS, the corresponding peak is also present in the isomer at a relatively low intensity.

The quantitative imaging method described herein requires analysis of standards on an agar surface, therefore we sought to determine the extent to which the standards absorbed into the agar during deposition. Using similar conditions to the standard curve preparation, 1 nL aliquots of the

100 µM standard solutions were deposited onto dried agar via chemical inkjet printing, and the resulting spots were evaluated with SEM. As can be seen in **Figures 5.4a** and **5.4b**, the deposited standards cover a circular region of approximately 200 µm in diameter and appear to form an even layer over the underlying agar. The features observable around and underneath the deposited standards in the 400× magnification electron micrograph (**Figure 5.4b**) show that the microstructure of the agar surface is retained during deposition and solvent evaporation, suggesting that the solution dries before dissolving surface salts or absorbing into the agar. Control spots, which contained only solvent, were unobservable by SEM.

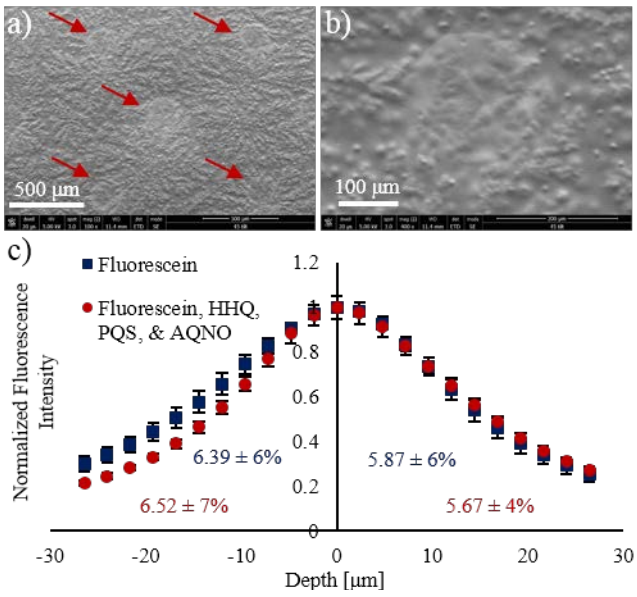

Figure 5.4. SEM and 3-D confocal fluorescence microscopy evaluation of standards deposited onto dehydrated agar via chemical inkjet printing. (**a**) Electron micrograph of five 1 nL depositions (as indicated by red arrows) containing 100 µM each of HHQ, PQS, and NQNO. (**b**) Higher magnification micrograph of a single standard spot from **a**. (**c**) Average fluorescence intensity depth profile for fluorescein in four spots containing either 20 µM fluorescein (blue squares) or 20 µM fluorescein and 100 µM each of HHQ, PQS, and NQNO (red circles). The integrated fluorescence intensity in the space below and above the agar surface is provided blue and red text for the two deposition conditions. Shown are 23 Z-stacks from -26.4 µm below the surface to 26.4 µm above the surface. The scale bars in **a** and **b** represent 500 µm and 100 µm respectively, and the error bars in **c** represent standard deviation.

For further verification, 1 nL droplets of a solution containing either 20 µM fluorescein and 100 µM each of HHQ, PQS, and NQNO or only 20 µM fluorescein were deposited on dried agar and examined with 3-D confocal fluorescence microscopy. As can be seen in **Figure 5.4c**, the fluorescence intensity profile for fluorescein in the standard mixture (red circles) takes the form of an asymmetric Gaussian point spread function with a maximum intensity at the agar surface (depth = 0 ± 1.2 µm). Significant fluorescence signal bleed prevents the determination of analyte depth, however the integrated fluorescence intensity is slightly greater above the surface than below ($p = 0.02$ for $n = 4$ spots). The control condition with spots containing only fluorescein (blue squares) exhibits less asymmetry and does not show a significant difference in integrated fluorescence intensity for regions below and above surface ($p = 0.4$). This suggests that the observed surface excess is not an artifact of

the refractive index difference between the air and the agar, but rather that it arises due to the presence of AQs and AQNOs.

In combination with the low water solubility of AQs and AQNOs[66] as well as our observation of endogenous AQ and AQNO crystals on the surface of biofilms (**Figure 5.2**), the SEM and confocal fluorescence microscopy data support the conclusion that the standards largely remain on the agar surface following deposition. It is possible that components of the agar (e.g. salts) migrate during droplet drying to co-crystalize with the exogenous standards or that a portion of the standards absorb into the agar. Both of these possibilities may affect the measured ion abundance.

We next optimized the chemical inkjet printing conditions to achieve reliable and repeatable standard curves and under manageable analysis times. Initially the multicomponent standard solutions were deposited as an ordered array of spots, however, following C_{60}-SIMS product ion imaging, the image-to-image constancy was found to be poor. The poor consistency most likely arose because the spot diameter (~200 μm) was too small for the width of the stage raster (100 μm) and the diameter of the primary ion beam (35 μm). To overcome this issue, 20 aliquots of each solution were deposited evenly at a spot-to-spot interval of 200 μm over an area of 200 μm × 2000 μm. Due to the overlapping and pooling of the standard solutions, these deposition conditions resulted in the formation of 2.2 mm × 0.6 mm regions containing between 40–8000 fmol of each analyte at a surface density range of 3.0–610 pmol/cm^2.

5.4.3. Relative Quantitation is Accomplished through Pixel-by-pixel Normalization to External Nonlinear Least Squares Regression Curves

Representative standard images from the optimized line deposition conditions are provided in **Figure 5.5**. The average relative standard deviation (RSD) of the ion intensity across all concentrations was 24%, 22%, 42%, and 24% for PQS, HQNO, C9-PQS and NQNO respectively.

The product ion intensities for each analyte were used to create second order polynomial linear regression curves of the form of **Equation 1**:

$$\mathbf{i = a\rho^2 + b\rho + c} \qquad (\mathbf{1})$$

where **i** is the measured ion intensity, **ρ** is the is surface density with units of mass × area^{-1}, and **a**, **b**, and **c** are constants (**Figure 5.4c**, **5.4d**, **5.4g**, and **5.4h**). We initially attempted to apply linear

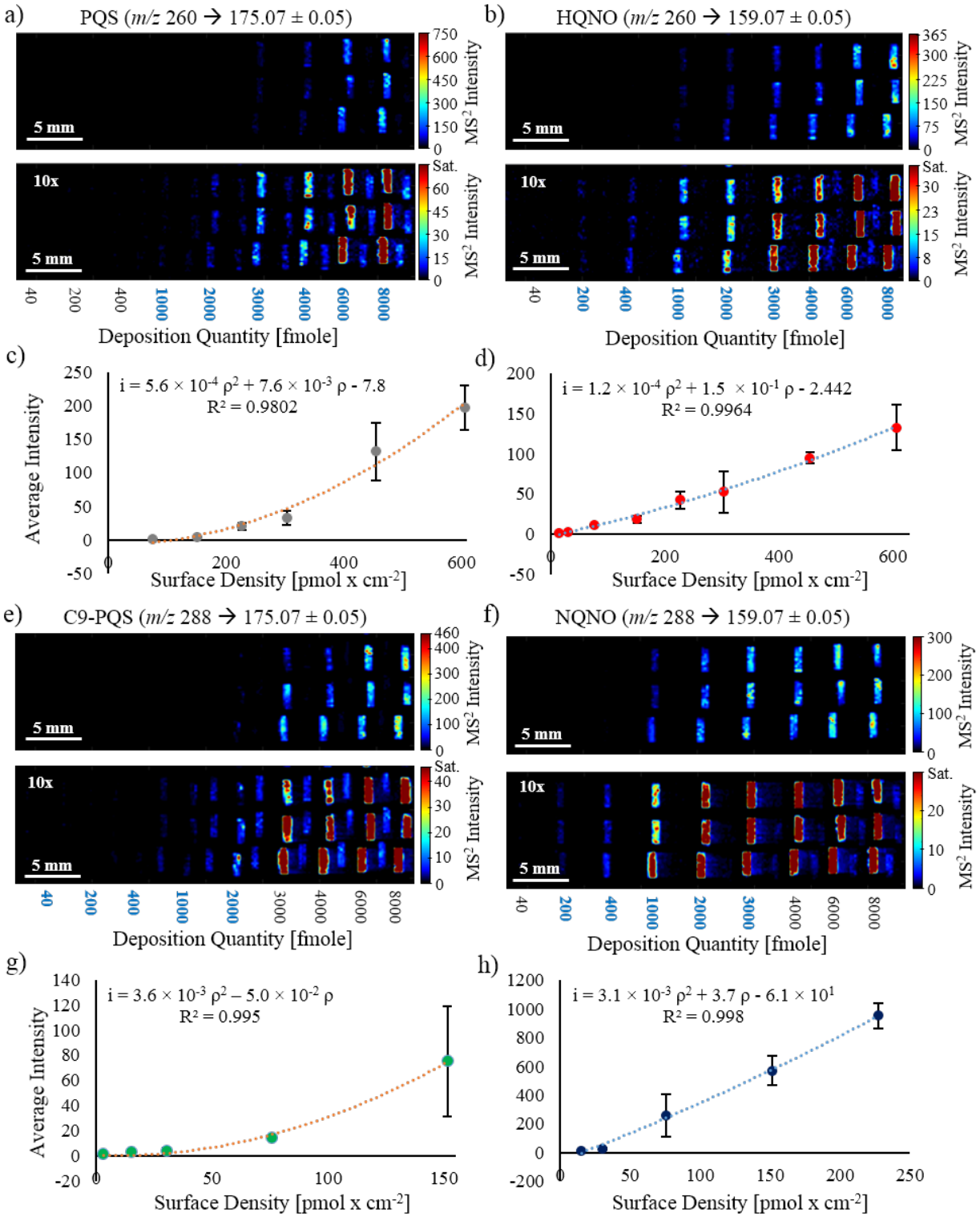

Figure 5.5. SIMS product ion quadratic calibration images, curves, and regression data: calibration images for (**a**) PQS, (**b**) HQNO, (**e**) C9-PQS, and (**f**) NQNO printed on dry agar; and calibration curves for (**c**) PQS, (**d**) HQNO, (**g**) C9-PQS, and (**h**) NQNO. The color scale is magnified by 10× in the lower images to accentuate the lower deposition quantities. The **blue** text indicates the quantitation range used.

regression curves, however they were found to be unreliable over a meaningful concentration range because of nonlinearity, which we speculate to arise from second order surface interactions (e.g., absorption, intercalation, or intermolecular forces) that suppress ionization at low concentrations, and surface saturation at high concentrations. A calculation in terms of three dimensional area (e.g. concentration of the first 40 nm) was considered in place of surface density, however the veracity of this calculation is uncertain in the absence of an accurate sputtering depth for every pixel.

The quadratic equation can be used to solve the second order polynomial regression curves from **Figure 5.4** to accommodate differences in ionization efficiency and directly calculate the analyte-specific surface density in each pixel. Using the product ion transition for PQS (*m/z* 260→175) as an example (**Equation 2**):

$$\boldsymbol{\rho_{PQS175(meas)}} = \frac{-\boldsymbol{b_{175}} \pm \sqrt{(\boldsymbol{b_{175}})^2 - 4 \cdot \boldsymbol{a_{175}} \cdot (\boldsymbol{c_{175}} - \boldsymbol{i_{175}})}}{2 \cdot \boldsymbol{a_{175}}} \quad \textbf{(2)}.$$

In instances where the discriminant is less than zero and no real solution is available, the free term ($\boldsymbol{c}$) can be set equal to zero; however, manual interpretation is necessary to ensure the accuracy of the fit.[67]

As previously discussed, the measured surface density for PQS ($\boldsymbol{\rho_{PQS(meas)}}$) is an overestimate of the actual surface density due to the competing product ion transition for HQNO (*m/z* 260→175). Examination of the four compounds over a series of concentrations revealed that the relative intensities of *m/z* 159 and *m/z* 175 take on a constant value for each analyte: the 159/175 ratios for PQS and C9-PQS are 0.04 ± 40% (RSD) and 0.020 ± 10%, respectively, and the 175/159 ratios for HQNO and NQNO are 0.13 ± 8% and 0.07 ± 20%, respectively. The corrected surface density for PQS ($\boldsymbol{\rho_{PQS175(corr)}}$) can be determined by removing the contribution of *m/z* 175 arising from HQNO ($\boldsymbol{\rho_{HQNO175(exp)}}$), as shown in **Equation 3**:

$$\boldsymbol{\rho_{PQS175(corr)}} = \boldsymbol{\rho_{PQS175(meas)}} - \boldsymbol{\rho_{HQNO175(exp)}} \quad \textbf{(3)}.$$

Of course $\boldsymbol{\rho_{HQNO175(exp)}}$ is still an unknown value and must be further defined by **Equations 4**–**6**:

$$\boldsymbol{\rho_{HQNO175(exp)}} = \boldsymbol{f_{HQNO}} \cdot \boldsymbol{\rho_{HQNO159(corr)}} \quad \textbf{(4)}$$

$$= \boldsymbol{f_{HQNO}} \cdot \left[\boldsymbol{\rho_{HQNO159(meas)}} - \boldsymbol{\rho_{PQS159(exp)}}\right] \quad \textbf{(5)}$$

$$= \boldsymbol{f_{HQNO}} \cdot \left[\boldsymbol{\rho_{HQNO159(meas)}} - \boldsymbol{f_{PQS}} \cdot \boldsymbol{\rho_{PQS159(corr)}}\right] \quad \textbf{(6)},$$

where the experimentally derived relative fragmentation ratios for HQNO and PQS are delineated by $\boldsymbol{f_{HQNO}}$ and $\boldsymbol{f_{PQS}}$ respectively, and $\boldsymbol{\rho_{HQNO159(meas)}}$ is given by **Equation 2** solved for HQNO. Combining **Equations 3** and **6** and solving for the $\boldsymbol{\rho_{PQS175(corr)}}$ term yields **Equation 7**, which is the final formula used to calculate the corrected surface density for PQS:

$$\boldsymbol{\rho_{PQS175(corr)} = \frac{\rho_{PQS175(meas)} - f_{HQNO} \cdot \rho_{HQNO(meas)}}{1 - f_{HQNO} \cdot f_{PQS}}} \quad \textbf{(7)}.$$

More generally, for any analyte $\boldsymbol{n}$ with an interfering compound $\boldsymbol{m}$, **Equation 8** can be used to calculate the corrected surface density of $\boldsymbol{n}$:

$$\boldsymbol{\rho_{n(corr)} = \frac{\rho_{n(meas)} - f_m \cdot \rho_{m(meas)}}{1 - f_m \cdot f_n}} \quad \textbf{(8)}.$$

By adding additional terms to **Equation 3,** this analysis can theoretically be extended to accommodate additional interfering species. It is therefore not limited to MS^2 data, but can also be extended to MS^1 in instances when the chemical composition and in-source fragmentation characteristics of the sample are known to a high degree of confidence.

Finally, the accurate interpretation of quantitative measurements requires information on the lower and upper limits of quantitation (LLOQ and ULOQ) for each analyte. Here the LLOQ is defined by two criteria. First, the initial (raw MS^2) intensity of a given pixel must be greater than the lowest intensity on the calibration curve. Second, the initial intensity must be greater than the average background intensity from the sample. If the intensity of a given pixel is lower than either of these values, the surface density for this analyte is set to zero. The ULOQ for each analyte is defined as being the highest intensity value on the calibration curve. Intensity values that are greater than the ULOQ are adjusted to 110% of the ULOQ in the quantitative image, effectively saturating the intensity scale for this pixel. In this way, for any given pixel, analyte intensities that are lower than the LLOQ will display a surface density of zero, and analytes with an intensity greater than the ULOQ will yield a "saturated" surface density.

Full calibration data for the four analytes used in this study, including the three calibration constants (**a**, **b**, and **c**), the coefficient of determination values (R^2), the ULOQs, and LLOQs, can be found in **Table 5.1**.

5.4.4. Quantitative SIMS Imaging of Alkyl-Quinolones in *P. aeruginosa* Colony Biofilm

To demonstrate the capability of our methods, we subjected a series of *P. aeruginosa* biofilms to the quantitative SIMS imaging protocols described above. An example image sequence for two

Table 5.1. Quadratic regression data.

	PQS	HQNO	C9-PQS	NQNO
m/z	175	159	175	159
a	5.6E-04	1.2E-04	3.6E-03	3.1E-03
b	7.5E-03	1.5E-01	-5.0E-02	3.7
c	-7.8	-2.4	0.0	-61
R^2	0.980	0.996	0.998	0.998
Fragmentation factor	0.044	0.13	0.020	0.070
LLOQ [intensity]	1.4	0.99	0.96	12
ULOQ [intensity]	200	130	75	950
LLOQ [pmol × cm^{-2}]	75	15	3.0	15
ULOQ [pmol × cm^{-2}]	610	610	150	230

AQs and two AQNOs in a 72 h PAO1C colony biofilm is shown in **Figure 5.6**. First, we show the raw images required in standard (MS^1) mode (**Figure 5.6a**), which is how ion images are overwhelmingly reported in the literature. Ion images for *m/z* 260.17 (the protonated molecular ion for both PQS and HQNO) and *m/z* 288.20 (the protonated molecular ion for both C9-PQS and NQNO) show the four analytes to be primarily confined to a region near the center of the biofilm community (**Figure 5.6a (i-ii)**). In SIMS, prominent *in source* fragment ions arising from the analytes of interest can sometimes be more intense than the molecular ion; therefore, images for these ions are also commonly displayed. An ion image for an AQ fragment (*m/z* 175.07) appears with high intensity near the sample center, and with a small ring of lower intensity around the biofilm edge (**Figure 5.6a (iii)**). The common *in source* fragment of both AQNOs and HHQ-type AQs (*m/z* 159.07) has a distribution similar to both *m/z* 260.17 and *m/z* 288.20; however, the edge of the sample center shows up at a higher intensity than the internal region (**Figure 5.6a (iv)**). Unfortunately, because of common *in source* fragmentation, ion images for *m/z* 175.07 and 159.07 are not specific to any one molecule, or even a single class of molecules, and thus, cannot reliably be used to assign the distribution of an analyte without extensive follow-up analysis.

In contrast to MS^1 images, product ion images have two criteria for discriminating the analyte from the chemical background—the precursor ion must be ionized to generate an *m/z* value within a certain range (± 0.5 Da in this case), *and* a product ion must be generated with a separate, specific *m/z* value within an additional selection window (± 0.05 Da in this case)—therefore product ion imaging is much more selective. Product ion images for PQS, HQNO, C9-PQS, and NQNO are provided in **Figure 5.6b (i–v)**, **5.6c (i–v)**, **5.6d (i–v)**, and **5.6e (i–v),** respectively, with each row (**i–v**) showing successive steps along the quantitation process.

The largest changes in both distribution and intensity are observed for PQS. The raw image (**Figure 5.6b (i)**), which is scaled to the maximum single-pixel ion intensity, shows a region of moderate signal intensity near the center with small regions (< 200–400 μm) containing high intensity pixels. Following correction for ionization efficiency by applying **Equation 2** (**Figure 5.6b (ii)**), a similar signal distribution is observed; however, the nonlinear calibration has the effect of amplifying low intensity signals, revealing an additional ring of PQS bordering the biofilm center.

Following subtraction of the signal contribution from HQNO by using **Equation 7** (**Figure 5.6b (iii)**), both the measured surface density and the perceived distribution change substantially, showing that, aside from a few isolated hotspots, the center of the sample has much less PQS than originally observed. In **Figure 5.6b (iv)** the surface density of pixels with an intensity less than the calibration and sample LLOQs are set equal to zero, and those with a surface density greater than the ULOQ are set to 110% of the ULOQ. In the case of PQS, no pixels have an intensity above the ULOQ, so the ULOQ adjustment has no effect. Finally, in **Figure 5.6b (v)**, the maximum surface density of the image is scaled to a common value of 610 pmol × cm^{-2} to enable direct analyte-to-analyte comparisons.

Analogous operations were performed on the remaining three analytes (**Figure 5.6c–e**) to generate quantitative ion images. Note that the change in surface density brought on by fragmentation is minor, and largely unobservable within these images. It can be helpful to view the quantitative progressions as two-dimensional scatter plots, with each pixel plotted as a function of intensity or surface density, as shown in **Figures 5.7**. This perspective shows, for example, the effect that fragmentation correction and LOQ filtration has on the perceived distribution of NQNO, which is actually quite significant at low concentrations (**Figure 5.7d**). Additional quantitative imaging examples are provided for both a 48 h PAO1C colony biofilm and a second 72 h PAO1C colony biofilm in **Figures 5.8** and **5.9** respectively. These example show changes in the AQ distribution and surface density that are similar to those observed in **Figure 5.6**, however the absolute surface density values are greater and the biofilm morphology is different, indicating large biological variability.

Although AQ and AQNO concentrations for agar-based PAO1C biofilms were not available in the literature, we can draw insight from quantitative analysis of *P. aeruginosa* liquid cultures. For example, Lépine and co-workers reported a maximum concentration of 1.7 μM PQS

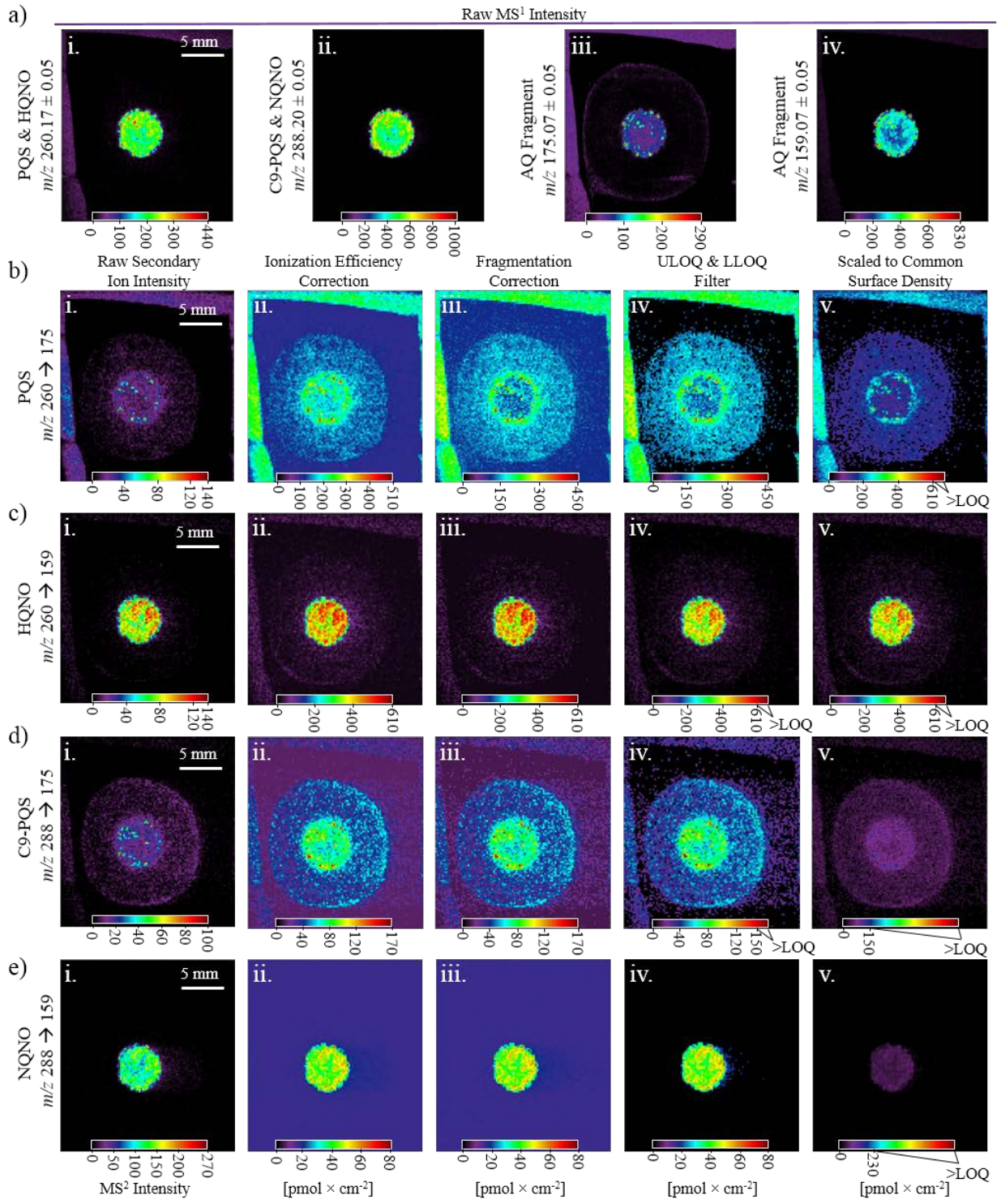

Figure 5.6. SIMS imaging of a 72 h *P. aeruginosa* colony biofilm: (**a**) Raw SIMS MS^1 images for **(i)**) PQS & HQNO, **(ii)** C9-PQS & NQNO, and AQ fragments **(iii)** *m/z* 175.07 and **(iv**) 159.07; (**b-e**) MS^2 quantitative image progressions for (**b**) PQS, (**c**) HQNO, (**d**) C9-PQS and (**e**) NQNO. Images in column **b-e (i)** show the uncorrected (raw) secondary ion intensity; column **b-e (ii)** is corrected for ionization efficiency; column **b-e (iii)** is corrected for common (interfering) product ions; column **b-e (iv)** shows the ULOQ and LLOQ correction; and images in column **b-e (v)** are scaled to a common maximum density of 610 pmol x cm^{-2} to facilitate direct and quantitative analyte-to analyte distribution comparisons.

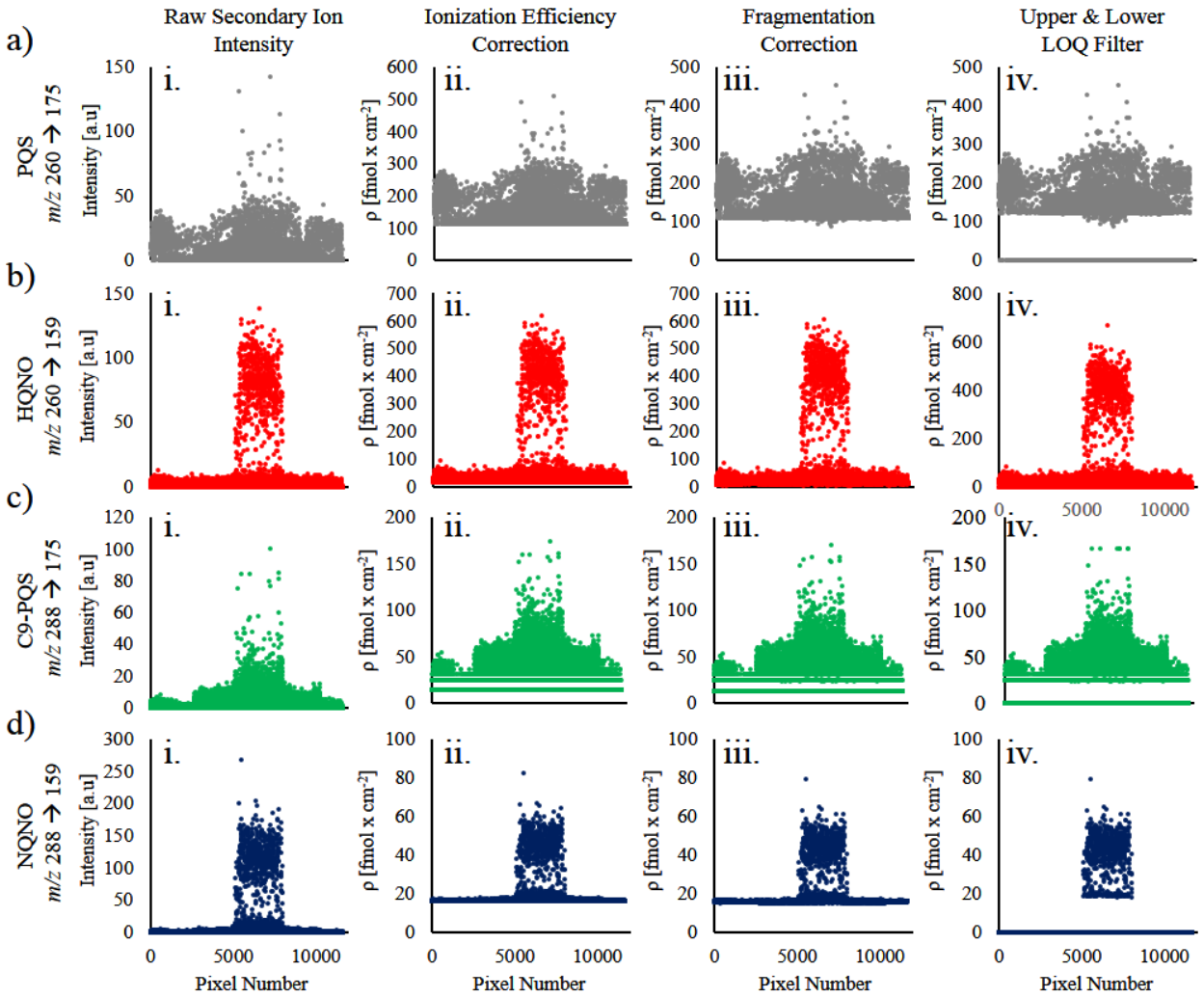

Figure 5.7. Quantitative analysis of (**a**) PQS, (**b**) HQNO, (**c**) C9-PQS, and (**d**) NQNO in the 72 h PAO1C biofilm from **Figure 5.6**. Each dot is a single pixel from the ion image. Column **i** shows the uncorrected (raw) secondary ion intensity; column **ii** is corrected for ionization efficiency; column **iii** is corrected for common (interfering) product ions; and column **iv** shows the ULOQ and LLOQ correction.

and 3.3 μM HQNO after 16 h of *P. aeruginosa* PAO1 planktonic growth in FAB media, a time point that corresponded to the early stationary phase.[66] For 16 h PA14 planktonic culture they measured PQS and HQNO concentrations of 5.0 μM and 6.94 μM respectively.[66] In separate work, Lépine *et al.* measured PQS and HQNO concentrations of 4.8 μM and 11 μM respectively in planktonic cultures of PA14 grown for 8 h in LB.[61]

For the measurements done here, even if we assume that none of the analyte is contained within the bulk of the biofilm, and that the biofilms are 50 μm thick, which would be on the upper end of most estimates,[68] the local concentrations for PQS and HQNO (**Figure 5.6)** are more than 10 times greater than these previous measurement. Examined from a different perspective, the

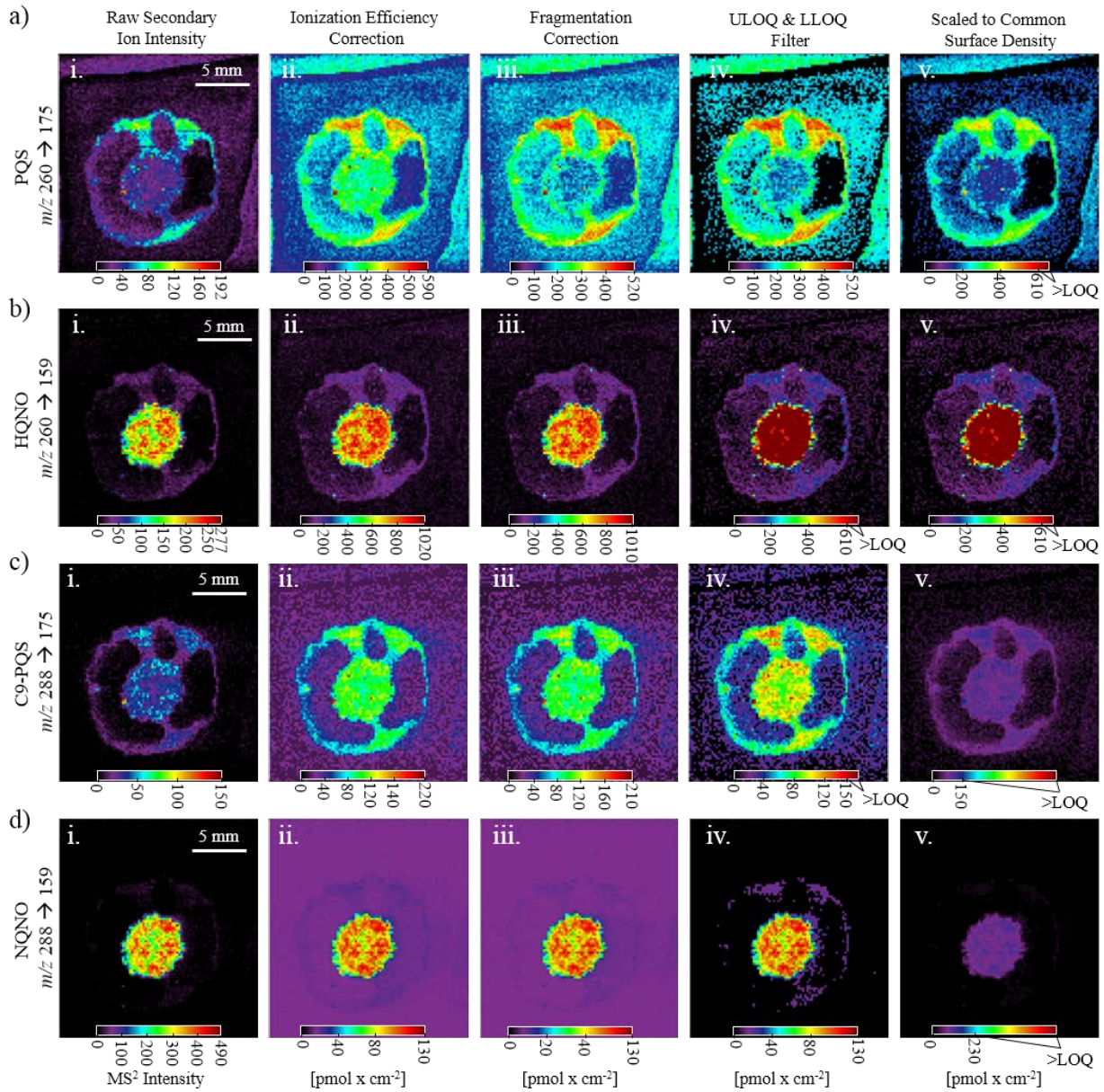

Figure 5.8. Quantitative analysis of (**a**) PQS, (**b**) HQNO, (**c**) C9-PQS, and (**d**) NQNO in a 48 h PAO1C biofilm. Column **i** shows the uncorrected (raw) secondary ion intensity; column **ii** is corrected for ionization efficiency; column **iii** is corrected for common (interfering) product ions; column **iv** shows the ULOQ and LLOQ correction; and images in column **v** are scaled to a common maximum density of 610 pmol x cm^{-2} to facilitate direct and quantitative analyte-to analyte distribution comparisons

average concentrations of PQS and HQNO over the entire area of the biofilm (again assuming a thickness of 50 μm) are 30 μM and 17 μM, respectively, values that are closer to the Lépine measurements.[61, 66] Our quantitative ion images and the calculations performed above do not consider the drying induced contraction of the biofilms, however this factor would only account for a small portion of the concentration disparity. Because of differences in both the specific *P. aeruginosa* strain examined and the cultivation conditions used, it is difficult to make direct

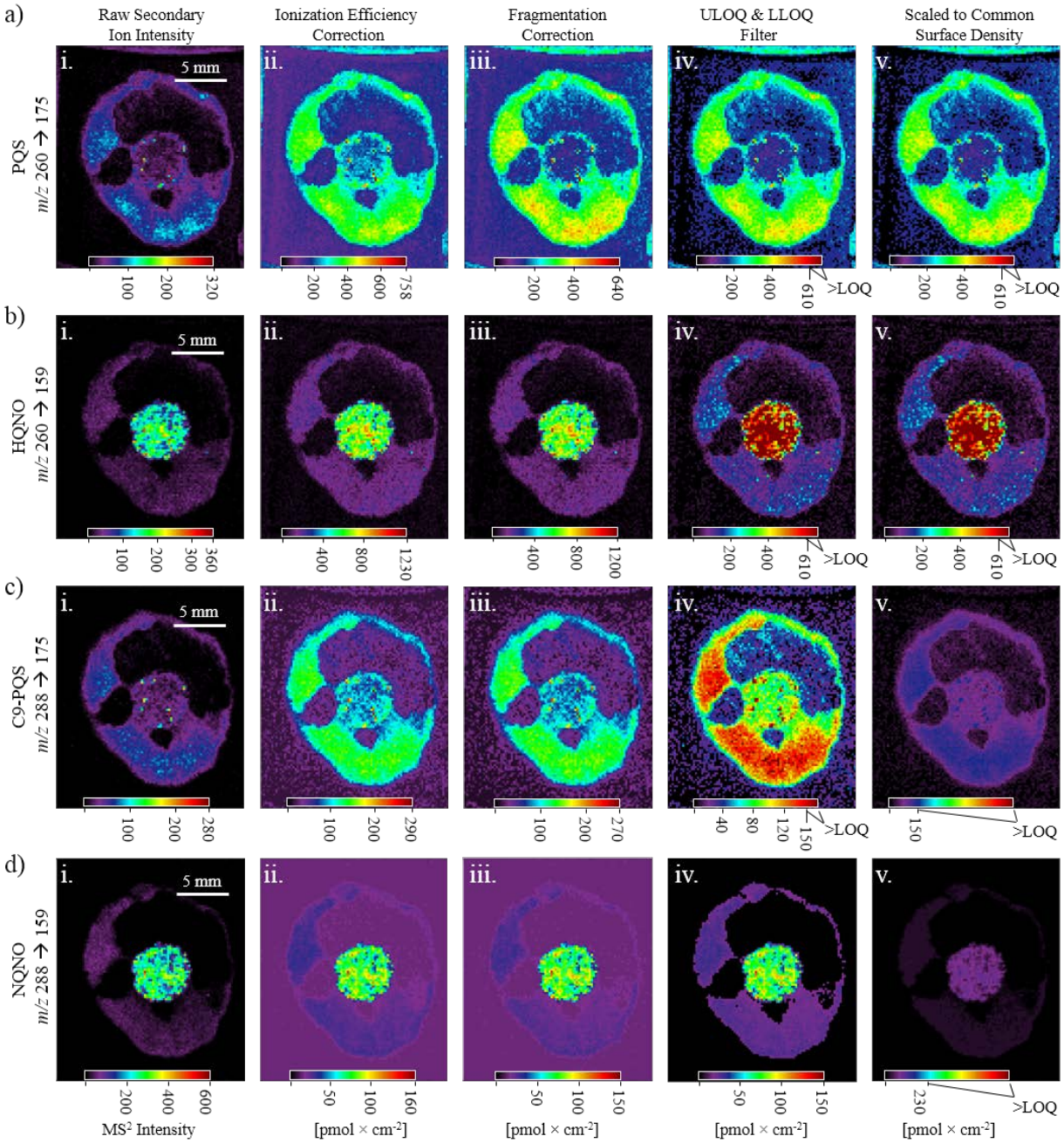

Figure 5.9. Quantitative analysis of (**a**) PQS, (**b**) HQNO, (**c**) C9-PQS, and (**d**) NQNO in a 72 h PAO1C biofilm. Column **i** shows the uncorrected (raw) secondary ion intensity; column **ii** is corrected for ionization efficiency; column **iii** is corrected for common (interfering) product ions; column **iv** shows the ULOQ and LLOQ correction; and images in column **v** are scaled to a common maximum density of 610 pmol x cm^{-2} to facilitate direct and quantitative analyte-to analyte distribution comparisons.

comparisons, however this suggests that the concentration of AQs and AQNOs is much higher in agar-based biofilms than it is in planktonic culture. Furthermore, the large differences in local surface density highlight the importance of performing imaging analyses over bulk measurements,

as the local chemical microenvironment can be very different than an analysis of the bulk might suggest.

5.5. Conclusions

We demonstrate that a simple nitrogen-assisted dehydration is adequate for the preservation of agar-bound microbial communities for SIMS imaging. Although the agar contracts during dehydration, the macroscopic biofilm morphology remains largely unchanged. By following several aggregates through the drying process, it is apparent that the endogenous molecular distribution is also retained, at least for the analytes examined in this study. We also report a method for quantitative SIMS imaging that is capable of correcting for both analyte-specific differences in ionization efficiency and the presence of isomeric interference. This method was applied to image the surface density of two AQs and two AQNOs in *P. aeruginosa* biofilms, and appears effective in such applications.

This work does not fully address several of the remaining challenges for quantitative MSI. First, we did not completely account for spatially dependent variations in ionization efficiency brought on by heterogeneous matrix effects, topography, hardness, conductivity, salt concentration, and other factors.[69-70] These variations in ionization efficiency hinder accurate determination of analyte distribution, and can prohibit the direct comparison of the distribution or intensity of one analyte to others. Here, matrix effects were mitigated by creating calibration curves on agar, but the effects of the local microenvironment have not been accounted for. Second, to construct accurate images, it is necessary to quantitate over a large dynamic range of at least several orders of magnitude. While quadratic and higher order polynomial calibrations improve the dynamic range, meaningful ranges can be difficult to achieve for some analytes. Finally, one of greatest strengths of MSI is its capacity for multiplexed chemical analysis; it is often desirable to examine the distribution of tens or hundreds of compounds in a single image, which would be time consuming to achieve with our methodology. Despite these challenges, we anticipate that this method can be effectively applied to image the surface density of a wide variety of analytes in many different sample types.

5.6. References

1. Vickerman, J. C.; Winograd, N., SIMS—A precursor and partner to contemporary mass spectrometry. *International Journal of Mass Spectrometry* **2015,** *377*, 568-579.
2. Winograd, N., The Magic of Cluster SIMS. *Analytical Chemistry* **2005,** *77* (7), 142 A-149 A.
3. Winograd, N., Imaging Mass Spectrometry on the Nanoscale with Cluster Ion Beams. *Analytical Chemistry* **2015,** *87* (1), 328-333.
4. Fletcher, J. S.; Rabbani, S.; Henderson, A.; Blenkinsopp, P.; Thompson, S. P.; Lockyer, N. P.; Vickerman, J. C., A New Dynamic in Mass Spectral Imaging of Single Biological Cells. *Analytical Chemistry* **2008,** *80* (23), 9058-9064.
5. Carado, A.; Passarelli, M. K.; Kozole, J.; Wingate, J. E.; Winograd, N.; Loboda, A. V., C(60) SIMS with a Hybrid-Quadrupole Orthogonal time-of-flight Mass Spectrometer. *Analytical chemistry* **2008,** *80* (21), 7921-7929.
6. Lanni, E. J.; Dunham, S. J. B.; Nemes, P.; Rubakhin, S. S.; Sweedler, J. V., Biomolecular Imaging with a C60-SIMS/MALDI Dual Ion Source Hybrid Mass Spectrometer: Instrumentation, Matrix Enhancement, and Single Cell Analysis. *Journal of The American Society for Mass Spectrometry* **2014,** *25* (11), 1897-1907.
7. Fisher, G. L.; Bruinen, A. L.; Ogrinc Potočnik, N.; Hammond, J. S.; Bryan, S. R.; Larson, P. E.; Heeren, R. M. A., A New Method and Mass Spectrometer Design for TOF-SIMS Parallel Imaging MS/MS. *Analytical Chemistry* **2016,** *88* (12), 6433-6440.
8. Passarelli, M. K.; Pirkl, A.; Moellers, R.; Grinfeld, D.; Kollmer, F.; Havelund, R.; Newman, C. F.; Marshall, P. S.; Arlinghaus, H.; Alexander, M. R.; West, A.; Horning, S.; Niehuis, E.; Makarov, A.; Dollery, C. T.; Gilmore, I. S., The 3D OrbiSIMS—label-free metabolic imaging with subcellular lateral resolution and high mass-resolving power. *Nature Methods* **2017,** *14*, 1175.
9. Robinson, M. A.; Graham, D. J.; Castner, D. G., ToF-SIMS Depth Profiling of Cells: z-Correction, 3D Imaging, and Sputter Rate of Individual NIH/3T3 Fibroblasts. *Analytical Chemistry* **2012,** *84* (11), 4880-4885.
10. Bloom, A. N.; Tian, H.; Winograd, N., C60-SIMS imaging of nanoparticles within mammalian cells. *Biointerphases* **2015,** *11* (2), 02A306.
11. Tian, H.; Six, D. A.; Krucker, T.; Leeds, J. A.; Winograd, N., Subcellular Chemical Imaging of Antibiotics in Single Bacteria Using C60-Secondary Ion Mass Spectrometry. *Analytical Chemistry* **2017,** *89* (9), 5050-5057.
12. Passarelli, M. K.; Ewing, A. G.; Winograd, N., Single Cell Lipidomics: Characterizing and Imaging Lipids on the Surface of Individual Aplysia Californica Neurons with Cluster SIMS. *Analytical chemistry* **2013,** *85* (4), 10.1021/ac303038j.
13. Monroe, E. B.; Jurchen, J. C.; Lee, J.; Rubakhin, S. S.; Sweedler, J. V., Vitamin E Imaging and Localization in the Neuronal Membrane. *Journal of the American Chemical Society* **2005,** *127* (35), 12152-12153.
14. Baig, N. F.; Dunham, S. J. B.; Morales-Soto, N.; Shrout, J. D.; Sweedler, J. V.; Bohn, P. W., Multimodal chemical imaging of molecular messengers in emerging Pseudomonas aeruginosa bacterial communities. *Analyst* **2015,** *140* (19), 6544-6552.
15. Dunham, S. J. B.; Comi, T. J.; Ko, K.; Li, B.; Baig, N. F.; Morales-Soto, N.; Shrout, J. D.; Bohn, P. W.; Sweedler, J. V., Metal-assisted polyatomic SIMS and laser desorption/ionization for enhanced small molecule imaging of bacterial biofilms. *Biointerphases* **2016,** *11* (2), 02A325.
16. Lanni, E. J.; Masyuko, R. N.; Driscoll, C. M.; Aerts, J. T.; Shrout, J. D.; Bohn, P. W.; Sweedler, J. V., MALDI-guided SIMS: Multiscale imaging of metabolites in bacterial biofilms. *Analytical Chemistry* **2014,** *86* (18), 9139-9145.
17. Lanni, E. J.; Masyuko, R. N.; Driscoll, C. M.; Dunham, S. J. B.; Shrout, J. D.; Bohn, P. W.; Sweedler, J. V., Correlated imaging with C60-SIMS and confocal raman microscopy: Visualization of cell-scale molecular distributions in bacterial biofilms. *Analytical Chemistry* **2014,** *86* (21), 10885-10891.

18. Debois, D.; Hamze, K.; Guérineau, V.; Le Caër, J.-P.; Holland, I. B.; Lopes, P.; Ouazzani, J.; Séror, S. J.; Brunelle, A.; Laprévote, O., In situ localisation and quantification of surfactins in a Bacillus subtilis swarming community by imaging mass spectrometry. *PROTEOMICS* **2008,** *8* (18), 3682-3691.
19. Davies, S. K.; Fearn, S.; Allsopp, L. P.; Harrison, F.; Ware, E.; Diggle, S. P.; Filloux, A.; McPhail, D. S.; Bundy, J. G., Visualizing Antimicrobials in Bacterial Biofilms: Three-Dimensional Biochemical Imaging Using TOF-SIMS. *mSphere* **2017,** *2* (4), e00211-17.
20. Ding, Y.; Zhou, Y.; Yao, J.; Szymanski, C.; Fredrickson, J.; Shi, L.; Cao, B.; Zhu, Z.; Yu, X.-Y., In Situ Molecular Imaging of the Biofilm and Its Matrix. *Analytical Chemistry* **2016,** *88* (22), 11244-11252.
21. Amaya, K. R.; Sweedler, J. V.; Clayton, D. F., Small molecule analysis and imaging of fatty acids in the zebra finch song system using time-of-flight-secondary ion mass spectrometry. *Journal of neurochemistry* **2011,** *118* (4), 499-511.
22. Angerer, T. B.; Dowlatshahi Pour, M.; Malmberg, P.; Fletcher, J. S., Improved Molecular Imaging in Rodent Brain with Time-of-Flight-Secondary Ion Mass Spectrometry Using Gas Cluster Ion Beams and Reactive Vapor Exposure. *Analytical Chemistry* **2015,** *87* (8), 4305-4313.
23. Shon, H. K.; Kim, S. H.; Yoon, S.; Shin, C. Y.; Lee, T. G., Molecular depth profiling on rat brain tissue sections prepared using different sampling methods. *Biointerphases* **2018,** *13* (3), 03b411.
24. Phan, N. T. N.; Fletcher, J. S.; Sjövall, P.; Ewing, A. G., ToF-SIMS imaging of lipids and lipid related compounds in Drosophila brain. *Surface and interface analysis : SIA* **2014,** *46* (Suppl 1), 123-126.
25. Phan, N. T. N.; Munem, M.; Ewing, A. G.; Fletcher, J. S., MS/MS analysis and imaging of lipids across Drosophila brain using secondary ion mass spectrometry. *Analytical and Bioanalytical Chemistry* **2017,** *409* (16), 3923-3932.
26. Philipsen, M. H.; Phan, N. N. T.; Fletcher, J. S.; Malmberg, P.; Ewing, A. G., Mass Spectrometry Imaging Shows Cocaine and Methylphenidate have Opposite Effects on Major Lipids in Drosophila Brain. *ACS Chemical Neuroscience* **2018**.
27. Biteen, J. S.; Blainey, P. C.; Cardon, Z. G.; Chun, M.; Church, G. M.; Dorrestein, P. C.; Fraser, S. E.; Gilbert, J. A.; Jansson, J. K.; Knight, R.; Miller, J. F.; Ozcan, A.; Prather, K. A.; Quake, S. R.; Ruby, E. G.; Silver, P. A.; Taha, S.; van den Engh, G.; Weiss, P. S.; Wong, G. C. L.; Wright, A. T.; Young, T. D., Tools for the Microbiome: Nano and Beyond. *ACS Nano* **2016,** *10* (1), 6-37.
28. Handelsman, J., FACT SHEET: Announcing the National Microbiome Initiative. White House Office of Science and Technology Policy, Ed. https://obamawhitehouse.archives.gov/blog/2016/05/13/announcing-national-microbiome-initiative, 2016.
29. Miller, M. B.; Bassler, B. L., Quorum Sensing in Bacteria. *Annual Review of Microbiology* **2001,** *55* (1), 165-199.
30. Dunham, S. J. B.; Ellis, J. F.; Li, B.; Sweedler, J. V., Mass Spectrometry Imaging of Complex Microbial Communities. *Accounts of Chemical Research* **2017,** *50* (1), 96-104.
31. Li, B.; Comi, T. J.; Si, T.; Dunham, S. J. B.; Sweedler, J. V., A one-step matrix application method for MALDI mass spectrometry imaging of bacterial colony biofilms. *Journal of Mass Spectrometry* **2016,** *51* (11), 1030-1035.
32. Si, T.; Li, B.; Zhang, K.; Xu, Y.; Zhao, H.; Sweedler, J. V., Characterization of Bacillus subtilis Colony Biofilms via Mass Spectrometry and Fluorescence Imaging. *Journal of Proteome Research* **2016**.
33. Yang, J. Y.; Phelan, V. V.; Simkovsky, R.; Watrous, J. D.; Trial, R. M.; Fleming, T. C.; Wenter, R.; Moore, B. S.; Golden, S. S.; Pogliano, K.; Dorrestein, P. C., Primer on Agar-Based Microbial Imaging Mass Spectrometry. *Journal of Bacteriology* **2012,** *194* (22), 6023-6028.
34. Hoffmann, T.; Dorrestein, P. C., Homogeneous Matrix Deposition on Dried Agar for MALDI Imaging Mass Spectrometry of Microbial Cultures. *Journal of The American Society for Mass Spectrometry* **2015,** *26* (11), 1959-1962.
35. Anderton, C. R.; Chu, R. K.; Tolić, N.; Creissen, A.; Paša-Tolić, L., Utilizing a Robotic Sprayer for High Lateral and Mass Resolution MALDI FT-ICR MSI of Microbial Cultures. *Journal of The American Society for Mass Spectrometry* **2016,** *27* (3), 556-559.

36. Angolini, C. F. F.; Vendramini, P. H.; Araújo, F. D. S.; Araújo, W. L.; Augusti, R.; Eberlin, M. N.; de Oliveira, L. G., Direct Protocol for Ambient Mass Spectrometry Imaging on Agar Culture. *Analytical Chemistry* **2015,** *87* (13), 6925-6930.
37. Watrous, J.; Hendricks, N.; Meehan, M.; Dorrestein, P. C., Capturing Bacterial Metabolic Exchange Using Thin Film Desorption Electrospray Ionization-Imaging Mass Spectrometry. *Analytical Chemistry* **2010,** *82* (5), 1598-1600.
38. Nguyen, S. N.; Liyu, A. V.; Chu, R. K.; Anderton, C. R.; Laskin, J., Constant-Distance Mode Nanospray Desorption Electrospray Ionization Mass Spectrometry Imaging of Biological Samples with Complex Topography. *Analytical Chemistry* **2017,** *89* (2), 1131-1137.
39. Komorek, R.; Wei, W.; Yu, X.; Hill, E.; Yao, J.; Zhu, Z.; Yu, X. Y., In Situ Characterization of Shewanella oneidensis MR1 Biofilms by SALVI and ToF-SIMS. *Journal of visualized experiments : JoVE* **2017,** (126), e55944.
40. Lechene, C. P.; Luyten, Y.; McMahon, G.; Distel, D. L., Quantitative Imaging of Nitrogen Fixation by Individual Bacteria Within Animal Cells. *Science* **2007,** *317* (5844), 1563-1566.
41. Popa, R.; Weber, P. K.; Pett-Ridge, J.; Finzi, J. A.; Fallon, S. J.; Hutcheon, I. D.; Nealson, K. H.; Capone, D. G., Carbon and nitrogen fixation and metabolite exchange in and between individual cells of Anabaena oscillarioides. *ISME J* **2007,** *1* (4), 354-360.
42. Groseclose, M. R.; Castellino, S., A Mimetic Tissue Model for the Quantification of Drug Distributions by MALDI Imaging Mass Spectrometry. *Analytical Chemistry* **2013,** *85* (21), 10099-10106.
43. Lanekoff, I.; Stevens, S. L.; Stenzel-Poore, M. P.; Laskin, J., Matrix effects in biological mass spectrometry imaging: identification and compensation. *Analyst* **2014,** *139* (14), 3528-3532.
44. Frisz, J. F.; Lou, K.; Klitzing, H. A.; Hanafin, W. P.; Lizunov, V.; Wilson, R. L.; Carpenter, K. J.; Kim, R.; Hutcheon, I. D.; Zimmerberg, J.; Weber, P. K.; Kraft, M. L., Direct chemical evidence for sphingolipid domains in the plasma membranes of fibroblasts. *Proceedings of the National Academy of Sciences* **2013,** *110* (8), E613–E622.
45. Chumbley, C. W.; Reyzer, M. L.; Allen, J. L.; Marriner, G. A.; Via, L. E.; Barry, C. E.; Caprioli, R. M., Absolute Quantitative MALDI Imaging Mass Spectrometry: A Case of Rifampicin in Liver Tissues. *Analytical Chemistry* **2016,** *88* (4), 2392-2398.
46. Pirman, D. A.; Yost, R. A., Quantitative Tandem Mass Spectrometric Imaging of Endogenous Acetyl-l-carnitine from Piglet Brain Tissue Using an Internal Standard. *Analytical Chemistry* **2011,** *83* (22), 8575-8581.
47. Ohman, D. E.; Chakrabarty, A. M., Genetic mapping of chromosomal determinants for the production of the exopolysaccharide alginate in a Pseudomonas aeruginosa cystic fibrosis isolate. *Infection and Immunity* **1981,** *33* (1), 142-148.
48. Centers for Disease Control and Prevention, Biosafety in Microbiological and Biomedical Laboratories. 5 ed.; U.S. Department of Health and Human Services, Ed. 2009; pp 1-405.
49. Morales-Soto, N.; Anyan, M. E.; Mattingly, A. E.; Madukoma, C. S.; Harvey, C. W.; Alber, M.; Deziel, E.; Kearns, D. B.; Shrout, J. D., Preparation, imaging, and quantification of bacterial surface motility assays. *J. Vis. Exp.* **2015,** (98), doi: 10.3791/52338.
50. Linkert, M.; Rueden, C. T.; Allan, C.; Burel, J.-M.; Moore, W.; Patterson, A.; Loranger, B.; Moore, J.; Neves, C.; MacDonald, D.; Tarkowska, A.; Sticco, C.; Hill, E.; Rossner, M.; Eliceiri, K. W.; Swedlow, J. R., Metadata matters: access to image data in the real world. *The Journal of Cell Biology* **2010,** *189* (5), 777.
51. Rueden, C. T.; Schindelin, J.; Hiner, M. C.; DeZonia, B. E.; Walter, A. E.; Arena, E. T.; Eliceiri, K. W., ImageJ2: ImageJ for the next generation of scientific image data. *BMC Bioinformatics* **2017,** *18* (1), 529.
52. Shard, A. G.; Brewer, P. J.; Green, F. M.; Gilmore, I. S., Measurement of sputtering yields and damage in C60 SIMS depth profiling of model organic materials. *Surface and Interface Analysis* **2007,** *39* (4), 294-298.
53. Cook, E. L.; Krantzman, K. D.; Garrison, B. J., Surface topography effects in C60 bombardment of Si. *Surface and Interface Analysis* **2013,** *45* (1), 93-96.

54. Chambers, M. C.; Maclean, B.; Burke, R.; Amodei, D.; Ruderman, D. L.; Neumann, S.; Gatto, L.; Fischer, B.; Pratt, B.; Egertson, J.; Hoff, K.; Kessner, D.; Tasman, N.; Shulman, N.; Frewen, B.; Baker, T. A.; Brusniak, M.-Y.; Paulse, C.; Creasy, D.; Flashner, L.; Kani, K.; Moulding, C.; Seymour, S. L.; Nuwaysir, L. M.; Lefebvre, B.; Kuhlmann, F.; Roark, J.; Rainer, P.; Detlev, S.; Hemenway, T.; Huhmer, A.; Langridge, J.; Connolly, B.; Chadick, T.; Holly, K.; Eckels, J.; Deutsch, E. W.; Moritz, R. L.; Katz, J. E.; Agus, D. B.; MacCoss, M.; Tabb, D. L.; Mallick, P., A cross-platform toolkit for mass spectrometry and proteomics. *Nat. Biotechnol.* **2012,** *30* (10), 918-920.
55. Race, A. M.; Styles, I. B.; Bunch, J., Inclusive sharing of mass spectrometry imaging data requires a converter for all. *J. Proteomics* **2012,** *75* (16), 5111-5112.
56. Robichaud, G.; Garrard, K. P.; Barry, J. A.; Muddiman, D. C., MSiReader: An Open-Source Interface to View and Analyze High Resolving Power MS Imaging Files on Matlab Platform. *Journal of The American Society for Mass Spectrometry* **2013,** *24* (5), 718-721.
57. Shrout, J. D.; Chopp, D. L.; Just, C. L.; Hentzer, M.; Givskov, M.; Parsek, M. R., The impact of quorum sensing and swarming motility on Pseudomonas aeruginosa biofilm formation is nutritionally conditional. *Molecular microbiology* **2006,** *62* (5), 1264-77.
58. Baig, N. F.; Polisetti, S.; Morales-Soto, N.; Dunham, S. J. B.; Sweedler, J. V.; Shrout, J. D.; Bohn, P. W., Label-free molecular imaging of bacterial communities of the opportunistic pathogen Pseudomonas aeruginosa. *SPIE Proceedings* **2016,** *9930*, 993004-993008.
59. Abdel-Mawgoud, A. M.; Lépine, F.; Déziel, E., Rhamnolipids: diversity of structures, microbial origins and roles. *Applied Microbiology and Biotechnology* **2010,** *86* (5), 1323-1336.
60. Calfee, M. W.; Shelton, J. G.; McCubrey, J. A.; Pesci, E. C., Solubility and Bioactivity of the Pseudomonas Quinolone Signal Are Increased by a Pseudomonas aeruginosa-Produced Surfactant. *Infection and Immunity* **2005,** *73* (2), 878-882.
61. Lépine, F.; Milot, S.; Déziel, E.; He, J.; Rahme, L. G., Electrospray/mass spectrometric identification and analysis of 4-hydroxy-2-alkylquinolines (HAQs) produced by Pseudomonas aeruginosa. *Journal of the American Society for Mass Spectrometry* **2004,** *15* (6), 862-869.
62. Rampioni, G.; Falcone, M.; Heeb, S.; Frangipani, E.; Fletcher, M. P.; Dubern, J.-F.; Visca, P.; Leoni, L.; Cámara, M.; Williams, P., Unravelling the Genome-Wide Contributions of Specific 2-Alkyl-4-Quinolones and PqsE to Quorum Sensing in Pseudomonas aeruginosa. *PLOS Pathogens* **2016,** *12* (11), e1006029.
63. Kogut, M.; Lightbown, J. W., Selective inhibition by 2-heptyl-4-hydroxyquinoline N-oxide of certain oxidation–reduction reactions. *Biochemical Journal* **1962,** *84* (2), 368-382.
64. Szamosvári, D.; Böttcher, T., An Unsaturated Quinolone N-Oxide of Pseudomonas aeruginosa Modulates Growth and Virulence of Staphylococcus aureus. *Angewandte Chemie International Edition* **2017,** *56* (25), 7271-7275.
65. Fletcher, M. P.; Heeb, S.; Chhabra, S. R.; Diggle, S. P.; Williams, P.; Cámara, M., 2-Alkyl-4(1H)-Quinolone Signalling in Pseudomonas aeruginosa. In *Pseudomonas: Volume 6: Molecular Microbiology, Infection and Biodiversity*, Ramos, J. L.; Filloux, A., Eds. Springer Netherlands: Dordrecht, 2010; pp 29-57.
66. Lépine, F.; Déziel, E.; Milot, S.; Rahme, L. G., A stable isotope dilution assay for the quantification of the Pseudomonas quinolone signal in Pseudomonas aeruginosa cultures. *Biochimica et Biophysica Acta (BBA) - General Subjects* **2003,** *1622* (1), 36-41.
67. US Environmental Protection Agency, *SW-846 Test Method 8000D: Determinative Chromatographic Separations*. 2014; Vol. 441 K, p 1-57.
68. Chopp, D. L.; Kirisits, M. J.; Moran, B.; Parsek, M. R., The dependence of quorum sensing on the depth of a growing biofilm. *Bulletin of Mathematical Biology* **2003,** *65* (6), 1053-1079.
69. Chughtai, K.; Heeren, R. M. A., Mass Spectrometric Imaging for Biomedical Tissue Analysis. *Chemical Reviews* **2010,** *110* (5), 3237-3277.
70. Heeren, R. M. A.; Smith, D. F.; Stauber, J.; Kükrer-Kaletas, B.; MacAleese, L., Imaging Mass Spectrometry: Hype or Hope? *Journal of the American Society for Mass Spectrometry* **2009,** *20* (6), 1006-1014.

CHAPTER 6

Method for Evaluating Heterogeneous Ionization Efficiency in Biomolecular Mass Spectrometry Imaging

6.1. Acknowledgements

This chapter has been adapted from a manuscript that, as of March 30th, 2018, is in preparation for submission to a peer-reviewed scientific journal. Co-authors include Sage J. B. Dunham, Joseph F. Ellis, Robert J. Mowery, Nameera F. Baig, Tianyuan Cao, Nydia Morales-Soto, Joshua D. Shrout, Paul W. Bohn, and Jonathan V. Sweedler. SJBD planned experiments, composed the manuscript, analyzed data, and performed experiments, including SIMS imaging, SEM, and stylus profilometry. JFE helped to plan and perform experiments (including most of the chemical inkjet printing), and helped with data analysis and manuscript composition. RJM helped to collect and analyze data. NFB and TC cultivated the biofilms and helped to plan experiments. NMS, JDS, PWB, and JVS helped to plan experiments, interpret the data, and compose the manuscript. The authors acknowledge intellectual contributions from Stephanie Lozano, Dr. Amit Patel, Kisurb Choe, Dr. Bin Li, and Dr. Troy Comi. We also thank Dr. Leilei Yin for help with stylus profilometry, as well as Alex David Jarez Roman and Travis Ross for assistance with 3-D structured light scanning. Funding for this research was provided through the National Institutes of Health under Awards R01 AI113219 and U01 MH109062. SJBD and JFE receive financial support from the Springborn Endowment, and SJBD is partially funded through the NSF Graduate Research Fellowship Program. This work was conducted, in part, at the Microscopy Suite of the Beckman Institute for Advanced Science and Technology at the University of Illinois at Urbana-Champaign (UIUC-BI-MS).

6.2. Introduction

Due to the broad chemical coverage, high analyte specificity, and the innate capacity for molecular discovery, mass spectrometry imaging (MSI) is widely used throughout much of the life sciences, including in microbiology,[1-2] neuroscience,[3] pharmacology,[4-6] forensics,[7] and food science.[8] Matrix assisted laser desorption ionization (MALDI) remains the most used MSI ionization modality,

however secondary ion mass spectrometry (SIMS), desorption electrospray ionization (DESI), and several other techniques are also widely applied.[9] Despite the wide utilization of MSI, several challenges impede realization of the techniques full potential, especially on the clinical front. One significant challenge is the presence of regiospecific variations in ionization efficiency, which can be caused by heterogeneous matrix effects, uneven salt content, sample topography, conductivity, sample hardness, and many other factors.[10] Position-dependent variations in ion suppression or enhancement have been recognized and studied for at least four decades,[11-12] and have recently been examined in great depth.[10, 13-19] Studies such as these have led many MSI practitioners to come to the troubling conclusion that *the intensity and distribution shown in an ion image may not accurately represent the genuine abundance and localization of the target analyte*.

In recognition of this, molecular distributions generated via MSI are commonly validated with more established analytical approaches, such as liquid chromatography-mass spectrometry (LC-MS).[15, 20-22] Avoiding the desorption/ionization approach altogether, Richard Smith and coworkers pioneered "mass spectrometry voxelation", in which the samples are sectioned into cubes and subjected to quantitative LC-MS to produce three-dimensional molecular maps.[23-25] This voxelation strategy is conceptually similar to the "molecular cartography" approach employed by Dorrestein and coworkers to map the chemical environment of human skin,[26] human habitats,[27-28] and plants.[29] Recently, innovative instrumentation has been developed that utilizes either laser ablation[30-31] or a liquid microjuntion[32-33] to extract specific sample components for analysis, thus circumventing many of the common issues with MSI signal variability. It is also common to compliment MSI with other *in situ* chemical imaging methods, such as confocal Raman microscopy,[34-39] infrared spectroscopy,[39-40] fluorescence imaging,[41-42] nuclear magnetic resonance,[43] or immunohistochemistry.[44-45] Multimodal imaging with a focus on MSI has been reviewed by Masyuko et al.[46] and Buchberger et al.[9]

Many of the aforementioned studies demonstrate that molecular distributions established through MSI can be quantitative, however secondary verification is still necessary – especially when examining novel analytes or sample types. To overcome the need for secondary verification, researchers have worked to develop sample treatment, data collection, or data normalization methodologies that eliminate regiospecific variations in ionization efficiency. One strategy is to separate the analytes from the sample entirely through imprint transfer to an amenable surface, such as

a silicon wafer. Imprint transfer MSI has produced high-quality ion images with MALDI,[22, 47] DESI,[48] and SIMS imaging.[49]

Specifically for DESI, improved results can be obtained by adding standards directly to the extraction solvent.[50] For MALDI imaging of proteins and peptides, it is common practice to remove ion suppressing compounds such as lipids and salts prior to imaging,[42, 51] however this treatment can result in the delocalization or removal of many small molecules and is incompatible with fragile or high water-content samples. It is also common to correct for regiospecific variations in ionization efficiency by normalizing the analyte signal to an exogenous standard, either applied underneath the tissue,[45, 52-53] over the tissue,[13, 19, 53-54] or as a component of the matrix.[13, 21, 55-56] A careful study of all three application strategies showed that, for results that best mimic the *in vivo* molecular dynamics, the standard should be applied on top of the sample prior to matrix deposition.[57]

Extending the internal standard normalization procedures described above, Hamm et al. developed an simple parameter for evaluating regiospecific ion suppression, which is dubbed the "tissue extinction coefficient" (TEC).[58] For a given analyte, the TEC is calculated by dividing the average ion intensity of an exogenously applied standard in a region of interest by the average ion intensity of that same standard in a control sample (e.g. an ITO glass slide). In addition to providing a regiospecific measurement of ion suppression, the TEC enables quantitation in multiple sample environments using a single external calibration curve. In their initial study, which sought to quantitatively image the distribution of two pharmaceutical compounds across whole-rat sections, Hamm et al. found TEC values that ranged from 0.07 to 0.38 for brain and stomach tissue respectively.[58] In an extension of this work, Taylor et al. applied the TEC concept in combination with image segmentation to explore regiospecific ion suppression in mouse brain with both MALDI and DESI imaging.[10] Among other findings, this work showed that TEC normalization outperforms many other published data normalization methods for correcting heterogeneous ion suppression.[10]

Homogeneous application of an exogenous standard layer can be challenging for samples with large variations in surface morphology or chemical composition, and this difficulty is exacerbated for SIMS due to the surface sensitivity of the technique. For SIMS imaging, researchers have historically sputtered biological samples with 1-3 nm of gold or silver to mitigate the effects of sample charging and reduce matrix effects.[59-60] This process can be difficult to implement in

practice, as the effectiveness is analyte, ion beam, and sample specific.[60] Also challenging, some compounds preferentially migrate to accessible regions of the sample during dehydration or matrix application, which can produce image inaccuracies.[61] For example cholesterol, which is known to broadly suppress ionization in some sample types (e.g. brain and spinal cord), preferentially partitions to the tissue surface after cryosectioning. In one innovative approach, researchers removed the enriched cholesterol and enhance ionization of other analytes through extended exposure to trifluoroacetic acid vapor.[62]

The aforementioned strategies can be used to mitigate or circumvent regiospecific variations in ionization efficiency, and more research is clearly warranted on this front. To aid in this effort, we present a microdroplet-array method for detecting and evaluating heterogeneous ionization. Using a chemical inkjet printer, a standard array is deposited across the sample and, following MSI, this array is utilized: (1) to investigate regiospecific variations in ionization efficiency, (2) as a fiducial system for multimodal chemical and morphological characterization of ion suppression, and (3) to evaluate the efficacy of different data normalization and data collection strategies. In practice this microdroplet array methodology is similar to the nanoparticle fiducial system for correlated imaging developed by Lanni et al.,[34] however here the droplets contain analytical standards (not nanoparticles) and the focus is on exploring differences in ionization efficiency. In other similar work microdroplet arrays have been used for regiospecific quantitation with MALDI,[57] SIMS,[63] and DESI.[63] Due to the availability of specific genetic knockouts and our own familiarity with this model, we chose to demonstrate this method on agar-based *Pseudomonas aeruginosa* biofilms, and the majority of the work is performed with time-of-flight (ToF)-SIMS, however the described method is not limited to this sample type or ionization modality.

6.3. Experimental

6.3.1. Materials and Reagents

LC-MS grade methanol, ethanol, 9-aminoacridine (9-AA), 2-heptyl-4-quinolone (HHQ) and 2-heptyl-3-hydroxy-4(1H)-quinolone (also known as "*Pseudomonas* quinolone signal" or PQS) were acquired from Sigma-Aldrich (St Louis, MO). 2-heptyl-4-hydroxyquinoline *N*-oxide (HQNO), 2-nonyl-4-hydroxyquinoline *N*-oxide (NQNO), 2-nonyl-4-quinolone (NHQ), and 2-nonyl-3-hydroxy-4(1H)-quinolone (C9-PQS) were purchased from Cayman Chemical (Ann Arbor, MI). All standards were acquired at 96% purity or better and used without further purification.

Custom aluminum sample plates were machined in the University of Illinois School of Chemical Sciences' Machine Shop, and double sided conductive copper tape, 3M 1182, was purchased from Ted Pella, Inc. (Redding, CA).

6.3.2. Colony Biofilm Cultivation and Preparation for SIMS Imaging

A detailed procedure for cultivating and preserving biofilms for SIMS imaging is provided in other work.[64] *P. aeruginosa* strains PAO1C,[65] PA14,[66] FRD1,[67] and PQSA^{-}[68] were cultured for 18 h at 37 ºC in a modified fastidious anaerobic broth (FAB) culture medium containing 30 mM filter-sterilized glucose. Solid growth medium was prepared by aliquoting 7.5 mL sterile FAB-noble agar (with 12 mM glucose) into 60 mm diameter Petri dishes. The growth medium was inoculated with 5 μL planktonic cell culture (OD_{600} = 1) and incubated at 37 ºC for 72 h. The PAO1C and FRD1 co-culture sample was prepared as above except 5 μL of each culture was deposited on the same agar plate at a distance of 1 cm. The biofilms and the underlying agar were transferred to SIMS sample plates containing double-sided copper tape and allowed to dehydrate under a gentle stream of nitrogen. The samples were stored in a positive pressure nitrogen dry box until further processing or SIMS analysis. All experiments, including biofilm cultivation, processing, and other handling, were performed in accordance with institutional and CDC guidelines. This included the use personal protective equipment, the application of aseptic techniques, and the use of appropriate sterilization procedures for the biosafety level of the organism.[69]

6.3.3. Chemical Printing

Pooled standard solutions containing either: (1) 500 μM HHQ and 250 μM 9-AA; (2) 250 μM each HHQ, PQS, and NQNO; or (3) 250 μM each of NHQ, C9-PQS and HQNO were prepared in 50% methanol (50% water, v/v). The solutions were deposited on dehydrated samples using a chemical inkjet printer (CHIP 1000, Shimadzu Corp., Kyoto, Japan) in multi-pass iterative mode with a spot-to-spot spacing of 1 mm. Each spot was generated from ten 100 pL droplets. The dwell voltage and dwell time were set to 25 V and 35 μs respectively and adjusted as required to maintain a stable drop profile.

6.3.4. SIMS and SIMS Tandem-MS Imaging

SIMS experiments were performed with a custom hybrid ToF imaging mass spectrometer described previously.[70] This instrument is a modified AB-SCIEX QSTAR XL (Framingham, MA) equipped with a Buckminsterfullerene (C_{60}) primary ion beam (Ionoptika Ltd., Hampshire, UK). The ion source was adjusted to produce 20 keV C_{60}^{+} primary ions at a spot size of 35 μm and 500

pA sample current. SIMS imaging was performed in positive secondary ion mode with the "slowest" raster setting (490 ms per pixel), a pixel size of 100 μm × 100 μm, and a mass range of *m/z* 60-850 (Q1 bias of 15%, 25% and 60% at *m/z* 100, 200, and 400 respectively). The approximate primary ion dose was 4 x 10^{13}. Mass calibration was performed to indium cluster ions.

Tandem-MS imaging was performed for product of *m/z* 260 with unit precursor mass resolution and "Enhance All" mode activated to selectively enhance transmission of product ions from *m/z* 60-265 (Q1 bias of 5%, 47.5% and 47.5% at *m/z* 40, 90, and 180 respectively). Collision induced disassociation (CID) was performed in argon at 30 eV. Other settings were set as described above. In cases were the sample was imaged multiple times, the image area was vertically offset by 25 μm to obtain a mostly unperturbed sampling area. *In situ* tandem-MS identification of AQs, AQNOs, and rhamnolipids was performed elsewhere.[34, 37, 60]

6.3.5. SIMS Data Analysis

The native AB SCIEX wiff data files were collected in Analyst v1.2 and oMALDI Server v5.1 (AB SCIEX), converted to mzML with the ProteoWizard msconvert function,[71] and to imzML using imzMLConverter.[72] The resulting imzML files were rendered in MSiReader v0.09[73] or v1.0[74] using a bin size of *m/z* 0.1 ("sum of window") and second order linear interpolation. The data used for quantitative spot-to-spot intensity comparisons and 3D color plots was gathered using the MSiReader ROI export tool with a constant area of 0.42 mm and processed in Microsoft Excel and Origin 2018. Imaging principal component analysis was performed in MATLAB (MathWorks, Natick, MA) using a custom script that incorporates the Statistics and Machine Learning Toolbox.

6.3.6. Scanning Electron Microscopy

Dehydrated samples were coated with Au/Pd using a Desk II sputter coater (Denton Vacuum, Moorestown, NJ), operated for 70 s with 64 mTorr Ar and a 40 mA current. Metalized samples were subsequently evaluated with a field-emission environmental scanning electron microscope (Philips XL30 ESEM-FEG, Hillsboro, OR). Secondary electrons were collected under high-vacuum conditions at 5 kV with a working distance of 5 mm.

6.3.7. 3-D Structured Light Scanning

A dehydrated co-culture sample was imaged with a Steinbichler Comet L3D 2M structured light scanner (Carl Zeiss Optotechnik GmbH, Neubeuern, Germany). The 100 mm volume setting was used, which provides a maximum resolution of 60 μm in each dimensions. The raw data was au-

tomatically parsed into a curvature based decimation algorithm and exported for downstream processing. The resulting ".stl" file was rendered in Maya (Autodesk, San Rafael, CA) to create the elevation profiles, and image overlays were performed in Photoshop (Adobe Systems, San Jose, CA).

6.3.8. Stylus Profilometry

The same dehydrated co-culture sample from above was examined with a stylus profiler (KLA-Tencor P-6, Milpitas, California), at a horizontal resolution of 10 μm and a raster width of 100 μm. The resulting data were processed in Microsoft Excel (Redmond, WA) and heat maps were rendered in Origin 2018 (Northampton, MA). Local surface roughness was calculated as the average absolute value of the deviation from the average height in a 1 mm square surrounding each spot. The horizontal resolution was down-sampled to 100 μm prior to calculation of surface roughness.

6.4. Result and Discussion

6.4.1 Application of the Microdroplet Array to Investigate Regiospecific Variations in Ionization Efficiency in *P. aeruginosa* Colony Biofilms

As is the case for many biological samples, biofilms represent a complex system for MSI, with both morphological and chemical variability. The biofilm extracellular polymeric substance (EPS) is a heterogeneous matrix of polysaccharides, proteins, nucleic acids, membrane vesicles, salts, and a wide assortment of small molecules, which can induce local ion suppression or enhancement.[75] Additional challenges are levied by changes in morphology. The EPS creates a heterogeneous structural scaffolding laced by open channels formed by rhamnolipid biosurfactants,[76] and bacteria are known to form towers of cells during late phases of biofilm development.[77] Although it is well known that differences in the sample microenvironment can obscure the endogenous intensity and distribution of biomolecules,[78] a stringent evaluation of this phenomenon is still needed for microbial samples.

We focused our work on several well-characterized molecules used by *P. aeruginosa* for cell-to-cell signaling and colony defense, namely molecules from the 2-alkyl-4(1H)-quinolone (AQ) and 2-alkyl-4-hydroxyquinoline *N*-oxide (AQNO) classes. Molecules within these classes differ by the length and saturation of the alkyl side chain, and the location or presence of hydroxyl or *N*-oxide functional groups. For more information on AQs and AQNOs produced by *P. aeruginosa* see the following review.[79]

To evaluate ionization homogeneity we deposited an array of standard spots across a PA14 biofilm with a spot-to-spot spacing of 1 mm. Each spot contained 500 fmol of HHQ and 250 fmol 9-AA, a common matrix for MALDI that also ionizes well under C_{60}^+ bombardment. Under ideal conditions the signal arising from each spot would exhibit uniform intensities within the uncertainties defined by the deposition process and the measurement precision. As can be seen in the ion image and 3-D false color plot for the protonated molecular ion of 9-AA (*m/z* 195.07) (**Figures 6.1a** and **6.1b**), substantial spot-to-spot intensity variations are present, with a measured coefficient of variation (CV or relative standard deviation) of 66%. The highest intensity is observed at the edge of the agar and strong ion suppression arises in regions that contain the microbial colony. A distinct suppression ring is also present at the biofilm perimeter. The elevated *m/z* 195.07 signal found at the sample center is the result of isobaric interference and should be discounted.

The PA14 biofilm is a complicated sample where any number of factors could combine to produce the observed variations in ionization. For example, many ions either exist at the center of the biofilm (AQs and AQNOs), reside primarily within the region of suppression (e.g. multiple unidentified ions including *m/z* 435.25 and *m/z* 437.25), or are found more uniformly throughout the agar (e.g. rhamnolipids and agar-specific ions). The isobaric interference is also challenging to overcome without isotopically labeled internal standards or an ultra-high-resolution mass analyzer. Therefore, to simplify the chemistry and morphology, we cultivated a biofilm from a *P. aeruginosa* strain ($pqsA^-$) that harbors a mutation to the pqsA operon, which is required for biosynthesis of AQs and AQNOs. Removal of the pqsA operon not only prevents the production of AQs and AQNOs, but also halts downstream gene expression and metabolite production and results in a much flatter and more homogeneous colony biofilm. For this study, we deposited two separate standard AQNO and AQ grids across the sample. To minimize isomeric interference, one mixture contained 250 μM each of HHQ, PQS, and NQNO, and a second contained 250 μM each of NHQ, C_9-PQS, and HQNO. Each spot in the grid therefore contained 250 fmol of each analyte in the corresponding mixture.

As can be seen in the ion image and 3-D false color plot (**Figures 6.1c** and **6.1d**) for the protonated molecular ion of HHQ (*m/z* 244.17), the ion intensity is highest at the sample periphery. There is a gradual decrease moving from the agar edge towards the biofilm boundary, where a sharp region of suppression is present. After this initial suppression region is passed, the ion inten-

sity rises and plateaus at a value approximately 1/3 of that seen at the agar edge. Despite the obvious visual improvement in the ion image for HHQ in the pqsA$^-$ sample (**Figure 6.1c**) in comparison to the ion image for 9-AA in the PA14 sample (**Figure 6.1a**), the overall spot-to-spot variability was still high (CV = 70%). More variability was observed at the sample periphery (CV = 60%) versus the center (CV = 20%). Examination of the ion images corresponding to the other four standards showed similar trends, suggesting that the ionization efficiency patterns shown in **Figure 6.1c** are universal for the six analytes examined here. Analogous analyses were performed on two other pqsA$^-$ biofilms and both exhibited ionization trends similar to that shown in **Figure 6.1c**.

Also of note, rhamnolipids are partially absent from the interior region in the PA14 sample (**Figure 6.1e**), but found in high abundance at the center of the pqsA$^-$ sample (**Figure 6.1f**). While the substantial genetic and phenotypic differences between these two strains prevents a direct comparison, there is a strong visual correlation between the 9-AA suppression zone and the region devoid of rhamnolipids in the PA14 sample. Furthermore, both gene expression[76] and lipid staining[80] studies of similar *P. aeruginosa* strains show rhamnolipids to be expressed in regions of high cell density, which is a feature of the central region of these biofilms.

To simplify the analysis further, the AQ and AQNO mixtures were deposited across a section of blank agar. A representative ion image for HHQ is provided in **Figure 6.1g**, and a 3-D false color plot is provided in **Figure 6.1h**. The ion intensity for exogenous HHQ is greatest near the top of the agar, falls sharply over the first 4 mm of the sample, and plateaus into a steady state near the lower 14 mm of the image. A spot-to-spot CV of 16% was observed for the full image, however omitting the first four rows of the array reduces this variability to 11%. This variation is attributable to both changes in instrument performance (e.g. quadrupole charging) and poor charge dissipation near the sample center. Similar variability trends were observed for the other five analytes examined here, with CV values of 16%, 28%, 38%, 18%, and 20% for PQS, NQNO, HQNO, NHQ, and C9-PQS respectively

The combined results shown in **Figure 6.1** highlight the difficulty in determining: (1) if a perceived ion intensity actually arises from the analyte of interest or if it is a manifestation of isobaric interference; and (2) if intensity variations arise from differences in concentration or differences in the local ionization efficiency. Despite the significant chemical and morphological simplification of the pqsA$^-$ mutant, variations in signal still exist. In both the PA14 and pqsA$^-$ biofilms these variations manifest as a ring of ion suppression at the biofilm boundary. Both ion suppression

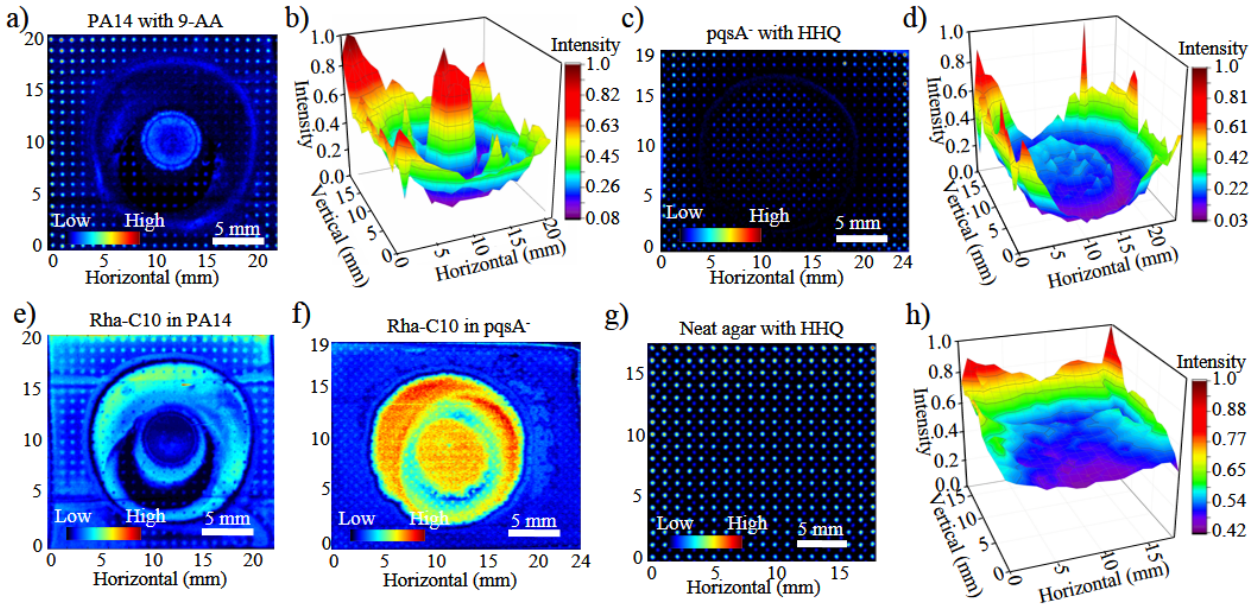

Figure 6.1. Evaluation of ion suppression in *P. aeruginosa* biofilms using the microdroplet array approach. Ion images and false color maps corresponding to (**a**–**b**) 250 fmol 9-AA (*m/z* 195.07) spotted on a PA14 biofilm in a 1 mm grid, and (**c**–**d**) exogenous HHQ (*m/z* 244.17) in a pqsA- biofilm containing 250 fmol spots of AQs and AQNOs deposited in staggered 1 mm grids. Ion images for a representative rhamnolipid, Rha-C10, in (**e**) PA14 and (**f**) pqsA$^-$ colony biofilms. Ion images and false color maps corresponding to (**g**–**h**) HHQ from FAB agar containing 250 fmol spots of AQs and AQNOs in a staggered 1 mm grid. Spots from regions outside of the sample area of **c** were omitted from the 3D color map for clarity.

and isobaric interference are present near the initial inoculation region (center) of the PA14 biofilm. Changes in ionization efficiency are also observed for the microdroplet array deposited on blank agar, however these changes are relatively small and are largely attributable to changes in instrument performance. The exposure of pervasive, spatially-depended variations in ionization efficiency highlights the need for routine evaluations of ion image veracity, and demonstrates the utility of this microdroplet array approach for performing these evaluations.

6.4.2. Utilization of the Microdroplet Array as a Fiducial System for Multimodal Chemical and Morphological Characterization of Ion Suppression

The distinct patterning of the pqsA$^-$ biofilm suppression offered a unique opportunity to investigate the origins of the ion suppression in greater depth. We first set out to establish if there was a relationship between fine-scale sample morphology and the signal arising from the deposited standards. A selected region of the ion image for exogenous NHQ (*m/z* 272.20) in the pqsA$^-$ biofilm from **Figure 6.1b** is provided in **Figure 6.2a**. This region contains four columns (C9-C12) and 10 rows (R1-R10) with spots outside, within, and interior to the ring of suppression. The four spots in Row 4 (R4) are within the ring of suppression and almost invisible in this ion image.

Representative electron micrographs for three regions, as indicated by the white box in **Figure 6.2a**, are given in **Figure 6.2b**. The first region (**Figure 6.2bi – iii**) corresponds to a spot lying outside of the suppression ring, the second region (**Figure 6.2biv – vi**) corresponds to a spot directly within the suppression zone, and the third region (**Figure 6.2bvii – ix**) corresponds to a

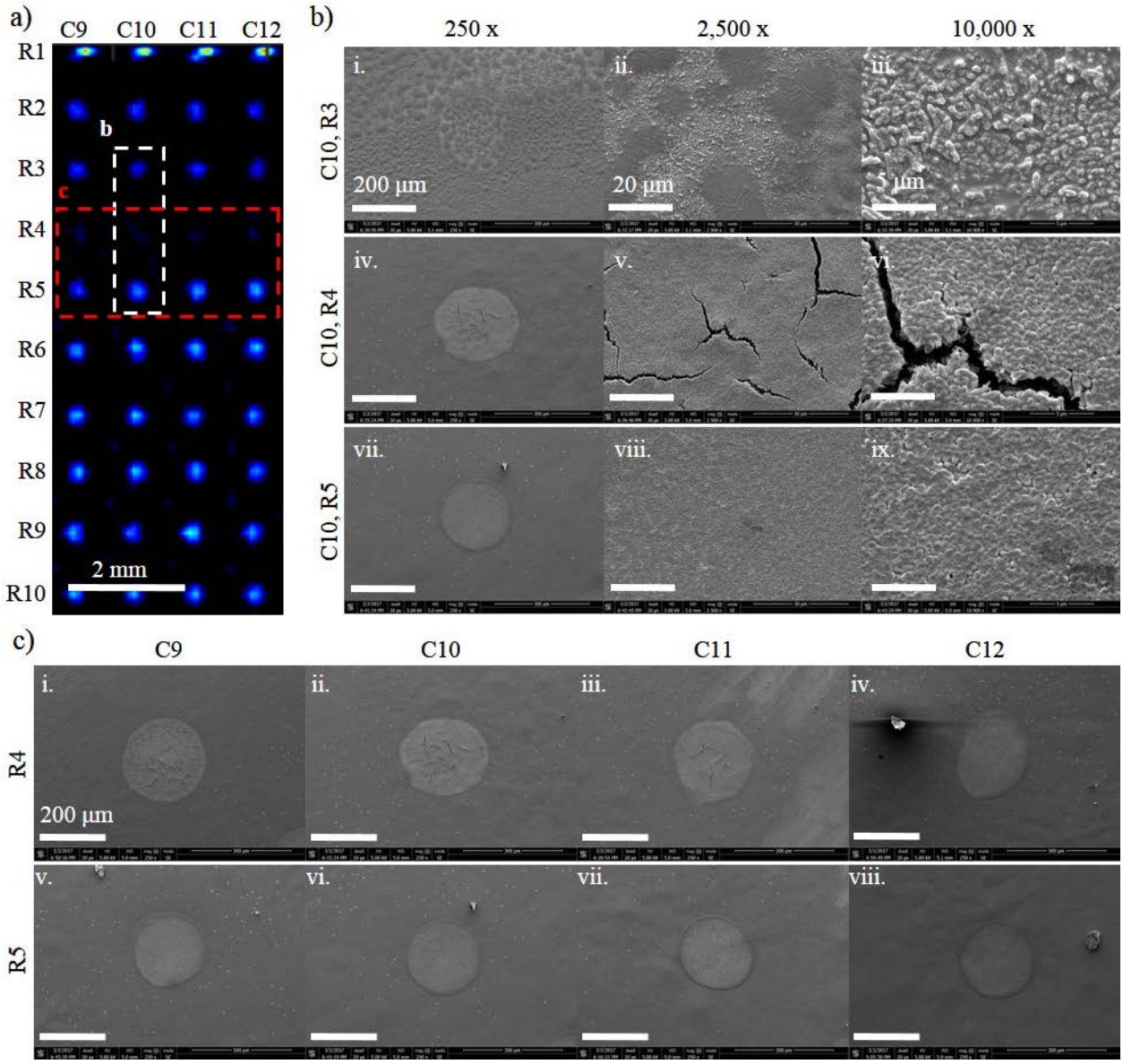

Figure 6.2. Investigations of ion suppression in the *P. aeruginosa* pqsA- biofilm from **Figure 6.1**. (**a**) SIMS image of exogenous NHQ (*m/z* 272.20). The white and red boxes outline the spots analyzed in **b** and **c** respectively. (**b**) Electron micrographs at a magnification of 250, 2,500, and 10,000 × acquired from three adjacent regions containing deposited standards: (**i**–**iii**) region outside of the biofilm with high SIMS signal intensity; (**iv**–**vii**) region at the biofilm boundary with low signal intensity; and (**vii**–**ix)** region inside the biofilm with high signal intensity. (**c**) Replicate electron micrographs for spots contained within (**i**–**iv**) and interior to (**v**–**viii**) the suppression zone. Scale bars represent 2 mm in a, 200 µm in **bi**, **biv**, **bvii**, and **ci**–**viii**, 20 µm in **bii**, **bv**, and **biii**, and 5 µm in **biii**, **bvi**, and **bix**.

spot interior to the suppression zone. Three key observations can be made from these micrographs. First, the suppression zone directly aligns with the beginning of the biofilm. Within and interior to the suppression ring cells are prolific and densely packed (**Figures 6.2bvi** and **6.2bix**), and outside the ring the cells become increasingly sparse (**Figure 6.2bviii**). Second, aside from the presence morphological difference is the formation of cracks exclusively on the surface of those micro-droplets residing within the suppression zone (**Figure 6.2bv**). Cracking is not observed for spots deposited on the biofilm surface (**Figure 6.2bviii**) or the surrounding agar (**Figure 6.2bii**). Third, measurements of representative spots (as outlined in red in **Figure 6.2a**) reveals that the deposited standards within the suppression zone have a larger area than those interior to the suppression zone. Measurement of several replicate spots within and interior to the suppression zone (Rows 4 and 5, **Figure 6.2c**) yield average areas of 5.1×10^4 μm^2 (± 2% SD, n = 4) and 4.2×10^4 μm^2 (± 2% SD, n = 4) respectively, representing a 17% difference ($p = 3 \times 10^{-5}$).

Investigations into crack formation during droplet deposition have found surface wettability to be a contributing factor. For example, Ghosh and coworkers deposited aqueous colloidal suspensions on functionalized glass substrates with variable wetting properties, and found that both the number of cracks and the crack propagation velocity increases with increasing hydrophilicity.[81] Therefore, in combination with the increases in droplet area, the presence of cracks suggest that the suppression area has a different hydrophobicity than the surrounding region. Importantly, the electron micrographs in **Figure 6.2** suggest that the surface structure in the suppression zone is similar to that of the surrounding regions, therefore this change in hydrophobicity likely arises from chemical, not morphological, properties of the surface.

The observed differences in hydrophobicity led us to search for a chemical origin to the ion suppression. We applied imaging principal component analysis (PCA) and manual data inspection to evaluate SIMS imaging data collected from the pqsA$^-$ biofilm (**Figure 6.3a-c**), and found several ions to be either exclusive to – or at much higher abundance in – the ring of suppression. Several ions – including *m/z* 415.25, 435.25, 437.25, 463.25, and 480.25 – fit this profile, with *m/z* 437.25 present in the greatest abundance.

Ion image for exogenous HHQ and endogenous *m/z* 437.25 in the pqsA- biofilm is provided in **Figure 6.4a**. An RGB colocalization plot showing exogenous NHQ (red), exogenous HHQ (green), and endogenous *m/z* 437.25 (blue) is also given in **Figure 6.4a**. The RGB colocalization plot shows that regions with high *m/z* 437.25 abundance precisely correlate with the suppression

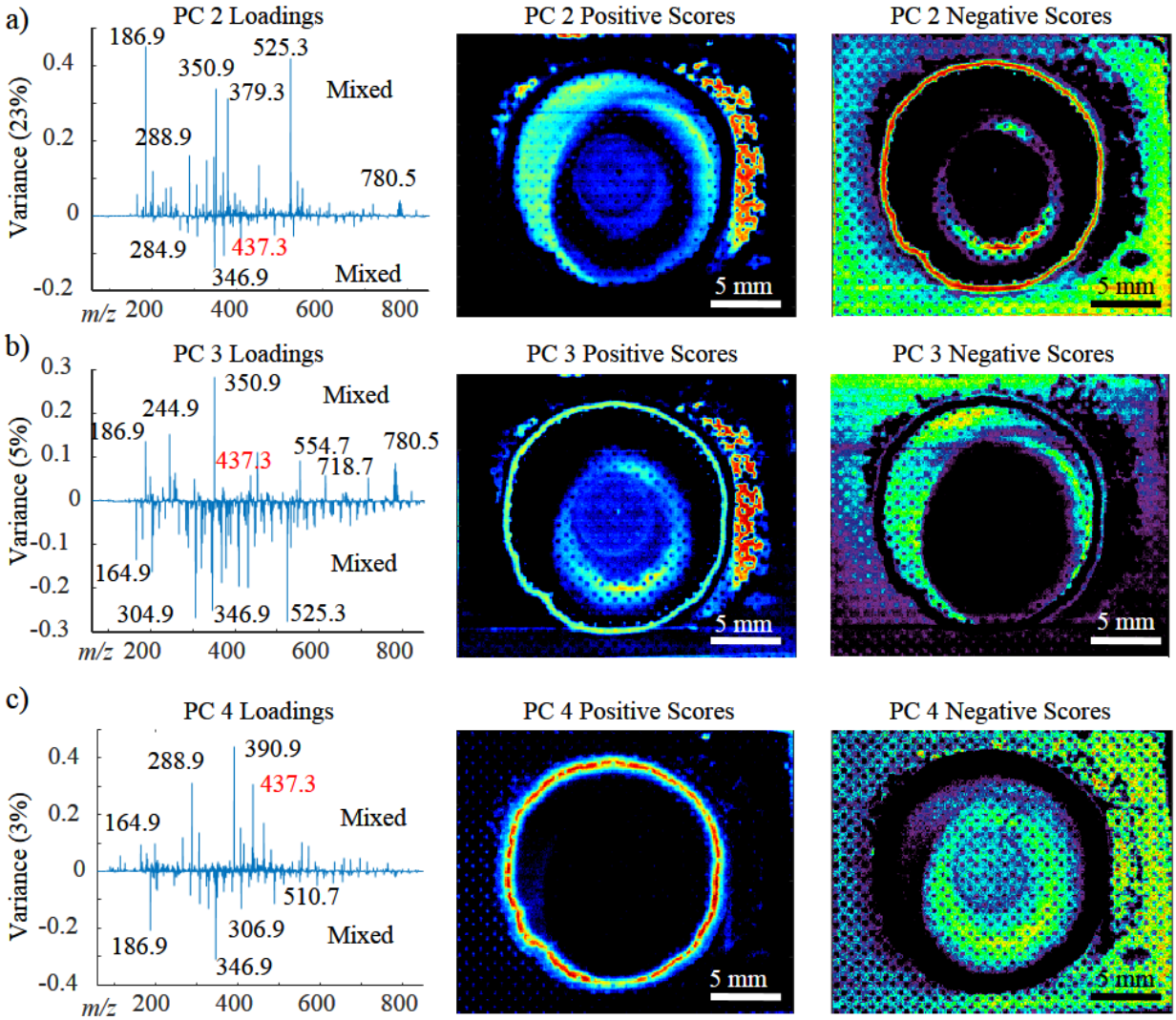

Figure 6.3. Investigation of the potential chemical origins of ion suppression in the pqsA$^-$ colony biofilm shown in **Figures 6.1** and **6.2** using untargeted SIMS imaging principal component analysis. (**a**) PC2, (**b**) PC3 and (**c**) PC4. Several ions, including *m/z* 437.25, are elevated in the suppression zone.

zone. A similar analysis of exogenous 9-AA (*m/z* 195.09) and endogenous *m/z* 437.25 in the PA14 biofilm examined in **Figure 6.1** (**Figure 6.4b**), as well as a biofilm from a different strain of *P. aeruginosa* (PA1OC) (**Figure 6.4c**), again shows regions of suppression correlating with *m/z* 437.25. Attempts at *in situ* SIMS tandem-MS identification of *m/z* 437.25 and the four other ions found in the suppression zone were stymied by inadequate fragmentation.

Finally, we examined the influence of large-scale morphology and surface roughness on secondary ion signal. Our own observations and those of others have shown that biofilm height and overall structure can fluctuate substantially depending on the specific strain of bacteria, the

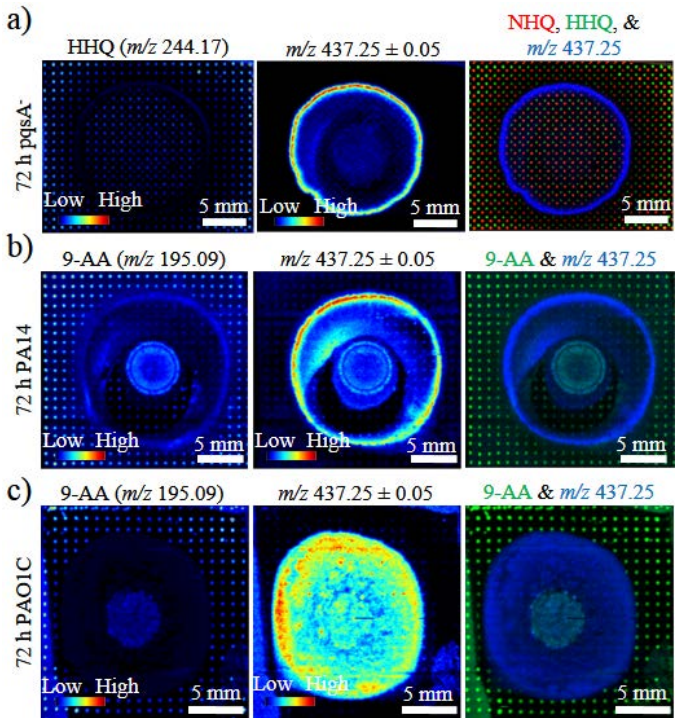

Figure 6.4. Comparison of the distribution of endogenous *m/z* 437.25 to the ion intensity of exogenous standards in 72 h *P. aeruginosa* colony biofilms of (**a**) pqsA$^-$, (**b**) PA14, and (**c**) PAO1C.

nutritional environment, and the growth phase of the colony.[65] Due to a number of factors, including differences in the incident angle of the primary ion beam and the strength of the local secondary ion extraction field, SIMS can be sensitive to sample topography.[82] Note that for linear ToF instruments – which are commonly used throughout the MSI community – sample height directly influences time of flight and therefore reduces mass resolution, however the instrument used in this work[70] contains an orthogonal ToF, and is therefore insensitive to height induced degradation of mass resolution.

For this experiment, two offset arrays of AQ and AQNO standards were deposited across a relatively complicated sample containing side-by-side colony biofilms of PAO1C and FRD1, and the sample was subjected to C_{60}-SIMS, 3D structured light imaging, and stylus profilometry (**Figure 6.5**). PAO1C and FRD1 were selected because of their contrasting growth modes. PAO1C is a motile strain that rapidly spreads to cover a large area,[65] while FRD1 expresses a hypermuciod phenotype resulting in thick, robust biofilms.[67]

As can be seen in the example ion image for NHQ, endogenous analyte is present in both strains and is most abundant in the FRD1 colony biofilm (**Figure 6.5a**). The intensity of exogenous NHQ (spots) is highest near the upper right of the sample and varies both vertically and horizontally. The ion intensity of exogenous NHQ in the middle of the agar is markedly reduced, even in areas devoid of biofilm, and a large region of ion suppression surrounds the PAO1C colony biofilm. The strange, jagged appearance on the right side of the image is the result of a software glitch during acquisition and should be disregarded.

3D structured light imaging reveals a total elevation change in excess of 1 mm, and substantial morphological variability (**Figure 6.5b**). The morphology variation arise from both natural

differences in biofilm thickness and artificial elevation changes caused by poor adhesion of the copper tape to the underlying substrate. Note that the poor tape adhesion is not typically observed, however, in this case, its occurrence resulted in an appropriate sample for the purposes of evaluating the relationship between ion signal and large-scale morphology. As expected, the thick FRD1 biofilm is higher than the surrounding area, however regions of the PAO1C biofilm are also elevated. An overlay of the ion image for NHQ and the structured light height profile (**Figure 6.5c**) shows a possible relationship between sample elevation and local ion signal, however this relationship appears to be inconsistent. For example, regions within and above the FRD1 colony biofilm are elevated and have a high ion intensity, while regions near to the left side of the PAO1C colony biofilm are similarly elevated yet have a low ion intensity. Similarly, the region on the far left side of the sample is among the lowest in elevation but the ion intensity for exogenous NHQ is high.

Due to the difficulty in generating conclusions through visual inspection alone, we subjected the sample to further morphological profiling using stylus profilometry and applied the Pearson correlation coefficient (r) to measure the linear correlation between the ion intensity of exogenous NHQ and several parameters, including height, surface roughness, and spot position. Although the correlation analysis could have conceivably been performed with the structured light data, the data format for stylus profilometry was computationally easier to work with and provided a more accurate representation of height and small-scale sample morphology. Anti-correlations of r = -0.25 and r = -0.31 were found for ion intensity versus height and ion intensity versus surface roughness respectively (**Figure 6.5d** and **Figure 6.5e**), suggesting a weak relationship between these variables. The overlay image (**Figure 6.5c**) shows a putative relationship between spot location and ion intensity, therefore similar measurements were performed to determine the linear correlation between ion intensity and distance to the edge of the agar (r = 0.23, **Figure 6.5f**) and distance to closest left or right edge (r = -0.54, **Figure 6.5g**).

Of all factors measured, the correlation between ion intensity and distance to the left or right edge was the strongest, suggesting that horizontal position is a primary factor affecting the ion signal, and that height or surface roughness have little impact. Although this cannot be determined for certain from our data, the horizontal signal variation is likely the result of the accumulation of surface charge. Since these correlative measurements were made using only exogenous analyte, they do not include regions lying inside the colony biofilms. Significant ion suppression

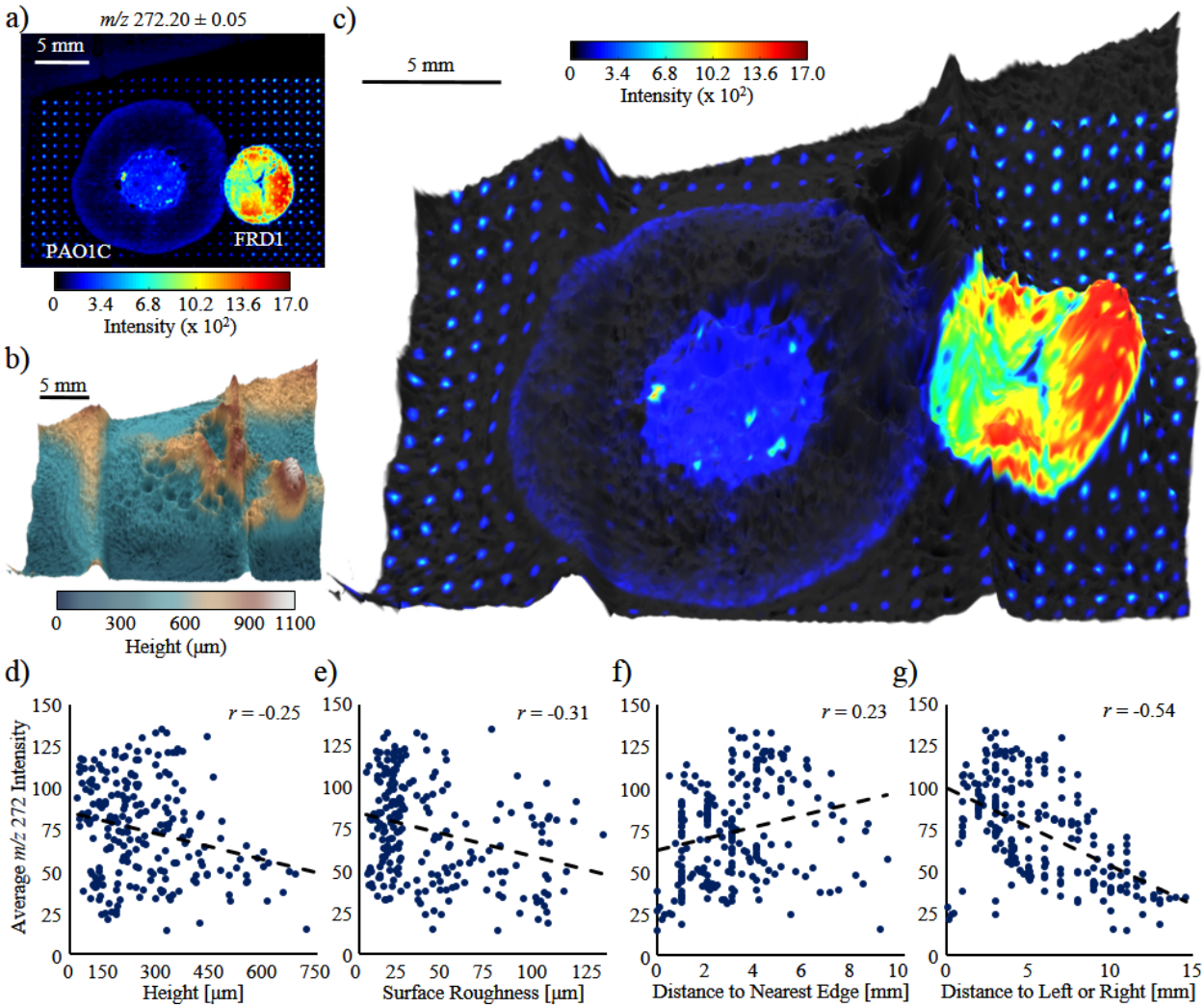

Figure 6.5. Evaluation of the relationship between surface morphology and ion suppression in a *P. aeruginosa* co-culture colony biofilm containing PAO1C (left) and FRD1 (right). (**a**) SIMS image of exogenous and endogenous NHQ. (**b**) 3D morphology profile. (**c**) Overlay of the ion image for NHQ and the 3D profile. (**d**–**f**) Correlation between the average intensity of exogenous NHQ and (**c**) height, (**b**) surface roughness, (**e**) distance to the nearest edge of the agar, and (**f**) distance to the left or right side of the agar. The elevation changes in **b** and **c** are amplified by a factor of 10 to aid visualization. Morphology data in **d**–**f** is from stylus profilometry, and the evaluations were performed only for regions without endogenous *m/z* 272.20. Parameter *r* is the Pearson correlation coefficient.

is observed in these regions and the same factors explored in **Figure 6.2** are likely at play. In support of this possibility, the distribution of *m/z* 437.25 matches the zone of ion suppression surrounding the PAO1C colony biofilm, however, in this case, direct comparison is complicated by the presence of endogenous AQs.

6.4.3. Application of the Microdroplet Array to Evaluate the Effectiveness of Different Data Collection and Data Normalization Approaches for the Mitigation of Ion Suppression

A significant benefit of the microdroplet array is that it enables systematic evaluation of the effect-

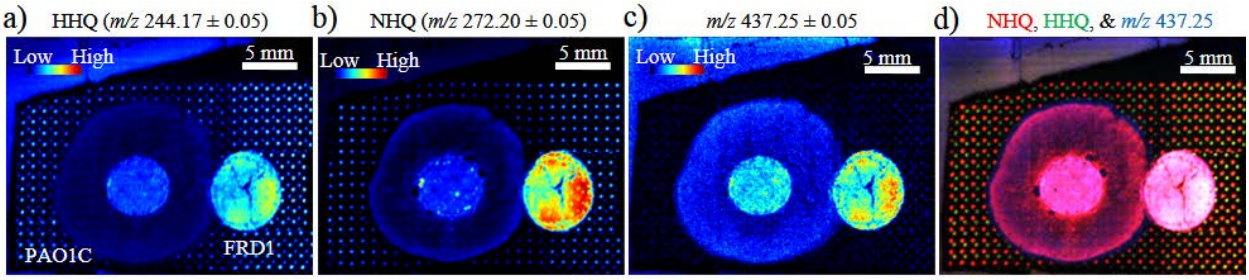

Figure 6.6. Evaluation of the distribution of *m/z* 437.25, HHQ, and NHQ in a 72 h *P. aeruginosa* co-culture colony biofilm containing PAO1C (left) and FRD1 (right). (**a**) HHQ, (**b**) NHQ, (**c**) *m/z* 437.25, and (**d**) overlay of NHQ (red), HHQ (green), & *m/z* 437.25 (blue).

tiveness of different data collection and data normalization strategies. We demonstrate this capability by exploring several questions.

Does normalization to the total ion count eliminate or mitigate regiospecific variations in ionization efficiency? Total ion count (TIC) normalization is commonly used to correct for both heterogeneous ionization efficiency and changes in instrument performance, however the underlying assumption of TIC normalization (i.e. that the total ion count for each pixel is approximately constant barring external influence) does not hold for all data sets.[83] For this reason, TIC normalization is not necessarily applicable when comparing different regions of a heterogeneous sample or when comparing several samples that are substantially different from one another.

To examine the effect of TIC normalization on our ion images, two staggered arrays containing AQ and AQNO standards were deposited across a pqsA$^-$ colony biofilm and imaged with SIMS. A comparison between ion images and average regional intensity values for exogenous PQS and HQNO (*m/z* 260.17) before (**Figure 6.7a**) and after (**Figure 6.7b**) TIC normalization shows a small improvement in variability. The intensity *m/z* 260.17 within and interior to the ring of suppression is more visible, however – because of the depressed TIC intensity in these regions – the improvement comes at the cost of increased isobaric interference, which is visible as a distinct ring in the ion image of **Figure 6.7b**. The CV value for PQS falls from 81% to 68% following normalization. Visual inspection of ion images of the other deposited analytes shows varying levels of improvement following normalization. These data show that TIC normalization can improve ion image quality by reducing matrix effects, however the procedure may also lead to image artifacts that should be considered when interpreting results.

Does tandem-MS imaging eliminate or mitigate regiospecific variations in ionization efficiency? Largely due to the pervasiveness of isobaric interference in biological SIMS imaging, many researchers are employing tandem-MS imaging (also known as product ion imaging or MS^2

imaging), where the ion of interest is internally isolated and fragmented to produce characteristic product ions. Because MS^2 imaging operates off of two selection criteria (i.e. both the precursor ion and the characteristic fragment ion match expected *m/z* values) there is a higher degree of confidence that the signal arises from the analyte of interest.

The effects of MS^2 imaging were examined by applying this operating mode to study the same $pqsA^-$ colony biofilm previously examined in **Figure 6.7a** and **Figure 6.7b**. Comparison of the PQS ion image in both modes (**Figure 6.7a** and **Figure 6.7c**) shows that the ring of suppression is actually more pronounced with MS^2 imaging. As evidenced by the average intensity values of PQS in the region outside, interior to, and on the ring of suppression (**Figure 6.7c** bar graphs), the ion signal in the interior region rises to match that of the outer area, while ion signal on the ring is significantly depressed. Despite the signal depression within the ring of suppression, a small improvement in variability was observed, with the average spot-to-spot variation dropping from 81% to 71%.

The conditions at the sample (matrix effects, charging, etc.) are identical for standard MS (MS^1) and MS^2 imaging, therefore one might expect no change in ion suppression between the two operating modes. How than can the differences between operating modes be explained? Because of isobaric interference, the ion intensity observed in MS^1 can arise from the combination of multiple chemical species. The magnitude of this interference can be contingent upon the same position dependent factors that cause differences in the ionization of the analyte. When this is the case, co-suppression of the analyte and the isobars leads to an *increase* in MS^1 intensity variability by amplifying ion signal in areas with low ion suppression and depressing ion signal in areas with high ion suppression. Differences in the distribution of isobaric interference can have a similar effect. For example, an excess local abundance of the isobars in the suppression region would lead to a *decrease* in MS^1 image variability. Removal of the isobaric interference through MS^2 imaging eliminates this amplification factor.

In the case of the MS^2 ion image for PQS (**Figure 6.7c**), the isobaric interference within the ring of suppression is successfully eliminated, however the sample specific factors influencing ionization of the analyte are still active. Ionization of PQS within the ring is still suppressed, and, without signal amplification from the isobaric interference, a lower ion intensity is observed. It is unclear why the ion intensity interior to the ring of suppression rises to match that of the edge.

Does normalization to an internal standard eliminate or mitigate regiospecific variations in ionization efficiency? We next used the microdroplet array method to examine the effects of internal standard normalization on variable ionization. Previous comparisons between LC-MS and MALDI-MSI have shown internal standard normalization to provide accurate results,[57, 84] however questions remain about its applicability to SIMS imaging. Using several different samples examined elsewhere throughout this report, we divided the ion intensity for exogenous HHQ by that of a second compound contained within the same microspot (9-AA for the PA14 and PAO1C samples and PQS for the pqsA$^-$ and agar samples) and compared the spot-to-spot variation (**Figure 6.7d**). As expected, the normalization approach produced more homogeneous results in comparison to the raw data, with substantially reduced CV values for HHQ following normalization. The greatest improvement was observed for the first pqsA$^-$ biofilm, with a CV change of 130% to 31%, and no detectable change was observed for the agar sample. Although this result is in line with previous observations, and therefore expected, it suggests that the application of a few-nm thin layer of standard to the sample surface prior to SIMS imaging may produce more accurate ion images. This remains the focus of ongoing investigations in our lab.

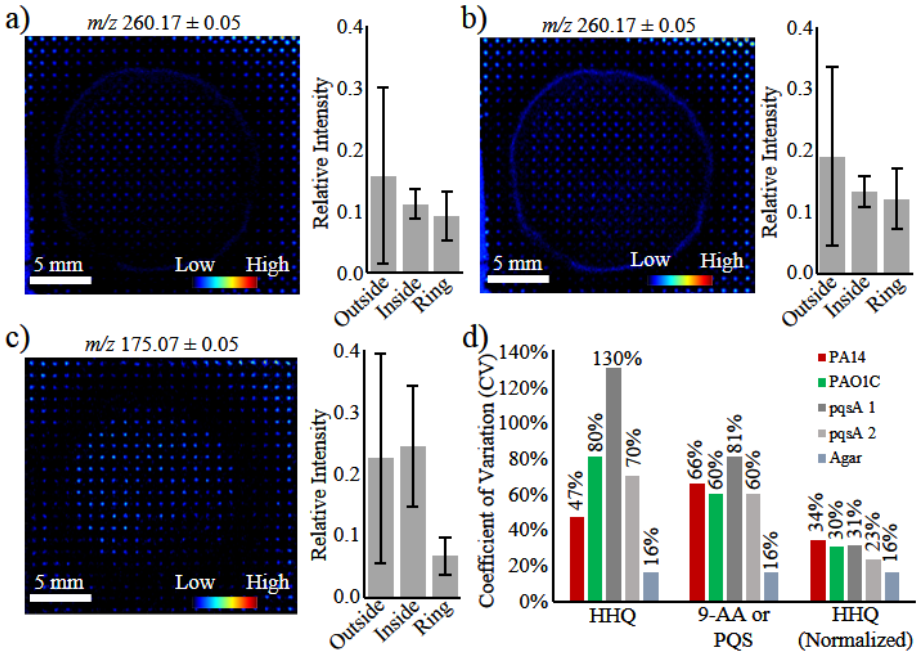

Figure 6.7. Utilization of the microdroplet array approach to evaluate the effectiveness of several sampling and data analysis approaches. (**a**) Raw MS1 ion image for exogenously applied PQS and HQNO in a pqsA- biofilm. (b) TIC normalized MS1 ion image PQS and HQNO in the same sample as **a**. (**c**) Raw MS2 ion image for PQS in the same biofilm as **a** and **b**. (**d**) CV values for HHQ in several samples before and after normalization to either 9-AA or PQS (as indicated in the main text). The graphs in **a**–**c** show the average relative intensity of PQS in microspots located outside, inside, and on the ring of suppression. The error bars show the standard deviation of the relative intensity values for spots within each region.

6.5. Conclusions

We described a microdroplet array methodology and demonstrated its application: (1) to investigate regiospecific variations in ionization efficiency, (2) as a fiducial system for multimodal chemical and morphological characterization of ion suppression, and (3) as a tool for evaluating the effects of different data collection and data normalization strategies. Application of this methodology to evaluate ion images for *P. aeruginosa* colony biofilms shows that heterogeneous ionization arises from both the distribution of endogenous compounds and surface charging, and that these effects can be partially corrected through both TIC and internal standard normalization. Although these findings are in line with previous observations, and therefore not surprising, they highlight the utility of the microdroplet array for evaluating the veracity of ion images and suggest further avenues for overcoming regiospecific variations in ionization efficiency. Avenues for further investigation include the application of the TEC normalization principal with a regiospecific dependence on surrounding standard spots, or the application of a few-nanometer layer of metal or sublimed internal standard to the sample surface.

In contrast to coatings of internal standard applied through other means (e.g. airbrush application or sublimation) the array has several advantages. The spot-based deposition circumvents many sample specific variables, such as differences in surface structure or hydrophobicity, which can lead to uneven coatings. Specifically for surface-sensitive SIMS imaging, the array leaves the majority of the sample unperturbed so that it can be examined in its native state. The technique is also compatible with any analyte that is soluble in the chosen solvent, and it is trivial to adjust concentrations or create complex arrays composed of multiple analytes. Finally, as previously shown,[34] arrays can be used as a fiducial system for examining specific sample regions with multiple analytical techniques, which – as shown in this report – can facilitate more thorough examinations of ion suppression.

As with any analytical methodology, there are also disadvantages. The approach requires a specialized chemical inkjet printer, which can be expensive. That being said, chemical inkjet printers are becoming more affordable,[57] and some researchers have reported lab-built models that would likely be adequate.[85] For MALDI MSI, or other MSI techniques with significant undersampling, it may be challenging to align the grid with the microprobe, however many instrument control software packages now come with this feature. Other obvious disadvantages include an

incompatibility with high resolution imaging, and the need for a representative (and bioorthogonal) standard for each analyte.

This work highlights, but does not solve, position-dependent variations in ionization efficiency. We hope that the standard array methodology will help other MSI practitioners to evaluate the validity of their ion images and generate sample treatment or data normalization methods for overcoming ion suppression.

6.6. References

1. Dunham, S. J. B.; Ellis, J. F.; Li, B.; Sweedler, J. V., Mass Spectrometry Imaging of Complex Microbial Communities. *Accounts of Chemical Research* **2017,** *50* (1), 96-104.
2. Watrous, J. D.; Dorrestein, P. C., Imaging mass spectrometry in microbiology. *Nature reviews. Microbiology* **2011,** *9* (9), 683-694.
3. Hanrieder, J.; Phan, N. T. N.; Kurczy, M. E.; Ewing, A. G., Imaging Mass Spectrometry in Neuroscience. *ACS Chemical Neuroscience* **2013,** *4* (5), 666-679.
4. Nilsson, A.; Goodwin, R. J. A.; Shariatgorji, M.; Vallianatou, T.; Webborn, P. J. H.; Andrén, P. E., Mass Spectrometry Imaging in Drug Development. *Analytical Chemistry* **2015,** *87* (3), 1437-1455.
5. Arnaud, C. H., Pharma embraces imaging mass spec. *Chemical & Engineering News* **2017,** *95* (23), 30-34.
6. Turker, S. D.; Dunn, W. B.; Wilkie, J., MALDI-MS of drugs: Profiling, imaging, and steps towards quantitative analysis. *Applied Spectroscopy Reviews* **2017,** *52* (1), 73-99.
7. Correa, D. N.; Santos, J. M.; Eberlin, L. S.; Eberlin, M. N.; Teunissen, S. F., Forensic Chemistry and Ambient Mass Spectrometry: A Perfect Couple Destined for a Happy Marriage? *Analytical Chemistry* **2016,** *88* (5), 2515-2526.
8. Li, B.; Dunham, S. J. B.; Dong, Y.; Yoon, S.; Zeng, M.; Sweedler, J. V., Analytical capabilities of mass spectrometry imaging and its potential applications in food science. *Trends in Food Science & Technology* **2016,** *47* (Supplement C), 50-63.
9. Buchberger, A. R.; DeLaney, K.; Johnson, J.; Li, L., Mass Spectrometry Imaging: A Review of Emerging Advancements and Future Insights. *Analytical Chemistry* **2018,** *90* (1), 240-265.
10. Taylor, A.; Dexter, A.; Bunch, J., Exploring ion suppression in mass spectrometry imaging of a heterogeneous tissue. *Anal Chem* **2018**.
11. Deline, V. R.; Katz, W.; Evans, C. A.; Williams, P., Mechanism of the SIMS matrix effect. *Applied Physics Letters* **1978,** *33* (9), 832-835.
12. Cooks, R. G.; Busch, K. L., Matrix effects, internal energies and MS/MS spectra of molecular ions sputtered from surfaces. *International Journal of Mass Spectrometry and Ion Physics* **1983,** *53*, 111-124.
13. Pirman, D. A.; Kiss, A.; Heeren, R. M. A.; Yost, R. A., Identifying Tissue-Specific Signal Variation in MALDI Mass Spectrometric Imaging by Use of an Internal Standard. *Analytical Chemistry* **2013,** *85* (2), 1090-1096.
14. Hansen, H. T.; Janfelt, C., Aspects of Quantitation in Mass Spectrometry Imaging Investigated on Cryo-Sections of Spiked Tissue Homogenates. *Analytical Chemistry* **2016,** *88* (23), 11513-11520.
15. Hankin, J. A.; Murphy, R. C., Relationship between MALDI IMS Intensity and Measured Quantity of Selected Phospholipids in Rat Brain Sections. *Analytical Chemistry* **2010,** *82* (20), 8476-8484.
16. Jones, E. A.; Lockyer, N. P.; Kordys, J.; Vickerman, J. C., Suppression and enhancement of secondary ion formation due to the chemical environment in static-secondary ion mass spectrometry. *Journal of the American Society for Mass Spectrometry* **2007,** *18* (8), 1559-1567.

17. Lanekoff, I.; Stevens, S. L.; Stenzel-Poore, M. P.; Laskin, J., Matrix effects in biological mass spectrometry imaging: identification and compensation. *Analyst* **2014,** *139* (14), 3528-3532.
18. Shard, A. G.; Spencer, S. J.; Smith, S. A.; Havelund, R.; Gilmore, I. S., The matrix effect in organic secondary ion mass spectrometry. *International Journal of Mass Spectrometry* **2015,** *377*, 599-609.
19. Stoeckli, M.; Staab, D.; Schweitzer, A., Compound and metabolite distribution measured by MALDI mass spectrometric imaging in whole-body tissue sections. *International Journal of Mass Spectrometry* **2007,** *260* (2), 195-202.
20. Wu, Q.; Comi, T. J.; Li, B.; Rubakhin, S. S.; Sweedler, J. V., On-Tissue Derivatization via Electrospray Deposition for Matrix-Assisted Laser Desorption/Ionization Mass Spectrometry Imaging of Endogenous Fatty Acids in Rat Brain Tissues. *Analytical Chemistry* **2016,** *88* (11), 5988-5995.
21. Prideaux, B.; Dartois, V.; Staab, D.; Weiner, D. M.; Goh, A.; Via, L. E.; Barry, C. E.; Stoeckli, M., High-Sensitivity MALDI-MRM-MS Imaging of Moxifloxacin Distribution in Tuberculosis-Infected Rabbit Lungs and Granulomatous Lesions. *Analytical Chemistry* **2011,** *83* (6), 2112-2118.
22. Si, T.; Li, B.; Comi, T. J.; Wu, Y.; Hu, P.; Wu, Y.; Min, Y.; Mitchell, D. A.; Zhao, H.; Sweedler, J. V., Profiling of Microbial Colonies for High-Throughput Engineering of Multistep Enzymatic Reactions via Optically Guided Matrix-Assisted Laser Desorption/Ionization Mass Spectrometry. *Journal of the American Chemical Society* **2017,** *139* (36), 12466-12473.
23. Petyuk, V. A.; Qian, W.-J.; Chin, M. H.; Wang, H.; Livesay, E. A.; Monroe, M. E.; Adkins, J. N.; Jaitly, N.; Anderson, D. J.; Camp, D. G.; Smith, D. J.; Smith, R. D., Spatial mapping of protein abundances in the mouse brain by voxelation integrated with high-throughput liquid chromatography–mass spectrometry. *Genome Research* **2007,** *17* (3), 328-336.
24. Petyuk, V. A.; Qian, W. J.; Smith, R. D.; Smith, D. J., Mapping protein abundance patterns in the brain using voxelation combined with liquid chromatography and mass spectrometry. *Methods (San Diego, Calif.)* **2010,** *50* (2), 77-84.
25. Chin, M. H.; Geng, A. B.; Khan, A. H.; Qian, W.-J.; Petyuk, V. A.; Boline, J.; Levy, S.; Toga, A. W.; Smith, R. D.; Leahy, R. M.; Smith, D. J., A genome-scale map of expression for a mouse brain section obtained using voxelation. *Physiological Genomics* **2007,** *30* (3), 313-321.
26. Bouslimani, A.; Porto, C.; Rath, C. M.; Wang, M.; Guo, Y.; Gonzalez, A.; Berg-Lyon, D.; Ackermann, G.; Moeller Christensen, G. J.; Nakatsuji, T.; Zhang, L.; Borkowski, A. W.; Meehan, M. J.; Dorrestein, K.; Gallo, R. L.; Bandeira, N.; Knight, R.; Alexandrov, T.; Dorrestein, P. C., Molecular cartography of the human skin surface in 3D. *Proceedings of the National Academy of Sciences* **2015,** *112* (17), E2120.
27. Petras, D.; Nothias, L.-F.; Quinn, R. A.; Alexandrov, T.; Bandeira, N.; Bouslimani, A.; Castro-Falcón, G.; Chen, L.; Dang, T.; Floros, D. J.; Hook, V.; Garg, N.; Hoffner, N.; Jiang, Y.; Kapono, C. A.; Koester, I.; Knight, R.; Leber, C. A.; Ling, T.-J.; Luzzatto-Knaan, T.; McCall, L.-I.; McGrath, A. P.; Meehan, M. J.; Merritt, J. K.; Mills, R. H.; Morton, J.; Podvin, S.; Protsyuk, I.; Purdy, T.; Satterfield, K.; Searles, S.; Shah, S.; Shires, S.; Steffen, D.; White, M.; Todoric, J.; Tuttle, R.; Wojnicz, A.; Sapp, V.; Vargas, F.; Yang, J.; Zhang, C.; Dorrestein, P. C., Mass Spectrometry-Based Visualization of Molecules Associated with Human Habitats. *Analytical Chemistry* **2016,** *88* (22), 10775-10784.
28. Kapono, C. A.; Morton, J. T.; Bouslimani, A.; Melnik, A. V.; Orlinsky, K.; Knaan, T. L.; Garg, N.; Vázquez-Baeza, Y.; Protsyuk, I.; Janssen, S.; Zhu, Q.; Alexandrov, T.; Smarr, L.; Knight, R.; Dorrestein, P. C., Creating a 3D microbial and chemical snapshot of a human habitat. *Scientific Reports* **2018,** *8* (1), 3669.
29. Floros, D. J.; Petras, D.; Kapono, C. A.; Melnik, A. V.; Ling, T.-J.; Knight, R.; Dorrestein, P. C., Mass Spectrometry Based Molecular 3D-Cartography of Plant Metabolites. *Frontiers in Plant Science* **2017,** *8* (429).
30. Cahill, J. F.; Kertesz, V.; Van Berkel, G. J., Characterization and Application of a Hybrid Optical Microscopy/Laser Ablation Liquid Vortex Capture/Electrospray Ionization System for Mass Spectrometry Imaging with Sub-micrometer Spatial Resolution. *Analytical Chemistry* **2015,** *87* (21), 11113-11121.
31. Cahill, J. F.; Kertesz, V.; Weiskittel, T. M.; Vavrek, M.; Freddo, C.; Van Berkel, G. J., Online, Absolute Quantitation of Propranolol from Spatially Distinct 20- and 40-μm Dissections of Brain, Liver, and

Kidney Thin Tissue Sections by Laser Microdissection–Liquid Vortex Capture–Mass Spectrometry. *Analytical Chemistry* **2016,** *88* (11), 6026-6034.
32. Comi, T. J.; Makurath, M. A.; Philip, M. C.; Rubakhin, S. S.; Sweedler, J. V., MALDI MS Guided Liquid Microjunction Extraction for Capillary Electrophoresis–Electrospray Ionization MS Analysis of Single Pancreatic Islet Cells. *Analytical Chemistry* **2017,** *89* (14), 7765-7772.
33. E. Naggar, M. S.; Barbier, C.; Van Berkel, G. J., Liquid Microjunction Surface Sampling Probe Fluid Dynamics: Computational and Experimental Analysis of Coaxial Intercapillary Positioning Effects on Sample Manipulation. *Journal of The American Society for Mass Spectrometry* **2011,** *22* (7), 1157.
34. Lanni, E. J.; Masyuko, R. N.; Driscoll, C. M.; Dunham, S. J. B.; Shrout, J. D.; Bohn, P. W.; Sweedler, J. V., Correlated Imaging with C60-SIMS and Confocal Raman Microscopy: Visualization of Cell-Scale Molecular Distributions in Bacterial Biofilms. *Analytical Chemistry* **2014,** *86* (21), 10885-10891.
35. Ahlf, D. R.; Masyuko, R. N.; Hummon, A. B.; Bohn, P. W., Correlated mass spectrometry imaging and confocal Raman microscopy for studies of three-dimensional cell culture sections. *Analyst* **2014,** *139* (18), 4578-4585.
36. Jadoul, L.; Malherbe, C.; Calligaris, D.; Longuespée, R.; Gilbert, B.; Eppe, G.; De Pauw, E., Matrix-assisted laser desorption/ionization mass spectrometry and Raman spectroscopy: An interesting complementary approach for lipid detection in biological tissues. *European Journal of Lipid Science and Technology* **2014,** *116* (8), 1080-1086.
37. Baig, N. F.; Dunham, S. J. B.; Morales-Soto, N.; Shrout, J. D.; Sweedler, J. V.; Bohn, P. W., Multimodal chemical imaging of molecular messengers in emerging Pseudomonas aeruginosa bacterial communities. *Analyst* **2015,** *140* (19), 6544-6552.
38. Bocklitz, T. W.; Crecelius, A. C.; Matthäus, C.; Tarcea, N.; von Eggeling, F.; Schmitt, M.; Schubert, U. S.; Popp, J., Deeper Understanding of Biological Tissue: Quantitative Correlation of MALDI-TOF and Raman Imaging. *Analytical Chemistry* **2013,** *85* (22), 10829-10834.
39. Lasch, P.; Noda, I., Two-Dimensional Correlation Spectroscopy for Multimodal Analysis of FT-IR, Raman, and MALDI-TOF MS Hyperspectral Images with Hamster Brain Tissue. *Analytical Chemistry* **2017,** *89* (9), 5008-5016.
40. Balbekova, A.; Bonta, M.; Torok, S.; Ofner, J.; Dome, B.; Limbeck, A.; Lendl, B., FTIR-spectroscopic and LA-ICP-MS imaging for combined hyperspectral image analysis of tumor models. *Analytical Methods* **2017,** *9* (37), 5464-5471.
41. Si, T.; Li, B.; Zhang, K.; Xu, Y.; Zhao, H.; Sweedler, J. V., Characterization of Bacillus subtilis Colony Biofilms via Mass Spectrometry and Fluorescence Imaging. *Journal of Proteome Research* **2016,** *15* (6), 1955-1962.
42. Ong, T. H.; Romanova, E. V.; Roberts-Galbraith, R. H.; Yang, N.; Zimmerman, T. A.; Collins, J. J., 3rd; Lee, J. E.; Kelleher, N. L.; Newmark, P. A.; Sweedler, J. V., Mass Spectrometry Imaging and Identification of Peptides Associated with Cephalic Ganglia Regeneration in Schmidtea mediterranea. *The Journal of biological chemistry* **2016,** *291* (15), 8109-20.
43. Horn, P. J.; Silva, J. E.; Anderson, D.; Fuchs, J.; Borisjuk, L.; Nazarenus, T. J.; Shulaev, V.; Cahoon, E. B.; Chapman, K. D., Imaging heterogeneity of membrane and storage lipids in transgenic Camelina sativa seeds with altered fatty acid profiles. *The Plant Journal* **2013,** *76* (1), 138-150.
44. Kuchar, L.; Faltyskova, H.; Krasny, L.; Dobrovolny, R.; Hulkova, H.; Ledvinova, J.; Volny, M.; Strohalm, M.; Lemr, K.; Kryspinova, L.; Asfaw, B.; Rybová, J.; Desnick, R. J.; Havlicek, V., Fabry disease: renal sphingolipid distribution in the α-Gal A knockout mouse model by mass spectrometric and immunohistochemical imaging. *Analytical and Bioanalytical Chemistry* **2015,** *407* (8), 2283-2291.
45. Buck, A.; Halbritter, S.; Späth, C.; Feuchtinger, A.; Aichler, M.; Zitzelsberger, H.; Janssen, K.-P.; Walch, A., Distribution and quantification of irinotecan and its active metabolite SN-38 in colon cancer murine model systems using MALDI MSI. *Analytical and Bioanalytical Chemistry* **2015,** *407* (8), 2107-2116.
46. Masyuko, R.; Lanni, E. J.; Sweedler, J. V.; Bohn, P. W., Correlated imaging - a grand challenge in chemical analysis. *Analyst* **2013,** *138* (7), 1924-1939.

47. Vidova, V.; Novak, P.; Strohalm, M.; Pol, J.; Havlicek, V.; Volny, M., Laser desorption-ionization of lipid transfers: tissue mass spectrometry imaging without MALDI matrix. *Anal Chem* **2010,** *82* (12), 4994-7.
48. Müller, T.; Oradu, S.; Ifa, D. R.; Cooks, R. G.; Kräutler, B., Direct Plant Tissue Analysis and Imprint Imaging by Desorption Electrospray Ionization Mass Spectrometry. *Analytical Chemistry* **2011,** *83* (14), 5754-5761.
49. Debois, D.; Hamze, K.; Guerineau, V.; Le Caer, J. P.; Holland, I. B.; Lopes, P.; Ouazzani, J.; Seror, S. J.; Brunelle, A.; Laprevote, O., In situ localisation and quantification of surfactins in a Bacillus subtilis swarming community by imaging mass spectrometry. *Proteomics* **2008,** *8* (18), 3682-91.
50. Bergman, H.-M.; Lundin, E.; Andersson, M.; Lanekoff, I., Quantitative mass spectrometry imaging of small-molecule neurotransmitters in rat brain tissue sections using nanospray desorption electrospray ionization. *Analyst* **2016,** *141* (12), 3686-3695.
51. Seeley, E. H.; Oppenheimer, S. R.; Mi, D.; Chaurand, P.; Caprioli, R. M., Enhancement of Protein Sensitivity for MALDI Imaging Mass Spectrometry after Chemical Treatment of Tissue Sections. *Journal of the American Society for Mass Spectrometry* **2008,** *19* (8), 1069-1077.
52. Pirman, D. A.; Yost, R. A., Quantitative Tandem Mass Spectrometric Imaging of Endogenous Acetyl-l-carnitine from Piglet Brain Tissue Using an Internal Standard. *Analytical Chemistry* **2011,** *83* (22), 8575-8581.
53. Landgraf, R. R.; Garrett, T. J.; Prieto Conaway, M. C.; Calcutt, N. A.; Stacpoole, P. W.; Yost, R. A., Considerations for quantification of lipids in nerve tissue using matrix-assisted laser desorption/ionization mass spectrometric imaging. *Rapid Communications in Mass Spectrometry* **2011,** *25* (20), 3178-3184.
54. Clemis, E. J.; Smith, D. S.; Camenzind, A. G.; Danell, R. M.; Parker, C. E.; Borchers, C. H., Quantitation of Spatially-Localized Proteins in Tissue Samples using MALDI-MRM Imaging. *Analytical Chemistry* **2012,** *84* (8), 3514-3522.
55. Schulz, S.; Gerhardt, D.; Meyer, B.; Seegel, M.; Schubach, B.; Hopf, C.; Matheis, K., DMSO-enhanced MALDI MS imaging with normalization against a deuterated standard for relative quantification of dasatinib in serial mouse pharmacology studies. *Analytical and Bioanalytical Chemistry* **2013,** *405* (29), 9467-9476.
56. Källback, P.; Shariatgorji, M.; Nilsson, A.; Andrén, P. E., Novel mass spectrometry imaging software assisting labeled normalization and quantitation of drugs and neuropeptides directly in tissue sections. *Journal of Proteomics* **2012,** *75* (16), 4941-4951.
57. Chumbley, C. W.; Reyzer, M. L.; Allen, J. L.; Marriner, G. A.; Via, L. E.; Barry, C. E.; Caprioli, R. M., Absolute Quantitative MALDI Imaging Mass Spectrometry: A Case of Rifampicin in Liver Tissues. *Analytical Chemistry* **2016,** *88* (4), 2392-2398.
58. Hamm, G.; Bonnel, D.; Legouffe, R.; Pamelard, F.; Delbos, J.-M.; Bouzom, F.; Stauber, J., Quantitative mass spectrometry imaging of propranolol and olanzapine using tissue extinction calculation as normalization factor. *Journal of Proteomics* **2012,** *75* (16), 4952-4961.
59. Inoue, M.; Murase, A., Reduction of matrix effects in TOF-SIMS analysis by metal-assisted SIMS (MetA-SIMS). *Surface and Interface Analysis* **2005,** *37* (12), 1111-1114.
60. Dunham, S. J.; Comi, T. J.; Ko, K.; Li, B.; Baig, N. F.; Morales-Soto, N.; Shrout, J. D.; Bohn, P. W.; Sweedler, J. V., Metal-assisted polyatomic SIMS and laser desorption/ionization for enhanced small molecule imaging of bacterial biofilms. *Biointerphases* **2016,** *11* (2), 02a325.
61. Van Nuffel, S.; Elie, N.; Yang, E.; Nouet, J.; Touboul, D.; Chaurand, P.; Brunelle, A., Insights into the MALDI Process after Matrix Deposition by Sublimation Using 3D ToF-SIMS Imaging. *Analytical Chemistry* **2018**.
62. Angerer, T. B.; Dowlatshahi Pour, M.; Malmberg, P.; Fletcher, J. S., Improved molecular imaging in rodent brain with time-of-flight-secondary ion mass spectrometry using gas cluster ion beams and reactive vapor exposure. *Anal Chem* **2015,** *87* (8), 4305-13.

63. Muramoto, S.; Forbes, T. P.; van Asten, A. C.; Gillen, G., Test Sample for the Spatially Resolved Quantification of Illicit Drugs on Fingerprints Using Imaging Mass Spectrometry. *Analytical Chemistry* **2015,** *87* (10), 5444-5450.
64. Dunham, S. J. B.; Ellis, J. F.; Baig, N. F.; Morales-Soto, N.; Cao, T.; Shrout, J. D.; Bohn, P. W.; Sweedler, J. V., Quantitative SIMS Imaging of Agar-Based Microbial Communities. *Analytical Chemistry* **Under Review**.
65. Shrout, J. D.; Chopp, D. L.; Just, C. L.; Hentzer, M.; Givskov, M.; Parsek, M. R., The impact of quorum sensing and swarming motility on Pseudomonas aeruginosa biofilm formation is nutritionally conditional. *Molecular microbiology* **2006,** *62* (5), 1264-77.
66. Ciofu, O.; Tolker-Nielsen, T.; Jensen, P. Ø.; Wang, H.; Høiby, N., Antimicrobial resistance, respiratory tract infections and role of biofilms in lung infections in cystic fibrosis patients. *Advanced Drug Delivery Reviews* **2015,** *85*, 7-23.
67. Ohman, D. E.; Chakrabarty, A. M., Genetic mapping of chromosomal determinants for the production of the exopolysaccharide alginate in a Pseudomonas aeruginosa cystic fibrosis isolate. *Infection and Immunity* **1981,** *33* (1), 142-148.
68. Coleman, J. P.; Hudson, L. L.; McKnight, S. L.; Farrow, J. M., 3rd; Calfee, M. W.; Lindsey, C. A.; Pesci, E. C., Pseudomonas aeruginosa PqsA is an anthranilate-coenzyme A ligase. *J Bacteriol* **2008,** *190* (4), 1247-55.
69. Centers for Disease Control and Prevention, Biosafety in Microbiological and Biomedical Laboratories. 5 ed.; U.S. Department of Health and Human Services, Ed. 2009; pp 1-405.
70. Lanni, E. J.; Dunham, S. J. B.; Nemes, P.; Rubakhin, S. S.; Sweedler, J. V., Biomolecular Imaging with a C60-SIMS/MALDI Dual Ion Source Hybrid Mass Spectrometer: Instrumentation, Matrix Enhancement, and Single Cell Analysis. *Journal of The American Society for Mass Spectrometry* **2014,** *25* (11), 1897-1907.
71. Chambers, M. C.; Maclean, B.; Burke, R.; Amodei, D.; Ruderman, D. L.; Neumann, S.; Gatto, L.; Fischer, B.; Pratt, B.; Egertson, J.; Hoff, K.; Kessner, D.; Tasman, N.; Shulman, N.; Frewen, B.; Baker, T. A.; Brusniak, M.-Y.; Paulse, C.; Creasy, D.; Flashner, L.; Kani, K.; Moulding, C.; Seymour, S. L.; Nuwaysir, L. M.; Lefebvre, B.; Kuhlmann, F.; Roark, J.; Rainer, P.; Detlev, S.; Hemenway, T.; Huhmer, A.; Langridge, J.; Connolly, B.; Chadick, T.; Holly, K.; Eckels, J.; Deutsch, E. W.; Moritz, R. L.; Katz, J. E.; Agus, D. B.; MacCoss, M.; Tabb, D. L.; Mallick, P., A cross-platform toolkit for mass spectrometry and proteomics. *Nat Biotech* **2012,** *30* (10), 918-920.
72. Race, A. M.; Styles, I. B.; Bunch, J., Inclusive sharing of mass spectrometry imaging data requires a converter for all. *Journal of Proteomics* **2012,** *75* (16), 5111-5112.
73. Robichaud, G.; Garrard, K. P.; Barry, J. A.; Muddiman, D. C., MSiReader: An Open-Source Interface to View and Analyze High Resolving Power MS Imaging Files on Matlab Platform. *Journal of The American Society for Mass Spectrometry* **2013,** *24* (5), 718-721.
74. Bokhart, M. T.; Nazari, M.; Garrard, K. P.; Muddiman, D. C., MSiReader v1.0: Evolving Open-Source Mass Spectrometry Imaging Software for Targeted and Untargeted Analyses. *Journal of The American Society for Mass Spectrometry* **2018,** *29* (1), 8-16.
75. Flemming, H. C.; Wingender, J., The biofilm matrix. *Nat Rev Microbiol* **2010,** *8* (9), 623-33.
76. Davey, M. E.; Caiazza, N. C.; O'Toole, G. A., Rhamnolipid Surfactant Production Affects Biofilm Architecture in Pseudomonas aeruginosa PAO1. *Journal of Bacteriology* **2003,** *185* (3), 1027-1036.
77. Sauer, K.; Camper, A. K.; Ehrlich, G. D.; Costerton, J. W.; Davies, D. G., Pseudomonas aeruginosa displays multiple phenotypes during development as a biofilm. *J Bacteriol* **2002,** *184* (4), 1140-54.
78. Heeren, R. M. A.; Smith, D. F.; Stauber, J.; Kükrer-Kaletas, B.; MacAleese, L., Imaging Mass Spectrometry: Hype or Hope? *Journal of the American Society for Mass Spectrometry* **2009,** *20* (6), 1006-1014.
79. Fletcher, M. P.; Heeb, S.; Chhabra, S. R.; Diggle, S. P.; Williams, P.; Cámara, M., 2-Alkyl-4(1H)-Quinolone Signalling in Pseudomonas aeruginosa. In *Pseudomonas: Volume 6: Molecular Microbiology, Infection and Biodiversity*, Ramos, J. L.; Filloux, A., Eds. Springer Netherlands: Dordrecht, 2010; pp 29-57.

80. Morris, J. D.; Hewitt, J. L.; Wolfe, L. G.; Kamatkar, N. G.; Chapman, S. M.; Diener, J. M.; Courtney, A. J.; Leevy, W. M.; Shrout, J. D., Imaging and Analysis of Pseudomonas aeruginosa Swarming and Rhamnolipid Production. *Applied and Environmental Microbiology* **2011,** *77* (23), 8310-8317.
81. Ghosh, U. U.; Chakraborty, M.; Bhandari, A. B.; Chakraborty, S.; DasGupta, S., Effect of Surface Wettability on Crack Dynamics and Morphology of Colloidal Films. *Langmuir* **2015,** *31* (22), 6001-6010.
82. Lee, J. L. S.; Gilmore, I. S.; Fletcher, I. W.; Seah, M. P., Topography and field effects in the quantitative analysis of conductive surfaces using ToF-SIMS. *Applied Surface Science* **2008,** *255* (4), 1560-1563.
83. Deininger, S.-O.; Cornett, D. S.; Paape, R.; Becker, M.; Pineau, C.; Rauser, S.; Walch, A.; Wolski, E., Normalization in MALDI-TOF imaging datasets of proteins: practical considerations. *Analytical and Bioanalytical Chemistry* **2011,** *401* (1), 167-181.
84. Pirman, D. A.; Reich, R. F.; Kiss, A.; Heeren, R. M. A.; Yost, R. A., Quantitative MALDI Tandem Mass Spectrometric Imaging of Cocaine from Brain Tissue with a Deuterated Internal Standard. *Analytical Chemistry* **2013,** *85* (2), 1081-1089.
85. Baluya, D. L.; Garrett, T. J.; Yost, R. A., Automated MALDI Matrix Deposition Method with Inkjet Printing for Imaging Mass Spectrometry. *Analytical Chemistry* **2007,** *79* (17), 6862-6867.

CHAPTER 7

Antibiotic Exposure Induces Spatially Dependent Variations in Alkyl Quinolone Signaling During *Pseudomonas aeruginosa* Swarming

7.1. Acknowledgements

This chapter is adapted from a research manuscript published in the *Journal of Biological Chemistry*, In Press, copyright 2018 American Society for Biochemistry and Molecular Biology, doi: 10.1074/jbc.RA118.002605. The co-authors of the manuscript include Nydia Morales-Soto, Sage J. B. Dunham, Nameera F. Baig, Joseph F. Ellis, Chinedu S. Madukoma, Paul W. Bohn, Jonathan V. Sweedler, and Joshua D. Shrout. NMS designed many of the experiments, cultivated the swarms, helped to write the manuscript, performed most of the microscopy, and analyzed much of the associated data. SJBD designed many of the experiments, performed most of the mass spectrometry experiments and analyzed the associated data, helped to analyze the Raman data, and helped to write the manuscript. NFB designed many of the experiments, performed the Raman experiments and associated data analysis, and helped to write the manuscript. JFE helped to perform the MSI experiments and helped to analyze the MSI data. CSM helped to perform some of the wet lab experiments. PWB, JVS, and JDS helped to design experiments and write the paper. This research was funded by the National Institute of Allergy and Infectious Diseases of the National Institutes of Health under Award Number R01AI113219.

7.2. Introduction

Bacteria do not respond to stressors such as antibiotics in any standard way. However, most of the detailed research performed to understand the bacterially secreted responses to specific antibiotics has utilized information from homogenized bacterial communities.[1-5] Indeed, most biological systems are assumed to exhibit diffusion-limited chemical distributions that are largely homogeneous. Yet, microbial communities, such as biofilms, are composed of individual cells that do not sense stress (or even cell death) equally throughout their occupied space. Thus, there is an urgent need to spatially map the biochemical profiles of these microbial communities. Here, we exploit multimodal chemical imaging to study spatial heterogeneities within motile 'pre-biofilm' swarm communities of the bacterium *Pseudomonas aeruginosa*. *P. aeruginosa* is an opportunistic

pathogen and one of many bacteria that displays numerous community behaviors, including an ability to readily form surface-attached biofilms. Prior to establishing stationary biofilm communities, *P. aeruginosa* is known to exhibit swarming,[1, 6-7] a group motility behavior employed by some bacteria to explore and expand during surface colonization. While many studies have addressed biofilm development and the transition to static bacterial biofilms, the community behaviors exhibited by motile bacteria are less understood. In this study, we show that the production of alkyl quinolones (AQs) by *P. aeruginosa* swarming communities is substantial, and quinolone secretion varies dramatically when exposed to the aminoglycoside antibiotic tobramycin as opposed to the β-lactam antibiotic carbenicillin.

Planktonic cells are generally sensitive to antibiotics, whereas surface attached biofilms and swarming communities display increased survival and resistance.[3, 8-11] Thus, it is imperative to understand how bacterial communities coordinate colonization of new surfaces and how this helps them endure the stress of traditional antibiotics. The apparent invulnerability of biofilms to antimicrobials is generally attributed to physical protection provided by the communal extracellular polymeric substances (EPS) layer[12] and a change in metabolic state. However, during the pre-biofilm stage of swarming, intracellular cyclic-di-GMP levels are low, EPS production is downregulated, and cells are actively growing—resulting in the hypothesis that antimicrobial survival in swarming communities is associated with high cell density.[3, 13-14] Because it is unlikely that survival arises from high cell density alone in swarming communities, it is vital to understand if and how the secretome of swarming communities promotes antimicrobial tolerance.

One critically important class of molecules produced and secreted by *P. aeruginosa* is the nitrogen containing heterocyclic aromatic 2-alkyl-4(1*H*)-quinolones (AQs).[15] We have previously identified members of the AQ family as principal swarm community metabolites.[16] Over 50 distinct AQs have been identified in *P. aeruginosa* falling under three primary subclasses: AQs such as (i) 2-heptyl-4(1*H*)-quinolone (HHQ) and 2-nonyl-4(1*H*)-quinolone (NHQ), which have the simplest base structure with only one oxygen; (ii) 2-alkyl-3-hydroxy-4(1*H*)-quinolones, such as 2-heptyl-3-hydroxy-4(1*H*)-quinolone (*Pseudomonas* quinolone signal; PQS) and 2-heptyl-3-nonyl-4(1*H*)-quinolone (C_9-PQS); and (iii) 2-alkyl-4-hydroxyquinoline *N*-oxides (AQNOs) such as 2-heptyl-4-hydroxyquinoline *N*-oxide (HQNO) and 2-nonyl-4-hydroxyquinoline *N*-oxide (NQNO), which are characterized by the presence of an amine oxide bond.[17] Of the molecules that belong to this family, the roles of HHQ, PQS, and HQNO are particularly well-documented. The

AQs belonging to the PQS pathway participate in processes as diverse as intercellular quorum sensing signaling, virulence regulation, biofilm development, iron chelation, antimicrobial activity, stress response, and control of cell death.[15, 18-27] In the *Pseudomonas* literature, AQs are generally presented to contain 7-Carbon (7C) side chains (HHQ, PQS, and HQNO), yet 9-Carbon (9C; NHQ, C9-PQS, and NQNO) and 11-Carbon (11C; UHQ, C11-PQS, and UQNO) side chain variants of these molecules are also common.[16-17] Although a universal secretion mechanism for AQ molecules has not been identified, the extracellular presence of PQS within *P. aeruginosa* communities could be due to cell lysis[28] and packaging and secretion in outer membrane vesicles (OMVs).[29] Cell lysis could also contribute to the release of other AQ molecules to the extracellular environment.[28]

We utilized two chemically information rich imaging approaches,[16, 30-31] secondary ion mass spectrometry (SIMS) and confocal Raman microscopy (CRM), to analyze the relative abundance and spatial distribution of AQs within 2D intact *P. aeruginosa* swarm communities both with and without antibiotic challenges. Absent antibiotics, our *in vitro* observations of *P. aeruginosa* swarms reveal that the PQS and AQNO classes act on different spatial scales within swarm communities. We also find AQ molecules in relatively large spatial aggregates that are easily visualized by light microscopy, even at low magnification. Collectively, we find that antibiotics elicit both universal and specific antibiotic-specific physiochemical behaviors and cell death for *P. aeruginosa* swarming cells. Our findings reveal a role for PQS in response to tobramycin exposure, but not carbenicillin exposure. Thus, we conclude that the PQS stress response[22, 27] is not a universal response mechanism to all antibiotics. Additionally, AQs belonging to the general PQS pathway appear to be under distinct regulatory control mechanisms, since modulations to PQS and targeted AQNOs are observed to be independent of one another, and they influence differing portions of these high density swarm communities. These surprising findings open a new window onto *P. aeruginosa* community behavior, which promises to provide deep insights into the spatial regulation of molecular secretion which mediates the critical motile-to-sessile transition at the onset of infection.

7.3. Results

7.3.1. Two Antibiotic Classes Elicit Universal *P. aeruginosa* Swarm Motility Responses but Radically Distinct Chemical Responses

Inhibitory levels of tobramycin and carbenicillin that elicited similar reductions in swarming at the macroscopic level, **Figure 7.1**, produced markedly different single cell phenotypes. Similar to previous single cell results,[32-34] the morphology of cells exposed to tobramycin (**Figure 7.1A**) closely resembled that of unexposed cells (**Figure 7.1B**), whereas cells exposed to carbenicillin were exceptionally elongated (**Figure 7.1C**). The differing phenotypes caused by these two antibiotics was startling, and we hypothesized that the *P. aeruginosa* responses to these two exposures is chemically distinct.

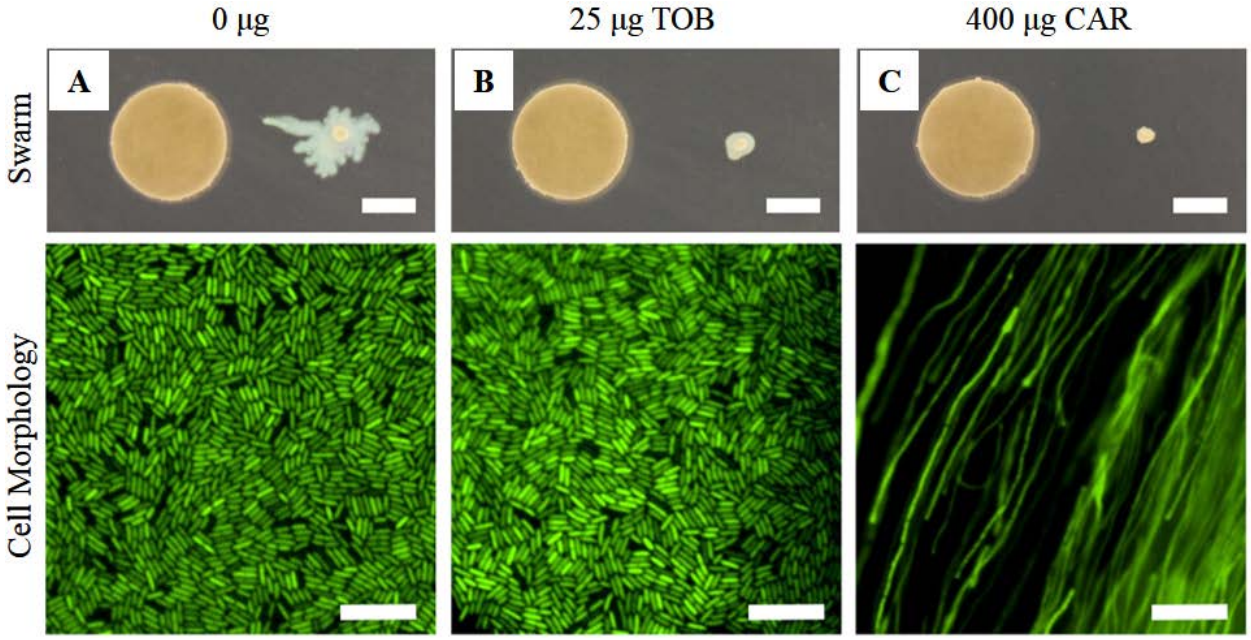

Figure 7.1. Impact of antibiotic treatment on *P. aeruginosa* swarm colonies. Cells were exposed to (**A**) 0 µg, (**B**) 25 µg tobramycin (TOB), and (**C**) 400 µg carbenicillin (CAR). Representative data for 48 h swarms is shown. Scale bars on swarm colony images represent 5 mm, and scale bars on microscopy images represent 10 µm.

To investigate the *in situ* biochemical response to tobramycin and carbenicillin, we examined intact *P. aeruginosa* swarms with non-destructive CRM and implemented principal component analysis (PCA) to profile spectral variations following exposure to these antibiotics. Due to the large space requirement for imaging results, we will only show representative images and analysis from a single set of samples, however each experiment was repeated at least 3 times. A total of 26 samples were examined, resulting in more than 150 CRM image acquisitions. Our previous investigations of *P. aeruginosa* with CRM revealed features of AQs that are distinguishable in the 1338-1376 cm^{-1} window, attributed to the quinolone ring stretch.[16] The PQS and AQNO classes produce specific CRM features (**Figure 7.2**) enabling differentiation.[16, 30, 35] PQS and C9-PQS exhibit spectral features at approximately 1158, 1372, 1466, and 1654 cm^{-1}

(**Figure 7.2A**), HQNO and NQNO exhibit spectral features at approximately 717,1358 and 1510 cm^{-1} (**Figure 7.2B**), and HHQ and NHQ exhibit spectral features at approximately 1175, 1354, 1503, and 1593 cm^{-1} (**Figure 7.2C**).

The distribution of PQS and AQNO-type AQs varied significantly within the *P. aeruginosa* swarms examined, and several aspects of the AQ profiles were uniquely linked to the response to

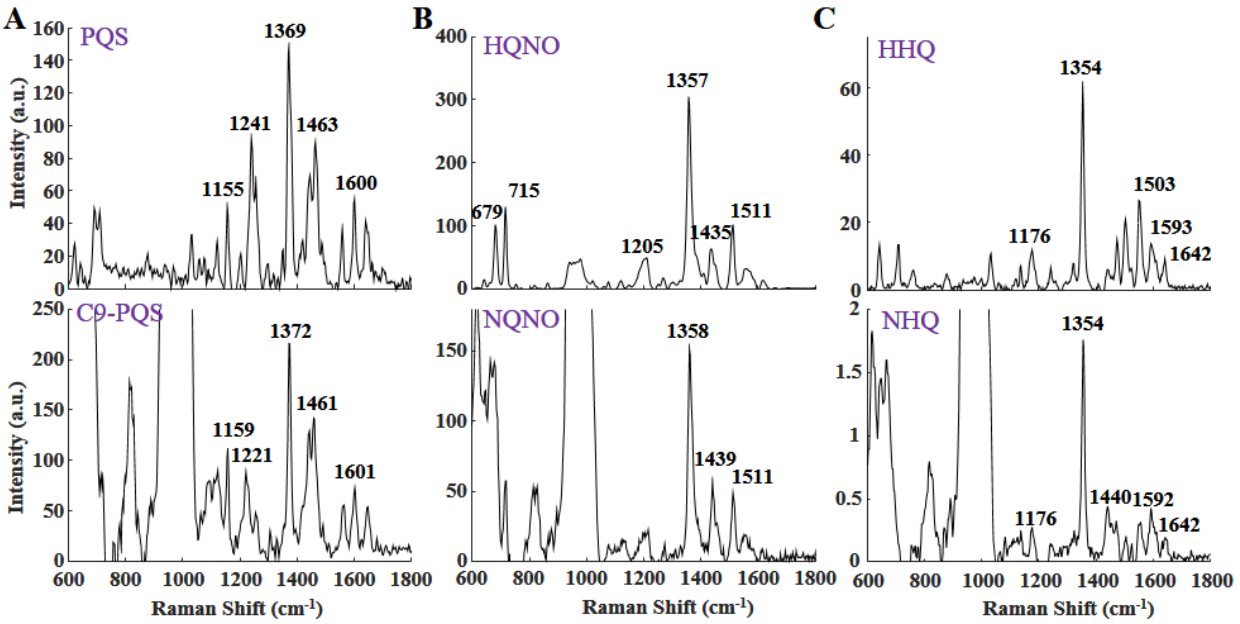

Figure 7.2. Raman spectra of analytical standards. (**A**) PQS and C9-PQS, (**B**) HQNO and NQNO, and (**C**) HHQ and NHQ.

either tobramycin or carbenicillin. Raman imaging PCA of the swarm colonies without antibiotics revealed PQS and its derivatives to be localized near the center of the swarms (**Figure 7.3A**), while AQNOs were distributed more uniformly throughout the entire colony (**Figure 7.3B)**. Principal component 1 (PC1) from the center of the unexposed swarm (**Figure 7.3A**) exhibits spectral features that are consistent with the HQNO and NQNO standards, while PC2 exhibits features of both *N*-oxide and PQS-type AQs. Both PC1 and PC2 from the edge of the swarm (**Figure 7.3A**) exhibit spectral features that are similar to the *N*-oxide standards. PQS is not detected near the edge of the swarm with Raman.

We next investigated a moderately inhibitory tobramycin exposure condition (10 µg) that resulted in a diminished swarm response. CRM analysis of this exposure condition reveals that the region close the antibiotic source is dominated by PQS-type AQs, with some *N*-oxides also present (**Figure 7.3C**). This is in stark contrast to the region far from the antibiotic source, at the end of

the tendrils, which primarily shows spectral features indicative of *N*-oxide AQs and no PQS-type AQs (**Figure 7.3D**).

Comparisons were made between swarms exposed to an inhibitory dose of tobramycin (25 µg) and a similar community exposed to an inhibitory dose of carbenicillin (400 µg) (**Figure 7.4**).

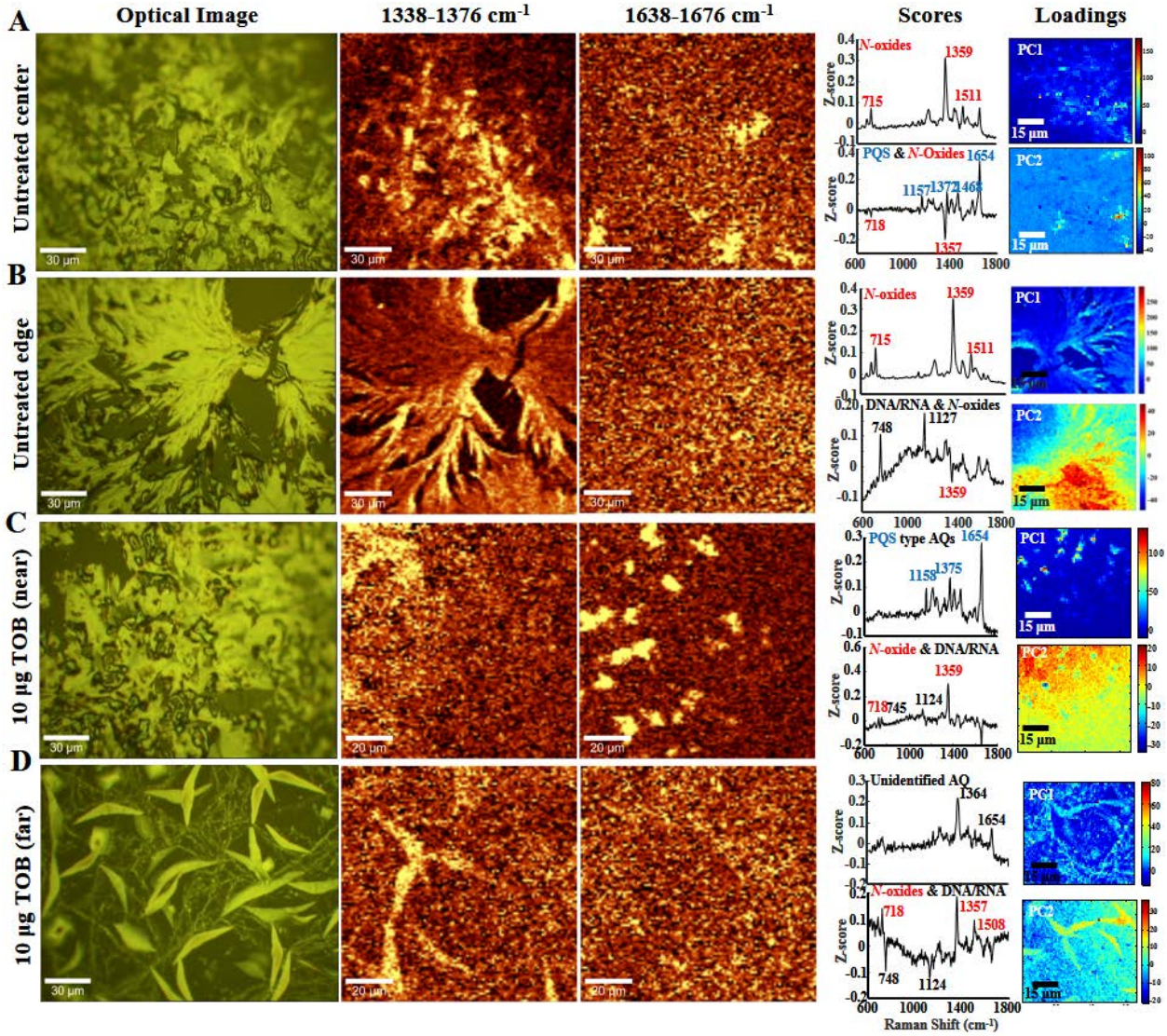

Figure 7.3. Representative CRM and imaging PCA of a wild-type swarm community exposed to (**A-B**) 0 µg and (**C-D**) 10 µg tobramycin. Loading plots for PC1 and PC2 include features corresponding to Raman spectra from cellular components (black), PQS (blue), and AQNOs (HQNO/NQNO; red). Cellular components are identified by the presence of the thymine ring stretch in DNA (~745 cm^{-1}), and to the C-N stretch in proteins and C-O stretch in lipids (1127 cm^{-1}). PQS is associated with features at 1158, 1372, 1466, and 1654 cm^{-1}, and AQNOs with features in 715, 1205, 1359, and 1508 cm^{-1}. The center of the unexposed swarm (**A**) exhibits spectral features that match those of both PQS and *N*-oxide type AQ standards, while edge of the unexposed swarm (**B**) exhibits spectral features that only match the *N*-oxide standards. The sample region of the 10 µg exposure condition that is closest to the tobramycin source (**C**) has spectral features that match both *N*-oxides and PQS-Type AQs, while the region that is farthest away from tobramycin (**D**) exhibits only *N*-oxides. Scale bars on Raman images represent 30 µm.

As expected, the high tobramycin dose results in inhibition of swarming and the production of PQS-type AQs (**Figure 7.4A**). Strong AQNO features are also observed, again indicating that both AQ classes aggregate within the swarms exposed to tobramycin. The metabolite profile of swarms exposed to carbenicillin (**Figure 7.4B**) stands in stark contrast to that of swarms exposed to tobramycin. While exposure to 400 µg carbenicillin resulted in the characteristic reduction in swarming, PQS was notably absent.

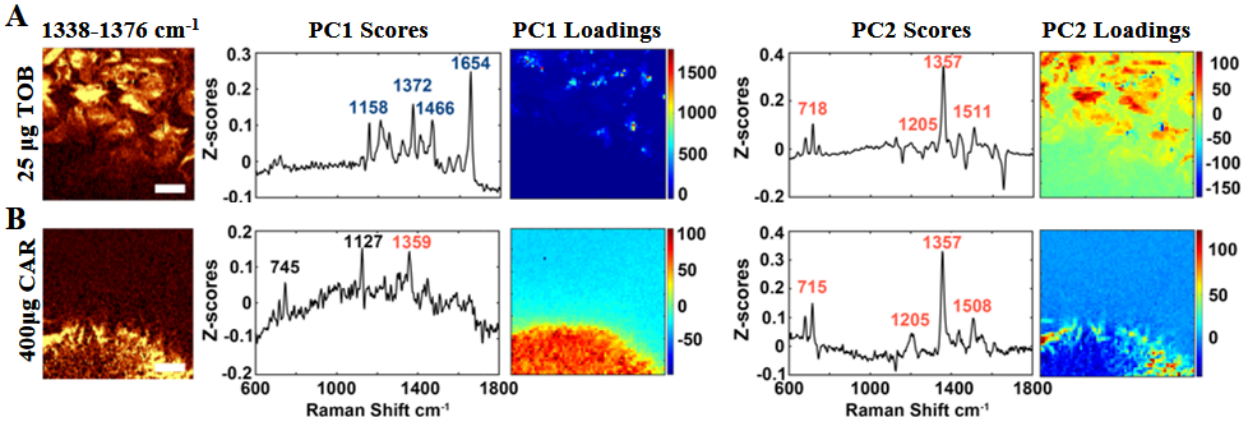

Figure 7.4. *P. aeruginosa* swarms exhibit chemically distinct responses to specific antibiotics. Swarm colonies exposed to (**A**) 25 µg tobramycin (TOB), and (**B**) 400 µg carbenicillin (CAR) were analyzed 48 h after exposure to antibiotics by combining CRM and PCA to identify chemically significant variations within the samples. Shown are representative CRM data collected from swarm regions proximal to the antibiotic treatment. Scale bars on Raman images represent 30 µm. Loading plots for PC1 and PC2 include features corresponding to Raman spectra from cellular components (black), PQS (blue), and AQNOs (HQNO/NQNO; red). Cellular components are identified by the presence of the thymine ring stretch in DNA (~745 cm^{-1}), and to the C-N stretch in proteins and C-O stretch in lipids (1127 cm^{-1}). PQS is associated with features at 1158, 1372, 1466, and 1654 cm^{-1}, and AQNOs with features in 715, 1205, 1359, and 1508 cm^{-1}.

7.3.2. PQS Promotes Cell Death and Reduced Swarming for Cells Exposed to Tobramycin

Because previous reports have shown various roles for PQS, namely as a stress response, for planktonic *P. aeruginosa* cells exposed to antimicrobials,[22, 26, 36-38] we were interested to explore how AQs mediate *P. aeruginosa* behavior during swarming. Additionally, the CRM chemical profile of *P. aeruginosa* swarms provided evidence that tobramycin exposure cues aspects of PQS production or regulation (**Figure 7.3**). Thus, we probed the swarming behavior of *P. aeruginosa* wild-type, and PQS (Δ*pqsH*) and AQNO (Δ*pqsL*) deficient strains in the presence of tobramycin using confocal laser scanning microscopy (CLSM).

While increased concentrations of tobramycin led to a decrease in swarm coverage area for all strains (**Figure 7.5A-B**), overall expansion of the PQS^- (Δ*pqsH*) swarm was significantly less affected. Cells within swarms of PQS^+ strains that were not exposed to tobramycin showed cell

death localized toward the swarm center as determined by propidium iodide (PI) staining (**Figure 7.5A**). This result agrees with prior reports that show PQS to be involved in cell death and swarm repression[22, 24] as well as our CRM results that show PQS present at the swarm center under these conditions (**Figure 7.3A**). Cell death in both wild-type and AQNO$^-$ strains is primarily localized toward the side of the swarm closest to tobramycin at the 10 µg dose condition, and distributed evenly in swarms exposed to 25 µg (**Figure 7.5A**). The Δ*pqsL* strain, which produces PQS and its derivatives but not *N*-oxides, does not show a reduced swarm phenotype in comparison to the wild-type at any of the tested tobramycin exposures (0, 10, 25 µg) (**Figure 7.5B**). Similarly, this Δ*pqsL* strain does not show increased cell death (**Figure 7.5C**). However, swarms of the PQS$^-$ strain (Δ*pqsH*) are less sensitive to tobramycin and present significantly reduced PI signal intensity compared to PQS$^+$ strains (**Figure 7.5B-C**).

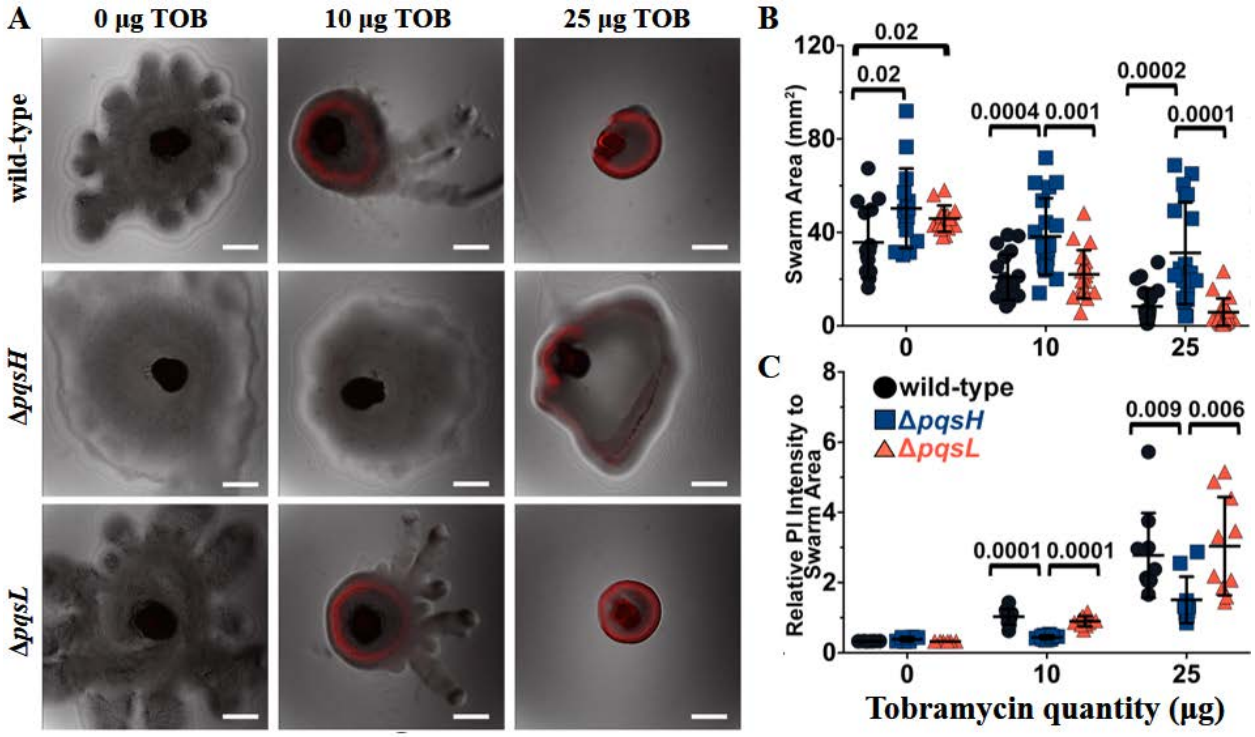

Figure 7.5. Impact of the PQS and *N*-oxide AQs on the response of *P. aeruginosa* swarm colonies to tobramycin. (**A**) Representative CLSM images show *P. aeruginosa* swarms stained with propidium iodide (PI). For each strain at 0 µg (n = 3), 10 µg and 25 µg TOB (n = 5) (**B**) Scattered plots of swarm coverage area from optical images of the full swarm showing the trend in swarm area reduction for each strain at 0 µg TOB (n = 15), 10 µg and 25 µg TOB (n = 19). SD error bars shown. (**C**) Scattered plots show the relationship between cell-death and antibiotic concentration normalized to swarm coverage area (PI stain I_{Max} / Swarm area) for each strain at 0 µg TOB (n = 6), 10 µg and 25 µg TOB (n = 10). SD error bars shown. For both (**B**) and (**C**) P-values were calculated from an unpaired *t*-test and are provided above comparison brackets.

Our combined results show that although swarms of wild-type *P. aeruginosa* exposed to tobramycin undergo a chemical shift that favored PQS (**Figure 7.3**), swarms of the PQS$^-$ strain (Δ*pqsH*) appeared better suited for survival of tobramycin treatment compared to swarms of wild-type and AQNO deficient (Δ*pqsL*) strains (**Figure 7.5**).

As expected, untreated planktonic cells of the three strains behave similarly (**Figure 7.6A**), while the PQS$^-$ strain (Δ*pqsH*) was less susceptible to tobramycin than wild-type and AQNO$^-$ strains (**Figure 7.6B**). However, this was not the case for cells exposed to carbenicillin, which does not elicit a PQS response (**Figure 7.4B**). No survival differences were observed between the wild-type and AQ mutants in planktonic cultures exposed to carbenicillin (**Figure 7.6C**).

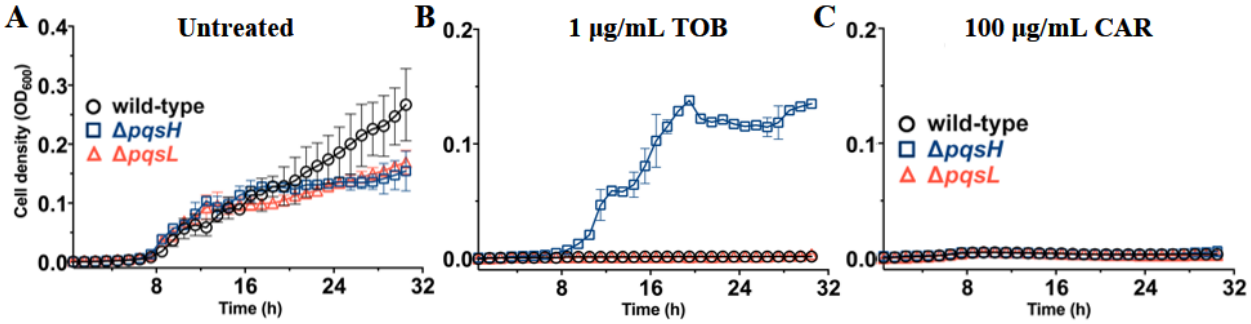

Figure 7.6. The growth response of *P. aeruginosa* to antimicrobial treatment is antibiotic specific. The growth of *P. aeruginosa* wild-type (circles), ΔpqsH (squares), and ΔpqsL (triangles) strains exposed to (**A**) no antibiotics, (**B**) 1 µg/mL tobramycin (TOB) and (**C**) 100 µg/mL carbenicillin (CAR) was monitored over 30 h. Mean values and SD error bars for three replicates shown.

7.3.3. *P. aeruginosa* Independently Modulates PQS- and *N*-Oxide-Type AQs in the Presence of Tobramycin

While the AQ response of *P. aeruginosa* to tobramycin varied in a dose dependent manner, the relative AQ levels are also spatially heterogeneous within the swarms. In an effort to better understand how swarming communities modulate AQ production in the presence of tobramycin we conducted a series of SIMS imaging experiments on 9 independent swarm samples (3 replicates for each experimental condition). SIMS product ion imaging was used to specifically target the 7 and 9 carbon AQs (i.e. PQS, C9-PQS, HQNO, and NQNO). Imaging results for all four AQs are shown in **Figure 7.7**.

In contrast to the CRM results of **Figures 7.3** and **7.4**, the SIMS product ion images in **Figure 7.7** shows that all four AQs are present under all tobramycin dosage conditions. This difference is not surprising, as the sensitivity of SIMS to these analytes is better than CRM, allowing it to image otherwise unobservable chemical species. For the 0 and 10 µg TOB treatment conditions, the distribution of all four AQs roughly follows that of the cell density (data not shown)

with little apparent distribution differences between individual AQs or AQ classes. At the 25 µg treatment condition however, in addition to the presence of PQS in regions of high cell density, a

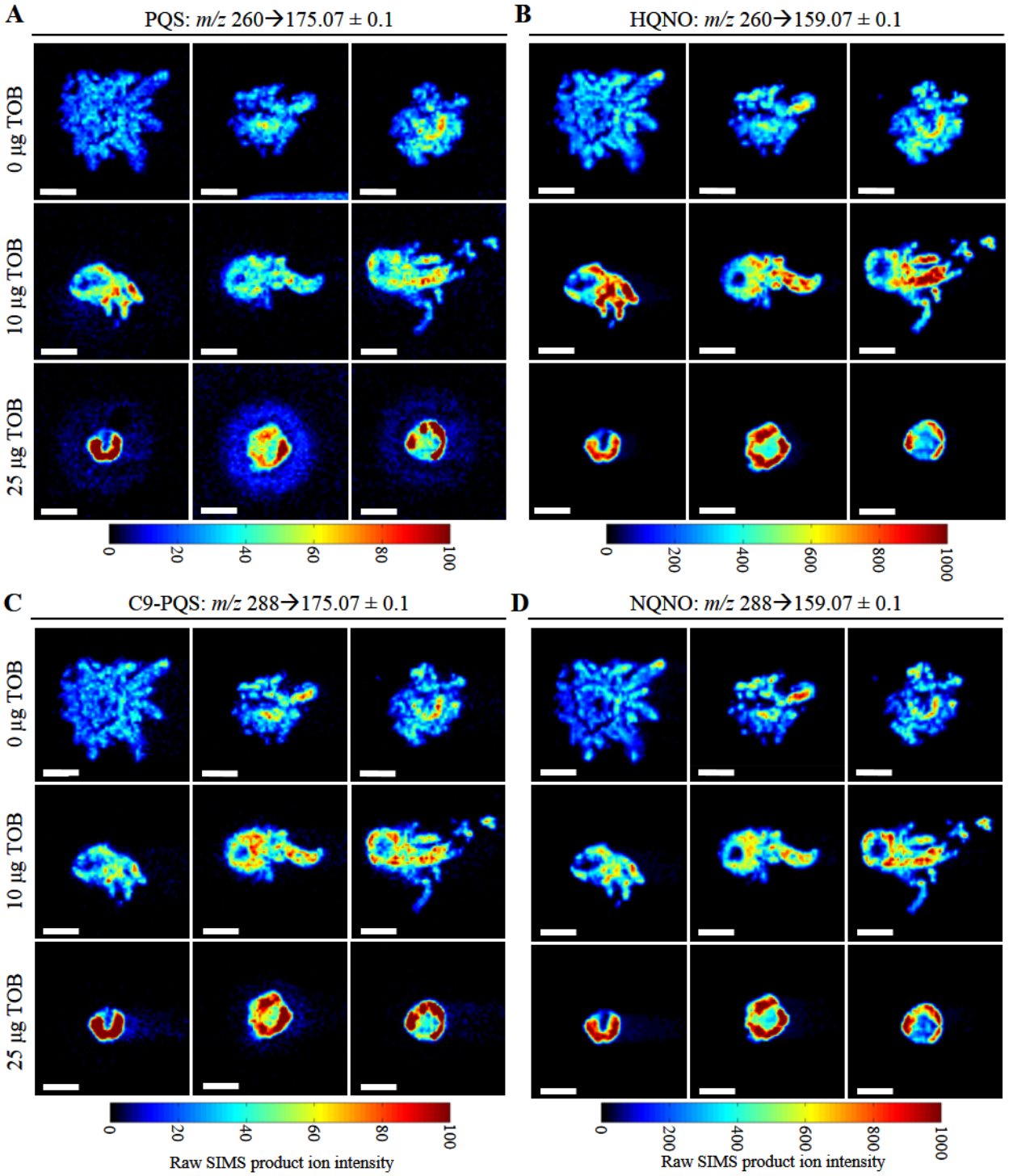

Figure 7.7. SIMS product ion imaging of (**A**) PQS, (**B**) HQNO, (**C**) C9-PQS, and (**D**) NQNO in 48 h *P. aeruginosa* swarms in the presence of 0, 10, and 25 µg of tobramycin. The maximum ion intensity has been set to a common value for each ion to enable inter-sample comparison. All scale bars represent 2 mm.

ring of low abundance PQS ion signal is observable around the outer perimeter of the swarm (**Figure 7.7A**). This ring is only present for PQS; it is unobservable in the corresponding ion images for HQNO (**Figure 7.7B**), C9-PQS (**Figure 7.7C**), and NQNO (**Figure 7.7D**). After further saturating the intensity scale for C9-PQS, some low intensity signal can be observed but it is inconsistent and difficult to separate from the background for two of the samples. We did not observe HQNO and NQNO at the periphery even after fully saturating the intensity scale.

We performed relative quantitation on the SIMS product ion images from **Figure 7.7** to compared the relative abundance of PQS/HQNO and C9-PQS/NQNO in swarm regions containing the less motile and more protected cells (swarm center) with the most motile and most exposed cells (swarm edge) (**Figure 7.8A-B**). In swarms exposed to 0 or 10 µg tobramycin, the relative abundance of PQS/HQNO and C9-PQS/NQNO is significantly higher toward the center of the swarm than the edge. This is in stark contrast to the 25 µg exposure condition, where the ratio shifts to reveal a significantly greater relative abundance of PQS/HQNO and C9-PQS/NQNO at the edge of the swarm in comparison to the center).

We also assessed the relative abundance of AQs among swarming cells closest to the antibiotic exposure (near) compared to swarming cells farthest from the antibiotic exposure (away) (**Figure 7.8C-D**). Alterations in the PQS/HQNO and C9-PQS/NQNO ratios were observed over 2D space for the 10 µg tobramycin condition, with significantly higher intensities of the PQS family relative to the corresponding AQNOs 'near' to the tobramycin source. The region 'near'

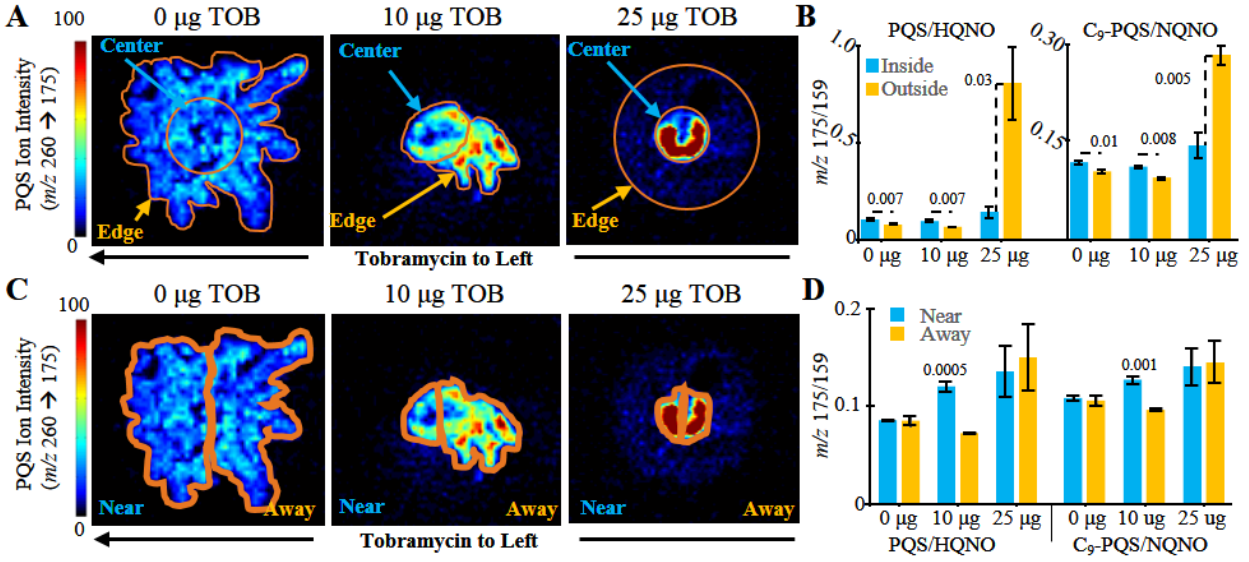

Figure 7.8. Relative quantitation with SIMS product ion imaging. (**A-B**) Relative abundance of PQS/HQNO and C9-PQS/NQNO for the center and the edge of the neat and tobramycin exposed swarms. (**C-D**) Relative abundance of PQS/HQNO and C9-PQS/NQNO near to and away from the tobramycin.

the 10 µg tobramycin presented reduced levels of AQNOs compared to the region away from tobramycin. Notably, no difference in the ratio of PQS-type/AQNO was observed between the 'near' and 'away' regions of the 0 and 25 µg exposure levels, likely due to the symmetry of the swarm colonies.

Imaging PCA was performed on the SIMS product ion images to explore the complex interactions of the multiple product ions associated with each AQ (**Figure 7.9**). For both the 10 µg (**Figure 7.9A**) and 25 µg (**Figure 7.9B**) treatment condition, separation between the two AQ subclasses was observed on the second principal component, with product ions corresponding to PQS found on the positive loadings and product ions corresponding to HQNO found on the negative loadings. The scores images show a bias of PQS toward areas where the tobramycin exposure is greatest, i.e. at the center and left side of the 10 µg sample and around the periphery of the 25 µg sample. Interestingly, product ions corresponding to PQS are also separated towards the very center of the 25 µg sample, resulting in an alternating three-three ring system of PQS-HQNO-PQS. Similar trends are observed for the product ion images of the C9-PQS/NQNO

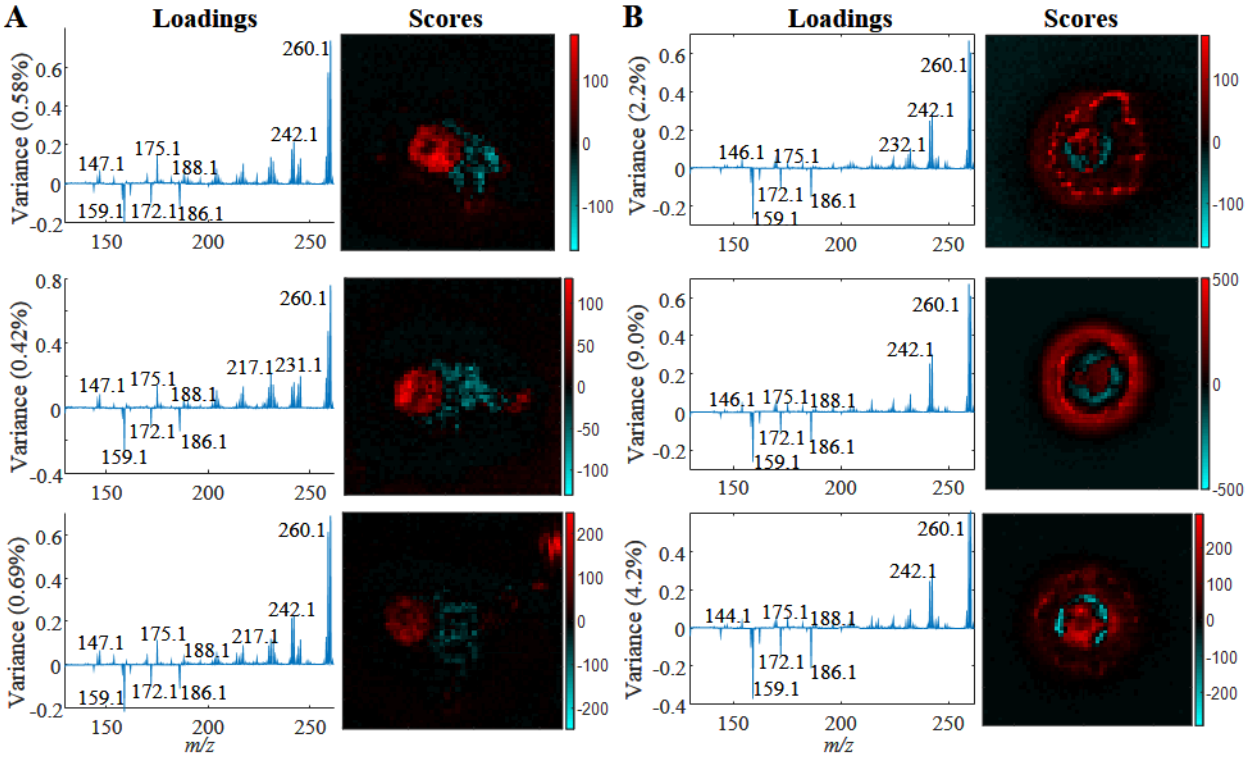

Figure 7.9. SIMS product ion imaging PCA of the three (**A**) 10 µg and (**B**) 25 µg tobramycin treated swarms from **Figure 6.7**. PC2 from product of 260 is shown. In each case the product ions arising from PQS (e.g. *m/z* 147, 175, and 188) are found on the positive loadings (red scores) and the product ions arising from HQNO (e.g. *m/z* 159, 172, and 186) are found on the negative loadings (cyan scores).

precursor ion (*m/z* 288), however they are less pronounced. A similar analysis was performed on the untreated samples, however no clear patterns of separation were observed.

The SIMS product ion imaging PCA results corroborate the relative quantification results (**Figure 7.8**) and validate the CRM observations (**Figure 7.3** and **7.4**), indicating that when exposed to the aminoglycoside tobramycin, *P. aeruginosa* cells undergo a metabolite shift that results in independent modulations to PQS, C9-PQS, HQNO, and NQNO that is dependent on the proximity to the antibiotic treatment. This change is more distinct for PQS and C9-PQS than for HQNO and NQNO. The PQS response was heterogeneous throughout the swarm community at both exposures. Although AQNO levels also increased in a dose-dependent manner, the recorded response was more homogeneous throughout the swarm community.

A series of SIMS product ion imaging calibration curves for the four AQs were created by depositing standards onto dried agar followed by SIMS product ion imaging (**Figure 7.10**). The resulting images were processed by averaging the ion intensity in each ROI and plotting the average intensity per pixel vs the surface density of the spots (see the **Materials and Methods** section). A plot of the average surface density vs average intensity per pixel yielded a quadratic relationship with coefficient of determination (R^2) values better than 0.995 in all cases. The lower and upper limits of quantitation (LLOQ and ULOQ respectively; defined as the lowest and highest surface density on the calibration curve) were 50 pmol x cm^{-2} and 710 pmol x cm^{-2} for PQS (**Figure 7.10A**), 20 pmol x cm^{-2} and 370 pmol x cm^{-2} for HQNO (**Figure 7.10B**), 40 pmol x cm^{-2} and 360 pmol x cm^{-2} for C9-PQS (**Figure 7.10C**), and 210 pmol x cm^{-2} and 1430 pmol x cm^{-2} for NQNO (**Figure 7.10D**).

Using the quadratic equation and the ion specific second order polynomial calibration equations from **Figure 7.10**, the average surface density for the 9 tobramycin exposed swarm communities from **Figure 7.7** was computed. While the detailed 3D geometry of these swarms is not known, we estimated the swarm community height to be between 5-20 microns.[34] Accordingly, for the swarm exposed to no tobramycin, the PQS and C9-PQS concentrations are estimated to be between 50-210 μM and 50-180 μM, respectively (**Figure 7.11A**). The concentrations of HQNO and NQNO in the unexposed samples was found to be between 60-250 μM and 130-530 μM respectively (**Figure 7.11A**). The concentrations of all four analytes increases slightly for the swarms exposed to 10 μg tobramycin, and they are almost 2-fold higher for HQNO and NQNO in the center of the samples exposed to 25 μg tobramycin. An attempt was also made to measure the

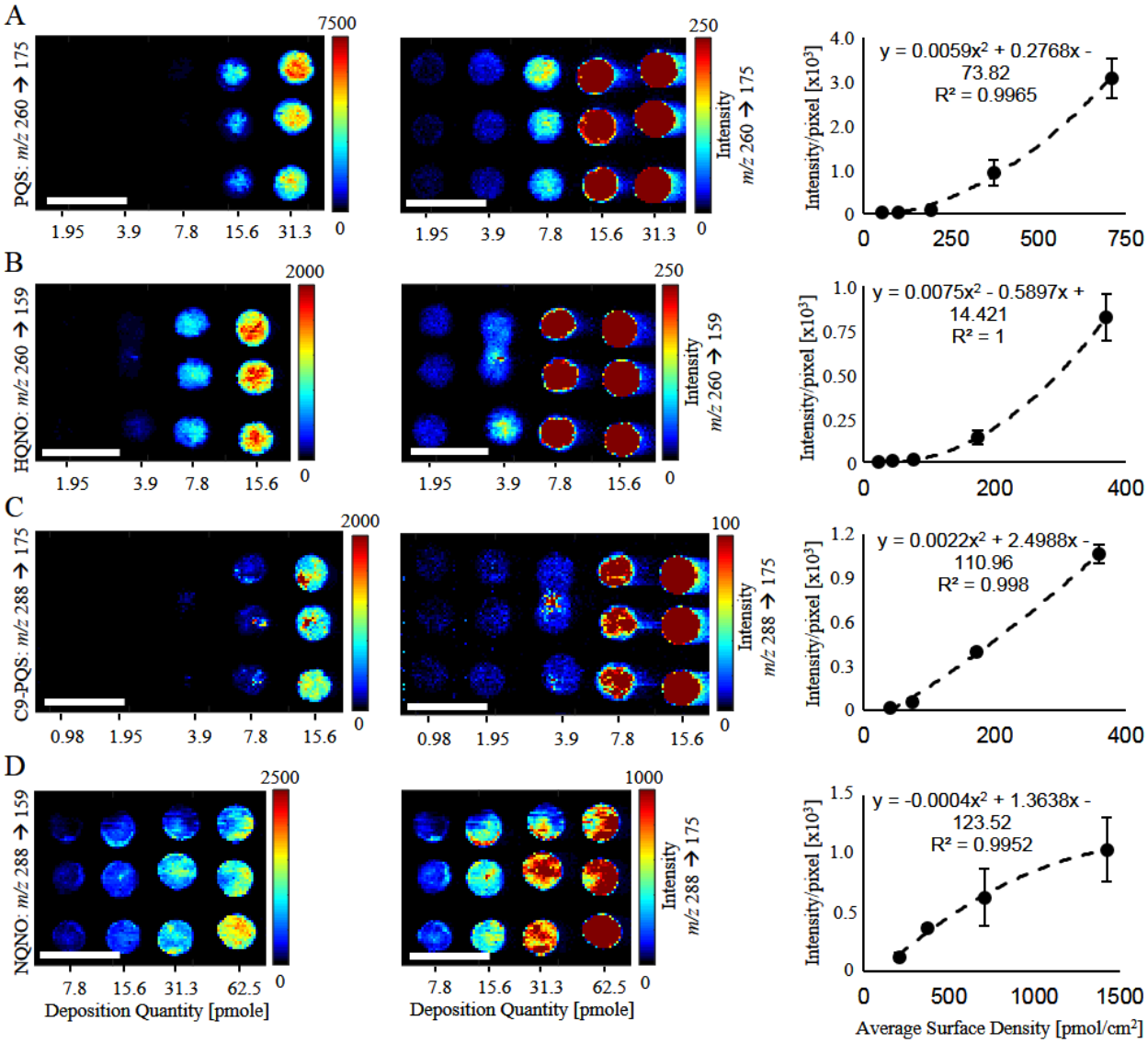

Figure 7.10. SIMS product ion imaging calibration spots and quadratic calibration curves for (**A**) PQS, (**B**) HQNO, (**C**) C9-PQS, and (**D**) NQNO on agar. Scale bars represent 5 mm in all images.

concentration in the PQS-rich outer ring of the sample exposed to 25 µg tobramycin, but the measured ion intensities were below the (LLOQ) in all cases.

The quantity of all four AQs in the swarms is more than 10 times greater than that previously reported for *P. aeruginosa* planktonic cells,[17] and the measured concentrations exceed the solubility of AQs in water,[39] a finding that is supported by the visual identification of aggregates using standard light microscopy (**Figure 7.12A-B**) and CRM (**Figure 7.12C**).

It is worth noting that we did not find evidence of membrane vesicles or membrane debris in our CRM results, which potentially indicates that these AQs were released from *P. aeruginosa* during swarming in the absence of membrane vesicles, a likely result of cell lysis. It is currently

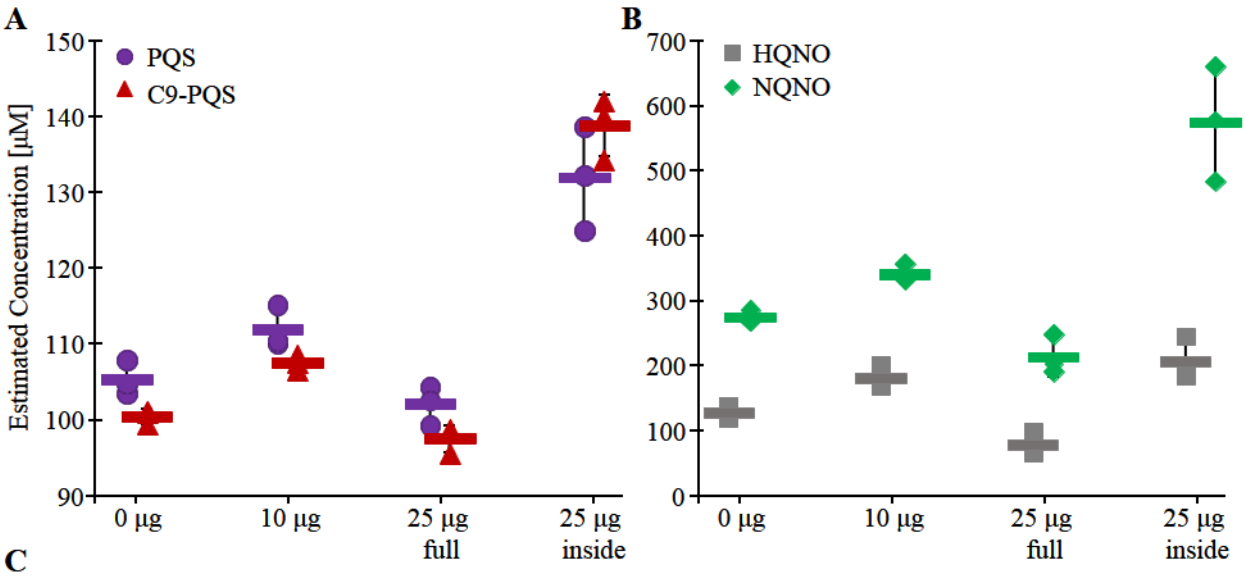

C

PQS p-values				
vs 0 µg		0.03	0.2	0.003
vs 10 µg	0.03		0.01	0.009
vs 25 µg F	0.2	0.01		0.002
vs 25 µg I	0.003	0.009	0.002	

HQNO p-values			
	0.01	0.01	0.02
0.01		0.002	0.3
0.01	0.002		0.004
0.02	0.3	0.004	

C9-PQS p-values			
vs 0 µg		0.001	0.06	0.00009
vs 10 µg	0.001		0.001	0.0002
vs 25 µg F	0.06	0.001		0.00008
vs 25 µg I	0.00009	0.0002	0.00008	

NQNO p-values			
	0.002	0.04	0.004
0.002		0.003	0.01
0.04	0.003		0.002
0.004	0.01	0.002	

Figure 7.11. Estimated concentrations of (**A**) PQS and C9-PQS and (**B**) HQNO and NQNO for *P. aeruginosa* swarms exposed to tobramycin. Each data point is plotted along with the mean (thick bar) and standard deviation (error bars) of the three measurements with an estimated swarm thickness of 10 µm. The p-values in (**C**) were calculated via a two-tailed student's t-test with homoscedastic variance, and p values greater than 0.05 are highlighted in blue.

unknown if these aggregates occur within the CF environment and the benefits (if any) of such structures to *P. aeruginosa* behavior during infection.

7.4. Discussion

Here we have shown that PQS and its associated signaling pathway are not universally invoked in response to antimicrobials during *P. aeruginosa* swarming. While exposure to the aminoglycoside tobramycin and the β-lactam carbenicillin produced analogous reductions in swarming, at the gross cellular morphology and chemical levels the responses were quite distinct. Additionally, we found that exposure to tobramycin, but not carbenicillin, resulted in profile shifts of both PQS and AQNO

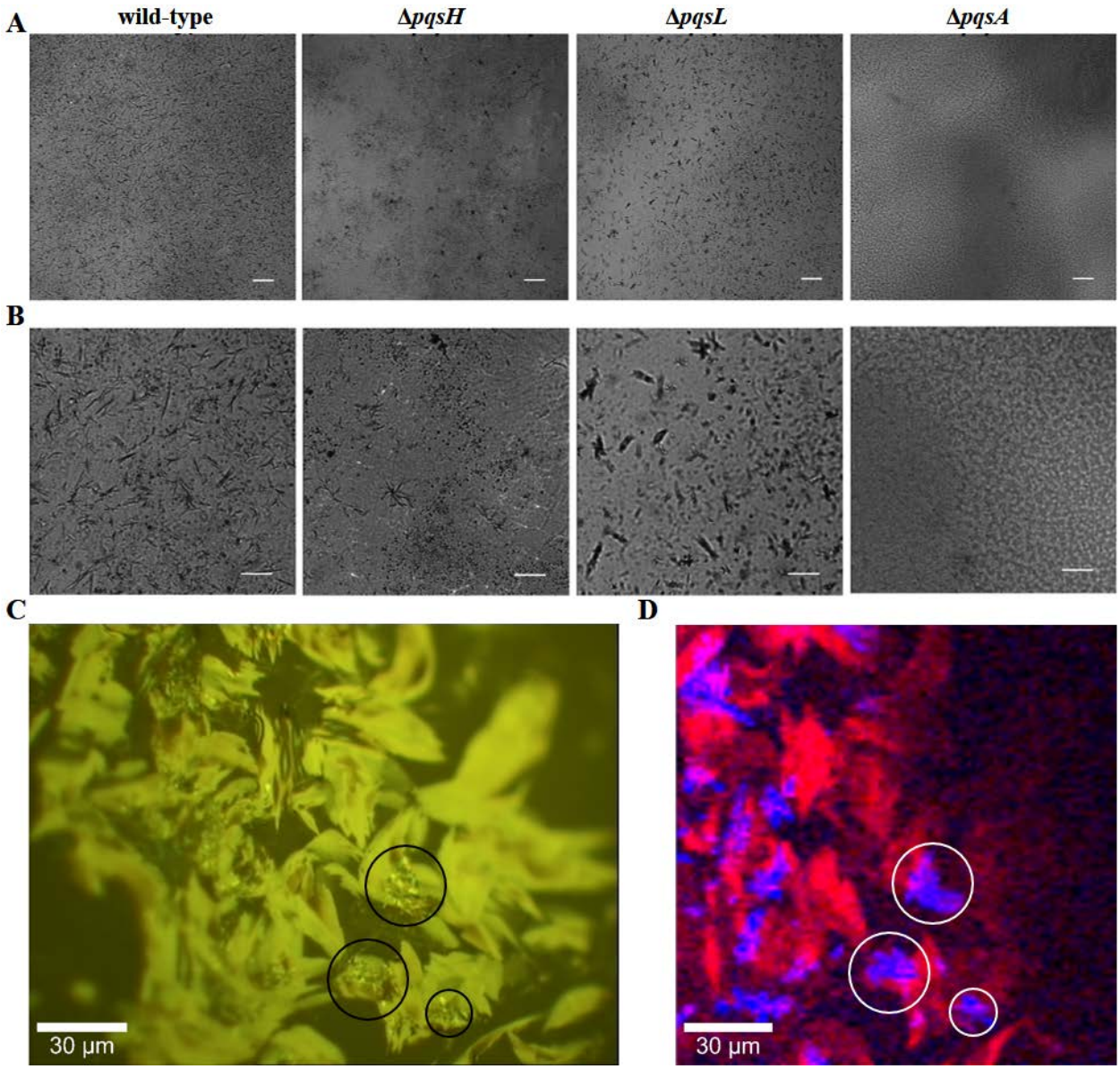

Figure 7.12. AQ aggregates are visible by standard light microscopy in *P. aeruginosa* swarm colonies. Representative microscopy images of AQ aggregates visualized from untreated swarm colonies of PA14 wild-type, PQS-type deficient (Δ*pqsH*), *N*-oxide deficient (Δ*pqsL*), and AQ deficient (Δ*pqsA*) strains are shown. (**A**) A wide view and (**B**) zoomed view of the structures is provided. (**C**) High resolution optical image and (**D**) corresponding CRM image of PQS-type (blue, 1638-1676 cm^{-1}) and *N*-oxide type (red, 1338-1376 cm^{-1}) AQs in a 48 h wild-type swarm treated with 25 µg tobramycin. Scale bars represent (**A**) 100 µm, (**B**) 50 µm, and (**C-D**) 30 µm.

families during swarming. This is in contrast to reports that have suggested a general PQS response to antimicrobial stress.[22, 26-27] Our findings are consistent with the hypothesis that AQ modulations following tobramycin exposure during 'pre-biofilm' swarming should contribute to antibiotic tolerance during infection,[22, 25, 36] however, other factors must control *P. aeruginosa* tolerance to carbenicillin.

Surprisingly, we routinely observe PQS and AQNOs in collective organized aggregates. The behavior of externally-applied HQNO on swarm media suggest that these structures arise from interactions of the AQ molecules with their immediate environment. On their own, these aggregates lack mobility (no spreading visible on swarm media) likely relying on the mobility of the swarm, be it by interactions with the cells or by the action of surfactants such as rhamnolipids[39] for translocation.

Much of what we had known regarding the chemical profile of *P. aeruginosa* swarms arises from some combination of homogenized samples and extrapolation of nucleic acid profile data.[1, 4-5, 40] There is less information about the spatial distribution of biomolecules associated with *P. aeruginosa* swarms. Here, we used multimodal chemical imaging to assess biochemical profiles and other aspects of cell behavior preserving the 2D heterogeneity of secreted factors. Employing CLSM, CRM, and SIMS imaging allowed both universal and antibiotic-specific chemical responses to be identified in these communities, as well as localized responses within each swarm colony that depend on the concentration of the antibiotic. These results model and preview the complex biological responses that surface attached biofilms are likely to exhibit in the clinical setting, where antibiotic gradients may alter the physiochemical profile of some, but not all, cells in a community, and cell concentrations as well as strain mutations could alter sensitivity to specific antimicrobials.

Our assessment of several metrics at different exposure levels leads us to conclude that PQS is a short range signal in comparison to AQNOs, both of which increase in response to tobramycin. Clear distinctions in the AQ spatial profile were apparent in 2D space. At 10 µg tobramycin exposure, which still allowed for some *P. aeruginosa* swarming, we observed PQS to be most prevalent in the region nearest the antibiotic while AQNOs localized furthest away from the tobramycin spot on the swarm tendrils. Swarms exposed to 25 µg tobramycin did not spread over surfaces, and these samples showed a clear distribution bias of PQS toward the swarm edge relative to the center. Our collective evidence indicates that PQS is the AQ signal associated with the most severe stress response and swarming repression. The spatial partitioning of PQS to the regions proximal to greatest tobramycin exposure could serve to protect swarm colonies from the deleterious effects of tobramycin, to condition swarms to antimicrobial stress, or be linked to the role of PQS in cell death and biofilm formation.[10, 20-22, 24, 41] In response to tobramycin, AQNOs

were distributed throughout the swarm, which leads us to conclude that these signaling molecules act at a community-wide scale.

Aminoglycoside antibiotics are known to primarily bind to the 30S ribosomal subunit, inhibiting protein synthesis.[42] As a consequence, aminoglycosides have also been shown to disrupt the cell envelope leading to cell death. Interestingly, due to its polycationic nature, tobramycin readily binds nucleic acids,[43] and is reported to bind to mucin- and DNA- rich fractions of Cystic Fibrosis (CF) sputum,[44] reducing effectiveness in the treatment of polymicrobial infections of *P. aeruginosa* and *S. aureus*.[18] Shifting the balance of PQS and AQNOs may alter cell-membrane permeability and damage leading to higher concentrations of easily accessible DNA at the edge of the swarm facing the aminoglycoside.

In *P. aeruginosa*, the PQS molecule and associated regulatory pathway are linked to numerous cellular processes including swarm repression, stress response, cell lysis, DNA release, outer membrane vesicles (OMV) biogenesis, and biofilm development.[20-22, 24, 41, 45] The AQNOs, HQNO and NQNO, are both effective anti-*Staphylococcal* molecules that modulate the interaction between *P. aeruginosa* and *Staphylococcus aureus*.[18, 25] Since both PQS and AQNOs serve critical roles, we expect that the ubiquitous nature of AQNOs may serve as protection to these expanding swarms, while the abundance of PQS at the center may promote a biofilm state. Although the PQS^- strain (Δ*pqsH*) shows swarm reduction in response to tobramycin, it shows significantly less cell death than either the wild-type or the AQNO mutant (Δ*pqsL*). The overall reduction of swarm expansion in response to tobramycin and carbenicillin for all strains, suggests that other mechanisms that control the physical behavior of the swarm may come into play.[34] Because neither the Δ*pqsH* or Δ*pqsL* strains show significant increases in AQNO or PQS, respectively, upon exposure to tobramycin, we conclude that AQs in general, and the PQS pathway specifically, are not regulated by a classical mechanism of transcriptional induction or feedback inhibition.

Wild-type (and Δ*pqsL*) swarms that produce PQS exhibited increased cell death response to tobramycin exposure. Our research showed greater levels of exposed DNA in the swarm region closer to tobramycin (Fig. 3). This barrier of highly accessible DNA or damaged cells could temporarily prevent swarm expansion to the region closer to the antibiotic, cue biofilm development, or serve as cellular decoys to bind and sequester tobramycin. Thus, DNA may protect swarming cells from the action of aminoglycosides, as has been found within stationary biofilms.[10, 43]

Our multiplexing approach allowed us to obtain a comprehensive picture of *P. aeruginosa* behavior in space that could not be observed in most lab-scale systems. The data argue against PQS serving as a generalized cellular 'preconditioning' cue to stress. Instead, they are more consistent with PQS serving as a short-term and short-range signal. We find dramatic spatial heterogeneity of PQS and other AQ molecules in these high-density *P. aeruginosa* swarm communities. Clearly our current understanding of *P. aeruginosa* quinolone signaling is limited, since the AQ distributions within these swarming communities cannot be explained solely by population dependent quorum sensing or stress response dogma. Our findings indicate that PQS and AQNO are independently regulated signals intended to communicate differing messages. After the closest *P. aeruginosa* cells sense tobramycin exposure, PQS signals reach only a nearby subset of the community while AQNOs propagate community-wide. Thus, prior to developing attached biofilms, *P. aeruginosa* may be capable of relaying a complex hierarchy of chemical messages to community members in response to a single environmental stimulus.

7.5. Materials and Methods

7.5.1. Strains, Standards, and Culturing Conditions

Strains, plasmids, and specialized materials used in this study are included in **Table 7.1**. Isolated bacterial colonies from Lysogeny Broth (LB) agar were used to inoculate 6 mL of modified FAB minimal medium supplemented with 30 mM glucose, and followed by overnight (<16 - 20 h) incubation at 37 °C, 240 rpm. Overnight cultures normalized to OD_{600nm} of 0.5 in FAB (without glucose for swarm assays and with 12 mM glucose for microtiter dish antibiotic susceptibility assays) were used for inoculations. The setup for swarm and microtiter dish assays are detailed below.

A GFP expressing version of *P. aeruginosa* PA14 was chromosomally labeled with green fluorescent protein (GFP) using a mini-Tn7-*gfpmut2* cassette introduced by four-parental mating.[51] GFP expression was confirmed via microscopy.

7.5.2. Swarm Assays

Swarm motility assays were performed in 60 mm dia. petri dishes containing 7.5 mL of modified FAB culture media supplemented with 12 mM glucose and solidified with 0.45% Noble agar (Sigma).[52] Response to antibiotics was tested by adding 5 μL of diluted antibiotics to 10 mm dia. filter discs (Sigma) placed on top of the swarm media. Normalized cultures at OD_{600nm} of 0.5 were

Table 7.1. Bacterial strains, plasmids, and specialized materials.

Strain or plasmid	Description	Source or reference
P. aeruginosa PA14:		
wild-type	wild-type strain	[46]
wild-type GFP	PA14::mini-Tn7-*gfp2*; Gm^r	This study
Δ*pqsH*	Δ*pqsH* in PA14 wild-type	[47]
Δ*pqsL*	Δ*pqsL* in PA14 wild-type	[17]
Δ*pqsA*	Δ*pqsA* (U479) in PA14 wild-type	PA14 Transposon Insertion Mutant Library
Plasmids:		
AKN66	mini-Tn7-*gfp2*; Gm^r, Cm^r	[48]
pUX-BF13	Conjugation helper plasmid, Ap^r	[49]
pRK600	Mobilization plasmid, Cm^r	[50]
Specialized materials:		
HHQ	2-heptyl-4-quinolone	Sigma
NHQ	2-nonyl-4-quinolone	Cayman chemicals
PQS	2-heptyl-3-hydroxy-4(1H)-quinolone	Cayman chemicals
C9-PQS	2-nonyl-3-hydroxy-4(1*H*)-quinolone	Cayman chemicals
HQNO	2-heptyl-4-hydroxyquinoline *N*-oxide	Cayman chemicals
NQNO	2-nonyl-4-hydroxyquinoline *N*-oxide	Cayman chemicals
Copper tape	0.088 mm thick double-sided conductive copper tape, 3M 1182	Ted Pella, USA

inoculated with an inoculation needle 10 mm away from the edge of the filter disc containing the antibiotic treatment. For assays in which the extent of cell damage or DNA release was determined by microscopy (detailed below) a final concentration of 20 μM propidium iodide (PI) was added to the media prior to solidification. Swarm assays were incubated inverted at 30°C, 85% RH, for 48 h, and removed for analysis. Swarms were analyzed directly without further preparation by confocal laser scanning microscopy (CLSM) and confocal Raman microscopy (CRM), or processed for second ion mass spectrometry (SIMS) imaging.

7.5.3. CLSM Imaging and Analysis

Optical images of swarms were acquired using a Nikon D3300 camera equipped with a Nikon AF-S DX NIKKOR (18-55 mm 1:3.5-5.6 VR II, ∞-0.28m/0.92ft ø52). Swarm coverage area was

determined from optical images using ImageJ64 as previously described.[52] Images were acquired using a Nikon Eclipse 90i confocal microscope equipped with a Nikon CFI Plan Apochromat λ 2× (NA 0.10, ∞/-, WD 8.5 mm) or a Ti-E Nikon fluorescence microscope equipped with an Andor iXon ultra CCD camera and a CFI LU Plan Fluor EPI 100×A dry objective (NA 0.90, ∞/0, WD 1.0 mm). The NIS-Elements AR Imaging Software was employed to analyze each swarm at the sample depth (Z- section) with the highest PI sum signal intensity. The ROI tool was used to delineate the swarm coverage area within each field of view, and the swarm coverage area to PI sum intensity ratio calculated. Data analysis for combined data replicates was performed with GraphPad Prism.

7.5.4. CRM Imaging and Analysis

CRM is a non-destructive spectroscopy technique that allows differentiation of chemical classes based on the presence or absence of class-specific functional groups. CRM imaging was performed as previously described,[16] briefly, Raman images were acquired using a 40x objective (NA = 0.6). Images were obtained by acquiring a full Raman spectrum from each image pixel (150 × 150, 100 × 100 or 80 × 80 pixel) over a selected region on the swarm sample with an integration time of 100 ms per spectrum. The alkyl-quinoline (AQ) standards were dissolved in either HPLC-grade ethanol or methanol (Sigma), then deposited and air-dried on clean Si wafers for SIMS and CRM analysis. MATLAB was used to perform Principal Component Analysis (PCA) using previously described custom scripts[53] to detect chemical variations in the samples.

7.5.5. SIMS Imaging and Product Ion Imaging

The agar containing the swarm colonies was excised from the petri dish and placed on custom aluminum SIMS plates covered with 0.088 mm thick double-sided conductive copper tape. Samples were dried under a gentle nitrogen stream. Dehydrated samples were examined via time-of-flight (TOF) SIMS imaging using a custom instrument described in detail elsewhere.[54] Briefly, the instrument is a modified AB SCIEX QTOF imaging mass spectrometer (AB SCIEX, Framingham, MA) equipped with a 20 keV Buckminsterfullerene (C_{60}^+) primary ion beam and tandem-MS capabilities. Each sample was imaged three times. First in untargeted mode to collect all positive secondary ions within the mass-to-charge (*m/z*) acceptance window of *m/z* 60–850, second in product ion mode to collect fragment ions arising from *m/z* 260 (the protonated molecular ion of PQS and HQNO), and third in product ion mode to collect fragment ions arising from *m/z* 288 (the protonated molecular ion of C9-PQS and NQNO). In all cases the imaging was

performed in raster mode with a pixel size of 150 μm x 150 μm and a 50 μm offset between images to avoid repeated sampling of the same region. The primary ion source was adjusted to produce a 40 μm dia. spot size with 500 pA of sample current, and external calibration was performed using In_{1-7}^+ cluster ions.

Untargeted imaging was performed with a Q1 bias of 15%, 25%, and 60% at *m/z* 100, 200, and 400 respectively. The "slower" raster setting was used, resulting in a 500 ms of bombardment/pixel and an approximate primary ion dose of 3 x 10^{13} ions/cm^2. Product ion imaging was conducted in "enhance all" mode with argon collision gas, 30 eV collision-induced dissociation energy, and a Q1 bias of 5%, 47.5%, and 47.5% at *m/z* 40, 90, and 180 respectively. The "slowest" raster setting was used, resulting in 750 ms of bombardment/pixel and an approximate primary ion dose of 4 x 10^{13} ions/cm^2.

The resulting data was collected in the native AB SCIEX wiff format, converted to mzML with the ProteoWizard msconvert function,[55] and further converted to imzML with the imzMLConverter program.[56] The images were rendered in MSiReader.[57] All images are presented without normalization.

We utilized highly sensitive C_{60}-SIMS product ion imaging to facilitate the detection and relative quantification of four targeted AQs (PQS, C9-PQS, HQNO, and NQNO) under the tested tobramycin exposure conditions. As with all mass spectrometry imaging (MSI) techniques, SIMS differentiates molecules based on their mass-to-charge ratio (*m/z*) and was therefore incapable of directly distinguishing structural isomers such as PQS and HQNO. To account for this, we conducted our analysis in product-ion mode, making it possible to differentiate between the molecular ions for each isomeric pair (i.e. PQS/HQNO and C9-PQS/NQNO). Our previous work with AQ standards,[16, 58] showed that the PQS family can be differentiated from AQNOs of the same alkyl side-chain length based on the presence of several distinguishing fragment ions; the most abundant of which were *m/z* 159.07 for AQNOs and *m/z* 175.07 for the PQS family.

7.5.6. SIMS Relative and Absolute Quantification

Relative quantification was performed to compare the PQS/HQNO and C9-PQS/NQNO ratios in the region of the swarm nearest to the antibiotic versus the region farthest away, and the center of the swarm versus the edge. In both cases the region of interest was outlined using the MSiReader ROI selection tool and the intensity was extracted for *m/z* 159.05 (which results from fragmentation of HQNO and NQNO) and *m/z* 175.05 (which results from fragmentation of PQS

and C9-PQS) using the following ion extraction settings: intensity = sum of window; *m/z* window = 0.1 Th; Normalization: none. The resulting values were summed over each ROI and the ratio of *m/z* 175.05/159.07 was computed. Error bars are standard deviation (from n = 3), and P-values were computed using the unpaired *t* test function from GraphPad Prism.

For absolute quantification, eight Log2 dilutions were prepared to contain between 0.98 μM and 125 μM of either PQS and NQNO or C9-PQS and HQNO and deposited in triplicate onto dried agar in 1 μL aliquots. The resulting spots were examined via SIMS product ion imaging via the previously described methods[54] and rendered in MSiReader.[57] The product ion intensity of the four analytes of interest in each spot and the PA14 wild-type swarm colonies, was exported into Excel using the MSiReader ROI and intensity export functions with a *m/z* window of 0.1, no normalization, and the "sum of window" option selected. Calibration curves (second order polynomial) of average surface density versus ion intensity per pixel were generated and the resulting quadratic equations were solved for the average surface density of each analyte in the swarm colonies, yielding results in pmol/cm^2.

7.5.7. Microtiter Dish Antibiotic Susceptibility Assays

Assays were performed in a 96-well microtiter dish containing 199 μL of normalized undiluted or 1,200 fold diluted *P. aeruginosa* cultures in FAB supplemented with 12 mM glucose. Three replicates containing 1 μL of antibiotic dilutions in sterile H_2O for final antibiotic concentrations of 0 μg/mL, 1.0 μg/mL tobramycin, and 100 μg/mL carbenicillin were included. Cultures were incubated in a Biotek H1 Synergy Microplate Reader at 37 °C and OD_{600nm} readings were collected every 1 h. Data analysis was performed with GraphPad Prism.

7.6. References

1. Köhler, T.; Curty, L. K.; Barja, F.; van Delden, C.; Pechère, J. C., Swarming of *Pseudomonas aeruginosa* is dependent on cell-to-cell signaling and requires flagella and pili. *J Bacteriol* **2000,** *182* (21), 5990-5996.
2. Yeung, A. T. Y.; Torfs, E. C. W.; Jamshidi, F.; Bains, M.; Wiegand, I.; Hancock, R. E. W.; Overhage, J., Swarming of *Pseudomonas aeruginosa* is controlled by a broad spectrum of transcriptional regulators, including MetR. *J Bacteriol* **2009,** *194* (19), 5388-5403.
3. Lai, S.; Tremblay, J.; Déziel, E., Swarming motility: a multicellular behaviour conferring antimicrobial resistance. *Environ Microbiol* **2009,** *11* (1), 126-136.
4. Tremblay, J.; Déziel, E., Gene expression in *Pseudomonas aeruginosa* swarming motility. *BMC Genomics* **2010,** *11*, 587.
5. Verstraeten, N.; Braeken, K.; Debkumari, B.; Fauvart, M.; Fransaer, J.; Vermant, J.; Michiels, J., Living on a surface: swarming and biofilm formation. *Trends Microbiol* **2008,** *16* (10), 496-506.

6. Morris, J. D.; Hewitt, J. L.; Wolfe, L. G.; Kamatkar, N. G.; Chapman, S. M.; Diener, J. M.; Courtney, A. J.; Leevy, W. M.; Shrout, J. D., Imaging and analysis of *Pseudomonas aeruginosa* swarming and rhamnolipid production. *Appl Environ Microbiol* **2011,** *77* (23), 8310-8317.
7. Partridge, J. D.; Harshey, R. M., Swarming: flexible roaming plans. *J Bacteriol* **2013,** *195* (5), 909-918.
8. Olsen, I., Biofilm-specific antibiotic tolerance and resistance. *Eur J Clin Microbiol Infect Dis* **2015,** *34* (5), 877-886.
9. Mah, T. F.; Pitts, B.; Pellock, B.; Walker, G. C.; Stewart, P. S.; O'Toole, G. A., A genetic basis for *Pseudomonas aeruginosa* biofilm antibiotic resistance. *Nature* **2003,** *426* (6964), 306-10.
10. Ciofu, O.; Tolker-Nielsen, T.; Jensen, P. Ø.; Wang, H.; Høiby, N., Antimicrobial resistance, respiratory tract infections and role of biofilms in lung infections in cystic fibrosis patients. *Adv Drug Deliv Rev* **2015,** *85*, 7-23.
11. Hoyle, B. D.; Costerton, J. W., Bacterial resistance to antibiotics: the role of biofilms. *Prog Drug Res* **1991,** *37*, 91-105.
12. Mann, E. E.; Wozniak, D. J., *Pseudomonas* biofilm matrix composition and niche biology. *FEMS Microbiol Rev* **2012,** *36* (4), 893-916.
13. Butler, M. T.; Wang, Q.; Harshey, R. M., Cell density and mobility protect swarming bacteria against antibiotics. *Proc Natl Acad Sci U S A* **2010,** *107* (8), 3776-3781.
14. Merritt, J. H.; Brothers, K. M.; Kuchma, S. L.; O'Toole, G. A., SadC reciprocally influences biofilm formation and swarming motility via modulation of exopolysaccharide production and flagellar function. *J Bacteriol* **2007,** *189* (22), 8154-64.
15. Pesci, E. C.; Milbank, J. B.; Pearson, J. P.; McKnight, S.; Kende, A. S.; Greenberg, E. P.; Iglewski, B. H., Quinolone signaling in the cell-to-cell communication system of *Pseudomonas aeruginosa*. *Proc Natl Acad Sci U S A* **1999,** *96* (20), 11229-34.
16. Baig, N. F.; Dunham, S. J. B.; Morales-Soto, N.; Shrout, J. D.; Sweedler, J. V.; Bohn, P. W., Multimodal chemical imaging of molecular messengers in emerging *Pseudomonas aeruginosa* bacterial communities. *Analyst* **2015,** *140* (19), 6544-6552.
17. Lépine, F.; Milot, S.; Déziel, E.; He, J.; Rahme, L. G., Electrospray/mass spectrometric identification and analysis of 4-hydroxy-2-alkylquinolines (HAQs) produced by *Pseudomonas aeruginosa*. *J Am Soc Mass Spectrom* **2004,** *15* (6), 862-9.
18. Hoffman, L. R.; Déziel, E.; D'Argenio, D. A.; Lépine, F.; Emerson, J.; McNamara, S.; Gibson, R. L.; Ramsey, B. W.; Miller, S. I., Selection for *Staphylococcus aureus* small-colony variants due to growth in the presence of *Pseudomonas aeruginosa*. *Proc Natl Acad Sci U S A* **2006,** *103* (52), 19890-5.
19. Diggle, S. P.; Matthijs, S.; Wright, V. J.; Fletcher, M. P.; Chhabra, S. R.; Lamont, I. L.; Kong, X.; Hider, R. C.; Cornelis, P.; Cámara, M.; Williams, P., The *Pseudomonas aeruginosa* 4-quinolone signal molecules HHQ and PQS play multifunctional roles in quorum sensing and iron entrapment. *Chem Biol* **2007,** *14* (1), 87-96.
20. Diggle, S. P.; Winzer, K.; Chhabra, S. R.; Worrall, K. E.; Cámara, M.; Williams, P., The *Pseudomonas aeruginosa* quinolone signal molecule overcomes the cell density-dependency of the quorum sensing hierarchy, regulates rhl-dependent genes at the onset of stationary phase and can be produced in the absence of LasR. *Mol Microbiol* **2003,** *50* (1), 29-43.
21. Allesen-Holm, M.; Barken, K. B.; Yang, L.; Klausen, M.; Webb, J. S.; Kjelleberg, S.; Molin, S.; Givskov, M.; Tolker-Nielsen, T., A characterization of DNA release in *Pseudomonas aeruginosa* cultures and biofilms. *Mol Microbiol* **2006,** *59* (4), 1114-28.
22. Häussler, S.; Becker, T., The *Pseudomonas* quinolone signal (PQS) balances life and death in *Pseudomonas aeruginosa* populations. *PLoS Pathog* **2008,** *4* (9), e1000166.
23. Hazan, R.; Que, Y. A.; Maura, D.; Strobel, B.; Majcherczyk, P. A.; Hopper, L. R.; Wilbur, D. J.; Hreha, T. N.; Barquera, B.; Rahme, L. G., Auto poisoning of the respiratory chain by a quorum-sensing-regulated molecule favors biofilm formation and antibiotic tolerance. *Curr Biol* **2016,** *26* (2), 195-206.

24. Guo, Q.; Kong, W.; Jin, S.; Chen, L.; Xu, Y.; Duan, K., PqsR-dependent and PqsR-independent regulation of motility and biofilm formation by PQS in *Pseudomonas aeruginosa* PAO1. *J Basic Microbiol* **2014,** *54* (7), 633-43.
25. Szamosvári, D.; Böttcher, T., An unsaturated quinolone *N*-oxide of *Pseudomonas aeruginosa* modulates growth and virulence of *Staphylococcus aureus*. *Angew Chem Int Ed Engl* **2017,** *56* (25), 7271-7275.
26. Cummins, J.; Reen, F. J.; Baysse, C.; Mooij, M. J.; O'Gara, F., Subinhibitory concentrations of the cationic antimicrobial peptide colistin induce the *Pseudomonas* quinolone signal in *Pseudomonas aeruginosa*. *Microbiology* **2009,** *155*, 2826-37.
27. Reis, R. S.; Pereira, A. G.; Neves, B. C.; Freire, D. M. G., Gene regulation of rhamnolipid production in *Pseudomonas aeruginosa* - a review. *Bioresour Technol* **2011,** *102* (11), 6377-84.
28. Turnbull, L.; Toyofuku, M.; Hynen, A. L.; Kurosawa, M.; Pessi, G.; Petty, N. K.; Osvath, S. R.; Carcamo-Oyarce, G.; Gloag, E. S.; Shimoni, R.; Omasits, U.; Ito, S.; Yap, X.; Monahan, L. G.; Cavaliere, R.; Ahrens, C. H.; Charles, I. G.; Nomura, N.; Eberl, L.; Whitchurch, C. B., Explosive cell lysis as a mechanism for the biogenesis of bacterial membrane vesicles and biofilms. *Nat Commun* **2016,** *7*, 11220.
29. Mashburn, L. M.; Whiteley, M., Membrane vesicles traffic signals and facilitate group activities in a prokaryote. *Nature* **2005,** *437* (7057), 422-5.
30. Lanni, E. J.; Masyuko, R. N.; Driscoll, C. M.; Dunham, S. J.; Shrout, J. D.; Bohn, P. W.; Sweedler, J. V., Correlated imaging with C60-SIMS and confocal Raman microscopy: Visualization of cell-scale molecular distributions in bacterial biofilms. *Anal Chem* **2014,** *86* (21), 10885-91.
31. Masyuko, R.; Lanni, E. J.; Sweedler, J. V.; Bohn, P. W., Correlated imaging--a grand challenge in chemical analysis. *Analyst* **2013,** *138* (7), 1924-39.
32. Formosa, C.; Grare, M.; Duval, R. E.; Dague, E., Nanoscale effects of antibiotics on *P. aeruginosa*. *Nanomedicine: NBM* **2012,** *8* (1), 12-16.
33. Neu, H. C., Penicillin-binding proteins and role of amdinocillin in causing bacterial cell death. *Am J Med* **1983,** *75* (2A), 9-20.
34. Anyan, M. E.; Amiri, A.; Harvey, C. W.; Tierra, G.; Morales-Soto, N.; Driscoll, C. M.; Alber, M. S.; Shrout, J. D., Type IV pili interactions promote intercellular association and moderate swarming of *Pseudomonas aeruginosa*. *Proc Natl Acad Sci U S A* **2014,** *111* (50), 18013-18018.
35. Baig, N.; Polisetti, S.; Morales-Soto, N.; Dunham, S. J. B.; Sweedler, J. V.; Shrout, J. D.; Bohn, P. W., Label-free molecular imaging of bacterial communities of the opportunistic pathogen *Pseudomonas aeruginosa*. *Proc SPIE 9930, Biosensing and Nanomedicine IX* **2016**.
36. Nguyen, D.; Joshi-Datar, A.; Lepine, F.; Bauerle, E.; Olakanmi, O.; Beer, K.; McKay, G.; Siehnel, R.; Schafhauser, J.; Wang, Y.; Britigan, B. E.; Singh, P. K., Active starvation responses mediate antibiotic tolerance in biofilms and nutrient-limited bacteria. *Science* **2011,** *334* (6058), 982-6.
37. Viducic, D.; Murakami, K.; Amoh, T.; Ono, T.; Miyake, Y., RpoN modulates carbapenem tolerance in *Pseudomonas aeruginosa* through *Pseudomonas* quinolone signal and PqsE. *Antimicrob Agents Chemother* **2016,** *60* (10), 5752-64.
38. Aendekerk, S.; Diggle, S. P.; Song, Z.; Høiby, N.; Cornelis, P.; Williams, P.; Cámara, M., The MexGHI-OpmD multidrug efflux pump controls growth, antibiotic susceptibility and virulence in *Pseudomonas aeruginosa* via 4-quinolone-dependent cell-to-cell communication. *Microbiology* **2005,** *151*, 1113-25.
39. Calfee, M. W.; Shelton, J. G.; McCubrey, J. A.; Pesci, E. C., Solubility and bioactivity of the *Pseudomonas* quinolone signal are increased by a *Pseudomonas aeruginosa*-produced surfactant. *Infect Immun* **2005,** *73* (2), 878-82.
40. Yeung, A. T.; Torfs, E. C.; Jamshidi, F.; Bains, M.; Wiegand, I.; Hancock, R. E.; Overhage, J., Swarming of *Pseudomonas aeruginosa* is controlled by a broad spectrum of transcriptional regulators, including MetR. *J Bacteriol* **2009,** *191* (18), 5592-602.
41. D'Argenio, D. A.; Calfee, M. W.; Rainey, P. B.; Pesci, E. C., Autolysis and autoaggregation in *Pseudomonas aeruginosa* colony morphology mutants. *J Bacteriol* **2002,** *184* (23), 6481-9.

42. Kotra, L. P.; Haddad, J.; Mobashery, S., Aminoglycosides: perspectives on mechanisms of action and resistance and strategies to counter resistance. *Antimicrob Agents Chemother* **2000,** *44* (12), 3249-3256.
43. Chiang, W.-C.; Nilsson, M.; Jensen, P. Ø.; Høiby, N.; Nielsen, T. E.; Givskov, M.; Tolker-Nielsen, T., Extracellular DNA shields against aminoglycosides in *Pseudomonas aeruginosa* biofilms. *Antimicrob Agents Chemother* **2013,** *57* (5), 2352-2361.
44. Mendelman, P. M.; Smith, A. L.; Levy, J.; Weber, A.; Ramsey, B.; Davis, R. L., Aminoglycoside penetration, inactivation, and efficacy in cystic fibrosis sputum. *Am Rev Respir Dis* **1985,** *132* (4), 761-5.
45. Florez, C.; Raab, J. E.; Cooke, A. C.; Schertzer, J. W., Membrane distribution of the *Pseudomonas* quinolone signal modulates outer membrane vesicle production in *Pseudomonas aeruginosa*. *MBio* **2017,** *8* (4).
46. Rahme, L. G.; Stevens, E. J.; Wolfort, S. F.; Shao, J.; Tompkins, R. G.; Ausubel, F. M., Common virulence factors for bacterial pathogenicity in plants and animals. *Science* **1995,** *268* (5219), 1899-902.
47. Xiao, G.; Déziel, E.; He, J.; Lépine, F.; Lesic, B.; Castonguay, M. H.; Milot, S.; Tampakaki, A. P.; Stachel, S. E.; Rahme, L. G., MvfR, a key *Pseudomonas aeruginosa* pathogenicity LTTR-class regulatory protein, has dual ligands. *Mol Microbiol* **2006,** *62* (6), 1689-99.
48. Koch, B.; Jensen, L. E.; Nybroe, O., A panel of Tn7-based vectors for insertion of the gfp marker gene or for delivery of cloned DNA into Gram-negative bacteria at a neutral chromosomal site. *J Microbiol Methods* **2001,** *45* (3), 187-95.
49. Bao, Y.; Lies, D. P.; Fu, H.; Roberts, G. P., An improved Tn7-based system for the single-copy insertion of cloned genes into chromosomes of gram-negative bacteria. *Gene* **1991,** *109* (1), 167-8.
50. Kessler, B.; de Lorenzo, V.; Timmis, K. N., A general system to integrate lacZ fusions into the chromosomes of gram-negative eubacteria: regulation of the Pm promoter of the TOL plasmid studied with all controlling elements in monocopy. *Mol Gen Genet* **1992,** *233* (1-2), 293-301.
51. Klausen, M.; Heydorn, A.; Ragas, P.; Lambertsen, L.; Aaes-Jørgensen, A.; Mølin, S.; Tolker-Nielsen, T., Biofilm formation by *Pseudomonas aeruginosa* wild type, flagella and type IV pili mutants. *Mol. Microbiol.* **2003,** *48* (6), 1511-1524.
52. Morales-Soto, N.; ME, A.; AE, M.; CS, M.; CW, H.; M, A.; E, D. z.; DB, K.; JD, S., Preparation, imaging, and quantification of bacterial surface motility assays. *J Vis Exp* **2015,** *98* (e52338).
53. Ahlf, D. R.; Masyuko, R. N.; Hummon, A. B.; Bohn, P. W., Correlated mass spectrometry imaging and confocal Raman microscopy for studies of three-dimensional cell culture sections. *Analyst* **2014,** *139* (18), 4578-85.
54. Lanni, E. J.; Dunham, S. J.; Nemes, P.; Rubakhin, S. S.; Sweedler, J. V., Biomolecular imaging with a C60-SIMS/MALDI dual ion source hybrid mass spectrometer: instrumentation, matrix enhancement, and single cell analysis. *J Am Soc Mass Spectrom* **2014,** *25* (11), 1897-907.
55. Chambers, M. C.; Maclean, B.; Burke, R.; Amodei, D.; Ruderman, D. L.; Neumann, S.; Gatto, L.; Fischer, B.; Pratt, B.; Egertson, J.; Hoff, K.; Kessner, D.; Tasman, N.; Shulman, N.; Frewen, B.; Baker, T. A.; Brusniak, M. Y.; Paulse, C.; Creasy, D.; Flashner, L.; Kani, K.; Moulding, C.; Seymour, S. L.; Nuwaysir, L. M.; Lefebvre, B.; Kuhlmann, F.; Roark, J.; Rainer, P.; Detlev, S.; Hemenway, T.; Huhmer, A.; Langridge, J.; Connolly, B.; Chadick, T.; Holly, K.; Eckels, J.; Deutsch, E. W.; Moritz, R. L.; Katz, J. E.; Agus, D. B.; MacCoss, M.; Tabb, D. L.; Mallick, P., A cross-platform toolkit for mass spectrometry and proteomics. *Nat Biotechnol* **2012,** *30* (10), 918-20.
56. Race, A. M.; Styles, I. B.; Bunch, J., Inclusive sharing of mass spectrometry imaging data requires a converter for all. *J Proteomics* **2012,** *75* (16), 5111-2.
57. Robichaud, G.; Garrard, K. P.; Barry, J. A.; Muddiman, D. C., MSiReader: an open-source interface to view and analyze high resolving power MS imaging files on Matlab platform. *J Am Soc Mass Spectrom* **2013,** *24* (5), 718-21.
58. Dunham, S. J.; Comi, T. J.; Ko, K.; Li, B.; Baig, N. F.; Morales-Soto, N.; Shrout, J. D.; Bohn, P. W.; Sweedler, J. V., Metal-assisted polyatomic SIMS and laser desorption/ionization for enhanced small molecule imaging of bacterial biofilms. *Biointerphases* **2016,** *11* (2), 02A325.

CHAPTER 8

A Versatile Workflow for Chemical and Architectural Characterization of Drip Flow Microbial Biofilms

8.1. Acknowledgements

This chapter has been reproduced in part with permission from *Analytical Chemistry*, submitted for publication. Unpublished work copyright 2018 American Chemical Society. Co-authors include Bin Li, Sage J. B. Dunham, Joseph F. Ellis, Justin D. Lange, Justin Smith, Ning Yang, Travis King, Kensey R. Amaya, Clint Arnett, and Jonathan V. Sweedler. BL planned experiments, helped to write the manuscript, developed sample preparation methods, and performed most of the MALDI and lipid-extract experiments. SJBD planned experiments, helped to write the manuscript, helped to design the flow cell reactors and growth substrates, developed sample preparation methods, and performed most of the SIMS experiments and some of the SEM and FTICR imaging experiments. JFE helped to write the manuscript, developed methods for and performed PCA, performed some of the FTICR and SIMS experiments, and performed most of the EDS and SEM experiments. NY helped with molecular identification and lipid extract experiments. JDL, JS, TK, and KRA helped to design experiments and cultivated the biofilms. CA and JVS helped to design experiments and write the manuscript. The authors acknowledge intellectual contributions from Troy Comi and Elizabeth Neumann and assistance from the University of Illinois at Urbana-Champaign School of Chemical Sciences machine shop. Help with EM was provided by Catherine Wallace and Scott Robinson from the Beckman Institute Imaging Technology Group, which is partially supported by the National Science Foundation Award No. DBI-9871103. Funding for this study was provided through a cooperative agreement with the Engineer Research and Development Center-Construction Engineering Research Laboratory under agreement number W9132T-15-2-0006. Although this research was sponsored by the Department of Defense, the content of the information does not necessary reflect the position or policy of the government and no official endorsement should be inferred.

8.2. Introduction

Biofilms are collections of microorganisms encased in a protective self-produced “slime” of extra-

cellular DNA, polysaccharides, proteins and other biomolecules, collectively referred to as the extracellular polymeric substance (EPS).[1] The EPS acts as a barrier, shielding the encased organisms from environmental and biological toxins. As a result of the biofilm phenotype, microbial communities can survive in some of the harshest environments imaginable, including on the inside of oil pipelines, and at the liquid-air interface in hydrocarbon fuel tanks.[2] The bacteria within a biofilm are distributed in a heterogeneous manner that depends on the properties of the surface and the local environmental conditions.[1] The biomolecular makeup is similarly heterogeneous, both in composition and distribution, necessitating versatile and multiplexed chemical imaging tools.

Biofilms play an important role in many industrial, clinical, and environmental processes, and therefore the chemical and physical processes behind biofilm formation and development are areas of intense interest for both academic and industrial researchers.[3-5] The identification and visualization of chemical species within microbial communities has contributed information to many different fields, including medicine, biology, and various factions of industry.[6-7] A fundamental understanding of biofilm dynamics, including the chemical processes behind their formation and resistance to disinfection, is of paramount importance to biofilm-associated human diseases as well as microbial induced corrosion (MIC).[8-9]

Mass spectrometry imaging (MSI) has emerged over the past two decades to become an indispensable tool for untargeted spatio-chemical characterization of biological systems.[7, 10] Although MSI is frequently employed to study bacteria biofilms, several challenges occur in the acquisition of reliable ion images due to the hydrated, absorbent, deformable, soft and non-uniform nature of the biofilm surface. This is particularly true for a high-vacuum and non-orthogonal mass spectrometers which are commonly coupled to both matrix-assisted laser desorption ionization (MALDI) and secondary ion mass spectrometry (SIMS) ionization sources.[11-12]

Our lab has developed a number of MSI-based analytical approaches for biofilm study, including those that employ MALDI MS and/or a lab-built Buckminsterfullerene (C_{60}^+) time-of-flight (TOF) SIMS.[12-14] Here we focus on the development of a cultivation and sample preparation strategy for untargeted mass spectrometry-based chemical imaging of flow-cell biofilms formed on metal substrates. Two model bacteria, *Pseudomonas putida* strain F1 and *Shewanella oneidensis* strain MR-1, were selected for the development and validation of the current platform. Gram-negative bacteria belonging to the genus *Pseudomonas* are well-studied biofilm forming

microorganisms know to promote MIC.[15-16] *S. oneidensis* MR-1 is a member of the gamma subdivision of the Proteobacteria and is a facultative anaerobe that can respire by using oxygen or ferric iron as its terminal electron acceptor.[17] Although investigations into the interaction between these two species are sparse, one previous study demonstrated that a co-culture system of *P. putida* OUS82 and *S. oneidensis* MR-1 exhibited both a competitive and a cooperative relationship in planktonic culture.[18]

Our workflow for constructing, cultivating, and characterizing drip-flow biofilms is shown in **Figure 8.1**. Generally, the microbial communities are cultivated in a low-sheer drip-flow reactor (DRF), flash frozen and dehydrated, imaged with SIMS, and either coated in an organic, light-absorbing matrix and imaged via MALDI MSI or examined with scanning electron microscopy (SEM) and energy-dispersive X-ray spectroscopy (EDS). This workflow is simple and easily adaptable for studying diverse microbial biofilms with a host analytical techniques. We demonstrate the utility and versitility here by examining three culture conditions, a monoculture of *P. putida* on stainless steel, a co-culture of *P. putida* and *S. oneidensis* on stainless steel, and a

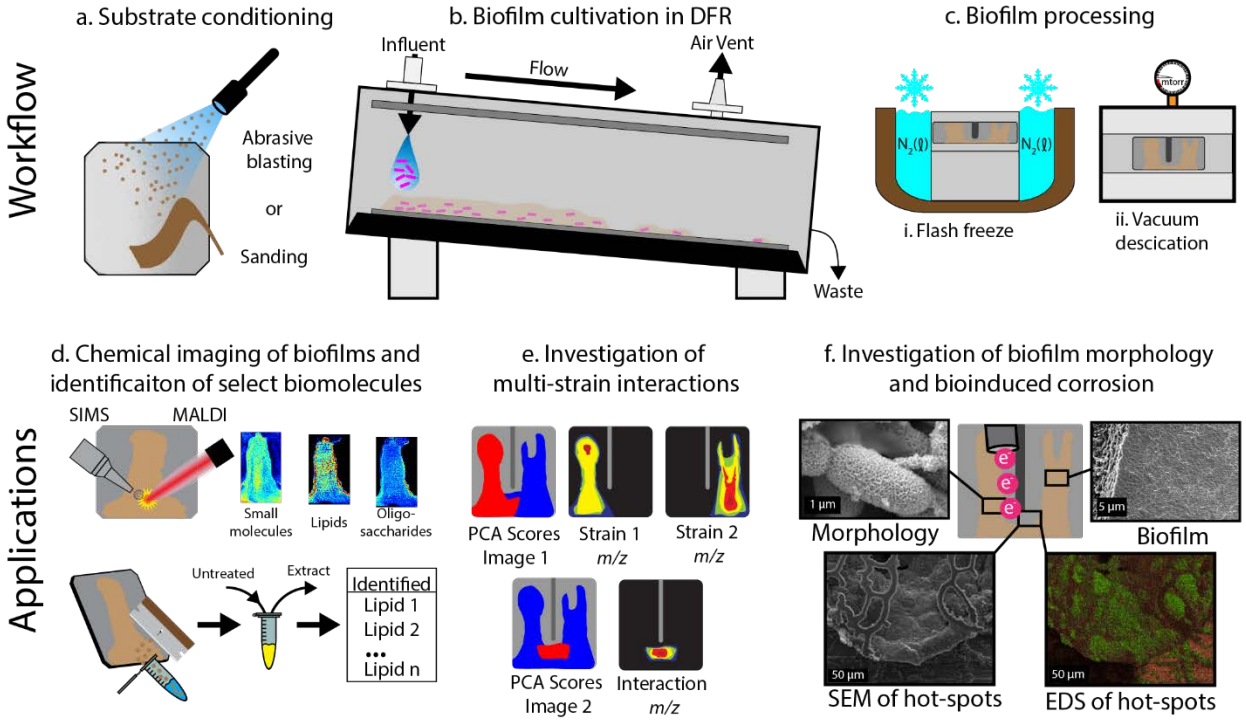

Figure 8.1. Workflow for constructing, developing, and characterizing drip-flow biofilms. (**a**) Metal substrate conditioning for control of biofilm adherence; (**b**) cultivation of bacterial biofilms in a customized drip flow reactor; (**c**) pretreatment of biofilms via flash freezing and vacuum desiccation; (**d**) chemical imaging with SIMS and MALDI; (**e**) multivariate image analysis to distinguish ions specific to different biofilm regions, such as the zone of interaction; and (**f**) examination of biofilm architecture and elemental composition with SEM and EDS.

co-culture of *P. putida* and *S. oneidensis* on low carbon steel. These samples were chosen for the utility of simplified molecular discovery, the capability to image strain-strain chemical and physical interactions, and the ability to examine the chemical processing underlying MIC.

8.3. Experimental

8.3.1. Chemicals and Reagents

All chemicals and reagents used were of the highest purity available. All MALDI matrices were purchased from Sigma-Aldrich (St. Louis, MO, USA) unless otherwise specified.

8.3.2. Customization of Metal Substrates for Biofilm Formation

Stainless and low carbon steel coupons were fabricated in the Department of Chemistry Machine Shop at the University of Illinois at Urbana-Champaign to fit both custom and commercially available drip flow biofilm reactors (DFR) and fit a Bruker Daltonics MALDI adapter plate (Bruker Daltonics, Billerica, MA, USA) and a lab-built C60-SIMS instrument. The coupons were constructed from Multipurpose 304 Stainless Steel and 1080 Low Carbon Steel (McMaster Carr, Elmhurst, IL, USA). The 304 Stainless Steel had a composition of 19% chromium, 10% nickel, 2% manganese, and 0.08% carbon. The 1080 Low Carbon Steel consisted of 0.7% manganese and 0.18% carbon by mass. Two dimensions of the stainless and low carbon steel coupons were made including 5.7 cm x 5.7 cm x 1.5 mm and 2.5 mm x 7.5 mm x 1.5 mm. Stainless steel coupons dripped with medium in one location were lightly roughed with 240 grit sand paper to create an unpolished surface to help promote biofilm adhesion. Coupons dripped in two locations on a single coupon were vaper blasted to promote adhesion. No surface treatment was required to adhere bacteria to the low carbon steel coupons as the raw material was textured.

8.3.3. Drip Flow Biofilm Reactor Construction

Drip flow biofilm reactors (DFR) were fabricated with inspiration from a similar design by BioSurface Technologies (DFR 110-4, Bozeman, MT, USA). The DFR body and cover were made out of a polysulfone and consisted of 2 parallel test channels capable of holding 1 metal coupon or glass slide each. Under continuous flow operation, the angle of the reactor was set at 5° to achieve low fluid shear conditions, which had a resistance time of less than 2 min. Influent was delivered through polytetrafluoroethylene septa ports at the top of the reactor (middle of the coupon, 1 cm from the top), and air/gas was vented at the bottom through 0.2 µm syringe filters. Effluent exited the base at the vented end of the reactor through a 1.3 cm exit port to waste. Similar reactors were

made to house the custom stainless steel coupons but were fabricated to allow them to be dripped with medium in two separate areas on the same coupon. These reactors differed only in that there were 2 influent ports and 2 vents per coupon (evenly spaced at 1/3 the coupon width, 1 cm from the top), which allowed side by side dripping to be achieved on the same coupon. Experiments with low carbon steel were performed using a BioSurface Technologies four-chamber DFR (BioSurface Technologies, MT, USA). All the reactors and coupons were sterilized by autoclaving at 120°C for 20 min before use.

8.3.4. Model Strains and Cultivation

Pseudomonas putida strain F1 (ATCC® 700007™) and *Shewanella oneidensis* strain MR-1 (ATCC® 700550™) were obtained from American Type Culture Collection (Manassas, VA, USA). Stock cultures used for biofilm experiments were propagated in nutrient broth overnight and archived at -80˚C in 10% glycerol until use.

To establish single strain biofilms on the steel surfaces, bacteria were allowed to grow statically at 30˚C for 6 h in a logarithmic growth phase with drip angle of 0˚. A 10% glycerol stock in 50 mL of 3g/L tryptic soy broth (TSB) was used as the inoculum. After 6 h, the drip angle was increased to 5˚, and a continuous flow of nutrients (TSB, 270 mg/L) was supplied at 50 mL/h via peristaltic pump through a glass flow break. Side-by-side drip-flow experiments with co-cultures were performed creating a hydrophobic barrier down the center of the coupons using a hydrophobic pen. Bacteria mixture or media-only was dripped on either side of the coupon and allowed to join only at the bottom third of the substrate forming an interaction region. To facilitate bacterial attachment, 3 g/L TSB was inoculated with 1% of each species individually. The cultures were stirred at room temperature and simultaneously dripped at 50 mL/h on the coupons at a 5˚ drip angle. After 6 h of drip-flow, the inoculation was halted and reactors were fed a continuous flow of 270 mg/L TSB.

Under all conditions, the DFRs were operated at 30˚C for 1 to 6 days under low fluid sheer conditions to promote growth near the air-liquid interface. Substrates were removed at predetermined time-points and the biofilms were preserved for subsequent analysis by placing them on a steel block half submerged in liquid nitrogen (substrates did not contact the liquid nitrogen). After 30 min, the coupons were removed from the block and dried in a vacuum desiccator for a minimum of 24 h at room temperature (**Figure 8.1c**).

8.3.5. C_{60}^+-SIMS Imaging and SIMS Tandem-MS

All SIMS measurements were conducted with a modified QSTAR XL (AB SCIEX, Framingham, MA, USA) imaging mass spectrometer equipped with a 20 keV Buckminsterfullerene (C_{60}^+) ion beam (Ionoptika Ltd, Hampshire, UK). A detailed description of this instrument can be found in our previous work.[19] Images were acquired in raster-mode with a pixel size of 300 μm × 300 μm for single strain biofilms (primary ion dose of 0.9 x 10^{13} ions/cm^2) and 500 μm × 500 μm for co-cultures and MIC samples (primary ion doses of 1.6 x 10^{13} ions/cm^2 and 2.3 x 10^{13} ions/cm^2). In all cases the spectrometer was set to collect secondary ions from *m/z* 60-850 with a Q1 bias of 15%, 25%, and 60% at *m/z* 100, 200, and 400 respectively. Mass Calibration was performed using indium clusters (In_{1-7}^+), and imaging data was converted from wiff to imzML format with ProteoWizard[20] and imzMLconverter[21] with subsequent visualization and analysis in MSiReader.[22] Tandem-MS spectra were acquired in positive product ion mode with argon collision gas and 10-40 eV CID energy as needed.

8.3.6. MALDI Matrix Application

Several methods for application of 2,5-dihydroxybenzoic acid (DHB) and α-cyano-4-hydroxycinnamic acid (CHCA) MALDI matrix were optimized and compared. Automated spray coating via a previously optimized protocol[23] and manual airbrush application were also explored for initial experiments but both application methods resulted in disruption of the thin biofilm, most likely due to the high gas pressures involved. Therefore, sublimation was selected for all subsequent experiments. The thickness of DHB and CHCA was optimized to achieve the most homogeneous coverage and the highest sensitivity (**Figure 8.2**) using an apparatus and procedure described previously.[19] Briefly, 1g of powdered DHB or CHCA was distributed evenly to an aluminum foil boat and the biofilm samples were affixed to a copper adaptor on the outside of the cold finger. The chamber was closed, placed in a heating mantle (Model No. 0408, Glas-Col, Terre Haute, IN, USA), pumped to intermediate vacuum (~10 mTorr), and the cold finger was filled with iced water. After 2 min of temperature equilibration, the desired matrix coating was achieved by supplying 120 V to the heating mantle 55% power with a Staco Inc. variable autotransformer (Dayton, OH, USA) for a controlled time. The chamber was removed from the mantle and vented to room temperature air, and the sample was promptly removed from the cold finger and transferred to a nitrogen-purged sample chamber. The sample was weighed before and after matrix

application to determine the average matrix density, which was estimated as the mass change/substrate area.

In agreement with previous experiments with nervous system tissue, the optimal DHB coating for MALDI imaging was found to be between 0.10 and 0.30 mg/cm^2, while a matrix coating thicker than 0.40 mg/cm^2 resulted in an elevated baseline and loss of sensitivity (**Figure 8.2a**). The optimal CHCA coating was achieved via 19 minutes of sublimation (**Figure 8.2b**). In

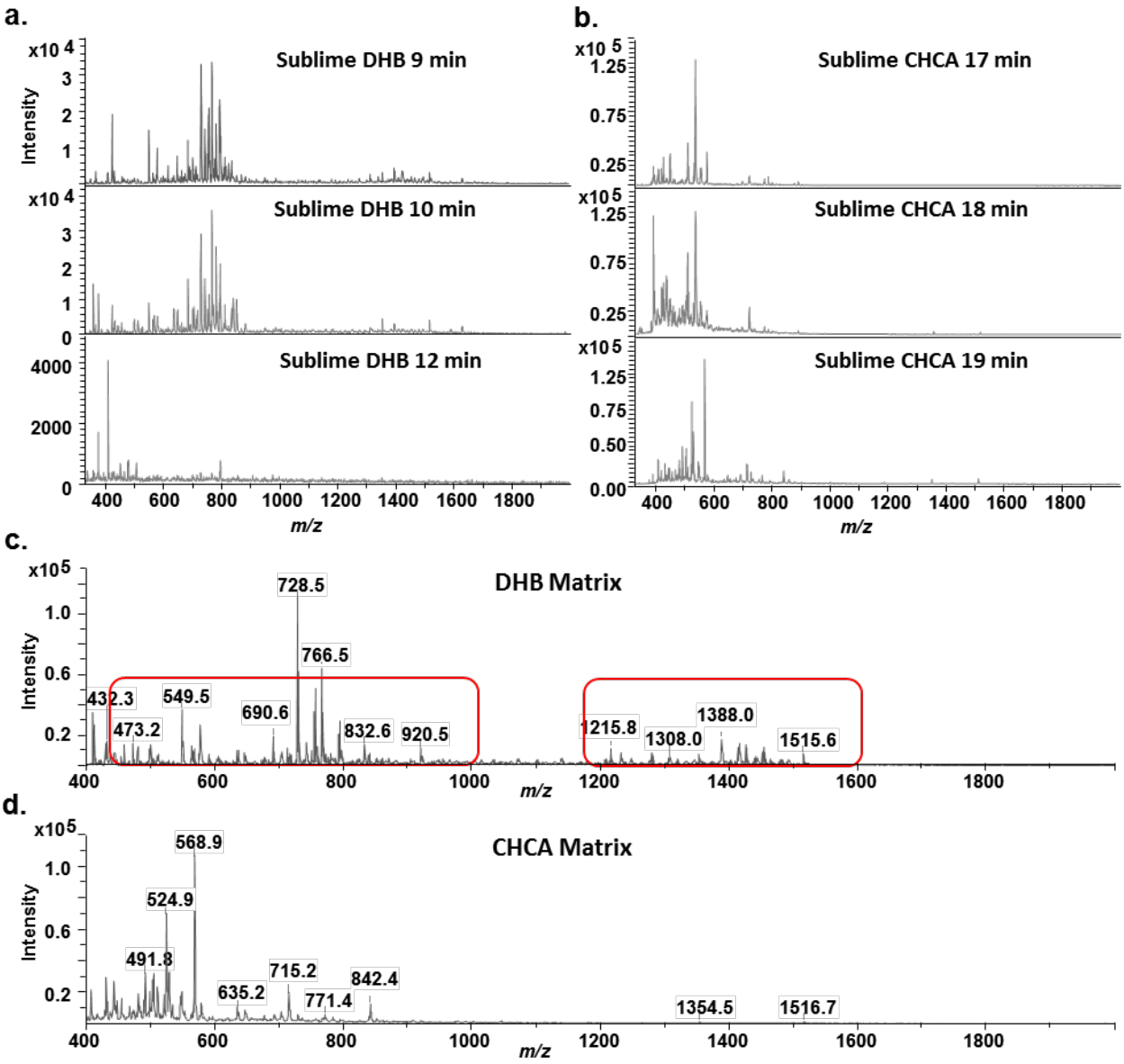

Figure 8.2. Matrix choice and sublimation time optimization for *P. putida* DFR biofilms on a metal substrate. Representative MALDI ToF mass spectra for at different sublimation times for (**a**) DHB and (**b**) CHCA. Representative mass spectra obtained after sublimation optimization: (a) 9.5 min DHB (the two primary mass ranges of interest are indicated with red boxes); and (b) 18.5 min CHCA.

general, DHB was found to give better signal than CHCA and was therefore the primary matrix used throughout these experiments (**Figure 8.2c** and **d**).

8.3.7. MALDI-MSI and Tandem-MS

The majority of the MALDI MSI measurements were performed with an UltrafleXtreme MALDI-ToF/ToF (Bruker Daltonics) mass spectrometer with a frequency tripled Nd:YAG solid-state laser (λ=355 nm). The laser footprint was set to "Ultra" to achieve an approximate spot diameter of 100 μm. Mass calibration was performed using DHB clusters and Peptide Calibration Standard Kit II (Bruker Daltonics). All data was acquired in positive reflection mode with pulsed ion extraction and a mass range of 100-2500 Da. The step size was set to 400 μm for single-strain biofilms and 500 μm for co-cultures. All images were collected with 500 laser shots/pixel at a frequency of 1000 Hz. *In situ* tandem MS was conducted using in LIFT mode. Spectra were baseline-corrected and analyzed in FlexAnalysis 3 (Bruker Daltonics). MALDI imaging was performed with FlexImaging 4 (Bruker Daltonics) and the resulting average mass spectrum was filtered manually in 0.3 Da increments with individual colors assigned to specific *m/z* values. Ion images were normalized to the total ion count (TIC) unless otherwise noted.

Select samples were subjected to follow-up analysis with a 7T SolariX XR ESI/MALDI FT-ICR (Bruker Daltonics). Coordinates from the previous UltrafleXtreme image were offset both laterally and horizontally by 250 μm to prevent resampling. The laser footprint, step size, shots, and frequency were adjusted to match the UltrafleXtreme parameters. The instrument was calibrated using sodium TFA (trifluoroacetic acid) clusters and imaged in positive mode with a mass range of *m/z* 250 to 2500 Da.

8.3.8. Principal Component Analysis of MALDI FT-ICR and SIMS Imaging Data

Principal component analysis (PCA) was performed on the co-culture biofilm MSI datasets. MALDI datasets were exported to imzML via FlexImaging. The MSI datacube was imported using a custom MATLAB script implementing imzMLConverter and MSiReader and binned at ±0.05, ±0.05, and ± 0.5 Da with a mass range defined by the acquisition method for SIMS, MALDI-FT-ICR, and MALDI-TOF/TOF, respectively. The binned datacube was mean-centered by singular value decomposition prior to PCA analysis using a custom MATLAB. The resulting coefficient matrix was reconstructed to produce false-colored images relating variance and spatial information, where red and cyan correspond to positive and negative variance, respectively.

3.9. Scanning Electron Microscopy

Parallel dehydrated biofilms were coated with approximately 7 nm of Au/Pd using a Desk II Turbo Sputter Coater (Denton Vacuum, Morristown, NJ, USA), operated for 70 s at 64 mTorr Ar and 40 mA current. SEM images were acquired at an accelerating voltage of 5 kV and a working distance of 10 mm with a Philips XL30 ESEM-FEG and a Quanta 650 ESEM-FEG (FEI Company, Amsterdam, Netherlands).

8.4. Results and Discussion

8.4.1. Drip Flow Biofilm Reactor Design and Optimization of Substrate and Culture Conditions

Initial biofilm cultivation and sample preparation tests were performed with indium tin oxide (ITO)-coated glass microscope slides (a common substrate for many MALDI measurements), as well as with both polished and roughened steel **Figure 8.3**. Substantial peeling and flaking of the biofilm was observed on both the ITO-glass slides and polished steel following sample preservation (flash freezing with liquid nitrogen and vacuum desiccation). This detachment is a common problem in many microbial MSI measurements.[24] Roughening the metal surface with fine grit sand paper or glass vapor blasting increased bacterial attachment during cultivation and prevented dehydration induced detachment without adversely affecting MSI measurements. It should be noted that while monoculture biofilms produced flaking on ITO-glass, the co-culture biofilms (*P. putida* and *S. oneidensis*) adhered well and did not peel. ITO glass slides should therefore not be excluded for consideration as substrates, especially in instances where optical microscopy is required.

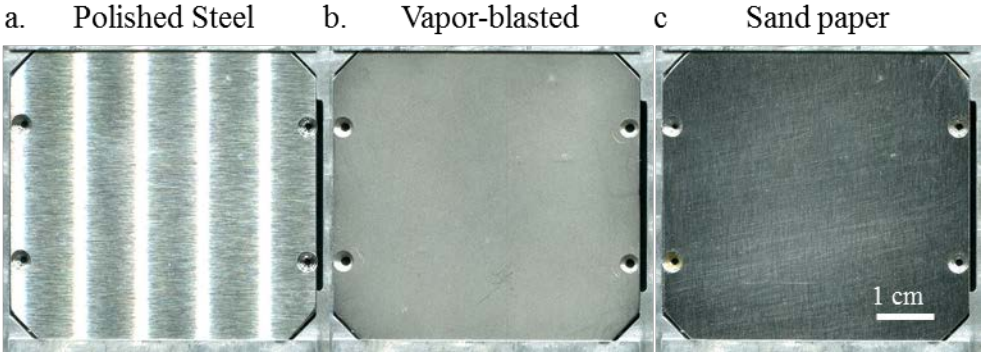

Figure 8.3. Substrate optimization. Stainless steel (a) as received from the manufacturer, (b) following vapor blasting, and (c) after roughening with sand paper. The vapor blasting was found provide the most uniform surface and provided the best biofilm adhesion and was therefore used throughout this work.

A custom DFR (detailed in the **Experimental** section and **Figure 8.4a**) was fabricated with inspiration from a similar design by BioSurface Technologies (DFR 110-4, Bozeman, MT, USA). Wide-application scope, ease of operation, and reliable performance are the main aims in the design of a biofilm production platform. The DFR is often used for biofilm cultivation because it produces pronounced and highly reproducible biofilms within relatively short incubation periods.[25] Biomass accumulation occurs rapidly because nutrients are supplied continually and waste is removed through gravitational force. Additionally, the customization of DFRs according to user-need can be achieved with relative ease. The modified design was made to accommodate

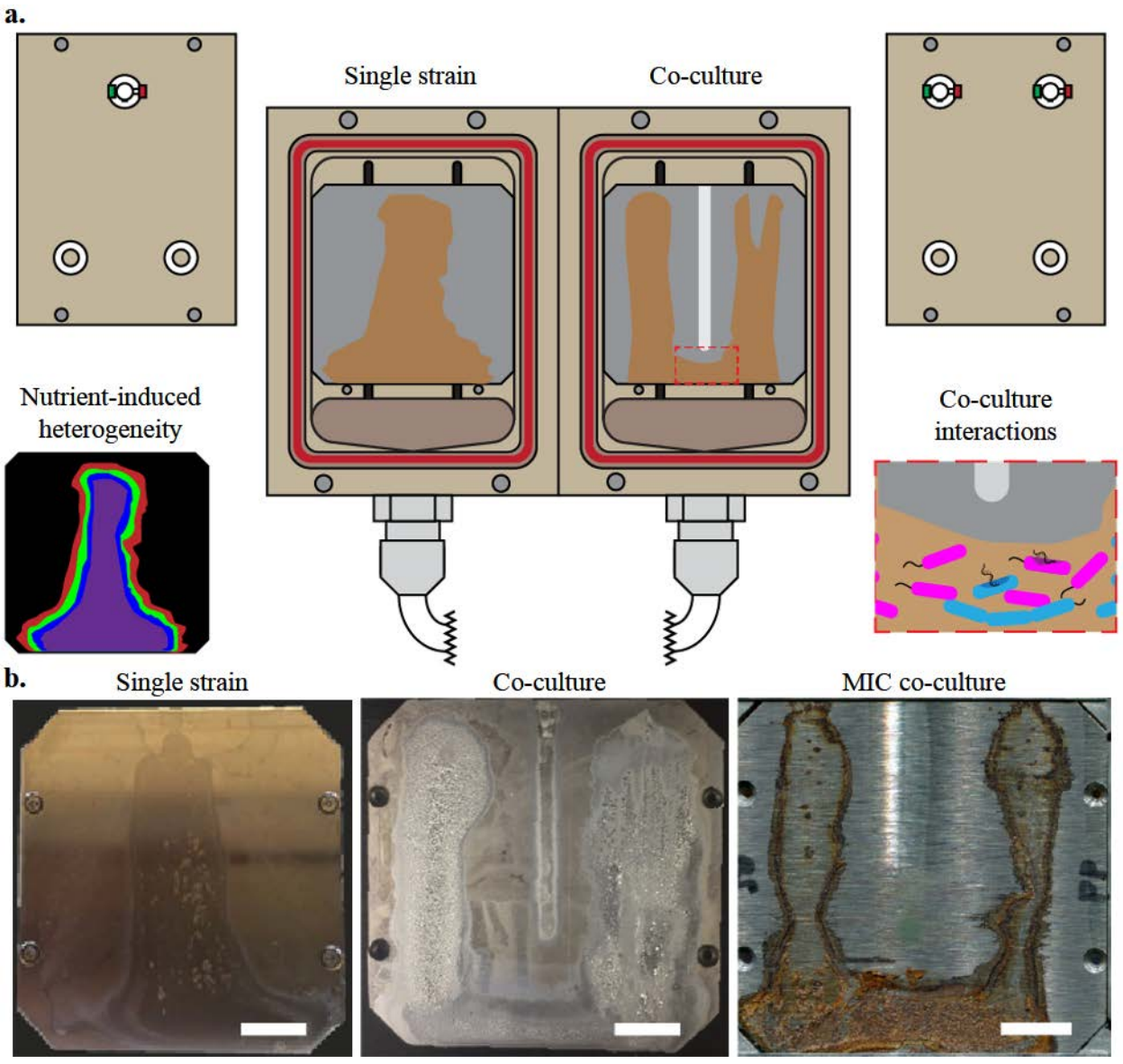

Figure 8.4. Diagram of modified drip-flow bioreactor (**a**). The DFR can accommodate single or co-cultured biofilms with a defined interaction region (location represented in dashed red lines), and enables the study of various growth phases and substrate types, as shown in (**b**).

the specific needs of our experiments, which included the use of abnormally sized substrates and the ability to simultaneously culture multiple bacterial species on the same substrate. For the purposes of the experiments described in this manuscript, we cultivated three types of biofilm samples (**Figure 8.4b**): monoculture biofilms on stainless steel for simple method development and molecular discovery experiments (**8.4bi**), co-culture biofilms on stainless steel for evaluation of strain-strain interactions (**8.4bii**), and co-culture biofilms on low carbon steel to evaluate MIC (**8.4biii**).

To optimize the culture conditions and develop MSI methods, single strain cultures of *P. putida* were cultivated adjacent to one another on roughened stainless steel and harvested at 1, 3, and 6 days of growth (**Figure 8.5a-c**). Under these conditions biofilm formation was detected after 1 day of incubation, and significant biomass accumulation was observed within 3 days. After 6 days the steel surface was covered with a dense biofilm. The 3-day growth period was selected for all subsequent MS measurements due to the uniform surface and superior substrate attachment. Mass deviations arising from variations in height, which can be problematic in many MSI applications, were found to be minimal in the present study due to the smooth, sheet-like biofilms formed in the DFR, as revealed by the optical images in **Figure 8.5a-c** and the SEM in **Figure 8.5e-g**.

8.4.2. SIMS and MALDI Imaging of *P. putida* F1 Biofilms Reveals a Diverse Collection of Lipids and Oligosaccharides

P. putida F1 was selected as a model organism for initial experiments due to its ability to rapidly form robust biofilms on a wide variety of surfaces. *Pseudomonas* is a common model organism for laboratory studies of biofilm-forming bacteria in many environments, which gives the study of this genus additional relevance in both the industrial and clinical settings.[26]

Lipids act as a useful biochemical signature for correlating the composition of a microbial community and the physiological state of a biofilm.[27] Modulations in lipid profile and content help bacteria to maintain an adequate ultrastructure and membrane barrier under extreme natural conditions.[28] A major limitation in the visualization of biofilm lipid distribution is the lack of chemical dyes and labeling techniques that can be applied for individual molecules. MSI is particularly useful for capturing the spatial distribution of lipids across various mammalian and plant tissues.[29] Here, a number of lipid distributions were mapped on dehydrated *P. putida* F1 biofilms using SIMS and MALDI-MS imaging (**Figure 8.6**).

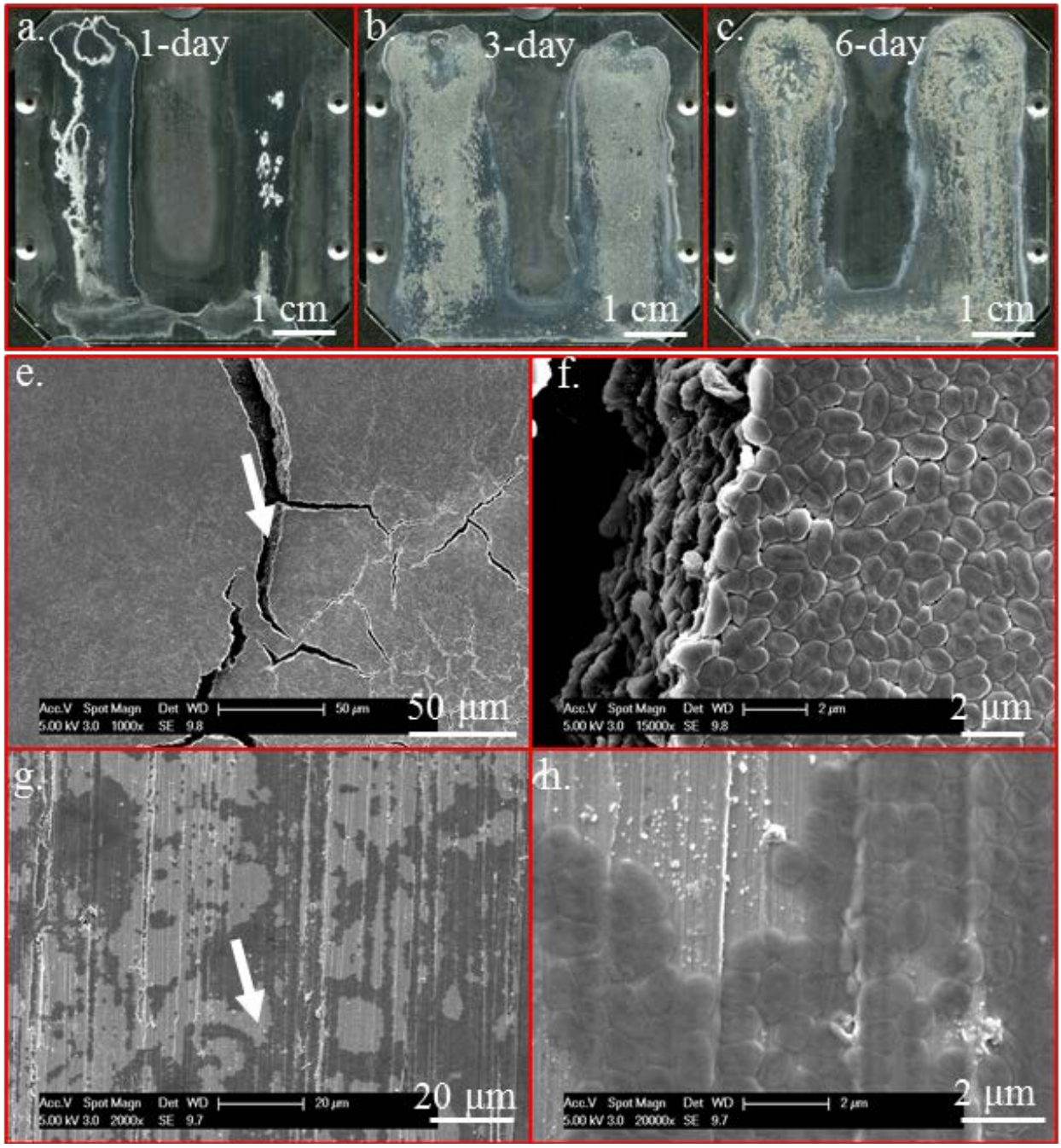

Figure 8.5. Characterization of *P. putida* F1 DFR biofilms with SEM. Optical images of (**a**) 1 day, (**b**) 3 day, and (**c**) 6 day biofilms grown adjacent to one another on a steel substrate. Electron micrographs of a 3-day-old biofilm acquired from (**e-f**) the colony center, and (**g-h**) the colony boundary. The electron micrographs in (**f**) and (**h**) were acquired from the approximate spots indicated by arrows in (**e**) and (**g**), respectively. All images were acquired after desiccation and the application of approximately 7 nm of Au/Pd. The flow direction was top to bottom in with the influent making contact in the barren region near the top.

As can be seen in the representative C_{60}-SIMS spectrum of **Figure 8.6a** and **Table 8.1**, multiple analytes were detected with SIMS, including the phosphatidylethanolamine (PE) head-

group at *m/z* 136.9, seven intact PE lipids, and five diacylglycerols (DGs) (as confirmed by in situ C_{60}-SIMS tandem MS). Representative C_{60}-SIMS ion images for the PE headgroup, PC(32:1), DG(32:1), DG(33:1), and DG(34:1) are provided in **Figure 3b**. In all cases the strongest lipid signals are observed near the biofilm boundary. The PE headgroup shows a more uniform distribution, with elevated ion intensity near the biofilm center. It should be noted that quorum sensing molecules such as quinolones and N-acyl-homoserine lactones were not observed. These analyte classes have been reported in some *P. putida* strains, such as KT2440[30] and IsoF[31]. Our previous examinations of *P. aeruginosa* biofilms revealed that C_{60}-SIMS is highly sensitive for quinolones and less sensitive for homoserine lactones.[32-33]

Additional identification of specific compounds within *P. putida* biofilms was achieved via a combination of *in situ* MALDI ToF-ToF MS and analysis of biofilm extracts with MALDI ToF-ToF and high-resolution FT-ICR MS. As shown in the spectra of **Figure 8.6c** and **8.6e**, two distinct ion groupings are readily detected in the mass ranges of *m/z* 500-800 and *m/z* 1000-2000 following DHB application. Overall, 18 lipids were detected directly on the biofilms, and 25 lipids were found in the biofilm extracts (**Table 8.1)**. These included diacylglycerols (DGs), phosphatidylethanolamines (PEs), *lyso*-PEs, and phosphatidylglycerols (PGs). The loss of a polar head-group was readily detected, facilitating identification. Characteristic fragments observed in previous studies that correspond to individual fatty acid side chains were not available for all lipids in positive ion mode.[34-35]

Interesting variations were observed between our data and previous reports including the detection of a number of DGs in *P. putida* F1 biofilms.[36-38] DGs can be formed transiently as intermediates in the biosynthesis of glycerophospholipids.[39] It is also known that DGs act as second messengers in mammalian and microbial cells and are implicated in the regulation of various cellular functions such as cell growth, differentiation, and apoptosis.[39-40] Therefore, the current results provides important clues for understanding the role of phospholipids in biofilm formation. It is important to note that even single species biofilms have enormous spatially-segregated phenotypical variation, and as such each cell can have a distinct role in promoting the fitness and propagation of the biofilm.[41] The combined SIMS and MALDI analysis shown in **Figure 8.6a-d** reveals that DGs are most abundant on the outer edge of the biofilm. PE, PG, and *lyso*-PE species are found throughout the biofilm, including the edge. Interestingly, SIMS imaging shows that the PE headgroup is found at almost uniform abundance throughout the biofilm,

possibly suggesting the presence of either isobaric interference or the presence of additional as-yet unidentified PEs. Additionally, the majority of the lipids identified were long chain and unsaturated. In batch cultures, higher molecular weight membrane lipids have been shown to decrease over time as nutrients become limited.[41] The relative even distribution of high molecular

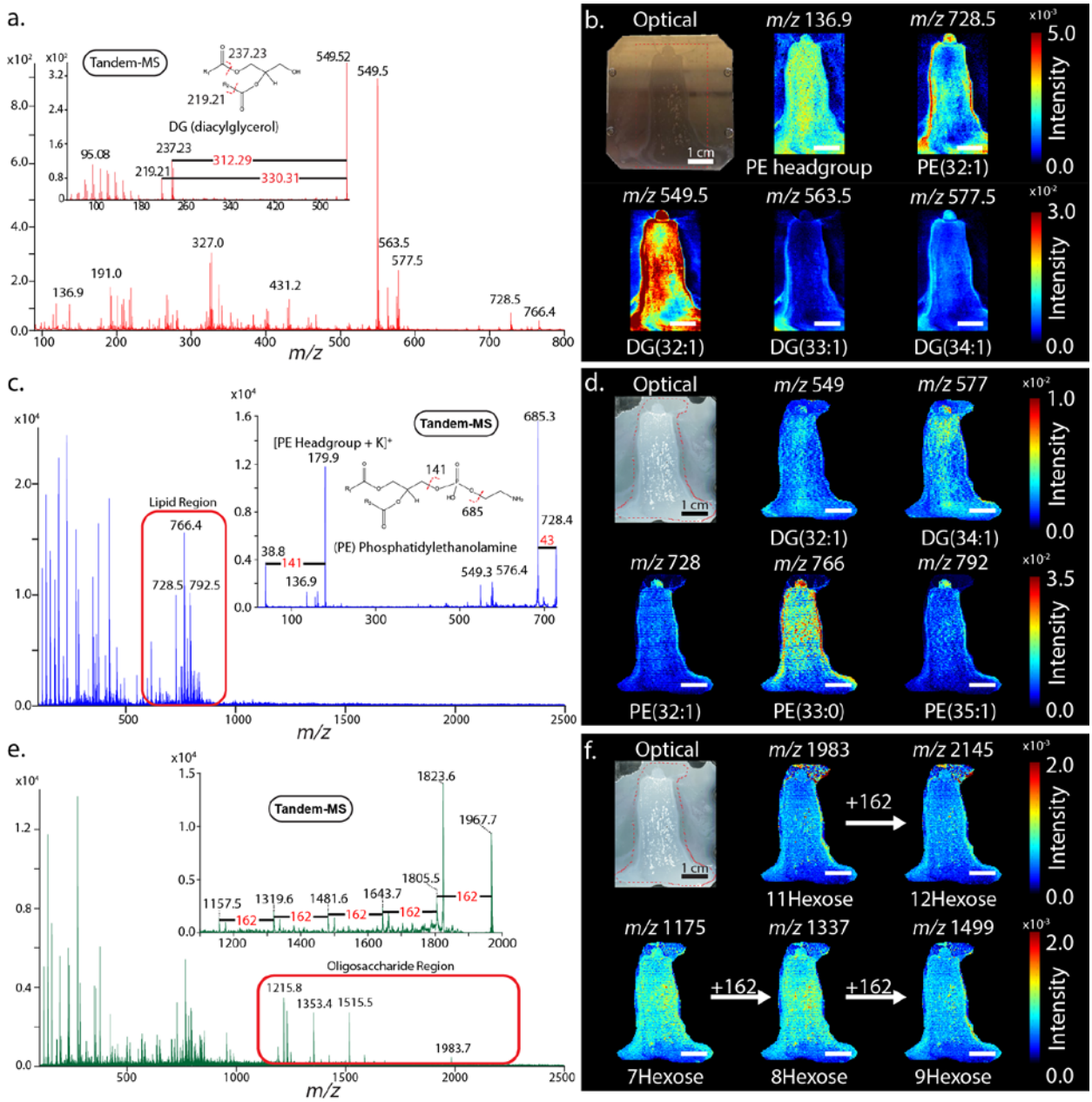

Figure 8.6. Representative SIMS and MALDI ToF/ToF spectra and ion images of a 3-day monoculture of *P. putida*. Relevant ions in the C_{60}-SIMS spectrum displayed in (**a**) primarily consists of DG and PE lipids and associated fragments. The inset is an example *in situ* SIMS tandem-MS spectrum assigned to DG(32:1). The MALDI spectra in (**c**) and (**e**) correspond to two regions of interest that contain high abundances of lipids and oligosaccharides. The inset tandem-MS spectra in (**c**) and (**e**) are assigned to PE(32:1) and 11hexose, respectively. Ion images show the distributions of several lipids (**b, d**) and oligosaccharides (**f**).

weight lipids over the biofilm suggested the biota of the biofilm was in good health, which is not surprising as the nature of the DFR is to continually deliver fresh nutrients and remove waste.

A series of ions with the mass difference of 162 Da were found in the mass range of *m/z* 1000-2000 (**Figure 8.6e**). Subsequent LIFT-ToF/ToF revealed that these ions are oligosaccharides

Table 8.1. Combined MALDI MSI, MALDI MS, and ESI FT-ICR MS results for lipids species detected from the *P. putida* F1 biofilm.

Compound ID	Molecular Formula	MS modalities			
		***In situ* analysis of biofilm**		**MS analysis of lipid extracts**	
		MALDI ToF/ToF Imaging	**ToF-SIMS imaging**	**MALDI MS**	**FT ICR-MS**
DG (32:1) [b]	$C_{35}H_{66}O_5$	√*	√	√*	√*
DG (33:1) [b]	$C_{36}H_{68}O_5$	√	√	√*	√*
DG (34:2)	$C_{37}H_{68}O_5$	√	√	√	√
DG (34:1) [b]	$C_{37}H_{70}O_5$	√	√	√*	√*
DG (35:2) [b]	$C_{38}H_{70}O_5$	√	√	√	√*
PE(30:1)	$C_{35}H_{68}NO_8P$	√	–	√	√
PE(30:0)	$C_{35}H_{70}NO_8P$	–	–	√	√*
PE(31:1)	$C_{36}H_{70}NO_8P$	–	–	√	√
PE(31:0)	$C_{36}H_{72}NO_8P$	√		√	√
PE(32:1) [b]	$C_{37}H_{72}NO_8P$	√*	√	√*	√*
PE(32:0)	$C_{37}H_{74}NO_8P$	√	√	√	√
PE(33:2)	$C_{38}H_{72}NO_8P$	–	–	√	√
PE(33:1)	$C_{38}H_{74}NO_8P$	√*	–	√*	√*
PE(34:2)	$C_{39}H_{74}NO_8P$	√*	√	√	√*
PE(34:1)	$C_{39}H_{76}NO_8P$	√*	√	√	√*
PE(35:2)	$C_{40}H_{76}NO_8P$	√*	√	√	√
PE(35:0)	$C_{40}H_{80}NO_8P$	√*	√	√	–
PE(35:1) [b]	$C_{40}H_{78}NO_8P$	√*	√	√*	√
PE(36:2)	$C_{41}H_{78}NO_8P$	–	–	√	√
PG(33:1) [b]	$C_{39}H_{75}O_{10}P$	–	–	√	√*
PG(35:2)	$C_{41}H_{77}O_{10}P$	√	–	√	√
PG(36:2)	$C_{42}H_{79}O_{10}P$	√	–	–	√
lyso-PE(16:0)	$C_{21}H_{44}NO_7P$	–	–	√	√
lyso-PE(16:1)	$C_{21}H_{42}NO_7P$	√	–	√	√
lyso-PE(18:1)	$C_{23}H_{46}NO_7P$	–	–	√	√

[a] The mass accuracy of lipids detected with FT-ICR MS was better than 1.5 ppm.
[b] The individual fatty acid side chains were assigned based on tandem mass spectra.
* indicates tandem mass spectrum of individual lipids is available.
– not detected

(S8), however the structural assignments are only tentatively made here. A more thorough study is needed for complete structure elucidation. As shown in **Figure 8.6f**, oligosaccharide ions are preferentially found at the biofilm boundary, with some increased intensity near the center. To our knowledge, this is the first imaging observation of oligosaccharides in *P. putida* F1 biofilms. While the role of these compounds is not clear from these experiments, these results suggest that oligosaccharides may be closely involved in the formation and maturation of bacterial biofilms and demonstrate that MALDI imaging is well suited for *in situ* detection and localization of oligosaccharides in biofilms.

8.4.3. MSI and SEM of *P. putida* and *S. oneidensis* Co-Cultures Reveals Molecules Specific to Each Strain and the Region of Interaction

Microbes within a biofilm not only respond to and influence the surrounding inanimate environment but they also interact with and influence other living organisms within their zone of influence. Microbe-microbe interactions are complex, and elucidation of meaningful information requires the development of new and innovative methodologies, particularly for the study of chemical communication. One of the most attractive features of the methodologies outlined in this manuscript is the development of a two-channel biofilm flow reactor capable of cultivating multiple strains on the same substrate, with a spatially defined interaction region (**Figure 8.4**).

Manual inspection of MSI datasets is both computationally and intellectually cumbersome, particularly for large and complex samples like those examined here. Fortunately, there have been significant advances in applying multivariate analysis to MSI data. One of the most common multivariate methods used in MSI is imaging PCA, where variables that exhibit co-variance are grouped together into a lower dimension space, allowing for visualization of multivariate data with minimal loss of information.[42] In general two types of imaging PCA are used – targeted PCA, which accounts for the variance of a previously selected small group of analytes in the dataset, and untargeted PCA, which includes every variable in the dataset and is especially useful for analyte discovery.

In this work we applied a combined approach, where initial untargeted PCA is used to discriminate ions that arise from the chemical background (e.g. hydrophobic pen, culture medium, DHB matrix) from ions specific to the biofilm (**Figure 8.7**). In general, the first principal component (PC1) discriminates on this basis, with the positive loadings comprised of the chemical background and the negative loadings comprised of biofilm-specific compounds (**Figure 8.7a**). A

second round of targeted PCA is then performed only on the ions contributing to the negative loadings, allowing for a determination of covariance based on the specific subpopulation of ions relevant to the bacteria under study (**Figure 8.7b**). For this multistep analysis, PC1 of the second step (targeted PCA) produces an empty negative leadings (resulting from the zero values in the matrix) and therefore only the principal components with a lower variance contain distinguishing information. This combined analysis reveals a greater amount of spatiochemical information than would be otherwise be observed with untargeted PCA alone, and, in relation to strictly targeted PCA that utilizes a list of known ions, it necessarily enables the discovery of new biomolecules.

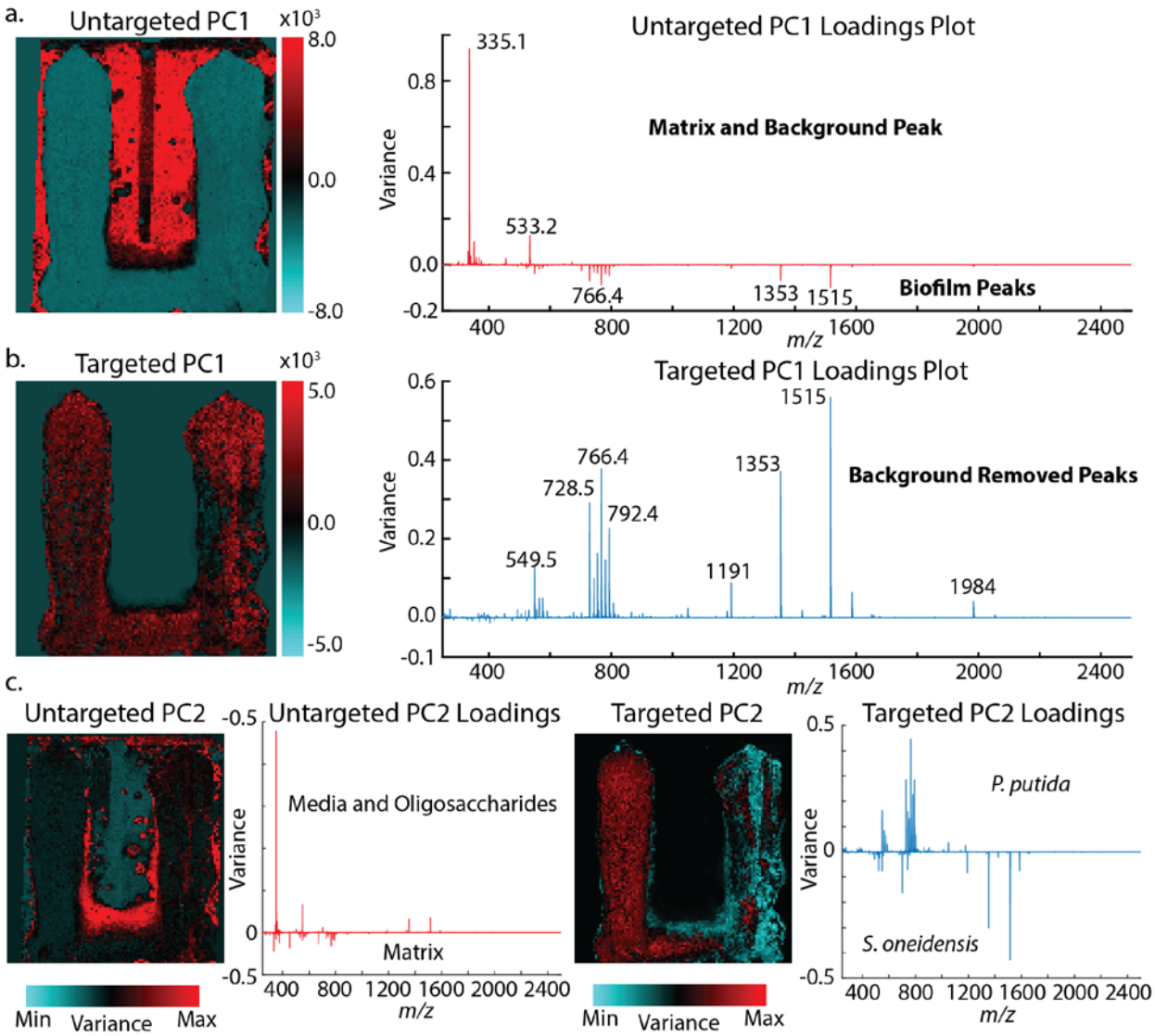

Figure 8.7. PCA of drip-flow biofilms possessed significant background contamination of media and matrix ions (**a**). Using the *m/z* ions contained in the negative loadings, a second targeted PCA analysis is performed to eliminate convoluting peaks (**b**). Removal of these obscuring analytes provides a more focused analysis in the biofilm region in subsequent PCs (**c**).

This enhanced information content can be seen in **Figure 8.7c**, where the second principal component from untargeted PCA is directly compared to the second principal component of the combined analysis. Even at the second component of the untargeted analysis the loadings are largely devoid of biofilm-specific molecules.

Performing this two-step PCA analysis on the MALDI imaging data of a *P. putida* and co-culture reveals compounds specific to the two bacterial species, with the positive loadings of PC2 corresponding to ions most abundant in *P. putida* and negative loadings corresponding to ions most abundant in *S. oneidensis* (**Figure 8.7a**). Ion images for the most significant distinguishing ions are shown in **Figure 8.8b**. It is also noteworthy that most of the lipids that we identify as being associated with *P. putida* appear on both sides of the substrate. It is possible that these same lipids are expressed by *S. oneidensis*, but further experiments are needed to determine whether or not this is the case. Several of the ions found to be distinct to one of the two species were subjected

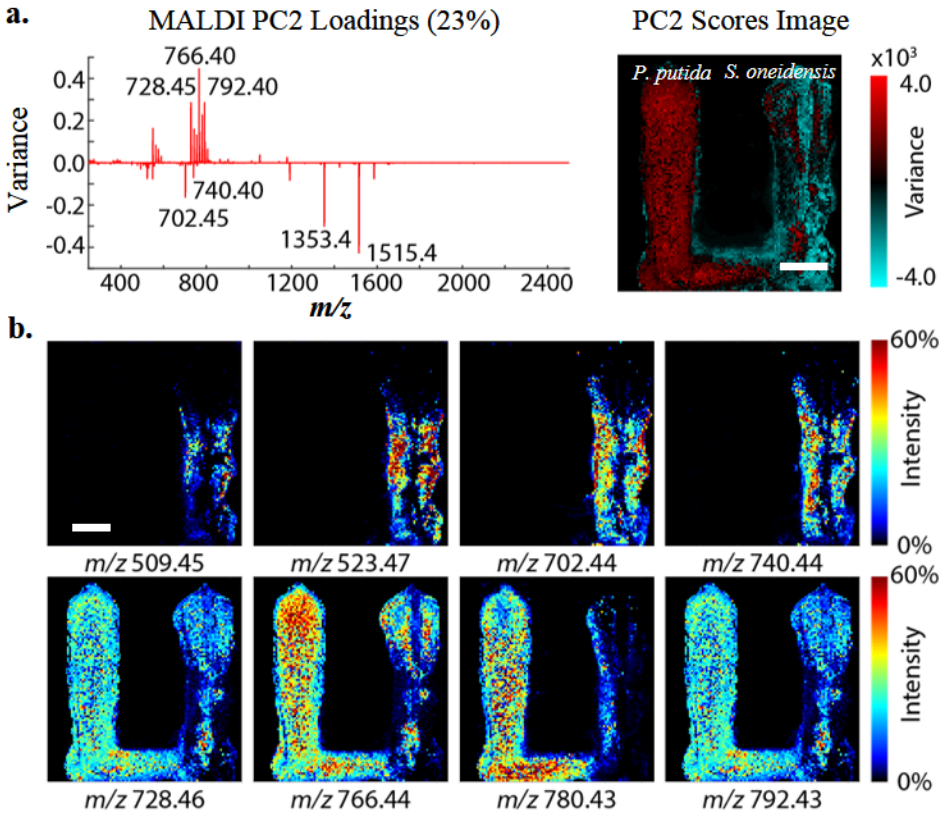

Figure 8.8. MALDI imaging followed by two-step PCA of *P. putida* (right) & *S. oneidensis* (left) co-culture biofilms. (**a**) PCA of a MALDI image set, showing separation between the two strains in PC2. (**b**) Select MALDI-MS images for ions specific to either bacterium as revealed by PCA. Scale bars represent 1 cm.

to identification via tandem MS. *P. putida* specific lipids included PE(32:1), PE(34:2), PE(35:1), and DG(33:1). *S. oneidensis* specific lipids were identified as DG(29:2) and PE(30:0).

In contrast to the MALDI imaging PCA, two-step PCA of the C_{60}-SIMS data not only pulled out ions specific to each species (data not shown), but also ions found exclusively in the interaction region (**Figure 8.9a** and **b**). Ions specific to, or more abundant in, the interaction region including *m/z* 120.1, 268.3, 417.2, 509.45, and 523.5. Attempts at identification via *in situ* SIMS tandem MS were unsuccessful due to the low abundance and specific localization. Taken together, the SIMS and MALDI results demonstrate that the DFR platform disclosed here is well suited for evaluating the spatiochemical heterogeneity of microbe-microbe interactions with MSI.

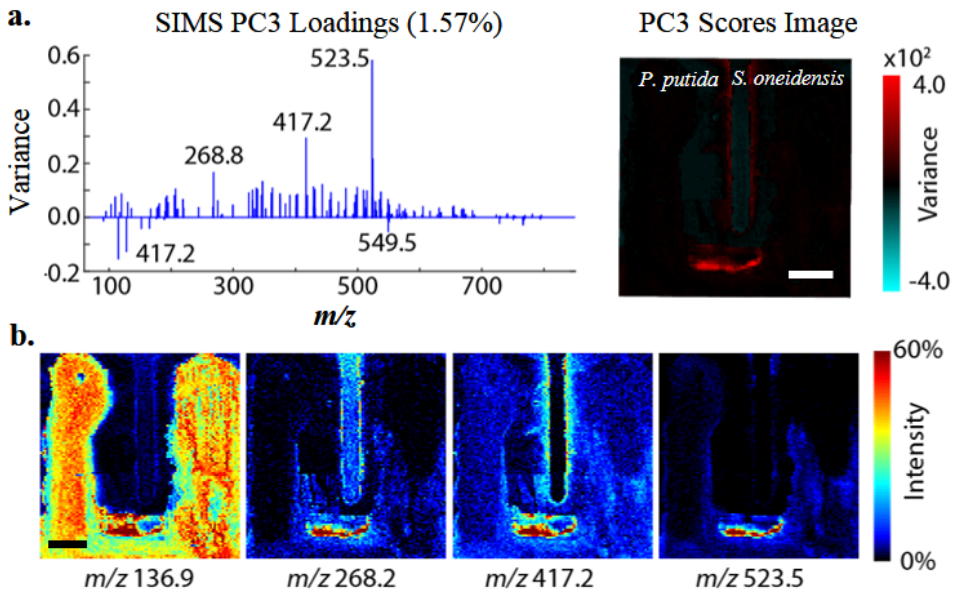

Figure 8.9. SIMS imaging followed by two-step PCA of *P. putida* (right) and *S. oneidensis* (left) co-culture biofilms. (**a**) PCA reveals ions that are almost exclusively found in the interaction region. (**b**) Ion images for the *m/z* values revealed in (**a**). Scale bars represent 1 cm.

8.4.4. Chemical, Elemental, and Morphological Investigations of Flow-Cell Biofilms on Low-Carbon Steel Reveal Features Unique to Microbial Induced Corrosion

Microbial induced corrosion (MIC) is a devastating phenomenon that threatens the integrity of the world's infrastructure – from oil and sewage pipelines, to historic buildings and military assets. MIC has a hugely negative impact on the global economy. It's estimated that the oil and gas industry alone spends more than $8 billion each year on corrosion repair and prevention, a significant portion of which is directly caused by or greatly accelerated by corrosion.[43] The scientific communities' mechanistic understanding of MIC is underdeveloped, however evidence

suggests that bacteria follow a general trend of colonizing the surface, form biofilms, and initiate the secretion of chemicals capable of oxidizing or reducing iron, sulfur, and manganese. In most cases in nature, these microbial communities are made up of multiple species, living both competitively and synergistically.[44] Because the phenomenon is inherently surface specific, and therefore multidimensional, both the spatial and chemical dimensions are necessary for true understanding of the causes and direct effects of MIC.

In this work we set out to test the viability of our platform for studying MIC by cultivating *P. putida* and *S. oneidensis* co-cultures on 304 low carbon steel (**Figure 8.10**). Other steel variants were tested, but were observed to develop either excessive amounts of corrosion, or no corrosion at all after three days of biofilm growth. **Figure 8.10a** shows an optical image for a representative sample, with *S. oneidensis* on the left and *P. putida* on the right with significant corrosion on both sides. The sample was first examined with SIMS (**Figure 8.10b** and **8.10c**), then coated in a thin layer of Au/Pd and examined with SEM and EDS (**Figure 8.10d**). The total ion count TIC image (**Figure 8.10b**) shows that the majority of the ions arise from the substrate itself, with a region of high ion abundance near the top of the *P. putida* side. Upon closer inspection the high ion abundance region was found to contain a polymer, most likely arising from sample handing. Surprisingly, Most of the ions observed in the SIMS spectra were distinct from those observed in the analogous culture on stainless steel. Our attempts at identifying the highest intensity ions were unsuccessful, but the high mass defect suggests an inorganic composition (**Figure 8.10c**). Although the chemical information garnered from this investigation was unsatisfactory, further optimization and molecular identification efforts will likely reveal molecules specific to MIC.

We next investigated specific regions of the sample using a combination of SEM and EDS (**Figure 8.10d**). The SEM images in **Figures 8.10d** labeled **i-iv** correspond to the analogously labeled regions in **Figure 8.10a**. Within the corroded section of the *S. oneidensis* side of the sample, the long pill-shaped cells appear to be damaged or partially lysed, with small holes present over their cell bodies (region **i**). Many cells are also coated in small (<1 nm) bulbous structures, which may indicate cell lysis. It is unlikely that these morphological characteristics arose from vacuum exposure as other cells in the immediate vicinity are intact. Bacteria on the *P. putida* side (region **ii**) appear to be healthier (i.e. not ruptured), however upon close inspection a filamentous phenotype can be observed. The expression of a filamentous phenotype has been previously observed in *P. putida* during environmental stressors, and is seen with *S. oneidensis* MR-1 during

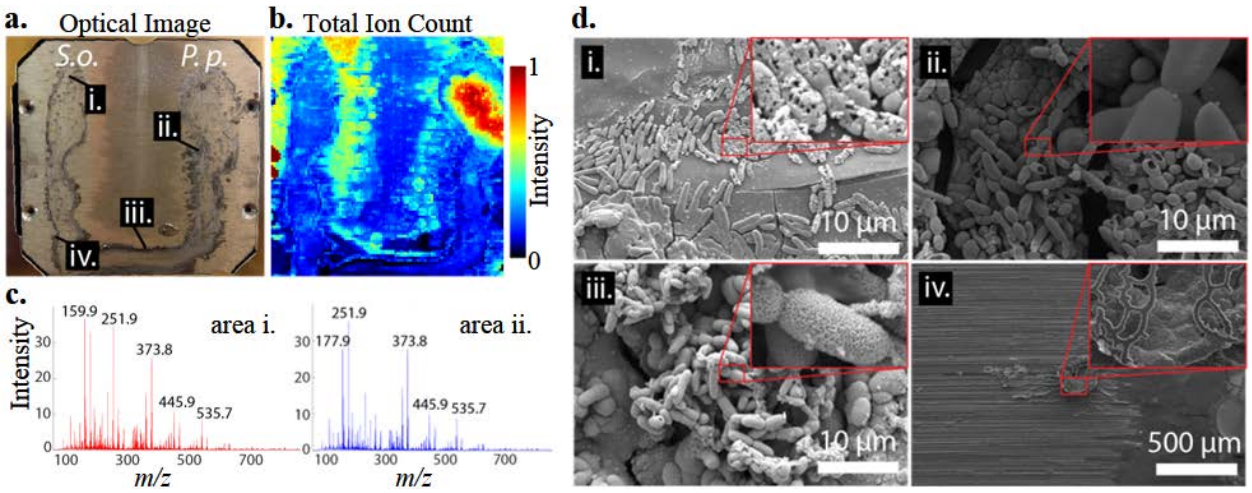

Figure 8.10. Examination of MIC of 304 low carbon steel with SIMS, and SEM: (**a**) Optical and (**b**) SIMS total ion count images of a co-culture systems on a corroded surface; (**c**) SIMS spectra of regions (**i.**) and (**iii.**) contain predominantly high mass defect ions; and (**d**) SEM of: (**i.**) Bacteria near *S. oneidensis* nutrient drip show signs of cell lysis and degradation; (**ii.**) Bacteria in the *P. putida* channel show increased size and iron oxide content on cellular wall; (**iii.**) Interaction zone bacteria that display changes in morphology; and (**iv.**) pitted surface formed during corrosion containing bacteria. Red boxes are 10× magnification with respect to the parent image.

biofilm formation and in the presence of iron.[45-46] Near the interaction zone (region **iii**) the cells appear more similar in size and shape to those observed in the *P. putida* region, and a significant quantity of iron oxide is found to be uniformly surrounding the cell with an exquisite nanostructure (**Figure 8.11**). Adhesion of iron and iron nanoparticles to *P. putida* and *S. oneidensis* has been demonstrated,[47-49] but this extent of iron oxide uniformly coating the surface of the bacteria has not been previously reported. Near the bottom of the *S. oneidensis* side of the sample (region **iv**), bacteria are packed into the corroded sections and large structures are present. Inspection with EDS reveals that these structures are primarily composed of iron oxide.

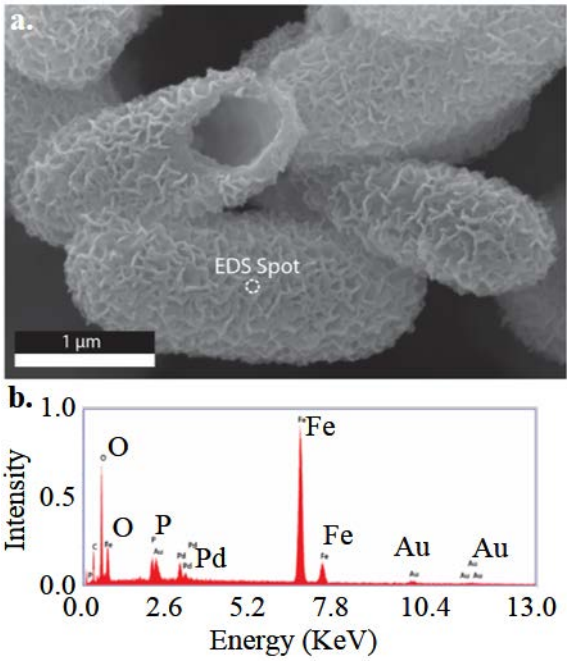

Figure 8.11. SEM and EDS of iron-coated bacteria from region **iii** of Figure 8.10 (**a**) Electron micrograph (**b**) single point EDS spectrum containing an Fe:O ratio of 0.84.

Electron microscopy investigation of a control sample containing a *P. putida* drip on one side and a nutrient only drip on the other revealed that *P. putida* actually "climbs" up the opposing channel against the nutrient flow (**Figure 8.12**).

Electron micrographs of the *P. putida* channel (**Figure 8.12a**) shows cell agglomerations covering the surface and seeding the steel crevices. As in the co-culture sample from **Figure 8.10**, these electron micrographs are mostly devoid of the hallmarks of a biofilm. Remarkably, the nutrient only channel (**Figure 8.12b**) also shows crevasses seeded with *P. putida* cell clusters. This same behavior is not observed in controls with nutrients dripped on both sides nor in controls with *S. oneidensis* on one side and media on the other, suggesting that it is not the result of reactor contamination. While more investigations are needed, this may suggest that the previously observed *P. putida* associated ions found on the *S. oneidensis* side of the coupon may actually arise from climbing *P. putida* (**Figure 8.8b**).

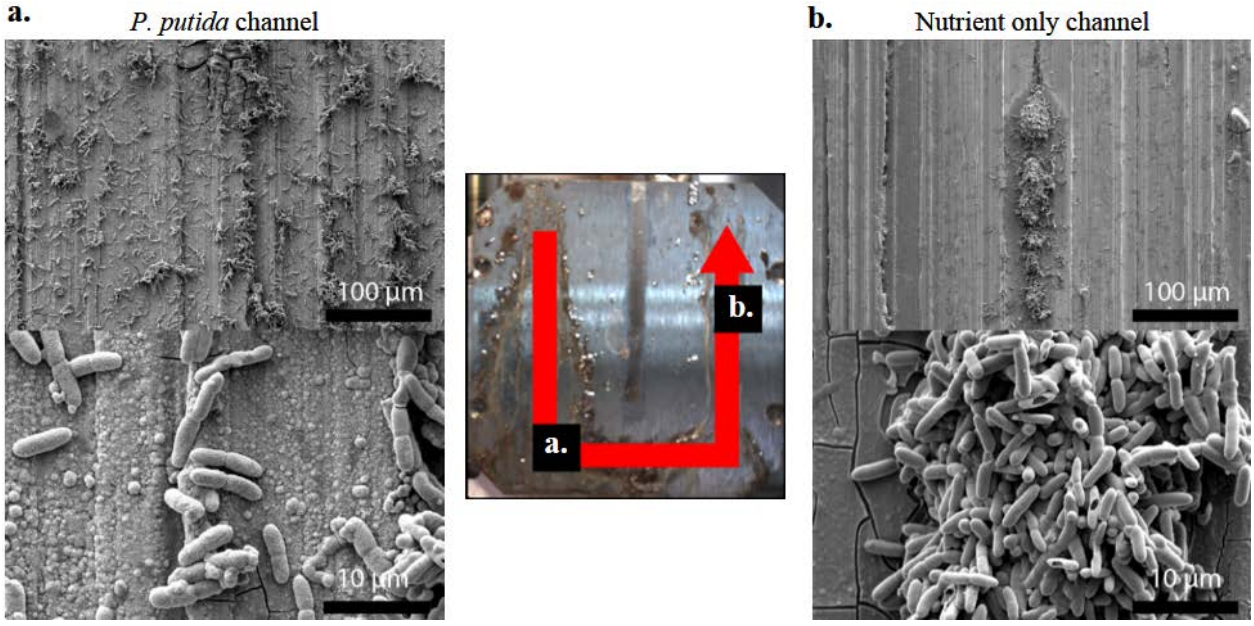

Figure 8.12. MIC control samples containing *P. putida* on the left (**a**) and a nutrient only channel on the right (**b**). Remarkably, these samples showed the presence of *P. putida* bacteria on both sides of the metal substrate, suggesting that *P. putida* actually migrates against the nutrient flow to "climb" up and colonize the opposing channel.

We are not the first to observe this phenomenon of climbing bacteria. In one noteworthy example, Shireen Kotay and coworkers seeding sink drains with green fluorescent protein expressing *Escherichia coli* and found that the bacteria climb up the drain pipe (against the flow of the waste water) at an average rate of 2.5 cm per day.[50]

8.5. Conclusions

In this work, we developed a modified DFR and applied it to a series of chemical and morphological studies of biofilms on steel substrates. Following optimization of the substrates,

growth modes, and sample preparation methodologies, we demonstrate the use of the DFR to study lipid and oligosaccharide distribution across a single culture biofilm using both MALDI and SIMS imaging. Using a combination of *in situ* tandem MS and FT-ICR MS-based accurate mass characterization of extracts, we elucidate the partial identity of lipids and oligosaccharides expressed by biofilm-bound *P. putida* and map their distribution across the colony surface.

We studied a co-culture system comprised of *P. putida* and *S. oneidensis* on stainless steel using a combination of SIMS and MALDI imaging followed by two-step imaging PCA. This study revealed ions exclusively associated with each species, as well as ions found to be elevated in the interaction zone. Next, we examined an MIC sample comprised of a low-carbon steel coupon with a co-culture of *P. putida* and *S. oneidensis*. SIMS imaging revealed several ions that could only be found during MIC. Follow-up SEM analysis showed clumps of bacteria residing in crevasses, many of which were expressing the filamentous phenotype. Remarkably, most of the growth appeared to be occurring without the presence of a strong biofilm phenotype, and many of the cells were coated in iron oxide.

This work establishes (among other avenues) a platform for studying biofilm metabolites and biomarkers, the interaction of multiple microbial species, and the ability to alter the environment for the study of MIC. The coupling of MSI with SEM and EDS provides a valuable opportunity to correlate unbiased and untargeted chemical information with biofilm morphology and microbial distribution. The highly adaptable DFR and associated methods described here can be applied and extended to monitor the spatially adaptive response of bacterial biofilms under a wide variety of experimental conditions.

8.6. References

1. Rodney, M. D., Biofilms: Microbial Life on Surfaces. *Emerging Infectious Disease journal* **2002,** *8* (9), 881.
2. Flemming, H.-C.; Wingender, J., The biofilm matrix. *Nature Reviews Microbiology* **2010,** *8* (9), 623-633.
3. Hall-Stoodley, L.; Costerton, J. W.; Stoodley, P., Bacterial biofilms: from the Natural environment to infectious diseases. *Nat Rev Micro* **2004,** *2* (2), 95-108.
4. Beech, I. B.; Sunner, J., Biocorrosion: towards understanding interactions between biofilms and metals. *Current Opinion in Biotechnology* **2004,** *15* (3), 181-186.
5. Dunham, S. J. B.; Ellis, J. F.; Li, B.; Sweedler, J. V., Mass Spectrometry Imaging of Complex Microbial Communities. *Accounts of Chemical Research* **2017,** *50* (1), 96-104.
6. Vertes, A.; Hitchins, V.; Phillips, K. S., Analytical Challenges of Microbial Biofilms on Medical Devices. *Analytical Chemistry* **2012,** *84* (9), 3858-3866.

7. Dunham, S. J.; Ellis, J. F.; Li, B.; Sweedler, J. V., Mass Spectrometry Imaging of Complex Microbial Communities. *Acc Chem Res* **2017,** *50* (1), 96-104.
8. Beech, W. B.; Sunner, J., Biocorrosion: towards understanding interactions between biofilms and metals. *Curr Opin Biotech* **2004,** *15* (3), 181-186.
9. Parsek, M. R.; Singh, P. K., Bacterial biofilms: an emerging link to disease pathogenesis. *Annual Reviews in Microbiology* **2003,** *57* (1), 677-701.
10. Cornett, D. S.; Reyzer, M. L.; Chaurand, P.; Caprioli, R. M., MALDI imaging mass spectrometry: molecular snapshots of biochemical systems. *Nat Meth* **2007,** *4* (10), 828-833.
11. Yang, J. Y.; Phelan, V. V.; Simkovsky, R.; Watrous, J. D.; Trial, R. M.; Fleming, T. C.; Wenter, R.; Moore, B. S.; Golden, S. S.; Pogliano, K.; Dorrestein, P. C., Primer on Agar-Based Microbial Imaging Mass Spectrometry. *Journal of Bacteriology* **2012,** *194* (22), 6023-6028.
12. Dunham, S. J. B.; Comi, T. J.; Ko, K.; Li, B.; Baig, N. F.; Morales-Soto, N.; Shrout, J. D.; Bohn, P. W.; Sweedler, J. V., Metal-assisted polyatomic SIMS and laser desorption/ionization for enhanced small molecule imaging of bacterial biofilms. *Biointerphases* **2016,** *11* (2), 02A325.
13. Lanni, E. J.; Masyuko, R. N.; Driscoll, C. M.; Aerts, J. T.; Shrout, J. D.; Bohn, P. W.; Sweedler, J. V., MALDI-guided SIMS: Multiscale Imaging of Metabolites in Bacterial Biofilms. *Analytical Chemistry* **2014,** *86* (18), 9139-9145.
14. Si, T.; Li, B.; Zhang, K.; Xu, Y.; Zhao, H.; Sweedler, J. V., Characterization of Bacillus subtilis Colony Biofilms via Mass Spectrometry and Fluorescence Imaging. *Journal of Proteome Research* **2016,** *15* (6), 1955-1962.
15. Wang, G.; Chai, K.; Wu, J. Y.; Liu, F. C., Effect of Pseudomonas putida on the degradation of epoxy resin varnish coating in seawater. *Int Biodeter Biodegr* **2016,** *115*, 156-163.
16. Li, H. B.; Zhou, E. Z.; Zhang, D. W.; Xu, D. K.; Xia, J.; Yang, C. G.; Feng, H.; Jiang, Z. H.; Li, X. G.; Gu, T. Y.; Yang, K., Microbiologically Influenced Corrosion of 2707 Hyper-Duplex Stainless Steel by Marine Pseudomonas aeruginosa Biofilm. *Sci Rep-Uk* **2016,** *6*.
17. Bretschger, O.; Obraztsova, A.; Sturm, C. A.; Chang, I. S.; Gorby, Y. A.; Reed, S. B.; Culley, D. E.; Reardon, C. L.; Barua, S.; Romine, M. F.; Zhou, J.; Beliaev, A. S.; Bouhenni, R.; Saffarini, D.; Mansfeld, F.; Kim, B.-H.; Fredrickson, J. K.; Nealson, K. H., Current Production and Metal Oxide Reduction by Shewanella oneidensis MR-1 Wild Type and Mutants. *Applied and Environmental Microbiology* **2007,** *73* (21), 7003-7012.
18. Wang, V. B.; Chua, S.-L.; Cai, Z.; Sivakumar, K.; Zhang, Q.; Kjelleberg, S.; Cao, B.; Loo, S. C. J.; Yang, L., A stable synergistic microbial consortium for simultaneous azo dye removal and bioelectricity generation. *Bioresource Technology* **2014,** *155*, 71-76.
19. Lanni, E. J.; Dunham, S. J. B.; Nemes, P.; Rubakhin, S. S.; Sweedler, J. V., Biomolecular Imaging with a C60-SIMS/MALDI Dual Ion Source Hybrid Mass Spectrometer: Instrumentation, Matrix Enhancement, and Single Cell Analysis. *Journal of The American Society for Mass Spectrometry* **2014,** *25* (11), 1897-1907.
20. Chambers, M. C.; Maclean, B.; Burke, R.; Amodei, D.; Ruderman, D. L.; Neumann, S.; Gatto, L.; Fischer, B.; Pratt, B.; Egertson, J.; Hoff, K.; Kessner, D.; Tasman, N.; Shulman, N.; Frewen, B.; Baker, T. A.; Brusniak, M.-Y.; Paulse, C.; Creasy, D.; Flashner, L.; Kani, K.; Moulding, C.; Seymour, S. L.; Nuwaysir, L. M.; Lefebvre, B.; Kuhlmann, F.; Roark, J.; Rainer, P.; Detlev, S.; Hemenway, T.; Huhmer, A.; Langridge, J.; Connolly, B.; Chadick, T.; Holly, K.; Eckels, J.; Deutsch, E. W.; Moritz, R. L.; Katz, J. E.; Agus, D. B.; MacCoss, M.; Tabb, D. L.; Mallick, P., A cross-platform toolkit for mass spectrometry and proteomics. *Nat Biotech* **2012,** *30* (10), 918-920.
21. Race, A. M.; Styles, I. B.; Bunch, J., Inclusive sharing of mass spectrometry imaging data requires a converter for all. *Journal of Proteomics* **2012,** *75* (16), 5111-5112.
22. Robichaud, G.; Garrard, K. P.; Barry, J. A.; Muddiman, D. C., MSiReader: An Open-Source Interface to View and Analyze High Resolving Power MS Imaging Files on Matlab Platform. *Journal of The American Society for Mass Spectrometry* **2013,** *24* (5), 718-721.

23. Li, B.; Comi, T. J.; Si, T.; Dunham, S. J. B.; Sweedler, J. V., A one-step matrix application method for MALDI mass spectrometry imaging of bacterial colony biofilms. *Journal of Mass Spectrometry* **2016,** *51* (11), 1030-1035.
24. Yang, J. Y.; Phelan, V. V.; Simkovsky, R.; Watrous, J. D.; Trial, R. M.; Fleming, T. C.; Wenter, R.; Moore, B. S.; Golden, S. S.; Pogliano, K.; Dorrestein, P. C., Primer on agar-based microbial imaging mass spectrometry. *J. Bacteriol.* **2012,** *194* (22), 6023-8.
25. Goeres, D. M.; Hamilton, M. A.; Beck, N. A.; Buckingham-Meyer, K.; Hilyard, J. D.; Loetterle, L. R.; Lorenz, L. A.; Walker, D. K.; Stewart, P. S., A method for growing a biofilm under low shear at the air-liquid interface using the drip flow biofilm reactor. *Nat. Protocols* **2009,** *4* (5), 783-788.
26. Nikel, P. I.; Martinez-Garcia, E.; de Lorenzo, V., Biotechnological domestication of pseudomonads using synthetic biology. *Nat Rev Micro* **2014,** *12* (5), 368-379.
27. van Baar, B. L. M., Characterisation of bacteria by matrix-assisted laser desorption/ionisation and electrospray mass spectrometry. *FEMS Microbiology Reviews* **2000,** *24* (2), 193-219.
28. Zhang, Y. M.; Rock, C. O., Membrane lipid homeostasis in bacteria. *Nat Rev Microbiol* **2008,** *6* (3), 222-33.
29. Goto-Inoue, N.; Hayasaka, T.; Zaima, N.; Setou, M., Imaging mass spectrometry for lipidomics. *Biochim Biophys Acta* **2011,** *1811* (11), 961-9.
30. Diggle, S. P.; Lumjiaktase, P.; Dipilato, F.; Winzer, K.; Kunakorn, M.; Barrett, D. A.; Chhabra, S. R.; Camara, M.; Williams, P., Functional genetic analysis reveals a 2-alkyl-4-quinolone signaling system in the human pathogen Burkholderia pseudomallei and related bacteria. *Chemistry & Biology* **2006,** *13* (7), 701-710.
31. Steidle, A.; Allesen-Holm, M.; Riedel, K.; Berg, G.; Givskov, M.; Molin, S.; Eberl, L., Identification and characterization of an N-acylhomoserine lactone-dependent quorum-sensing system in Pseudomonas putida strain IsoF. *Applied and Environmental Microbiology* **2002,** *68* (12), 6371-82.
32. Dunham, S. J.; Comi, T. J.; Ko, K.; Li, B.; Baig, N. F.; Morales-Soto, N.; Shrout, J. D.; Bohn, P. W.; Sweedler, J. V., Metal-assisted polyatomic SIMS and laser desorption/ionization for enhanced small molecule imaging of bacterial biofilms. *Biointerphases* **2016,** *11* (2), 02A325.
33. Baig, N. F.; Dunham, S. J.; Morales-Soto, N.; Shrout, J. D.; Sweedler, J. V.; Bohn, P. W., Multimodal chemical imaging of molecular messengers in emerging Pseudomonas aeruginosa bacterial communities. *Analyst* **2015,** *140* (19), 6544-52.
34. Gidden, J.; Denson, J.; Liyanage, R.; Ivey, D. M.; Lay, J. O., Lipid Compositions in Escherichia coli and Bacillus subtilis During Growth as Determined by MALDI-TOF and TOF/TOF Mass Spectrometry. *International journal of mass spectrometry* **2009,** *283* (1-3), 178-184.
35. Marto, J. A.; White, F. M.; Seldomridge, S.; Marshall, A. G., Structural Characterization of Phospholipids by Matrix-Assisted Laser Desorption/Ionization Fourier Transform Ion Cyclotron Resonance Mass Spectrometry. *Analytical Chemistry* **1995,** *67* (21), 3979-3984.
36. Fang, J.; Barcelona, M. J.; Alvarez, P. J. J., A direct comparison between fatty acid analysis and intact phospholipid profiling for microbial identification. *Organic Geochemistry* **2000,** *31* (9), 881-887.
37. Pinkart, H. C.; White, D. C., Phospholipid biosynthesis and solvent tolerance in Pseudomonas putida strains. *Journal of bacteriology* **1997,** *179* (13), 4219-26.
38. Fang, J.; Barcelona, M. J.; Alvarez, P. J. J., Phospholipid compositional changes of five pseudomonad archetypes grown with and without toluene. *Applied Microbiology and Biotechnology* **2000,** *54* (3), 382-389.
39. Carrasco, S.; Mérida, I., Diacylglycerol, when simplicity becomes complex. *Trends in Biochemical Sciences* **2007,** *32* (1), 27-36.
40. Rhome, R.; Del Poeta, M., Lipid signaling in pathogenic fungi. *Annu Rev Microbiol* **2009,** *63*, 119-31.
41. Benamara, H.; Rihouey, C.; Abbes, I.; Ben Mlouka, M. A.; Hardouin, J.; Jouenne, T.; Alexandre, S., Characterization of Membrane Lipidome Changes in Pseudomonas aeruginosa during Biofilm Growth on Glass Wool. *PLOS ONE* **2014,** *9* (9), e108478.
42. Jones, E. A.; Deininger, S.-O.; Hogendoorn, P. C. W.; Deelder, A. M.; McDonnell, L. A., Imaging mass spectrometry statistical analysis. *Journal of Proteomics* **2012,** *75* (16), 4962-4989.

43. Bartling, C., Microbially Induced Corrosion: Silent Killer of Infrastructure. *Pipeline and Gas Journal* **2016,** *243* (1).
44. Kip, N.; van Veen, J. A., The dual role of microbes in corrosion. *The ISME Journal* **2015,** *9* (3), 542-551.
45. Godeke, J.; Paul, K.; Lassak, J.; Thormann, K. M., Phage-induced lysis enhances biofilm formation in Shewanella oneidensis MR-1. *ISME J* **2011,** *5* (4), 613-626.
46. Binnenkade, L.; Teichmann, L.; Thormann, K. M., Iron Triggers λSo Prophage Induction and Release of Extracellular DNA in Shewanella oneidensis MR-1 Biofilms. *Applied and Environmental Microbiology* **2014,** *80* (17), 5304-5316.
47. Parikh, S. J.; Chorover, J., ATR-FTIR spectroscopy reveals bond formation during bacterial adhesion to iron oxide. *Langmuir* **2006,** *22* (20), 8492-500.
48. Li, B.; Logan, B. E., Bacterial adhesion to glass and metal-oxide surfaces. *Colloids Surf. B. Biointerfaces* **2004,** *36* (2), 81-90.
49. Lee, A. K.; Newman, D. K., Microbial iron respiration: impacts on corrosion processes. *Appl. Microbiol. Biotechnol.* **2003,** *62* (2-3), 134-9.
50. Kotay, S.; Chai, W.; Guilford, W.; Barry, K.; Mathers, A. J., Spread from the Sink to the Patient: in situ Study Using Green Fluorescent Protein (GFP) Expressing- Escherichia coli to Model Bacterial Dispersion from Hand Washing Sink Trap Reservoirs. *Applied and Environmental Microbiology* **2017**.